Nanotechnology of Pinning Centres in High Temperature Superconducting $YBa_2Cu_3O_7$ Films

By

Van-Son Dang

UNIVERSITY OF BIRMINGHAM

A thesis submitted to The University of Birmingham for the degree of

DOCTOR OF PHILOSOPHY

School of Metallurgy and Materials

The University of Birmingham

December 2010

Abstract

For cost-efficient power applications of superconducting coated conductors based on $YBa_2Cu_3O_7$ (YBCO) films, in applied fields or in self-field, further improvement of critical current by artificial flux pinning centres is required. This project investigated the increase in critical current density (J_c) and related physical properties of YBCO films by self-assembling nanotechnology of pinning centres, using substrate decoration, quasi-multilayers (using noble metals and $PrBa_2Cu_3O_7$ (PBCO) in both cases), and targets containing $BaZrO_3$ (BZO) nano-inclusions.

Samples were prepared by pulsed laser deposition (PLD) on single crystal $SrTiO_3$ (STO) substrates and on Ni-W Rolling-Assisted Biaxially Textured Substrates (RABiTS). Optical lithography and chemical etching were used to prepare samples for transport measurements. The superconducting properties were characterised by AC susceptibility, magnetisation loops and transport measurements using a “Quantum Design” Magnetic Property Measurement System (MPMS) and a Physical Properties Measurement System (PPMS). Scanning and Transmission Electron Microscopy (SEM) and (TEM), Atomic Force Microscopy (AFM) and X-ray diffraction were also used to characterise the micro-structure of the films and the structure of artificially-induced pinning centres.

The optimum conditions for the growth of YBCO films, Ag and PBCO nano-dots, and BZO nano-columns were investigated. Combinations of all three nanostructuring approaches resulted in a maximum J_c in applied fields and self-field. The related physical properties such as angular dependence of J_c, vortex melting line, pinning force, frequency dependence of J_c, were also investigated to understand pinning mechanisms in the films. The combination of Ag

nano-dots and BZO nano-inclusions in the YBCO target provided the greatest improvement of critical currents of the film in applied fields.

Dedicated to my late father

Acknowledgements

My work could not be done without much help from many people. Firstly, I am grateful to my co-supervisor, Dr. Adrian Crisan, for trusting in me by accepting me in his EU Marie Curie Excellence Team and for his valuable guidance during my work and to my co-supervisor Prof. John Stuart Abell for his supervision, discussions and suggestions throughout my PhD research in The University of Birmingham. This work was supported financially by the European Commission through the Marie Curie Excellence Grant "NanoTechPinningHTS".

Secondly, I would like to thank Dr. P. Mikheenko for training me to use many experimental types of equipment and to perform several measurements. Many magnetic and transport measurements presented in this project were performed by Dr. Mikheenko, as part of his duties in the MC team.

Thirdly, I would like to thank all my colleagues: Dr. A. Sarkar for doing FIB, Mr. M. M. Awang Kechik, Dr J. Tanner, for good cooperation in doing experiments. I would like to thank Mr Andy Bradshaw and Dr. M. Chu for technical help on PLD and TEM, respectively.

I would like to thank 3-Cs Limited for supplying Ni:5W substrates for our experiments.

Last but not least I would like to thank my family, especially my wife who has supported me a lot while I have been working in The University of Birmingham.

Abbreviations

AC	Alternating current
AFM	Atomic force microscopy
Ag	Silver
Al	Aluminium
APC	Artificial pinning centre
Au	Gold
BCS	Bardeen, Cooper, Schrieffer theory
BZO	Barium zirconate oxides ($BaZrO_3$)
CC	Coated conductor
DC	Direct current
EBSD	Electron backscattered diffraction
EDS	Energy dispersive spectroscopy
F	Frequency
f_0	macroscopic attempt of about 10^6 Hz
FIB	Focused ion beam
F_p	Pinning force
h_{ac}	AC field amplitude
H_c	Critical magnetic field
H_i	Irreversibility field
Hg	Mercury
HTS	High temperature superconductor
IBAD	Ion beam assisted deposition
I_c	Critical current
J_c	Critical current density
MPMS	Magnetic property measurement system
Nb	Niobium
Ni:5W	Nickel-tungsten intermetallic compound
Pb	Lead
PBCO	$PrBa_2Cu_3O_7$
PLD	Pulsed laser deposition

PPMS	Physical properties measurement system
RABiTS	Rolling assisted biaxially textured substrate
REBCO	(Rare earth)$Ba_2Cu_3O_7$
SEM	Scanning electron microscopy
Sn	Tin
STEM	Scanning transmission electron microscopy
STO	$SrTiO_3$
T_c	Critical temperature
T_i	Irreversibility temperature
TEM	Transmission electron microscopy
T_m	Vortex melting temperature
U_0	Pinning potential
XRD	X-ray diffraction
YBCO	$YBa_2Cu_3O_7$
YSZ	Yttria-stabilised zirconia
Y-CC	Thin superconducting film on flexible metallic substrate
χ	Susceptibility
$\chi 3$	Third-harmonic susceptibility
γ	Anisotropic factor
λ	Penetration depth
ζ	Coherence length

Contents

List of publications

1. A. Crisan. A. Sarkar, P. Mikheenko, V.S. Dang, M.M. Awang Kechik, J.S. Abell *"Improvement of Pinning Force and Critical Current Density in Thick YBa2Cu3O7−δ Films Grown on SrTiO3 Substrates Decorated with LaNiO3 Nanodots"* J Supercond Nov Magn **22** (2009) 631-636
2. M M Awang Kechick, P Mikheenko, A Sarkar, V S Dang, N Hari Babu, D A Cardwell, J S Abell and A Crisan " *Artificial pinning centres in $YBa_2Cu_3O_{7-d}$ thin films by $Gd_2Ba_4CuWO_y$ nanophase inclusions"* Supercond. Sci. Technol. 22 (2009) 034020 (5pp)
3. **A. Crisan , M. M. Awang Kechick, P. Mikheenko, V. S. Dang, A. Sarkar, J. S. Abell, P Paturi, and H Huhtinen *"Critical current density and pinning potential in YBa2Cu3O7−δ thick films ablated from a BaZrO3-doped nanocrystalline target"* Supercond. Sci. Technol. 22 (2009) 045014 (5pp)**
4. **A. Crisan, V.S. Dang, P. Mikheenko, A. Sarkar, J.S. Abell *"Pinning potential in thick PrBa2Cu3Ox/YBa2Cu3O7-δ quasi-multilayers"* Physica C 470 (2010) 55-60**
5. **P. Mikheenko, A. Sarkar, V.S. Dang, J.L. Tanner, M.M. Awang Kechik, J.S. Abell, A. Crisan *"Pinning centres induced in YBCO films by nano-dots in substrate decoration and quasi-superlattice approaches"* IEEE transaction on Appl. Super. 19 (2009) 3491**
6. **P. Mikheenko, A. Sarkar, V.-S. Dang, J.L. Tanner, J.S. Abell, A. Crisan *"c-Axis correlated extended defects and critical current in YBa2Cu3Ox films grown on Au and Ag-nano dot decorated substrates"* Physica C. 469 (2009) 798–804**
7. A. Sarkar, P. Mikheenko, V.S. Dang, J.S. Abell, A. Crisan *"Enhancing critical current in YBCO thick films: Substrate decoration and quasi-superlattice approach"* Physica C 469 (2009) 1550–1553
8. **V. S. Dang, P. Mikheenko, A. Sarkar, M. M. Awang Kechik, J S Abell1 and A Crisan *"Critical current density and pinning in Ag/YBa2Cu3Ox and PrBa2Cu3Oy/YBa2Cu3Ox multilayers"* J. Phys.: Conf. Ser. 234 (2010) 012010**
9. **P Mikheenko, J S Abell, A Sarkar, V S Dang, M M Awang Kechik, J L Tanner, P Paturi, H Huhtinen, N Hari Babu, D A Cardwell and A Crisan "*Self-assembled artificial pinning centres in thick YBCO superconducting films*" J. Phys.: Conf. Ser. 234 (2010) 022022**

10. **V. S. Dang, P. Mikheenko, A. Sarkar, M. M. Awang Kechik, J S Abell1 and A Crisan *"Increased critical current density and pinning in thick Ag/YBa2Cu3O7-x multilayers"* Physica C, 470 (2010) 1238**
11. **A. Crisan, P. Mikheenko, A. Sarkar, V. S. Dang, M. M. Awang Kechik, J. S. Abell, P. Paturi, H. Huhtinen *"Artificial pinning in thick YBCO films: Pinning potential and* c*-axis correlation"* Physica C,470 (2010) 840**
12. **P. Mikheenko, J.L. Tanner, J. Bowen, A. Sarkar, V.-S. Dang, J.S. Abell, A. Crisan *"Nanodots induced columnar growth of $YBa_2Cu_3O_x$ films"* Physica C, 470 (2010) S234-S236**
13. A. Sarkar, V.S. Dang; P. Mikheenko; M.M Awang Kechik; J.S. Abell; A. Crisan "*Improved critical current densities in thick $YBa_2Cu_3O_{7-x}$ multilayer films interspaced with non-superconducting $YBa_2Cu_3O_x$ nanodots*" Thin Solid films, 519(2010) 876.
14. **P Mikheenko, V-S Dang, Y Y Tse, M M Awang Kechik, P Paturi, H Huhtinen, Y Wang, A Sarkar, J S Abell and A Crisan *"Integrated nanotechnology of pinning centers in $YBa_2Cu_3O_x$ films"* Supercond. Sci. Technol. 23 (2010) 125007**
15. **V. S. Dang, A. Sarkar, P. Mikheenko, M. M. Awang Kechik, J. S. Abell, P. Paturi, H. Huhtinen, A. Crisan *"Combination of Ag Substrate Decoration with Introduction of BaZrO3 Nano-Inclusions for Enhancing Critical Current Density of YBa2Cu3O7 Films"* J Supercond Nov Magn, Accepted**, DOI: 10.1007/s10948-010-0981-8
16. **P. Mikheenko, V.S. Dang, M.M. Awang Kechik , Y. Wang, A. Sarkar, J.L. Tanner, J. S. Abell, A. Crisan *"Nano Techniques for Enhancing Critical Current in Superconducting YBCO Films"* J Supercond Nov Magn, Accepted**, DOI: 10.1007/s10948-010-0861-2
17. A. Sarkar, P. Mikheenko, V.S. Dang, M.M. Awang Kechik, J. S. Abell, A. Crisan "*Improved Critical Current Densities in $YBa_2Cu_3O_{7-\delta}$ Multilayer Films Interspaced with Palladium Nanodots*" J Supercond Nov Magn, Accepted, DOI: 10.1007/s10948-010-0914-6
18. **P. Mikheenko, V.-S. Dang, M. M. Awang Kechik, A. Sarkar, P. Paturi, H. Huhtinen, J. S. Abell and A. Crisan *"Synergetic pinning centers in $YBa_2Cu_3O_x$ films through a combination of Ag nano-dot substrate decoration, Ag/YBCO quasi-multilayers, and the use of $BaZrO_3$-doped target"* IEEE Trans. Appl. Supercond. Accepted**, DOI: 10.1109/TASC.2010.2086041

Chapter 1. **Introduction**

1.1 Nano-Artificial pinning centres in HTS

Not so long after the discovery of the high-temperature superconductor (HTS) $YBa_2Cu_3O_7$ (YBCO) in 1987 [1], a world-wide research effort led to the demonstration of a wide range of applications, based on both HTS thin films (cryo-electronic devices) and on HTS wires, tapes and conductors (power devices), with the potential of making a huge impact on science, technology, sustainable growth and quality of life. However, a few serious problems are still remaining to be solved. The most concerning is the thermally-activated movement of magnetic flux lines (vortices), which can be suppressed by sufficiently strong pinning centres in the HTS material. So, engineering of artificial pinning centres and fundamental studies regarding their effects on the vortex dynamics and other superconducting (SC) properties are of great importance for science and technology of HTS, and, consequently, for the market penetration of HTS devices.

In HTS, critical current density (J_c) is determined by the pinning of flux lines through crystalline defects [2] such as dislocations, grain and twin boundaries, non-superconducting precipitates… Although the natural growth-induced defect density in epitaxial thin films is already much higher than in bulk material, allowing critical current density at 77 K of about 10^6 A/cm^2, their density are often too small to maintain sufficiently high critical currents in a technically relevant magnetic field [3]. Many groups demonstrated that an improvement of J_c can be obtained by the introduction of artificial defects acting as pinning centres. A number of different methods have been successfully used to enhance J_c in thin films in which heavy-ion and neutron irradiation proved to be very efficient, but less suitable than alternative routes for practical applications [4, 5, 6]. Another successful approach was through doping with various elements and compounds, like Zn, $BaZrO_3$, LiF, Ca, etc., [7-11], that proved to be useful also

for polycrystalline superconductors due to the attractive interaction between intra- and inter-granular vortices [12, 13]. In HTS films, regular arrays of (sub)-micron defects (holes, metallic and magnetic dots) fabricated through photolithography were shown to pin the magnetic flux lines [14, 15].

The earliest cost-effective method used for introducing artificial pinning centres in superconducting films was the so-called substrate decoration approach [16] that consists of growing nano-scale islands (nano-dots) of certain non-superconducting materials on the substrate prior to the deposition of the superconducting thin film. Later on, two other approaches proved to be successful in the nanotechnology of pinning centres: building up a layered distribution of a second phase using multilayer deposition (quasi-superlattices) [17], and, secondly, by the distribution of a secondary phase in the film achieved by a modified target composition [18]. Several materials have now been used as nano-scale pinning centres. In the case of substrate decoration, Ag nano-dots were first used for Tl-based superconducting films [16, 19-20] and then for $YBa_2Cu_3O_{7-\delta}$ (YBCO) grown by Pulsed Laser Deposition (PLD) [21], followed by MgO [22], Y_2O_3 [23, 24], Ce_2O_3 [25], Ir [26], Au and Pd [27]. For the quasi-superlattices (quasi-multilayers) approach the nano-dot materials used till now are Y_2BaCuO_5 [17], Y_2O_3 [28, 29], yttria stabilized zirconia (YSZ) [30], Ba*TM*O_3 (*TM* = transition metal = Ir, Ti, Zr, Hf) [31], transition metals [32], Ag, Au, Pd and non-superconducting YBCO [27]. In the case of compositionally changed targets, $BaZrO_3$ (BZO) has been used most commonly as an impurity addition to $YBa_2Cu_3O_{7-\delta}$ targets [18, 34, 35]. More recently, $BaNb_2O_6$ and $BaSnO_3$ have been added as impurities to $ErBa_2Cu_3O_{7-\delta}$ targets [36, 37], $BaSnO_3$ has been added to YBCO [37], $Gd_2Ba_4CuWO_{12}$ was added to YBCO targets [38, 39] and *RE*TaO_7 (*RE* = rare earth = Er, Gd, Yb) was also added to YBCO targets [40], RE was also mixed to YBCO targets [41].

In this project, we present a very high critical current of YBCO films deposited on Ag nanoparticles substrate decoration and Ag/YBCO quasi-superlattices with thickness of several microns. This is a very promising deposition route for applications and suitable for further study. Furthermore, $PrBa_2Cu_3O_7$ (PBCO) which has a crystal structure close to that of YBCO was first used in this project as a substrate decoration material with results showing an improvement of J_c in high applied fields. In the last part of this thesis, the combination of Ag nano-dots substrate decoration with self-organisation of BZO nano-rods was first presented on $SrTiO_3$ (STO) single crystal substrate and "rolling assisted biaxially textured substrate" (RABiTS) Ni:5W substrate which show a large improvement of J_c in applied fields. The physical properties of the films such as isotropic flux pinning, vortex melting line were also studied by transport critical current measurement and TEM. Most of our results have been published in international journals since 2009 as seen in the publications list.

1.2 Objectives

This project was supported by a Marie Curie Excellent Grant; the objectives of the research and the methodological approach follow a logical sequence of film preparation:

- Finding the best materials suitable for 3D growth and controlling nano-dots architecture; Ag and PBCO were chosen to try in the first stage. The type of growth in the initial stage (3D or 2D) was determined by substrate material, nano-dots material and the growth conditions (temperature, gas pressure, and target-substrate distance, laser pulse energy, laser repetition and number of shots). For both YBCO films on flexible metallic substrate (Ni:5W) (Y-CC) and YBCO thin films on STO, the task of finding suitable materials and deposition conditions for nano-dots is a trial-and-error approach, implying a certain number of PLD depositions in various conditions and surface studies using AFM to establish the

type of growth and the correlations between materials, growth conditions and nano-dots architecture (dimensions and mean surface density of the self-assembled nano-dots) in the case of 3D growth.

- Growth of YBCO thin films, BZO-doped YBCO on STO and Ni:5W substrates with and without nano-dots. On various conditions of interest with 3D nano-dots of various materials and architecture, films have been grown by PLD. For comparison, control samples without nano-dots have been grown in similar conditions.

- Structural characterisation of nano-dots induced pinning centres, of YBCO, BZO-doped YBCO thin films, and Y-CC. Depending on the lattice mismatch between YBCO and nano-dots material, the existence or non-existence of chemical poisoning and the occurrence/absence of diffusion, several types of extended defects can appear, in addition to the very existence of nano-scale particles embedded in the YBCO matrix, which are: dislocations, columnar defects (columns of non-superconducting material), and δT_c pinning centres. On the other hand, the presence of nano-dots may influence the structural properties of YBCO, BZO-doped YBCO thin films and Y-CC. All these have been extensively investigated by X-ray diffraction, Scanning Electron Microscopy (SEM) with Energy Dispersive X-ray Spectroscopy (EDX) and Electron Backscattering Diffraction (EBSD), Transmission Electron Microscopy (TEM) and Atomic force microscopy (AFM).

- Studies of the superconducting properties of YBCO, BZO-doped YBCO thin films and Y-CC with various nano-dots architecture in comparison with those of control samples. J_c in various applied magnetic fields and temperatures was determined by transport measurements, *AC* susceptibility and magnetisation. Other superconducting aspects such as vortex melting lines, which are important for a better understanding of the influence of

nano-dots pinning centres on the vortex dynamics and for further optimisation of YBCO, BZO-doped YBCO thin films and Y-CC, were studied by transport angular dependence of J_c characteristics and frequency-dependent *AC* susceptibility and higher harmonics. Measurements of the field-orientation dependence of J_c were used for probing the c-axis correlation of nano-dots induced pinning centres. Patterning of films by lithographic techniques and chemical etching is necessary to provide suitable geometry micro-bridges.

- Optimisation of critical current density and other properties of YBCO, BZO-doped YBCO thin films and Y-CC. The results and conclusions of the above-mentioned studies have allowed the selection of the best materials and architecture of nano-dots for the optimisation of the parameters of practical interest in various conditions. Obviously, the optimum material and nano-dot architecture may depend on the specific parameter intended for optimisation, i.e., on the desired future application of that particular thin film. In the case of Y-CC, optimisation of J_c in various applied magnetic fields will be achieved by finding the best materials for nano-dots and the optimum volume density of nano-dots, i.e., by finding the optimum nano-dots architecture in each layer of nano-dots and the optimum thickness of YBCO between two consecutive layers of nano-dots.

References

[1] R.M. Hazen, L.W. Finger, R.J. Angel, C.T. Prewitt, N.L. Ross, H.K. Mao, C.G. Hadidiacos, P.H. Hor, R.L. Meng, C.W. Chu, Physical Review B 35/13 (1987) 7238.

[2] G. Blatter, M.V. Feigel'man, V. B. Geshkenbein, A. I. Larkin, V. M. Vinokur, Reviews of Modern Physics 66/4 (1994) 1125.

[3] J.M. Huijbregtse, F.C. Klaassen, A. Szepielow, J.H. Rector, B. Dam, R. Griessen, B.J. Kooi, J.T.M. de Hosson, Superconductor Science & Technology 15/3 (2002) 395.

[4] L. Civale, A. D. Marwick, T. K.Worthington, M. A. Kirk, J. R. Thompson, L. Krusin-Elbaum, Y. Sun, J. R. Clem, and F. Holtzberg, Physical Review Letter 67, (1991) 648.

[5] L. Civale, Superconductor Science & Technology 10/7A (1997) A11.

[6] H. Kito, A. Iyo, M. Hirai, A. Crisan, M. Tokumoto, S. Okayasu, M. Sasase and H. Ihara, Physica C 378, (2002) 329.

[7] A. Crisan, S.K. Agarwal, T. Koganezawa, R. Kuroda, K. Tokiwa, T. Watanabe, A. Iyo, Y. Tanaka, H. Ihara, Journal of Physics and Chemistry Solids 63, (2002) 1073.

[8] V. Mihalache, G. Aldica, S. Popa, P. Nita, and A. Crisan, Journal of Superconductivity 14, (2001) 381.

[9] A.V. Berenov, R. Marriott, S.R. Foltyn, J.L. MacManus-Driscoll, IEEE Transactions on Applied Superconductivity 11/1 (2001) 3780.

[10] V. Mihalache, G. Aldica, S. Popa, and A. Crisan, Physica C 384, (2003) 451.

[11] P. Badica, A. Iyo, G. Aldica, H. Kito, A. Crisan, and Y. Tanaka, Superconductor Science & Technology 17, (2004) 430.

[12] L.Miu, A. Crisan, S. Popa, V. Sandu, L. Nistor, Journal of Superconductivity 3, (1990) 391.

[13] L. Miu, S. Popa, A. Crisan, G. Aldica, J. Jaklovszky, Journal of Superconductivity 6, (1993) 279.

[14] M. Baert, V. V. Metlushko, R. Jonkheere, V. V. Moshchalkov, and Y. Bruynseraede, Physical Review Letter 74, (1995) 3269.

[15] A. Crisan, A. Pross, D. Cole, S.J. Bending, R. Wördenweber, P. Lahl, E.H. Brandt, Physical Review B 71, (2005) 144504.

[16] A. Crisan, S. Fujiwara, J.C. Nie, A. Sundaresan, H. Ihara, Applied Physics Letters 79/27 (2001) 4547.

[17] T. Haugan, P.N. Barnes, R. Wheeler, F. Meisenkothen, M. Sumption, Nature 430/7002 (2004) 867.

[18] J.L. Macmanus-Driscoll, S.R. Foltyn, Q.X. Jia, H. Wang, A. Serquis, L. Civale, B. Maiorov, M.E. Hawley, M.P. Maley, D.E. Peterson, Nature Materials 3/7 (2004) 439.

[19] A. Crisan, P. Badica, S. Fujiwara, J.C. Nie, A. Sundaresan, Y. Tanaka and H. Ihara, Applied Physics Letter 80, (2002) 3566.

[20] A. Crisan, P. Badica, S. Fujiwara, J.C. Nie, A. Sundaresan, A. Iyo, and Y. Tanaka, , IEEE Transactions on Applied Superconductivity, 13, (2003) 3726.

[21] M. Ionescu, A.H. Li, Y. Zhao, H.K. Liu and A. Crisan, Journal of Physics D: Applied Physics 37 (2004) 1824

[22] P. Badica, A. Sundaresan, A. Crisan, J.C. Nie, M. Hirai, S. Fujiwara, H. Kito and H. Ihara, Physica C 383, (2003) 482.

[23] K. Matsumoto, T. Horide, K. Osamura, M. Mukaida, Y. Yoshida, A. Ichinose, and S. Horii, Physica C 412-414, (2004) 1267.

[24] P. Mele, K. Matsumoto, T. Horide, O. Miura, A. Ichinose, M. Mukaida, Y. Yoshida, and S. Horii, Superconductor Science & Technology 19, (2006) 44.

[25] J.C. Nie, H. Yamasaki, H. Yamada, Y. Nakagawa, K. Develos-Bagarinao, and Y. Mawatari, Superconductor Science & Technology 17, (2004) 845.

[26] T. Aytug, M. Paranthaman, A.A. Gapud, S. Kang, H.M. Christen, K.J. Leonard, P.M. Martin, J.R. Thompson, D.K. Christen, R. Meng, I. Rusakova, C.W. Chu, and T.H. Johansen, Journal of Applied Physics 98, (2005) 114309.

[27] P. Mikheenko, A. Sarkar, V.S. Dang, J.L. Tanner, M.M. Awang Kechik, J.S. Abell, and A. Crisan, IEEE Transactions on Applied Superconductivity 19/3(2009) 3491.

[28] P.N. Barnes, T.J. Haugan, C.V. Varanasi, T.A. Campbell, Applied Physics Letter 85, (2004) 4088.

[29] C. Cai, J. Hänisch, R. Hühne, V. Stehr, C. Mickel, T. Gemming, and B. Holzapfel, Journal of Applied Physics 98, (2005) 123906.

[30] C. Cai, J. C. Zhang, S.X. Cao, J. Hänisch, R. Hühne, and B. Holzapfel, Physica C 460-462, (2007) 1355.

[31] E. Backen, J. Hänisch, R. Hühne, K. Tscharntke, S. Engel, T. Thersleff, L. Schultz, and B. Holzapfel, IEEE Transactions on Applied Superconductivity 17, (2007) 3733.

[32] J. Hänisch, C. Cai, V. Stehr, R. Hühne, J. Lyubina, K. Nenkov, G. Fuchs, L. Schultz, and B. Holzapfel, Superconductor Science & Technology 19, (2006) 534.

[33] A. Goyal, S. Kang, K. J. Leonard, P.M. Martin, A.A. Gapud, M. Varela, M. Paranthaman, A.O. Ijaduola, E.D. Specht, J.R. Thompson, D.K. Christen, S.J. Pennycook, and F.A. List, Superconductor Science & Technology 18, (2005) 1533.

[34] A. Crisan, M.M. Awang Kechik, P. Mikheenko, A. Sarkar, J.S. Abell, P. Paturi, H. Huhtinen, Superconductor Science & Technology. 22 (2009) 045014.

[35] S. Horii, K. Yamada, H. Kai, A. Ichinose, M. Mukaida, R. Teranishi, R. Kita, K. Matsumoto, Y. Yoshida, J. Shimoyama, K. Kishio, Superconductor Science & Technology 20, (2007) 1115.

[36] K. Yamada, A. Ichinose, S. Yasunaga, R. Teranishi, M. Mukaida, S. Horii, R. Kita, S. Kato, Y. Yoshida, K. Matsumoto, S. Toh, Japaness Journal of Applied Physics 47, (2008) 899.

[37] P. Mele, K. Matsumoto, T. Horide, A. Ichinose, M. Mukaida, Y. Yoshida, S. Horii, R. Kita, Superconductor Science & Technology 21, (2008) 032002.

[38] M.M. Awang Kechik, P. Mikheenko, A. Sarkar, V.S. Dang, N. Hari Babu, D.A. Cardwell, J.S. Abell and A. Crisan, Superconductor Science & Technology 22, (2009) 034020.

[39] A. Koblischka-Veneva, F. Mucklich, M.R. Koblischka, N.H. Babu, D.A. Cardwell, Journal of the American Ceramic Society 90/8 (2007) 2582

[40] S.A. Harrington, J.H. Durrell, B. Maiorov, H. Wang, S.C. Wimbush, A. Kursumovic, J.H. Lee, J.L. MacManus-Driscoll, Superconductor Science & Technology 22, (2009) 022001.

[41] J.L. MacManus-Driscoll, S.R. Foltyn, Q.X. Jia, H. Wang, A. Serquis, B. Maiorov, L. Civale, Y. Lin, M.E. Hawley, M.P. Maley, D.E. Peterson, Applied Physics Letters 84/26 (2004) 5329.

Chapter 2. **Literature review**

2.1 Superconductivity: a brief of history

It is now the 100-years anniversary of the discovery of superconductivity by H. Kamerlingh-Onnes. In 1911 he observed an interesting phenomenon that at a temperature T^* of about 4 K, the resistance of a Hg sample dropped suddenly to zero and remained immeasurable at all attainable temperature below T^*. This temperature is called the critical temperature, and is often written as T_c. Soon after the discovery of superconductivity in Hg, the same property was found in several other metals such as: Sn, Pb, In, Al, Nb and others. Many other intermetallic compounds and alloys also turned out to be superconductors [1].

After 22 years since the discovery of superconductivity, in 1933, W. Meissner and R. Ochsenfield found that a superconductor is not only a perfect conductor but also shows perfect diamagnetism, the so-called *Meissner effect*. In the normal state the magnetic field would pass through the material but when cooling down to the temperature below the critical temperature the superconductor would behave diamagnetically and the field is forced around the sides of the superconductor as in Figure 2-1.

In 1957 J. Bardeen, L. N. Cooper and J. R. Schrieffer introduced their remarkable pairing theory of superconductivity, called BCS theory. In the BCS theory, it was shown that even a weak attractive interaction between electrons, mediated through electron-phonon interaction, causes an instability of the ordinary Fermi-sea ground state of the electron gas with respect to the formation of bound pairs of electrons occupying states with equal and opposite momentum and spin [2], so-called Cooper pairs.

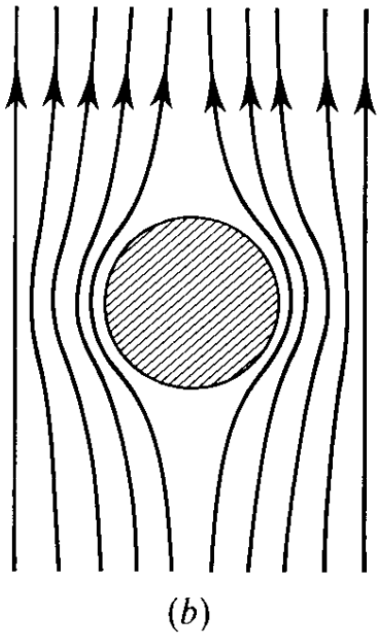

Figure 2-1 Meissner effect, magnetic fields do not penetrate a superconductor

A breakthrough was made, 75 years after the discovery of superconductivity, by J. G. Bednorz and K. A. Muller when they found a compound of La-Ba-Cu-O that became superconducting at 35 K [3], establishing the classification of high temperature superconductors (HTS). A year later, Prof. Chu's group [4] reported a remarkable high T_c superconductor of 92 K on replacing La by Y. The discovery of superconductivity above the boiling point of liquid nitrogen, which is considerably cheaper than liquid helium led to an extensive search for new superconductors. Soon after that, several HTS materials were discovered based on Cu-O layers such as Ba-Sr-Ca-Cu-O (BSSCO) [5], Tl–Ba–Ca–Cu–O (TBCCO) [6] and HgBa2CuO*x* (Hg-1201) [7]. The highest T_c in normal condition until now is that of the Hg based superconductor $HgBa_2Ca_2Cu_3O_8$ (Hg-1223) which has T_c up to 134K and a bit higher under pressure, as seen in Figure 2-2. More recently, the discovery of intermetallic MgB_2 in 2001 [8] and iron-based [9] superconductors have opened a door of hope for the discovery of new classes of superconductors in the future.

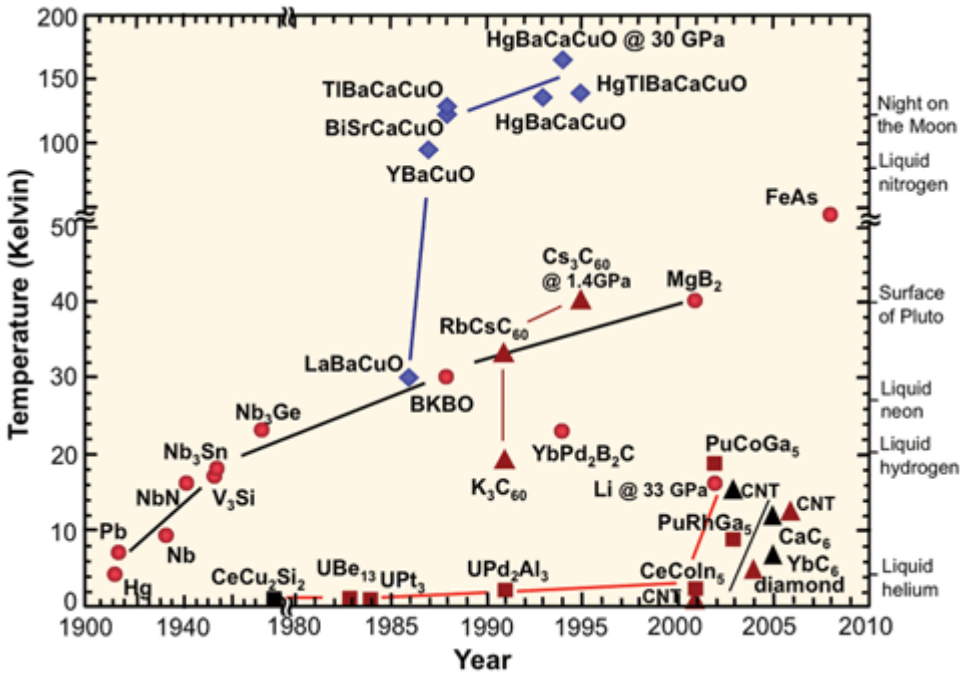

Figure 2-2 The evolution of the transition temperature (T_c) subsequent to the discovery of superconductivity, image from http://www.ccas-web.org/superconductivity/ (Feb 2011)

2.2 Fundamental physics properties of superconductivity

2.2.1 The Ginsburg-Landau theory

Based on theories of phase transitions and critical phenomena, the phenomenological Ginsburg-Landau (G-L) theory was developed 7 years before the BCS theory and in 1959 Gorkov was able to show that the G-L theory was, in fact, a limiting form of the microscopic BCS theory. Briefly, the G-L theory is based on Landau's phase-transition quantum mechanical theory in which ψ is defined as a superconducting electron wave function and n_s is local density of superconducting electrons. The superconducting electrons were then treated as free particles in quantum mechanical theory but with a nonlinear term. One of the results of the G-L theory is the induction of the so-called intermediate state of superconductors, in

which superconducting and normal domains coexist in the presence of a magnetic field H near the critical field H_c. The interface between two such domains is shown in Figure 2-3

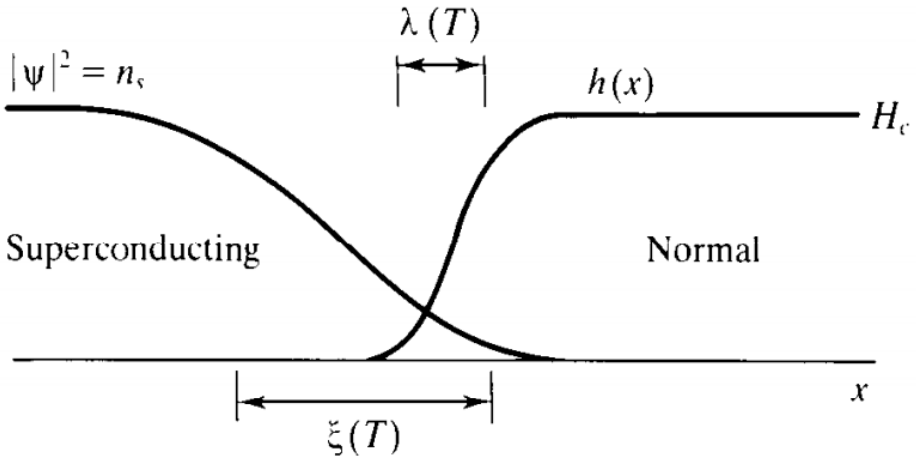

Figure 2-3 Coexistence of superconducting and normal domain in the intermediate state of a superconductor [2]

Another aspect of G-L theory is the introduction of a characteristic length usually called the GL coherence length,

$$\xi(T)=\frac{\hbar}{|2m^{*}\alpha(T)|^{1/2}} \quad (2.1)$$

which characterises the distance over which ψ(r) can vary without undue energy increase, and is actually considered to be the distance over which the superconducting carriers concentration decreases by Euler's number e. Another characteristic length is the (London) penetration depth which describes the length scale over which the applied magnetic field decreases by e. The ratio of the two characteristic lengths defining the GL parameter

$$\kappa=\frac{\lambda}{\xi} \quad (2.2)$$

is approximately temperature independent [2].

2.2.2 Type I and type II superconductor

The concept of type I and type II superconductors was first introduced by Abrikosov [2] in 1957. By investigating the GL parameter, he found that the breakpoint of GL parameter is at $\kappa = {}^{1}/_{\sqrt{2}}$. The traditional low temperature superconductors (Hg, Nb...) with $\kappa < {}^{1}/_{\sqrt{2}}$ display superconductivity and diamagnetism below the critical field H_c. The superconducting state will disappear when the applied field is above H_c. However, for superconductors with $\kappa > {}^{1}/_{\sqrt{2}}$, instead of a discontinuous breakdown of superconductivity in a first-order transition at H_c, there is a continuous increase in flux penetration starting at a lower critical field H_{c1} and reaching $B = H$ (normal state) at an upper critical field H_{c2}. The schematic phase diagram of type I and type II superconductors in applied fields is shown in Figure 2-4

In type II superconductors at high fields in the mixed state, between H_{c1} and H_{c2}, it is energetically favourable for the external magnetic field to penetrate the superconductor. However, the magnetic field does not penetrate the superconductor homogeneously. Instead, the calculations indicated that the magnetic flux should divide itself into small bundles of flux lines. The minimum bundle allowed, the flux quantum, is given by: $\phi_0 = \frac{h}{2e} \approx 2.07 \bullet 10^{-15}$ Wb.

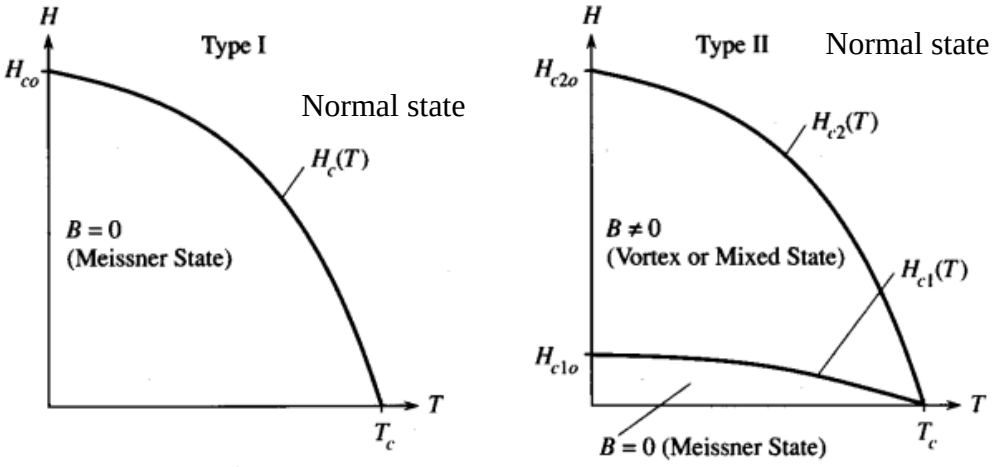

Figure 2-4 Schematic diagram of type I and type II superconductor

2.2.3 Critical parameters

Apart from the critical temperature and critical field(s), there is another critical parameter, the critical current I_c. Like in the case of T_c and H_c, superconductivity disappears when a current higher than the critical one is passed through the material. The critical current depends on size and geometry of the superconductor so the size-independent parameter normally used is critical current density (J_c). The three critical parameters depend on each other, so we actually have the three critical parameters as $T_c(H,J)$, $H_c(T,J)$ and $J_c(T,H)$. Figure 2-5 shows a diagram of these inter-dependent critical parameters. Superconductivity only exists in the space under the dome (3D surface) in the figure. The critical parameters of a few well known superconductors are shown in Table 2-1. Improvement of critical parameters is a great goal for the R&D community in the field.

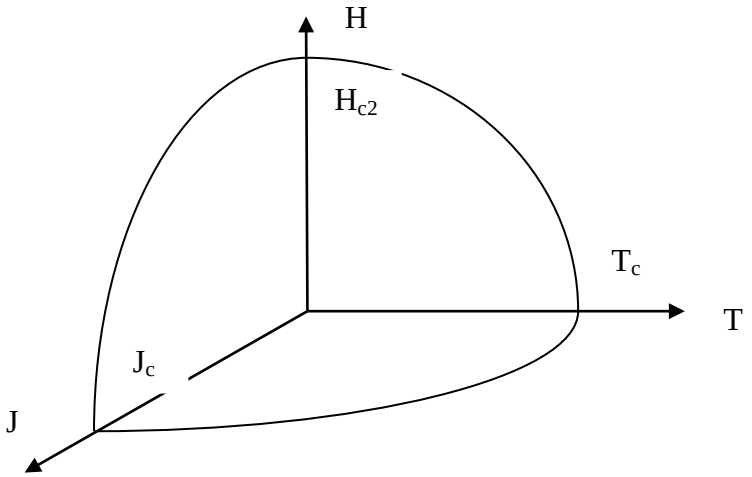

Figure 2-5 Inter-dependent critical parameters of a superconductor

Table 2-1 Critical parameters of some well-known superconductors [1]

Material	T_c(K)	H_{c2}(T)	J_c(A/cm^2)
Nb_3Sn	18	25 (4K)	$6x10^5$ (9.5T, 4K)
NbTi	9	12 (4K)	$4x10^5$ (5T, 4K)
MgB_2	39	15 (4K)	10^6 (0T, 4K)
YBCO	92	>100 (4K)	10^6 (0T, 77K)
Bi-2223	108	> 100 (4K)	10^6 (0T, 77K)

2.3 High temperature superconductor (HTS) $YBa_2Cu_3O_7$

2.3.1 Introduction

$YBa_2Cu_3O_7$ (YBCO) superconductor which has T_c of about 92 K has opened a new challenge for researchers for applications at liquid nitrogen temperature. The structure of YBCO is shown in Figure 2-6. The high J_c of YBCO thin films makes it an attractive material for power applications, particularly since it is maintained in high applied field. However, there are some problems that have been not resolved until now, such as the rapidly decreasing

of J_c when the film thickness increases up to microns, and the anisotropy of J_c in magnetic fields [10].

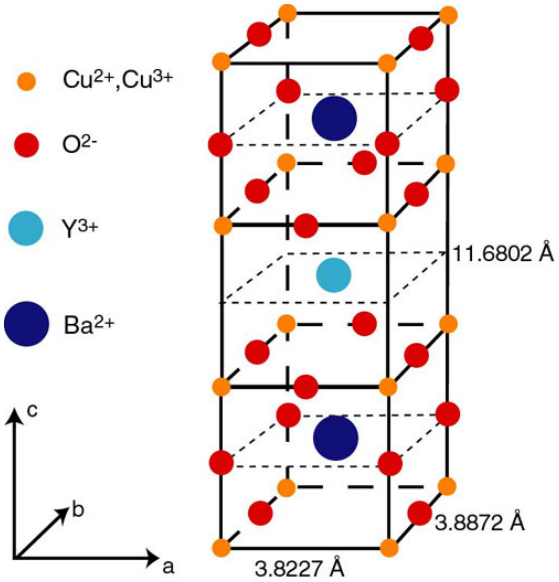

Figure 2-6 Orthorhombic structure of $YBa_2Cu_3O_7$ with the lattice parameter of a = 3.82 Å, b = 3.89 Å and c = 11.68 Å, picture from: http://tfy.tkk.fi/nanospin/facilities/pld/basics/supercond.php (May 2011)

2.3.2 Mechanism of superconductivity of YBCO

The mechanism of superconductivity in HTS such as YBCO is a controversial topic. The classical theory of BCS which provides the concept of a macroscopic quantum state of Cooper pairs and Ginzburg-Landau which provides the starting functional (free-energy) for the charged superfluid coupled to electromagnetism remain the common basic in almost all proposed mechanisms for HTSs. However, there is no general agreement about the origin of the pairing.

The presence of the Abrikosov lattice in HTC results in many new concepts that are not present in low temperature superconductor. The flux line in YBCO is influenced by novel phenomena such as strong thermal and quantum fluctuations, resulting in several features

such as a vortex liquid phase below H_{c2} and a vortex glass phase separated from the vortex liquid phase by the irreversibility field.

Another property that makes YBCO different from classical low temperature superconductors is the layer structure. The YBCO exhibits interesting properties due to electromagnetic coupling between the various layers in its structure. The YBCO superconductor is structured by Cu-O planes as shown in Figure 2-7 separated by buffer layers which act as charge reservoirs. The transport properties shown in section 2.3.4 are roughly uniaxial due to the layered structure and essentially isotropic behaviour within the Cu-O layers.

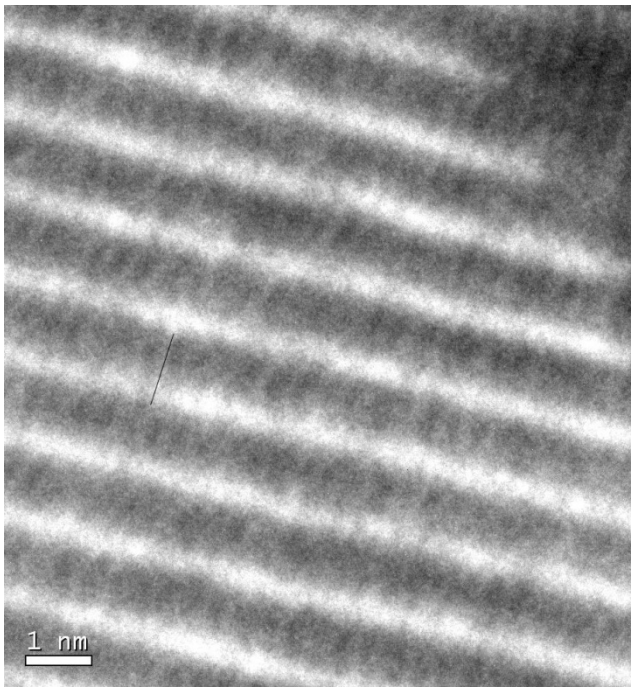

Figure 2-7 Cross section HRTEM image of Cu-O layers in YBCO film

2.3.3 Dependence of critical current density on film thickness and applied magnetic fields

Critical parameters such as magnetic field, temperature and current are very important ones. Critical current is defined as maximum current (I_c) a superconductor can carry and a superconductor will be turned to a normal conductor if a current higher than I_c is injected into the superconductor. Critical current density (J_c) is I_c divided by the cross-section of the specimen. J_c is the parameter normally used for thin film samples.

The relationship between thickness and J_c is very important for applications, normally, J_c drastically decreases with increasing thickness of the film to several micrometres. Thickness dependence of critical current density is still a controversial problem; there are several explanations recently published [11-14];

- When a thicker film is deposited, it requires longer time at high temperature, normally from 750 to 800^o C, which allows impurity diffusion from the substrate to contaminate the YBCO layer nearest the interface.
- As YBCO thickness increases, the crystalline orientation of the YBCO perpendicular to the substrate can switch from c-axis to a-axis resulting in decreasing J_c.
- As YBCO thickness increases, the film morphology becomes much rougher, suggesting that the drop in J_c is related to a change in microstructure.

To overcome the rapid J_c fall with film thickness, the introduction of nanotechnology and multilayer structures are possible ways which were investigated in this work.

Another important factor is that J_c sharply decreases with increasing applied magnetic field. The effect of thickness and magnetic field on J_c is shown in Figure 2-8 and Figure 2-9. The decrease of J_c in applied magnetic fields is due to the movement of vortices caused by the Lorentz force.

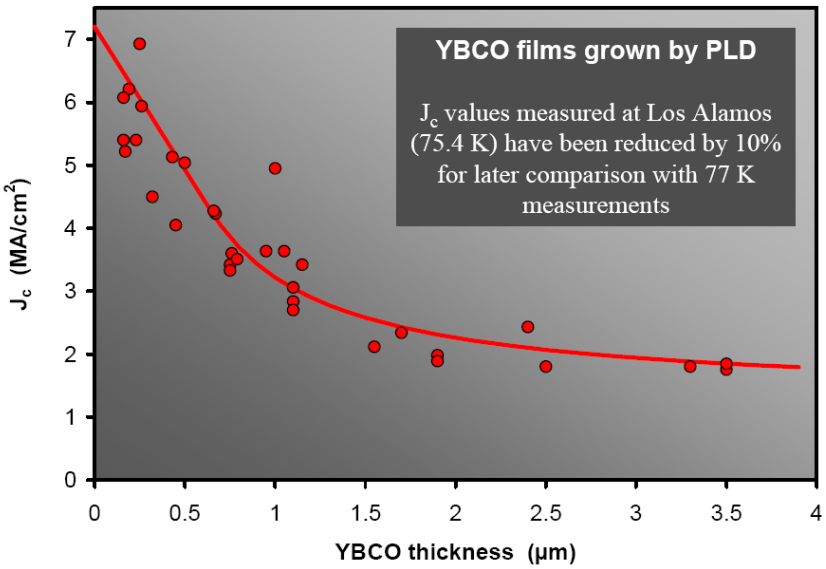

Figure 2-8 Foltyn et al.[15] The critical current density of YBCO decreases sharply with film thickness.

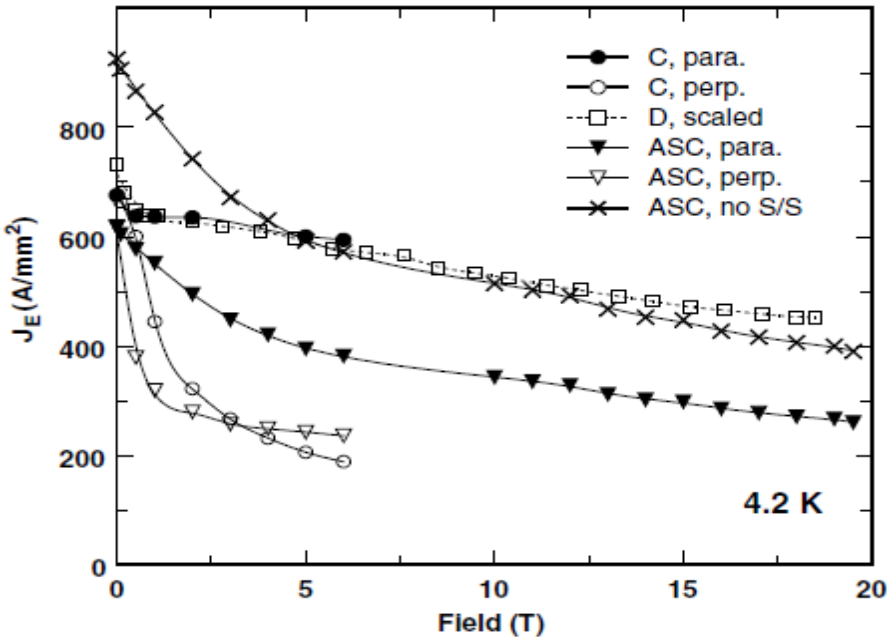

Figure 2-9 Dependence of engineering critical current densities of YBCO coated conductor on parallel (para) and perpendicular (perp) field up to 20 T and 4.2 K with several samples (C, D, ASC), results from Oxford Instruments group 2003 [16]

2.3.4 Anisotropy in YBCO

One of the properties of the crystal structure of oxide superconductors with high critical temperature is an alternating multi-layer of CuO_2 planes which generate superconductivity and charge-reservoir blocks which are almost insulating. This structure causes a large anisotropy in normal conducting and superconducting properties. Thus the magnetic field (H) dependence of critical current density is anisotropic, with J_c highest with H parallel to the ab-planes and no local peak of J_c observed with H parallel to the c-axis in perfect YBCO films. With few exceptions, the peak of J_c along the c-axis appears due to the defects along the c-axis. The relation between J_c^{ab} (J_c in plane) and J_c^c (J_c out of plane) is well described by the Blatter [17, 18] scaling approach based on anisotropic Ginzburg-Landau theory,

$$j_c^c = \frac{1}{\varepsilon_0} j_c^{ab}(\theta) \quad (2.3)$$

and $\varepsilon_0^2 = sin^2(\theta) + \gamma^2 cos^2(\theta)$ (2.4)

where θ is the angle between applied magnetic field and the ab-plane and γ is the anisotropy parameter in Ginzburg-Landau theory (γ ~5–7 for YBCO).

Figure 2-10 is an example of the angular dependence of critical current density of a multilayer film [19] which shows a small peak along the c-axis due to the extended c-axis defects caused by the multilayer structure of the film. The curve is fitted with the theory of Blatter scaling in the angle range far from c-axis orientation.

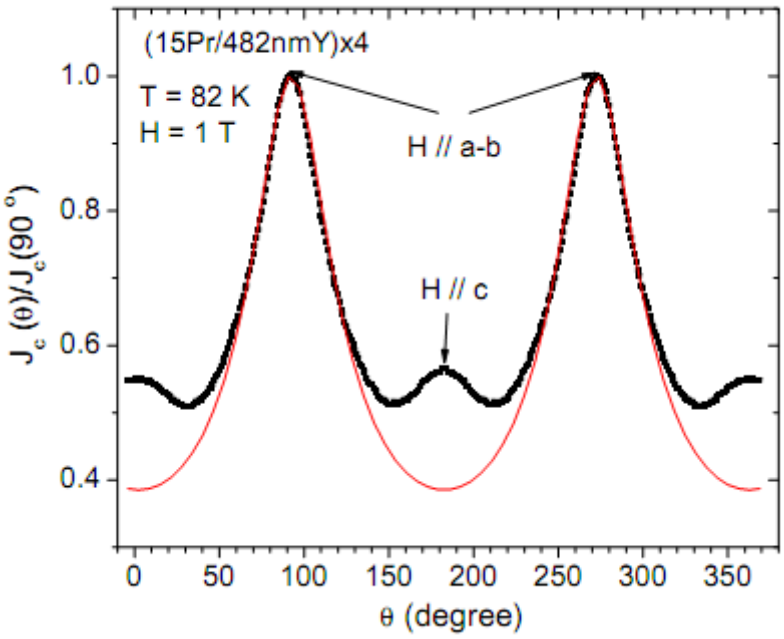

Figure 2-10 [19] Angle dependence of normalised critical current density of multilayers film, red line is theory fit with Blatter scaling

In the case of YBCO films with BZO or BSO nanoinclusions (which, in certain conditions, are re-arranged to form nanorods), it was shown that J_c is higher in the c-axis direction due to the dominance of extrinsic anisotropic pinning [20-25], and the Blatter scaling is not suitable. The vortex path model presented by N. J. Long [26] that emphasises the combination of isotropic and anisotropic, in plane and out-of-plane defects, is very good to fit the data in this case, as will be shown later on.

2.4 Flux pinning

2.4.1 The flux pinning mechanism

In the interior of type II superconductors such as YBCO, magnetic field exists in the form of tubular structures called flux lines or vortices, each of them carrying one unit of magnetic flux or flux quantum [2]. The energy of the flux line will be different if it passes

through an inhomogeneity. The resulting force tends to “pin” flux lines in a particularly favourable way relative to the underlying material. It is this pinning force which allows the system to “fight” the Lorentz force generated by the flux and the current without flux motion and dissipation, thus giving the material a nonzero critical current, an essential property of practical superconductors.

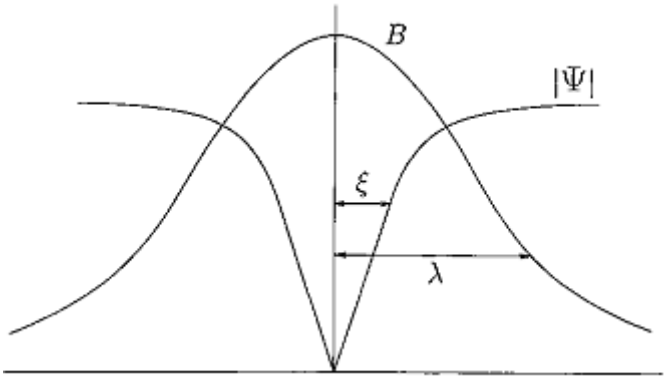

Figure 2-11 Structure of quantised flux line [27]

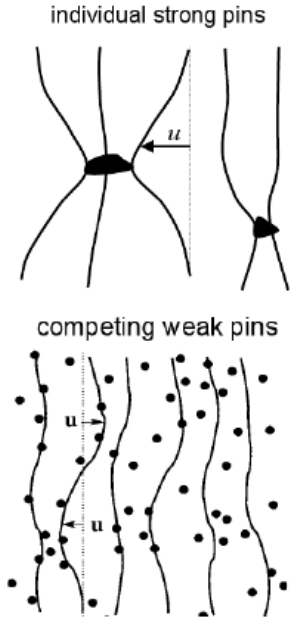

Figure 2-12 Blatter et al, [28]. Individual strong pins and competing weak pins in superconductors

Figure 2-11 shows the structure of the quantised flux line which creates the occurrence of the flux pinning interaction. The superconducting order parameter, Ψ, has a zero point at the centre of the flux line with a sharp variation within a range of the coherence length, ξ.
The magnetic flux is concentrated within a range of penetration depth, λ, from the centre. Hence, when the flux line moves to a region where the superconducting properties change spatially, it feels a change in the free energy, which results in the flux pinning interaction [27], which can be strong, or weak, as shown in Figure 2-12.

2.4.2 Kinds of pinning sites

Based on their origin, the flux pinning centres in superconducting materials can be divided into 2 categories, natural pinning sites and artificial (engineered) pinning sites.

2.4.2.1 "Natural" pinning sites

Defects may occur during deposition or in the target itself, creating the so-called natural pinning. All superconductors have some pinning sites themselves which are the defects such as: point defects; vacancies, interstitials, atomic substitutions, columnar defects; dislocations, antiphase boundaries, nanorods, plane defects; twin boundaries, stacking faults…(see Figure 2-13) Either a perfect superconductor or a superconductor with a too high density of defects is not good for high critical current, so the tip to make "enough" pinning sites is not perfect crystallinity but control of defects [15]. The natural pinning sites themselves may not be effective enough or their density might be too low, so, to increase effective pinning and, consequently, the critical current density, the combination of natural pinning and artificial pinning is necessary [20-25].

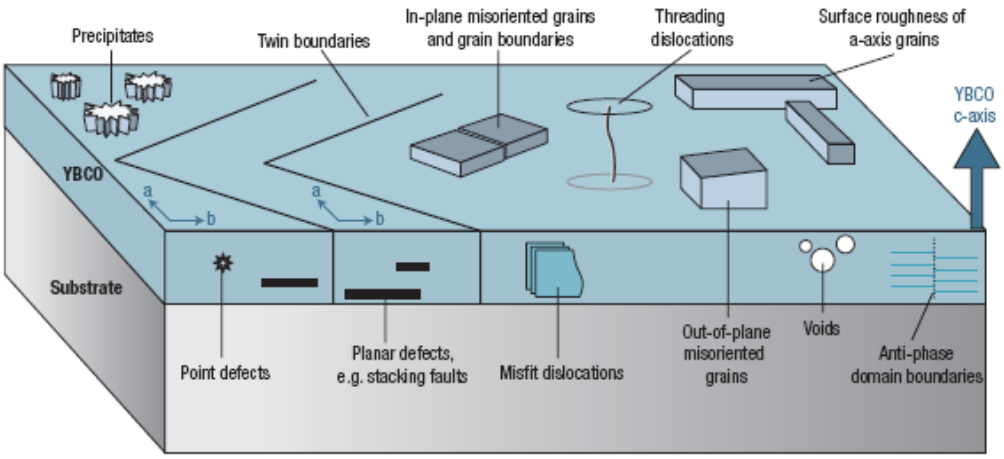

Figure 2-13 Foltyn *et al* [15] Many thin film defects have been proposed as flux pinning sites in YBCO; anything that locally disturbs the crystalline perfection over a scale of 0.1 – 1 nm is a candidate.

2.4.2.2 Artificial pinning sites

To increase J_c of superconducting films, many groups are trying to make more defects in superconductors by adding artificial pinning sites using various methods such as: heavy ion irradiation [29-31], antidots (holes) (1-Dimensional) [32, 33], magnetic-dots [33-36] (1D) and, recently substrate decoration and multilayer or nano-inclusions [10, 21, 37-51] (1, 2, and 3-Dimensional). From a particular point of view, the artificial pinning centres (APC) can be classified by dimensionality as shown in Figure 2-14, namely there are 3 kinds of defects: 1D-APC such as dislocations and columnar defects; 2D-APC such as small angle grain boundaries, anti-phase and surfaces of precipitates; 3D-APC such as nanoparticles and different phases of the scale of ξ or more.

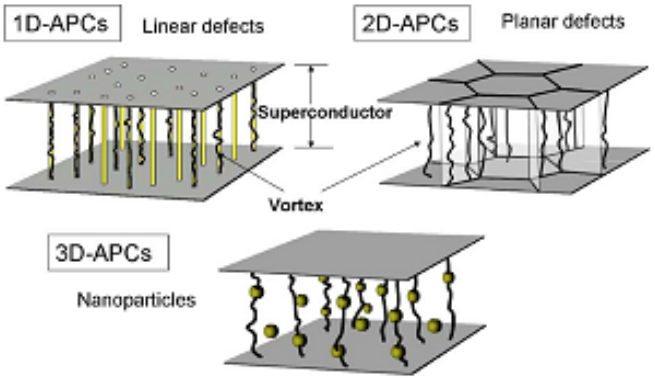

Figure 2-14 Three kinds of artificial pinning centre by their dimensionality, there are linear, planar and particle-like defects [52]

The mechanism of artificial pinning is very complicated, but in general, adding artificial pinning sites causes more defects in superconductors, but too many defects may damage the structure of the samples and reduce the total cross-section for the supercurrent flow, so many groups are trying to find out the most suitable condition for their deposition. The artificial pinning sites are very sensitive to the conditions of deposition.

Figure 2-15 and Figure 2-16 show an example of substrate decoration with Ag nano-dots reported in ref [53] (1D-APC); one can see that the Ag nano-particles diameters are less than 10-20 nm in Figure 2-15, while an improvement of J_c in magnetic fields for the sample with Ag substrate decoration is shown in Figure 2-16.

The strongest defect which enhances J_c in its direction (c-axis) is a columnar defect (1D-APC), shown schematically in Figure 2-17. Normally, columnar defects can be formed by nanorods of secondary phase such as BZO. The effect of columnar defects on J_c is easily recognised by the angular dependence of J_c which shows a maximum in the direction of the column, the c-axis (see Figure 2-18).

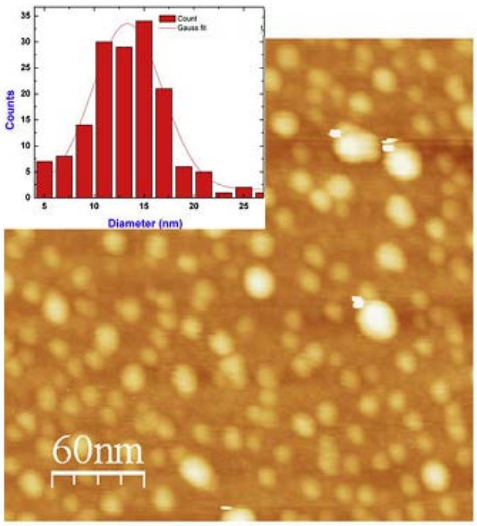

Figure 2-15 AFM images of Ag nanoparticles grown on STO substrate [53]

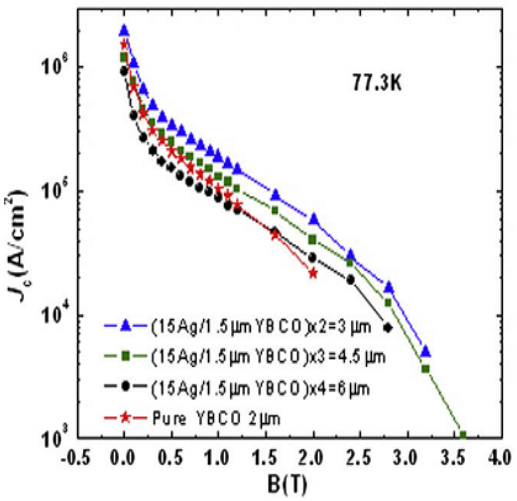

Figure 2-16 Improvement of J_c in comparison between YBCO and Ag decoration [53]

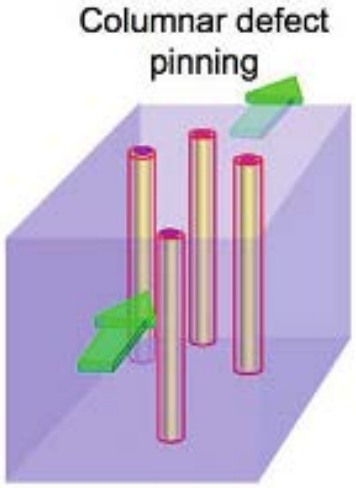

Figure 2-17 Columnar defect pinning

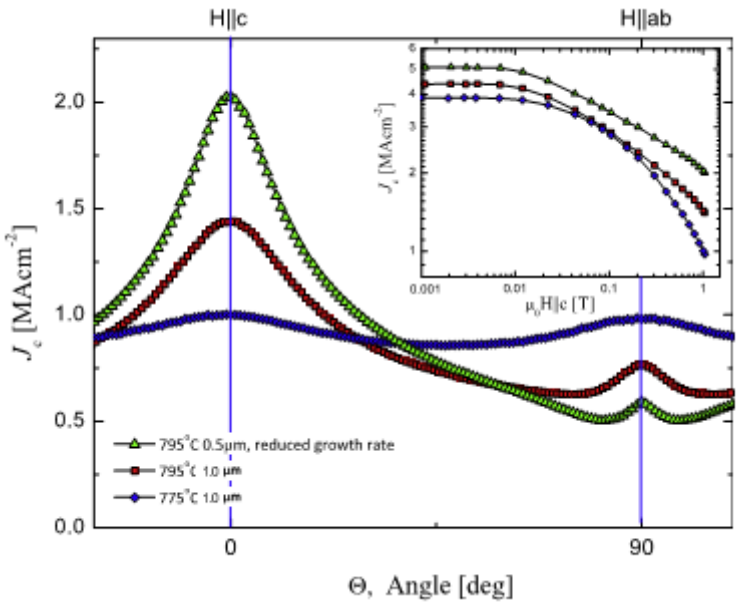

Figure 2-18 An example of columnar defect which create a peak of J_c along the c-axis [54], The peak of J_c does not appear in perfect YBCO films.

2.4.3 Enhancement of J_c by artificial pinning centres

As mentioned above, there are many ways to increase the J_c of the samples by artificial pinning centres. In this section, the most popular methods which are usually used in YBCO films will be introduced.

2.4.3.1 Substrate surface decoration

The easiest and cost-effective method used is substrate decoration which has been achieved by depositing metal or oxide such as: Ag [41, 43], Ir [55, 56], Y_2O_3 [45, 57] … The particles, ranging in size from 10 to 100 nm [38, 42, 44-46, 56, 58, 59], produce a disruption in the YBCO that can enhance flux pinning. Until now, there is no clear and consistent picture regarding the nature of the disruption and the effect on performance. The most likely explanation is that the YBCO lattice planes are buckled or distorted above the nanoparticles, resulting in low-angle grain boundaries or dislocations that may thread to the substrate surface

[15]. However, the increase of critical current in the YBCO films by this method solely is not as impressive as in the case of some of the other methods mentioned below, and the increase of J_c was only observed in thin films of about hundreds nanometres as most of the defects caused by nano-dots materials are in the areas near the substrate, as in refs [39-56].

2.4.3.2 Rare-earth substitutions and mixing

The simplest idea is to replace yttrium with one of the rare-earth elements while maintaining the 123 stoichiometry ., [60, 61], [62]. Gadolinium is a potential candidate to replace yttrium, and some recent results [61, 63-67] show very significant in-field enhancement over YBCO, perhaps due to an increased density of stacking faults [68]. Promising levels of improvement have also reported for EuBCO [62, 69], SmBCO [60, 70, 71], ErBCO [72], and NdBCO [22, 73].

A more complex method is a mixture of RE elements together with yttrium that retain the 123 composition (RE, Y) $Ba_2Cu_3O_7$ [60, 68, 74, 75]. The benefit here is that additional enhancement will result from the strain induced by lattice mismatch between the various 123 components [15].

The replacement of Y by Gd in YBCO compound results not only in improvement of J_c but also in T_c [63-67]. The improvement of J_c in rare-earth substitution in YBCO or rare-earth mixing was clearly observed in refs [63-67], the main reason being the presence of additional stacking faults.

2.4.3.3 Impurity additions

A little easier method than RE-substitutions or mixing is impurity additions in which other phases are added to the YBCO phase. The first approach to impurity-doped films was adding a few % of $BaZrO_3$ (BZO) to the source material of YBCO target, introduced by

MacManus-Driscoll et. el [76]. The BZO-doped YBCO films had a significant c-axis-correlated improvement of J_c. Because of the ease with which nanoparticles can be incorporated [15] this technique has been widely applied by numerous researchers [51, 68, 77]. Recently, $BaWO_4$ (BWO) and $BaSnO_3$ (BSO) were also shown as significant pinning centres in YBCO film [38, 78], as well as tantalite, double perovskite and combinations of two such impurities [79]

It is also very interesting to combine both addition and rare earth substitution as in some recent publications [69, 80-83].

$Y_2Ba_4CuMO_x$ (M = Nb, Zr, Ag) is also used as an impurity addition to YBCO [84, 85] bulk material, but no thin film properties are reported on this material.

Perovskite (BZO, BWO, BSO) doping is the most used efficient method in increasing J_c of YBCO films till now, especially the J_c in applied field along the c-axis. The formation of perovskite nano-rods inside the YBCO matrix (1-D) and also nano-particles (3-D) is the main reason of the increase in J_c in such nanostructured superconductor, as it combines natural defects with 1D and 3D artificial defects. A small decrease of T_c (about 2 to 5 K in comparison with pure YBCO) in such doped superconductor is a side effect, but for low temperature applications, this decrease is insignificant.

2.5 Coated conductors

2.5.1 Introduction

A long length and flexible wire is required for power applications such as transmission lines, motors, and generators. Nb based alloy (Nb-Ti, Nb-Zr, Nb_3Sn) were the first commercial products in long length conductors [86]. Later on, kilometre lengths of $Bi_2Sr_2Ca_2Cu_3O_{10}$ or Bi(2223) were fabricated by several manufacturers. The fabrication approach (see Figure 2-19) involves a powder-in-tube process in which the superconductor precursors are encased in Ag and then processed as filaments [87]. This is the so-called first generation (1G) conductor, which is based on BSCCO (2212 or 2223).

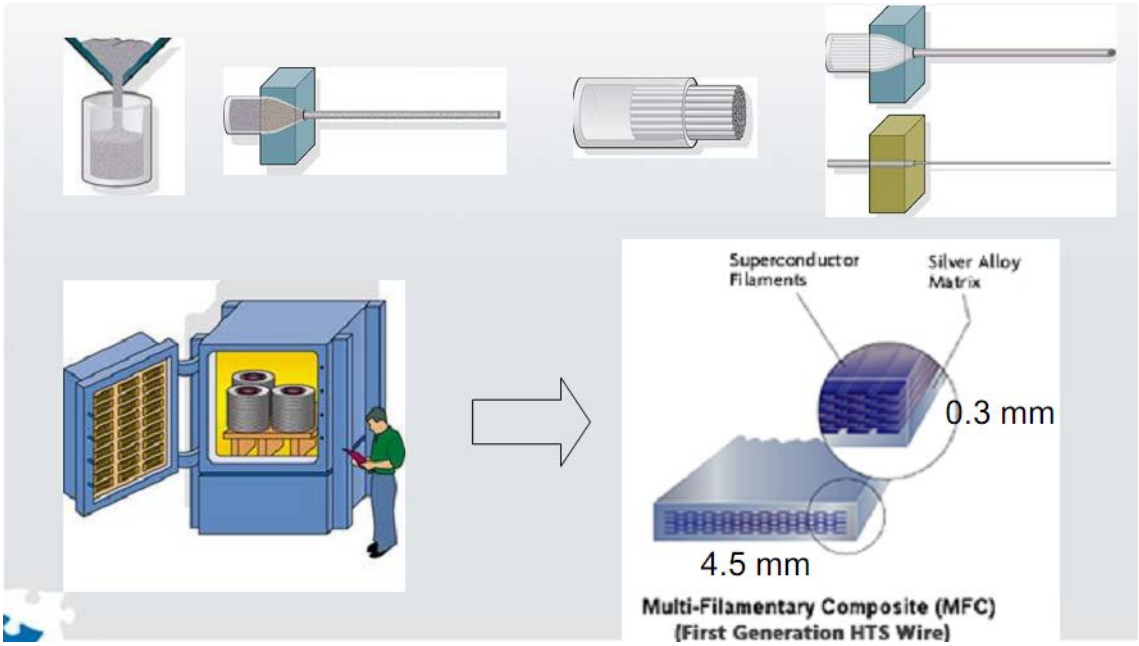

Figure 2-19 Synthesis of 1G superconductor cable by NKT Cable company

The discovery of cuprates HTS has opened a new window for HTS cables as they can carry super current at liquid nitrogen temperature and have a very high J_c. The idea of coated conductor has been developed in recent years. Coated conductor consists usually of Ni alloy,

buffer layers such as, YZO, MgO, CeO_2 and YBCO layer(s) to produce the so-called 2G (second generation) conductor. The 2G conductor is totally different from the 1G conductor, including from the point of view of fabrication method. It has the fundamental advantage because it benefits from the much better irreversibility line of YBCO at high fields and temperatures. Also the replacement of Ag by Ni alloy reduces the cost of the product. Currently, there are three competing methods, the ion beam-assisted deposition (IBAD), the inclined substrate deposition (ISD) process represented in Figure 2-20, and the rolling-assisted biaxially textured substrate (RABiTS) process shown in Figure 2-21. The processing methods are quite different in detail, but the overall final structures are rather similar. In this project, RABiTS substrate provided by 3-Cs Ltd (Malvern) was also used to deposit YBCO and BZO-doped YBCO films.

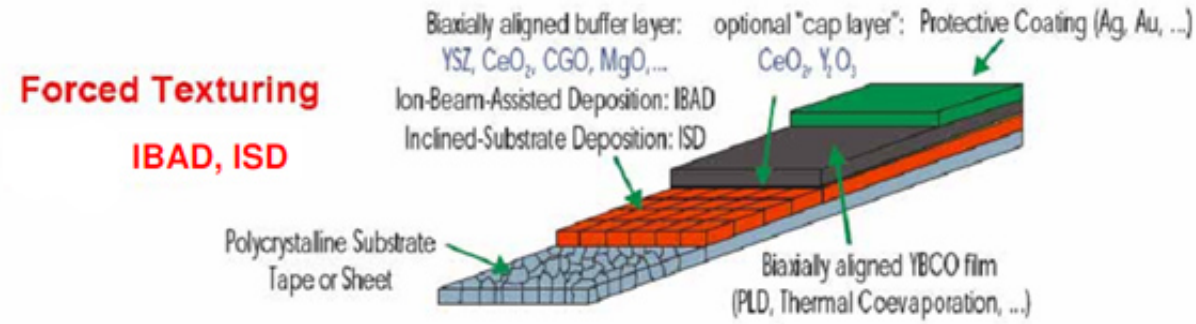

Figure 2-20 Coated conductor based on IBAD substrate

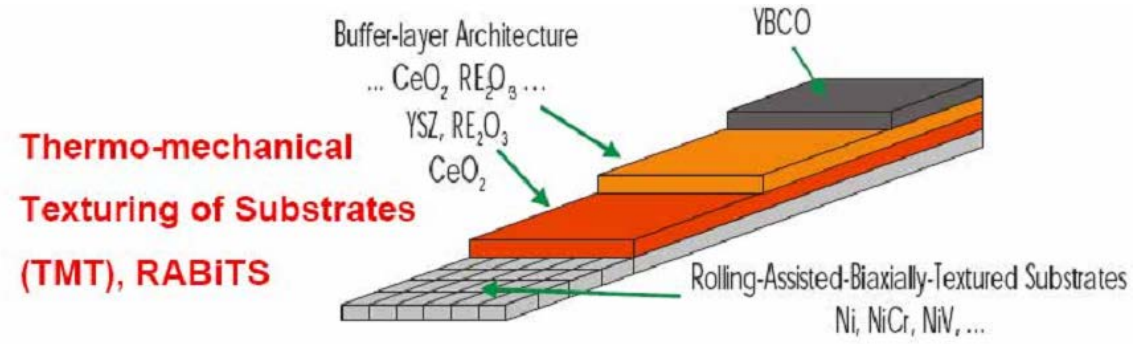

Figure 2-21 Coated conductor based on RABiTS substrate

2.5.2 Rolling-assisted biaxially textured substrates (RABiTS)

Flexible polycrystalline metallic substrates have been used to deposit YBCO films by many research groups. But this was not initially successful due to low J_c caused by high angle mis-orientation grain boundaries, the significance of which was studied early by Dimos et al [88]

The Rolling Assisted Biaxially Textured Substrate (RABiTS) approach appears to be more attractive for long-length coated conductors than alternative technologies for highly textured templates such as Ion-beam-assisted deposition (IBAD)[89] due to lower cost and availability of long-length substrate, and the easily controlled growth of buffer layers [90].

The idea of using nickel as a base material to produce rolling-assisted biaxially textured substrates (RABiTS) was developed by Oak Ridge National Laboratory (ORNL) in 1996 [90-92]. Initially, Ni polycrystalline billets with random orientation were consecutively rolled to form biaxially textured Ni substrate. The biaxially textured Ni substrate then was recrystallized and annealed to produce low angle misorientations grain boundaries and smooth surface as shown in Figure 2-22.

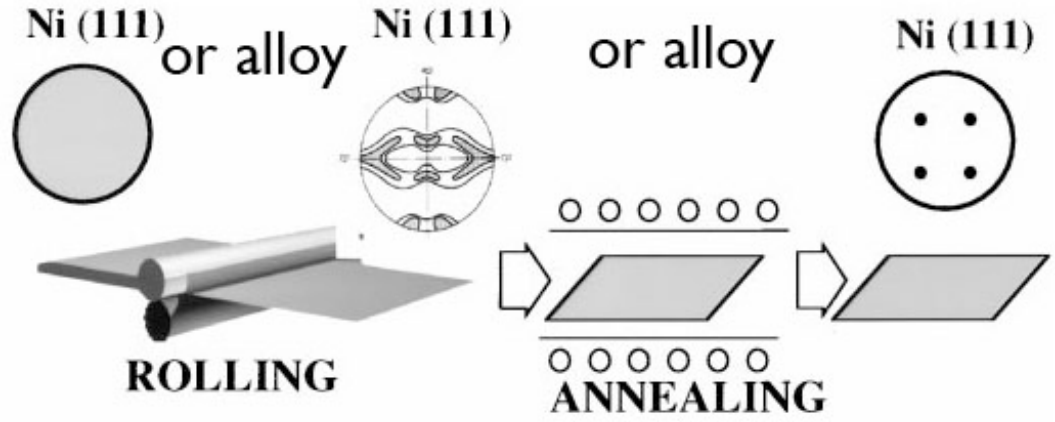

Figure 2-22 Schematic of the Rolling-assisted biaxially-textured substrates (RABiTS) process [91]

Later on, to improve mechanical strength, the stability of the cube texture at high temperature and to reduce ferromagnetism, many Ni based alloys have been introduced such as Ni-Cr [93], Ni-Ag, Ni-Pd [94], Ni-V, Ni-Mo [95], Ni-Fe [96]. Among those Ni-alloys candidates, Ni-W [97] appears to be most attractive due to high J_c as shown in Figure 2-23.

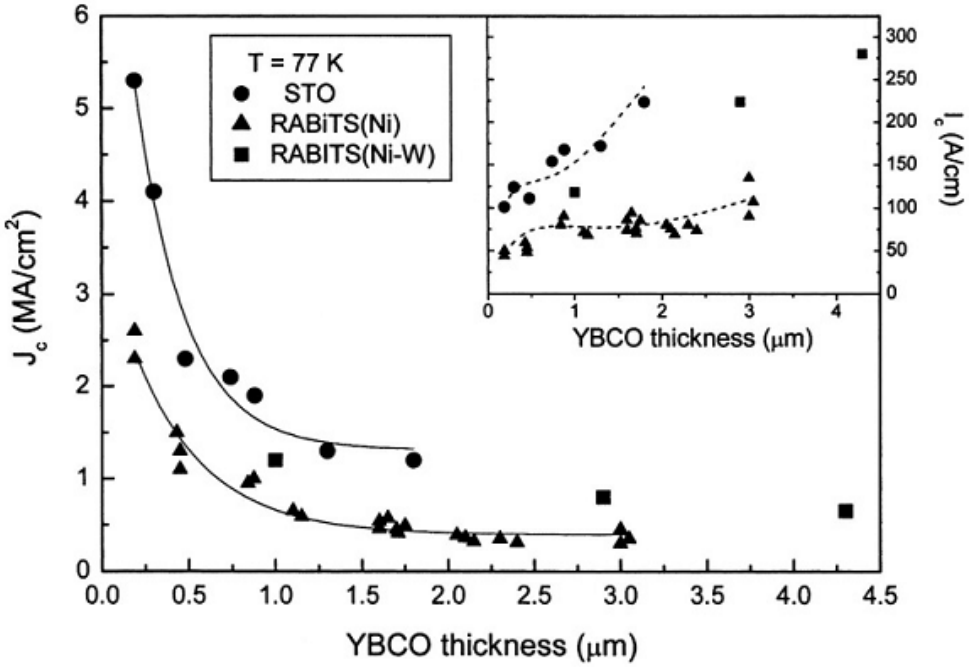

Figure 2-23 J_c dependence of thickness of Ni, Ni:5W and STO substrate [98]

An intensive research has been carried out on Ni:5W substrate to optimise deposition parameters, J_c and T_c so far [99-108] and Ni-5 at% W (Ni5W) is found to be most suitable as a substrate and stability for sub-sequent high temperature processing for YBCO high temperature superconductor (HTS) due to low-angle grain boundaries (less than 10^0), reduced ferromagnetism, and high texture quality[97, 109].

2.5.3 Buffer layers for Ni/Ni:5W RABiTS substrate

Popularly used buffer layers which consist of 3 layers are seed layer/barrier layer/cap layer as shown in Figure 2-24. Each layer plays a different role in the whole process of deposition.

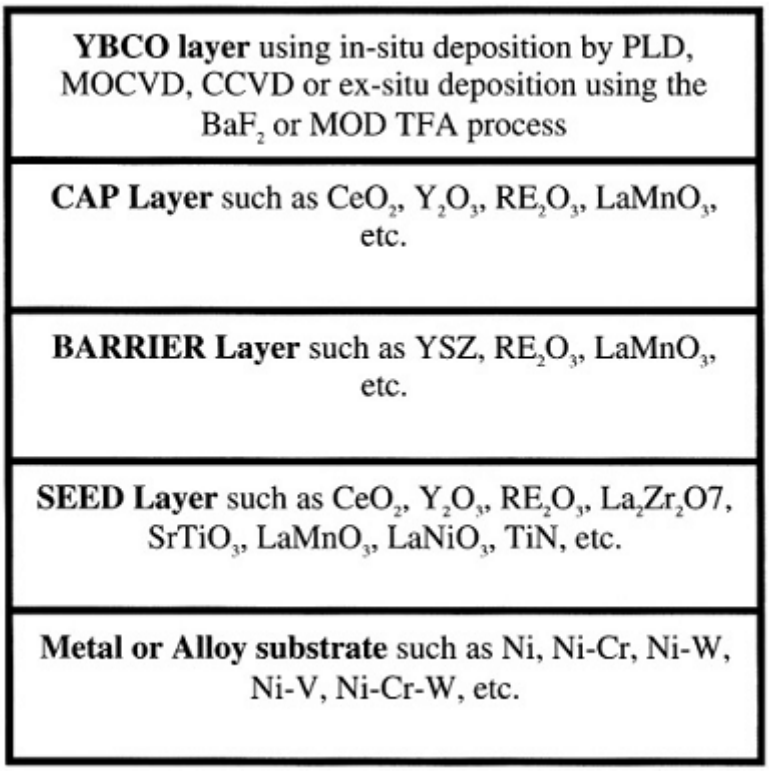

Figure 2-24 Various option of buffer layers for metallic substrate [98]

To prevent oxidation of the metallic substrate (Ni, or Ni alloy), the seed layer is necessary. The seed layer should be thermodynamically more stable than NiO, and there are several candidates such as CeO_2, and Y_2O_3 stabilized ZrO_3 (YSZ). The lattice mismatch between the metal substrate and oxide buffer layer is the main factor influencing the epitaxial growth. The formation of NiO is unpreventable in nature; therefore, to reduce the NiO layer on the surface of the substrate, a mixture of 96%Ar + 4% H_2 is used prior to the seed layer growth to treat the substrate and reduce the NiO. A typical thickness of the seed layer is about 30 – 80 nm [110].

When the good epitaxial seed layer is grown, deposition of barrier and cap layers is relatively straightforward. The most common barrier layer which prevents diffusion of metal from substrate to the film is YSZ. A typical thickness of a barrier layer is in range of 300 – 900 nm [97, 98].

The cap layer commonly used is CeO_2, which is intended to provide a good lattice match to the YBCO layer [111-114]. A typical thickness of a cap layer is about 30-80 nm.

Presently, single buffer layer architecture is being developed to simplify the complex 3 layers as mentioned above; Y_2O_3 was first used as a single buffer layer[115] then $La_2Zr_2O_7$ [116, 117], Sm doped CeO_2 [118] and La doped CeO_2 [119, 120] are also reported. However, the conventional three buffer layer architecture is favourable due to its stability and high J_c.

2.5.4 Potential applications

The whole project was aimed at enhancingto enhance Jc of YBCO thin film on single crystal substrates and then on NiW substrates. The enhancement of Jc is good for many particular applications such as cables, motors, generators, transformers and magnets…

The improvement of Jc in low applied magnetic fields is required for applications involving motors, transformers, magnets ic (eg for magnetic resonance imaging (MRI) [121] while the improvement of Jc in self-field in coated conductors is necessary for cables and the improvement of Jc in high applied fields is particularly relevant specific for applications in high field magnets as shown in Figure 2 25.

Kilometre lengths of HTS cable based on BSSCO have been demonstrated recently, but the general consensus is that it is difficult to reduce the price much further because of the silver matrix required and in applications where coils are required eg., motors, generators, transformers etc., the properties of BSCCO are rather poor because of the critical current dependence on magnetic field [122] due to a high anisotropy factor. In comparison Therefore, YBCO based coated conductors have much better in-field characteristics and are therefore particularly attractive in applications requiring coils, such as cable, motors and transformers.

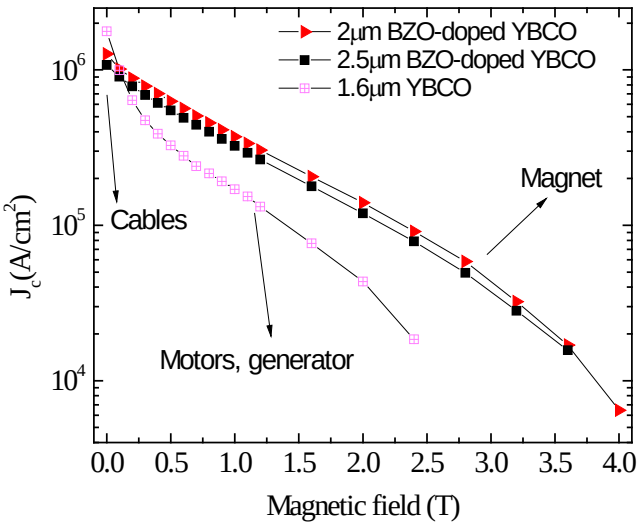

Figure 2-25 Improvement of J_c of YBCO films in self-field and in applied field has different applications

Recently, the invention of multilayer coated conductor cylinders by 3-Cs Ltd could result in new architecture for many potential applications in power systems designs based on “magnetic modules”. This could dramatically shorten the time to market for HTS electrical machines [123] as a result of higher yield and higher power density..

References

[1] V.V. Schmidt, The Physics of Superconductor Springer (1997).

[2] M. Tihkham, Introduction to Superconductivity, Second edition (1996).

[3] J.G. Bednorz, K.A. Muller, Zeitschrift Fur Physik B-Condensed Matter 64/2 (1986) 189.

[4] R.M. Hazen, L.W. Finger, R.J. Angel, C.T. Prewitt, N.L. Ross, H.K. Mao, C.G. Hadidiacos, P.H. Hor, R.L. Meng, C.W. Chu, Physical Review B 35/13 (1987) 7238.

[5] R.M. Hazen, C.T. Prewitt, R.J. Angel, N.L. Ross, L.W. Finger, C.G. Hadidiacos, D.R. Veblen, P.J. Heaney, P.H. Hor, R.L. Meng, Y.Y. Sun, Y.Q. Wang, Y.Y. Xue, Z.J. Huang, L. Gao, J. Bechtold, C.W. Chu, Physical Review Letters 60/12 (1988) 1174.

[6] Z.Z. Sheng, A.M. Hermann, Nature 332/6160 (1988) 138.

[7] A. Schilling, M. Cantoni, J.D. Guo, H.R. Ott, Nature 363/6424 (1993) 56.

[8] J. Nagamatsu, N. Nakagawa, T. Muranaka, Y. Zenitani, J. Akimitsu, Nature 410/6824 (2001) 63.

[9] Y. Kamihara, T. Watanabe, M. Hirano, H. Hosono, Journal of the American Chemical Society 130/11 (2008) 3296.

[10] S.R. Foltyn, H. Wang, L. Civale, Q.X. Jia, P.N. Arendt, B. Maiorov, Y. Li, M.P. Maley, J.L. MacManus-Driscoll, Applied Physics Letters 87/16 (2005).

[11] S.R. Foltyn, Q.X. Jia, P.N. Arendt, L. Kinder, Y. Fan, J.F. Smith, Applied Physics Letters 75/23 (1999) 3692.

[12] Y.V. Cherpak, V.O. Moskaliuk, A.V. Semenov, V.L. Svetchnikov, C.G. Tretiatchenko, V.M. Pan, Superconductor Science & Technology 20/12 (2007) 1159.

[13] S.I. Kim, F. Kametani, Z. Chen, A. Gurevich, D.C. Larbalestier, T. Haugan, P. Barnes, Applied Physics Letters 90/25 (2007).

[14] X. Wang, J.Z. Wu, Physical Review B 76/18 (2007).

[15] S.R. Foltyn, L. Civale, J.L. Macmanus-Driscoll, Q.X. Jia, B. Maiorov, H. Wang, M. Maley, Nat Mater 6/9 (2007) 631.

[16] C.M. Friend, C. Wellstood, D. Vazquez, E. Maher, Superconductor Science & Technology 16/1 (2003) 65.

[17] G. Blatter, V.B. Geshkenbein, A.I. Larkin, Physical Review Letters 68/6 (1992) 875.

[18] G. Blatter, M.V. Feigelman, V.B. Geshkenbein, A.I. Larkin, V.M. Vinokur, Reviews of Modern Physics 66/4 (1994) 1125.

[19] A. Crisan, V.S. Dang, P. Mikheenko, Y.Y. Tse, A. Sarkar, J. Bowen, J.S. Abell, Physica C 470/1 (2010) 55.

[20] A. Goyal, S. Kang, K.J. Leonard, P.M. Martin, A.A. Gapud, M. Varela, M. Paranthaman, A.O. Ijaduola, E.D. Specht, J.R. Thompson, D.K. Christen, S.J. Pennycook, F.A. List, Superconductor Science & Technology 18/11 (2005) 1533.

[21] P. Mele, K. Matsumoto, T. Horide, A. Ichinose, M. Mukaida, Y. Yoshida, S. Horii, R. Kita, Superconductor Science & Technology 21/3 (2008).

[22] S.H. Wee, A. Goyal, P.M. Martin, J. Li, M. Paranthaman, L. Heatherly, Superconductor Science & Technology 19/10 (2006) L42.

[23] F.J. Baca, P.N. Barnes, R.L.S. Emergo, T.J. Haugan, J.N. Reichart, J.Z. Wu, Applied Physics Letters 94/10 (2009).

[24] S. Kang, K.J. Leonard, P.M. Martin, J. Li, A. Goyal, Superconductor Science & Technology 20/1 (2007) 11.

[25] C.V. Varanasi, J. Burke, L. Brunke, H. Wang, M. Sumption, P.N. Barnes, Journal of Applied Physics 102/6 (2007).

[26] N.J. Long, Superconductor Science & Technology 21/2 (2008).

[27] T. Matsushita, Superconductor Science and Technology 13/6 (2000) 730.

[28] M.V.F.m. G. Blatter, V. B. geshkenbein, A. I. Larkin, v. M. Vinokur, Reviews of Modern Physics 66/4 (1994) 1125.

[29] T. Matsushita, G. Isobe, K. Kimura, M. Kiuchi, S. Okayasu, W. Prusseit, Superconductor Science & Technology 21/5 (2008).

[30] L. KrusinElbaum, A.D. Marwick, R. Wheeler, C. Feild, V.M. Vinokur, G.K. Leaf, M. Palumbo, Physical review letters 76/14 (1996) 2563.

[31] J.J. R Biswal, D Behera, P Mallick, Sandeep Kumar, D Kanjilal, T Mohanty, P Raychaudhuri and N C Mishra, Superconductor Science & Technology 21 (2008) 085016.

[32] V.V. Moshchalkov, M. Baert, V.V. Metlushko, E. Rosseel, M.J. VanBael, K. Temst, R. Jonckheere, Y. Bruynseraede, Physical Review B 54/10 (1996) 7385.

[33] A. Silhanek, L. Van Look, R. Jonckheere, B.Y. Zhu, S. Raedts, V.V. Moshchalkov, Physica C 460 (2007) 1434.

[34] W. Gillijns, A.V. Silhanek, V.V. Moshchalkov, Applied Physics Letters 91/20 (2007).

[35] A.V. Silhanek, W. Gillijns, M.V. Milosevic, A. Volodin, V.V. Moshchalkov, F.M. Peeters, Physical Review B 76/10 (2007).

[36] V.F. Solovyov, H.J. Wiesmann, L. Wu, Q. Li, L.D. Cooley, M. Suenaga, B. Maiorov, L. Civale, Superconductor Science & Technology 20/4 (2007) L20.

[37] P.N. Barnes, J.W. Kell, B.C. Harrison, T.J. Haugan, J.L. Burke, C.V. Varanasi, IEEE Trans. Appl. Supercond. 17/2 (2007) 3717.

[38] C.V. Varanasi, P.N. Barnes, J. Burke, Superconductor Science & Technology 20/10 (2007) 1071.

[39] A.V. Pan, S. Pysarenko, S.X. Dou, Applied Physics Letters 88/23 (2006).

[40] M. Ionescu, A.H. Li, Y. Zhao, H.K. Liu, A. Crisan, Journal of Physics D-Applied Physics 37/13 (2004) 1824.

[41] A.H. Li, H.K. Liu, M. Lonescu, X.L. Wang, S.X. Dou, E.W. Collings, M.D. Sumption, M. Bhatia, Z.W. Lin, J.G. Zhu, Journal of Applied Physics 97/10 (2005).

[42] M. Sparing, E. Backen, T. Freudenberg, R. Huhne, B. Rellinghaus, L. Schultz, B. Holzapfel, Superconductor Science & Technology 20/9 (2007) S239.

[43] A. Crisan, S. Fujiwara, J.C. Nie, A. Sundaresan, H. Ihara, Applied Physics Letters 79/27 (2001) 4547.

[44] K. Matsumoto, T. Horide, K. Osamura, M. Mukaida, Y. Yoshida, A. Ichinose, S. Horii, Physica C 412-14 (2004) 1267.

[45] P. Mele, K. Matsumoto, T. Horide, O. Miura, A. Ichinose, M. Mukaida, Y. Yoshida, S. Horii, Physica C 445 (2006) 648.

[46] C. Cai, J. Hanisch, R. Huhne, V. Stehr, C. Mickel, T. Gemming, B. Holzapfel, Journal of Applied Physics 98/12 (2005) 123906.

[47] H. Huhtinen, P. Paturi, E. Lahderanta, Physics of Low-Dimensional Structures 9-10 (1999) 25.

[48] P. Paturi, H. Huhtinen, K. Laajalehto, R. Laiho, Superconductor Science & Technology 13/5 (2000) 622.

[49] P. Paturi, M. Peurla, K. Nilsson, J. Raittila, Superconductor Science & Technology 17/3 (2004) 564.

[50] J. Raittila, M. Peurla, H. Huhtinen, P. Paturi, R. Laiho, Physica C 408-10 (2004) 647.

[51] H. Huhtinen, M. Peurla, M.A. Shakhov, Y.P. Stepanov, P. Paturi, J. Raittila, R. Palai, R. Laiho, IEEE Trans. Appl. Supercond. 17/2 (2007) 3620.

[52] K. Matsumoto, P. Mele, A. Ichinose, M. Mukaida, Y. Yoshida, S. Horii, R. Kita, IEEE Trans. Appl. Supercond. 19/3 (2009) 3248.

[53] V.S. Dang, P. Mikheenko, A. Sarkar, M.M. Awang Kechik, J.S. Abell, A. Crisan, Physica C: Superconductivity 470/20 (2010) 1238.

[54] D.M. Feldmann, et al., Superconductor Science and Technology 23/9 (2010) 095004.

[55] T. Aytug, M. Paranthaman, H.Y. Zhai, K.J. Leonard, A.A. Gapud, J.R. Thompson, P.M. Martin, A. Goyal, D.K. Christen, IEEE Trans. Appl. Supercond. 15/2 (2005) 2977.

[56] M.P. Aytug. T, A. A. Gapud, S. Kang, H. M. Christen, K. J. Leonard, P. M. Martin, J. R. Thompson, and D. K. Christen, R. Meng, I. Rusakova, C. W. Chu, T. H. Johansen, Journal of Applied Physics 98 (2005) 114309.

[57] P. Mele, K. Matsumoto, T. Horide, O. Miura, A. Ichinose, M. Mukaida, Y. Yoshida, S. Horii, Superconductor Science & Technology 19/1 (2006) 44.

[58] J. Gutierrez, A. Llordes, J. Gazquez, M. Gibert, N. Roma, S. Ricart, A. Pomar, F. Sandiumenge, N. Mestres, T. Puig, X. Obradors, Nature Materials 6/5 (2007) 367.

[59] E. Backen, J. Hanisch, R. Huhne, K. Tscharntke, S. Engel, T. Thersleff, L. Schultz, B. Holzapfel, IEEE Trans. Appl. Supercond. 17/2 (2007) 3733.

[60] J.L. MacManus-Driscoll, S.R. Foltyn, B. Maiorov, Q.X. Jia, H. Wang, A. Serquis, L. Civale, Y. Lin, M.E. Hawley, M.P. Maley, D.E. Peterson, Applied Physics Letters 86/3 (2005).

[61] K. Matsumoto, D. Takahara, T. Horide, A. Ichinose, S. Horii, Y. Yoshida, M. Mukaida, K. Osamura, IEEE Trans. Appl. Supercond. 15/2 (2005) 2719.

[62] Q.X. Jia, B. Maiorov, H. Wang, Y. Lin, S.R. Foltyn, L. Civale, J.L. MacManus-Driscoll, IEEE Trans. Appl. Supercond. 15/2 (2005) 2723.

[63] K. Develos-Bagarinao, H. Yamasaki, K. Ohki, Y. Nakagawa, Superconductor Science & Technology 20/6 (2007) L25.

[64] K. Yokoyama, R. Kita, A. Ichinose, O. Miura, K. Matsumoto, Y. Yoshida, M. Mukaida, S. Horii, Physica C 445 (2006) 587.

[65] T. Horide, K. Matsumoto, A. Ichinose, M. Mukaida, Y. Yoshida, S. Horii, IEEE Trans. Appl. Supercond. 17/2 (2007) 3729.

[66] R. Kita, T. Nakamura, A. Ichinose, O. Miura, K. Matsumoto, Y. Yoshida, M. Mukaida, S. Horii, Modern Physics Letters B 21/21 (2007) 1377.

[67] T. Horide, K. Matsumoto, A. Ichinose, M. Mukaida, Y. Yoshida, S. Horii, Superconductor Science & Technology 20/4 (2007) 303.

[68] Y. Yamada, K. Takahashi, H. Kobayashi, M. Konishi, T. Watanabe, A. Ibi, T. Muroga, S. Miyata, T. Kato, T. Hirayama, Y. Shiohara, Applied Physics Letters 87/13 (2005).

[69] M. Miura, M. Mukaida, K. Matsumoto, Y. Yoshida, A. Ichinose, S. Horii, R. Kita, A. Saito, K. Kaneko, K. Yamada, N. Mori, Physica C 445 (2006) 845.

[70] M. Itoh, Y. Yoshida, Y. Ichino, M. Miura, Y. Takai, K. Matsumoto, A. Ichinose, M. Mukaida, S. Horii, Physica C 412-14 (2004) 833.

[71] M. Miura, M. Itoh, Y. Ichino, Y. Yoshida, Y. Takai, K. Matsumoto, A. Ichinose, S. Horii, M. Mukaida, IEEE Trans. Appl. Supercond. 15/2 (2005) 3078.

[72] M. Mukaida, T. Horide, Y. Shingai, A. Ichinose, K. Matsumoto, S. Horii, R. Kita, Y. Yoshida, S. Awaji, K. Watanabe, R. Teranishi, K. Yamada, N. Mori, IEEE Trans. Appl. Supercond. 17/2 (2007) 3688.

[73] S.H. Wee, A. Goyal, J. Li, Y. Zhang, L. Heatherly, Journal of Electronic Materials 36/10 (2007) 1230.

[74] R. Honda, Y. Ichino, Y. Yoshida, Y. Takai, K. Matsumoto, A. Ichinose, R. Kita, M. Mukaida, S. Horii, Physica C 426 (2005) 1005.

[75] C. Cai, B. Holzapfel, J. Hanisch, L. Fernandez, L. Schultz, Physical Review B 69/10 (2004).

[76] J.L. Macmanus-Driscoll, S.R. Foltyn, Q.X. Jia, H. Wang, A. Serquis, L. Civale, B. Maiorov, M.E. Hawley, M.P. Maley, D.E. Peterson, Nature Materials 3/7 (2004) 439.

[77] T. Aytug, M. Paranthaman, K.J. Leonard, S. Kang, P.M. Martin, L. Heatherly, A. Goyal, A.O. Ijaduola, J.R. Thompson, D.K. Christen, R. Meng, I. Rusakova, C.W. Chu, Physical Review B 74/18 (2006).

[78] Y. Shingai, T. Numasawa, M. Mukaida, R. Teranishi, R. Kita, A. Ichinose, S. Horii, Y. Yoshida, K. Matsumoto, S. Awaji, K. Watanabe, A. Saito, K. Yamada, N. Mori, Physica C 463 (2007) 909.

[79] J.L. MacManus-Driscoll, S.C. Wimbush, Applied Superconductivity, IEEE Transactions on PP/99 (2011) 1.

[80] M. Ito, M. Mukaida, T. Ohazama, R. Kita, A. Ichinose, S. Horii, A. Saito, K. Matsumoto, Y. Yoshida, K. Koike, F. Hirose, S. Ohshima, Physica C 426 (2005) 1415.

[81] M. Haruta, T. Fujiyoshi, T. Sueyoshi, K. Dezaki, D. Ichigosaki, K. Miyahara, R. Miyagawa, M. Mukaida, K. Matsumoto, Y. Yoshida, A. Ichinose, S. Horii, Superconductor Science & Technology 19/8 (2006) 803.

[82] S. Yasunaga, M. Mukaida, S. Horii, R. Kita, S. Kato, A. Ichinose, Y. Yoshida, K. Matsumoto, R. Teranishi, K. Yamada, N. Mori, Physica C 463 (2007) 900.

[83] Y. Shi, N.H. Babu, K. Iida, D.A. Cardwell, Physica C 468/15-20 (2008) 1408.

[84] A. Koblischka-Veneva, F. Mucklich, M.R. Koblischka, N.H. Babu, D.A. Cardwell, 7th European Conference on Applied Superconductivity (Eucas'05) 43 (2006) 438.

[85] A. Koblischka-Veneva, F. Mucklich, M.R. Koblischka, N.H. Babu, D.A. Cardwell, Journal of the American Ceramic Society 90/8 (2007) 2582.

[86] H.C. Kanithi, C.G. King, B.A. Zeitlin, R.M. Scanlan, Ieee Transactions on Magnetics 25/2 (1989) 1922.

[87] D.K. Finnemore, K.E. Gray, M.P. Maley, D.O. Welch, D.K. Christen, D.M. Kroeger, Physica C 320/1-2 (1999) 1.

[88] D. Dimos, P. Chaudhari, J. Mannhart, Physical Review B 41/7 (1990) 4038.

[89] J.L. MacManus-Driscoll, Annual Review of Materials Science 28 (1998) 421.

[90] A. Goyal, E.D. Specht, D.M. Kroeger, T.A. Mason, Applied Physics Letters 68/5 (1996) 711.

[91] A. Goyal, D.P. Norton, D.K. Christen, E.D. Specht, M. Paranthaman, D.M. Kroeger, J.D. Budai, Q. He, F.A. List, R. Feenstra, H.R. Kerchner, D.F. Lee, E. Hatfield, P.M. Martin, J. Mathis, C. Park, Applied Superconductivity 4/10-11 (1996) 403.

[92] D.P. Norton, A. Goyal, J.D. Budai, D.K. Christen, D.M. Kroeger, E.D. Specht, Q. He, B. Saffian, M. Paranthaman, C.E. Klabunde, D.F. Lee, B.C. Sales, F.A. List, Science 274/5288 (1996) 755.

[93] D.P. Rodionov, I.V. Gervas'eva, Y.V. Khlebnikova, B.K. Sokolov, Physics of Metals and Metallography 93/5 (2002) 458.

[94] H.S. Guo, M.L. Zhou, D.M. Liu, T.Y. Zuo, Y.L. Zhou, R.P. Wang, S.H. Pan, H.H. Wang, Physica C 337/1-4 (2000) 96.

[95] P.P. Bhattacharjee, R.K. Ray, A. Upadhyaya, J. Mater. Sci. 42/6 (2007) 1984.

[96] B.A. Glowacki, M.E. Vickers, N.A. Rutter, E. Maher, F. Pasotti, A. Baldini, R. Major, J. Mater. Sci. 37/1 (2002) 157.

[97] J. Eickemeyer, D. Selbmann, R. Opitz, H. Wendrock, E. Maher, U. Miller, W. Prusseit, Physica C 372 (2002) 814.

[98] A. Goyal, Second-Generation HTS conductors Kluwer Academic Publishers (2005).

[99] R.C. Duckworth, A.J. Gouge, J. Caughman, J.W. Lue, J.A. Demko, J. Tolbert, C.L.H. Thieme, D.T. Verebelyi, IEEE Trans. Appl. Supercond. 15/2 (2005) 1578.

[100] S.M. Lim, H.S. Kim, K.C. Chung, B.S. Lee, D. Youm, Superconductor Science & Technology 17/1 (2004) 148.

[101] M.V. Rane, H. Efstathiadis, H. Bakhru, M.W. Rupich, X. Li, W. Zhang, T. Kodenkandath, P. Haldar, IEEE Trans. Appl. Supercond. 15/2 (2005) 2638.

[102] M.W. Rupich, U. Schoop, D.T. Verebelyi, C. Thieme, W. Zhang, X. Li, T. Kodenkandath, N. Nguyen, E. Siegal, D. Buczek, J. Lynch, M. Jowett, E. Thompson, J.S. Wang, J. Scudiere, A.P. Malozemoff, Q. Li, S. Annavarapu, S. Cui, L. Fritzemeier, B. Aldrich, C. Craven, F. Niu, R. Schwall, A. Goyal, M. Paranthaman, IEEE Trans. Appl. Supercond. 13/2 (2003) 2458.

[103] D.Q. Shi, R.K. Ko, K.J. Song, J.K. Chung, H.S. Ha, H.S. Kim, S.H. Moon, S.I. Yoo, C. Park, Superconductor Science & Technology 18/4 (2005) 561.

[104] Y.L. Cheung, E.F. Maher, J.S. Abell, I.P. Jones, Y.Y. Tse, Superconductor Science & Technology 20/6 (2007) 511.

[105] A. Nakai, J. Matsuda, Y. Sutoh, Y. Kitoh, M. Yoshizumi, T. Izumi, Y. Shiohara, M. Mimura, Physica C 463 (2007) 615.

[106] Y. Zhao, H.L. Suo, M. Liu, D. He, Y.X. Zhang, R.F. Fan, L. Ma, M.L. Zhou, IEEE Trans. Appl. Supercond. 17/2 (2007) 3424.

[107] V. Cloet, T. Thersleff, O. Stadel, S. Hoste, B. Holzapfel, I. Van Driessche, Acta Materialia 58/5 (2010) 1489.

[108] M. Lei, G. Li, R.P. Sun, M.H. Pu, W.T. Wang, W. Wu, X. Zhang, H. Zhang, Y. Zhang, C.H. Cheng, Y. Zhao, Rare Metal Materials and Engineering 38/8 (2009) 1458.

[109] J. Eickemeyer, D. Selbmann, R. Opitz, B. de Boer, B. Holzapfel, L. Schultz, U. Miller, Supercond. Sci. Technol 14/3 (2001) 152.

[110] C. Cantoni, D.K. Christen, A. Goyal, L. Heatherly, F.A. List, G.W. Ownby, D.M. Zehner, H.M. Christen, C.M. Rouleau, IEEE Trans. Appl. Supercond. 13/2 (2003) 2646.

[111] C. Cai, R.I. Chakalova, G. Kong, K. Kawano, T.W. Button, J.S. Abell, E. Maher, Physica C-Superconductivity and Its Applications 372 (2002) 786.

[112] R. Huhne, V.S. Sarma, D. Okai, T. Thersleff, L. Schultz, B. Holzapfel, Supercond. Sci. Technol 20/7 (2007) 709.

[113] M.P. Paranthaman, S. Sathyamurthy, M.S. Bhuiyan, A. Goyal, T. Kodenkandath, X. Li, W. Zhang, C.L.H. Thieme, U. Schoop, D.T. Verebelyi, M.W. Rupich, Ieee Transactions on Applied Superconductivity 15/2 (2005) 2632.

[114] R.I. Chakalova, C. Cai, T. Woodcock, T.W. Button, J.S. Abell, E. Maher, Physica C-Superconductivity and Its Applications 372 (2002) 846.

[115] T.G. Chirayil, M. Paranthaman, D.B. Beach, J.S. Morrell, E.Y. Sun, A. Goyal, R.K. Williams, D.F. Lee, P.M. Martin, D.M. Kroeger, R. Feenstra, D.T. Verebelyi, D.K. Christen, in: M.E. Hawley, D.H.A. Blank, C.B. Eom, D.G. Schlom, S.K. Streiffer (Eds.), Multicomponent Oxide Films for Electronics, vol. 574, Materials Research Society, Warrendale, 1999, p. 51.

[116] T. Caroff, S. Morlens, A. Abrutis, M. Decroux, P. Chaudouet, L. Porcar, Z. Saltyte, C. Jimenez, P. Odier, F. Weiss, Superconductor Science & Technology 21/7 (2008).

[117] T.G. Chirayil, M. Paranthaman, D.B. Beach, D.F. Lee, A. Goyal, R.K. Williams, X. Cui, D.M. Kroeger, R. Feenstra, D.T. Verebelyi, D.K. Christen, Physica C 336/1-2 (2000) 63.

[118] G. Li, M.H. Pu, R.P. Sun, W.T. Wang, W. Wu, X. Zhang, Y. Yang, C.H. Cheng, Y. Zhao, Journal of Alloys and Compounds 466/1-2 (2008) 429.

[119] R.P. Sun, M.H. Pu, G. Li, W.T. Wang, M. Pan, H. Zhang, M. Lei, W. Wu, X. Zhang, Y. Yang, Y. Zhang, Y. Zhao, Physica Status Solidi a-Applications and Materials Science 206/7 (2009) 1414.

[120] Y. Zhao, H.L. Suo, J.C. Grivel, S.A. Ye, M. Liu, L. Ma, M.L. Zhou, Journal of Inorganic Materials 24/6 (2009) 1201.

[121] P. Tixador, G. Donnier-Valentin, E. Maher, IEEE Trans. Appl. Supercond. 13/2 (2003) 2331.

[122] E. Maher, Gold 2003 conference procceding. (2003)

[123] E. Maher, J.S. Abell, R.I. Chakalova, Y.L. Cheung, T.W. Button, P. Tixador, Superconductor Science & Technology 17/12 (2004) 1440.

Chapter 3. **Experimental**

3.1 Sample preparation

3.1.1 Pulsed laser deposition

Pulsed laser deposition (PLD) is the most popular deposition system for growing high quality oxide films, including YBCO superconductors. Generally, a PLD system contains a high vacuum pumping system to achieve a vacuum of 10^{-7} to 10^{-9} Torr, a heater and a target rotation system. For superconducting films, an excimer KrF laser 248 nm is widely used nowadays as the laser source for PLD.

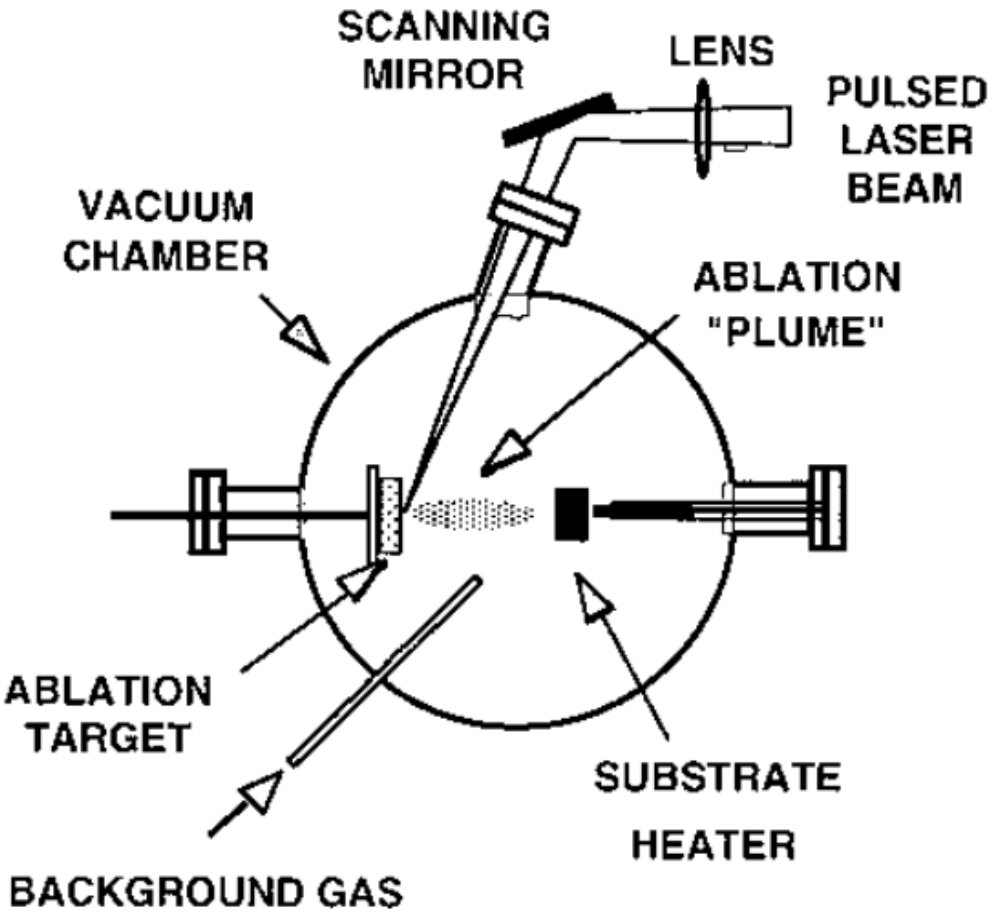

Figure 3-1 Schematic diagram of pulse laser deposition system [1]

A schematic diagram of PLD system is shown in Figure 3-1: a pulsed laser beam is focused onto a target of the material to be deposited, and normally a high energy density laser is used. Each laser pulse ablates a small amount of the material and the ablated material is ejected from the target in a forward-directed plume to the substrate. Typical thin film process can be divided into three stages, 1) Production of appropriate atomic, molecular, or ionic species, 2) Transport of these species to substrate through a medium, 3) Condensation onto the substrate either directly or via a chemical or electrochemical reaction. The size and energy of the plume depend on the base pressure inside the chamber and on the laser energy density, laser spot size. A typical plume is shown in Figure 3-2 and the chamber and laser in Figure 3-3 and Figure 3-4.

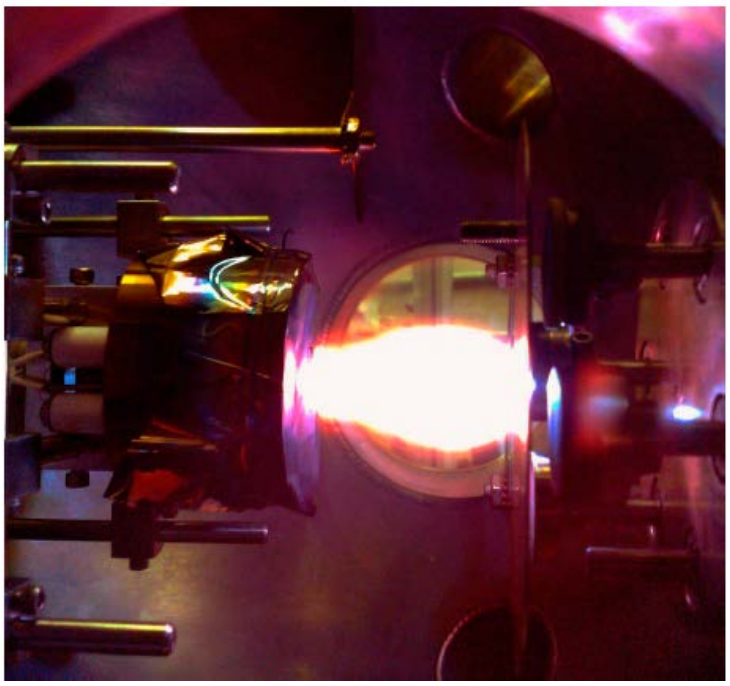

Figure 3-2 A laser plume inside the PLD chamber used in this project

Most of films were prepared on $SrTiO_3$ (STO) single crystal substrates by PLD which used a laser scanning system, and target rotation. Some films were grown on buffered RABiTS substrates. The substrates were ultrasonically cleaned in acetone and ethanol and

subsequently dried in air by hot air flow before each deposition. Commercial (Pi-Kem Ltd.) YBCO (99.9%), PBCO (99.9%), and Ag (99.99%) targets were used in the first part of the project, while BZO-doped YBCO samples were provided by collaborators from University of Turku, Finland.

Initially, a pure YBCO target was used to find out the optimum conditions for PLD chamber; all YBCO films can be reproducibly grown on STO with the same conditions as shown in Chapter 4. An excimer KrF 248 nm laser with pulse duration 30 ns, repetition rate of 4 Hz and laser energy density of 0.68 J/cm^2 was used in our depositions. The target – substrate distance was 5.8 cm, substrate temperature was set at 780^o C and the oxygen partial pressure during deposition was 450 mTorr. After the deposition, the films were cooled down in partial oxygen atmosphere of 450 Torr at the rate of 8^o C/min. With these optimum conditions high quality YBCO films have been obtained as shown in Chapter 4. Hundreds of YBCO samples were fabricated and all the samples can be reproduced by the same deposition conditions.

For YBCO films with Ag substrate decoration, the same condition for YBCO growth has been used. Prior to YBCO deposition Ag nanodots were optimised and grown, also by PLD at a substrate temperature of 400^o C in vacuum. For Ag/YBCO quasi-superlattices, the same conditions for YBCO and Ag were used, by alternating YBCO layers and Ag quasi-layers several times. The same growth conditions were used for YBCO/PBCO quasi-multilayers.

Later, an YBCO target doped with 4% wt BZO, provided by the group of Prof. Paturi, University Turku, Finland was used. The same growth procedures as for the pure YBCO target were carried out; the only difference being the deposition temperature of 800^o C instead of 780^o C as in the YBCO case. The reason of higher temperature deposition in comparison with pure YBCO will be explained in Chapter 4.

In the last part of the thesis, Ni-5at%W (Ni:5W) RABiTS substrates supplied by 3-Cs Ltd were used for the deposition of YBCO and BZO-doped YBCO, with intermediate buffer layers. The buffer layers chosen in this project follow the architecture CeO_2 95 nm/YSZ 600 nm/CeO_2 95 nm. The buffer layers were grown at a temperature of 750 ^oC. To prevent the oxidation of Ni:5W substrate, the first 300 laser pulses of CeO_2 were ablated in high vacuum of about 10^{-7} Torr and then the O_2 was introduced up to of 10^{-4} Torr for the rest of the growth of the buffer layers. Ag decoration, YBCO or BZO-doped YBCO were deposited on Ni:5W using the same conditions as for the STO substrate, except a slightly higher temperature of 800 ^oC.

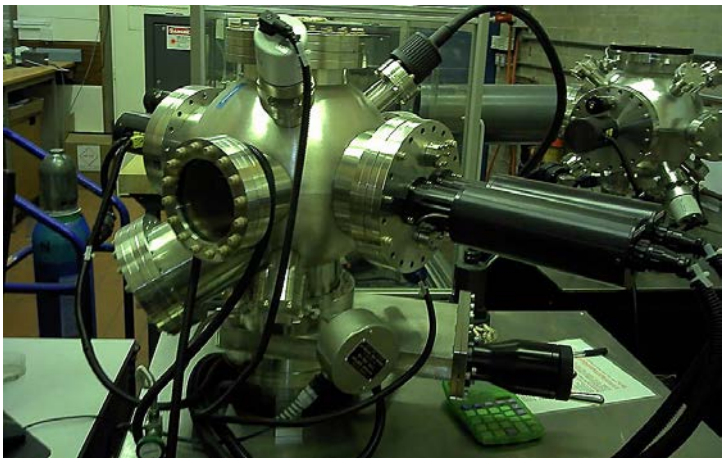

Figure 3-3 PLD chamber used in this project

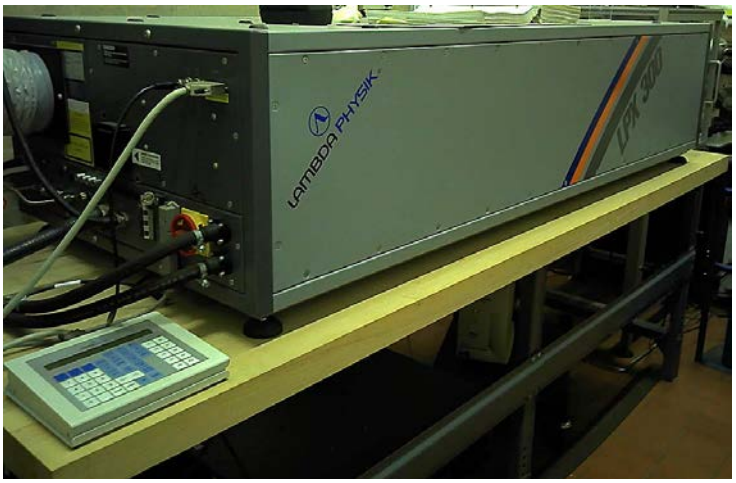

Figure 3-4 Lambda Physik LPX 300 laser system used in this project

3.1.2 Photolithography

To make a small bridge (nano to micrometres size) for transport measurements, patterning a sample using acid etching or ion beam milling by photolithography is required. In this project, due to the rather thick films grown, patterning using acid etching was employed. After cleaning with Acetone and 2- Isopropanol, the sample was placed on a speed controllable spinner, and, while rotating with a speed of 4000 rpm, 2 or 3 photoresist S1818 droplets were applied on the surface of the sample which continued to rotate for 30 seconds to a minute. The sample then was baked for a few minutes at a temperature of 120^{o} C before being exposed to an UV400 Exposure Optics (for 365nm and 405nm exposure) UV source through a mask, designed to form 4 bridges with lateral size from 5μm to 50μm, using a Karl Suss MJB3 Mask Aligner as shown in Figure 3-5. The exposed sample then was developed in Microsposit MF-319 developer for a few minutes, the time needed depending on the quality of the exposed sample.

Figure 3-5 Karl Suss MJB3 Mask Aligner system in Electronic and Electrical Engineering School was used in this project

Diluted Nitric acid 0.1% was used to etch the developed sample. The sample was immersed in the diluted acid for several minutes, depending on the thickness of the sample. Normally, a 1μm thick sample will take about 10 minutes etching. The etching time is not growing linearly with the thickness, the thicker the film, the more difficult is to etch the sample. Less than 1μm thick film is easily and quickly etched, but several microns thick films were etched successfully by acid etching method in this project. The etched samples were then cleaned by acetone again to remove the photoresist layers and remaining acid in an ultrasonic bath. In some cases, the smallest bridge (about 5μm) was broken due to ultrasonic vibration or over-etching. Figure 3-6 to Figure 3-8 show typical views of patterned sample with 4 bridges of different thickness.

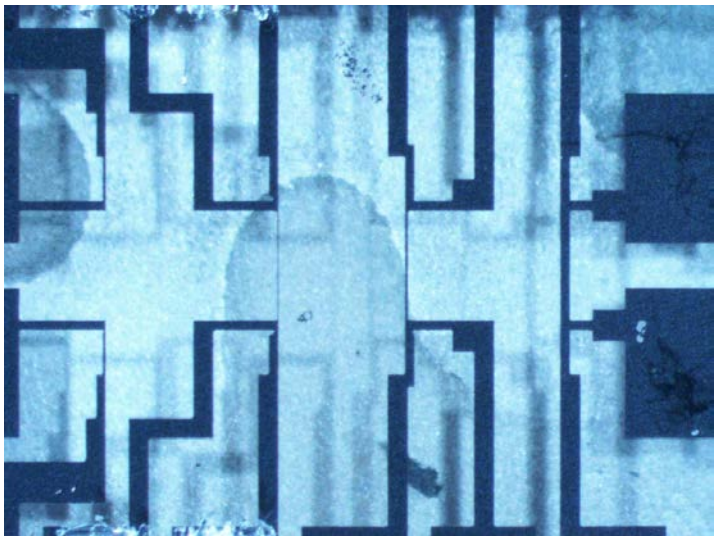

Figure 3-6 An overview of 4 bridges after etching, in this case, the smallest one was broken during etching

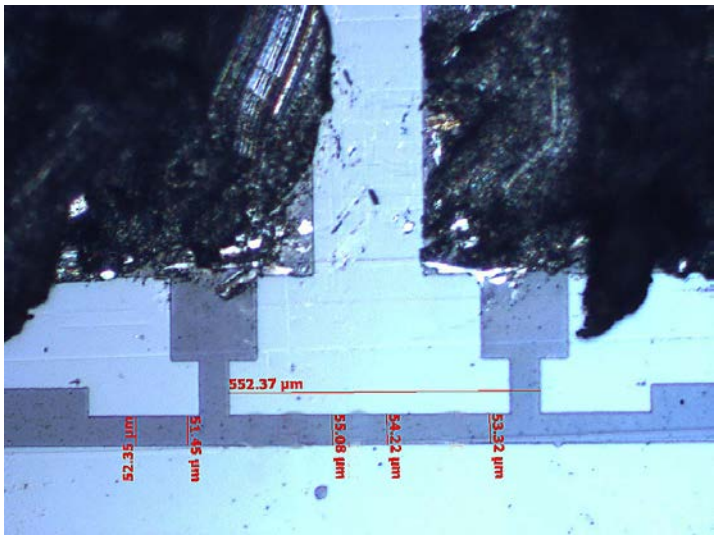

Figure 3-7 The bridge with the largest size, normally 53-55 µm width and 550 µm length

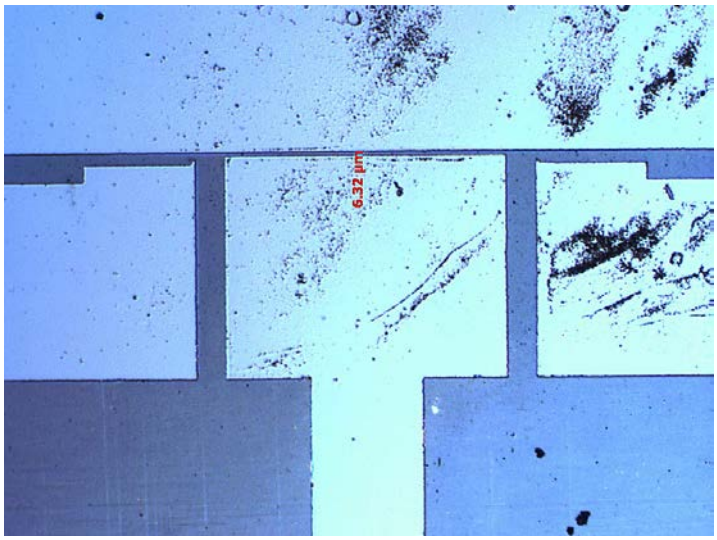

Figure 3-8 The smallest existing bridge, with about 6µm width

3.1.3 Preparing sample for transmission electron microscopy by focused ion beam (FIB)

To become transparent for electrons, a specimen needs to be thinned to less than 100 nm [2]. Thanks to the FIB system, this work can be done more easily than hand polishing which

was used before 2008 when the FIB was not in Metallurgy and Materials school. The versatile **Quanta 3D FEG** system (Figure 3-9) was used in this project to prepare samples for TEM. The Quanta 3D FEG dual beam combines two systems: scanning electron microscopy (SEM) and focused ion beam (FIB).

The whole sample surface was first coated with a thin gold layer. A selected area of interest on the sample was then coated with a tungsten (W) protective layer. A large trench on alternating sides of the protective layer was then milled and the membrane thinned below 2 μm. The thin sample was cut, lifted out and transferred to a TEM grid with an omniprobe. The final step was thinning the sample to the required thickness. The sequence of step is shown in gure 3-10.

Figure 3-9 The **Quanta 3D FEG system in The Metallurgy and Material School (Photo from:** http://www.cem.bham.ac.uk/quanta.shtml**)**

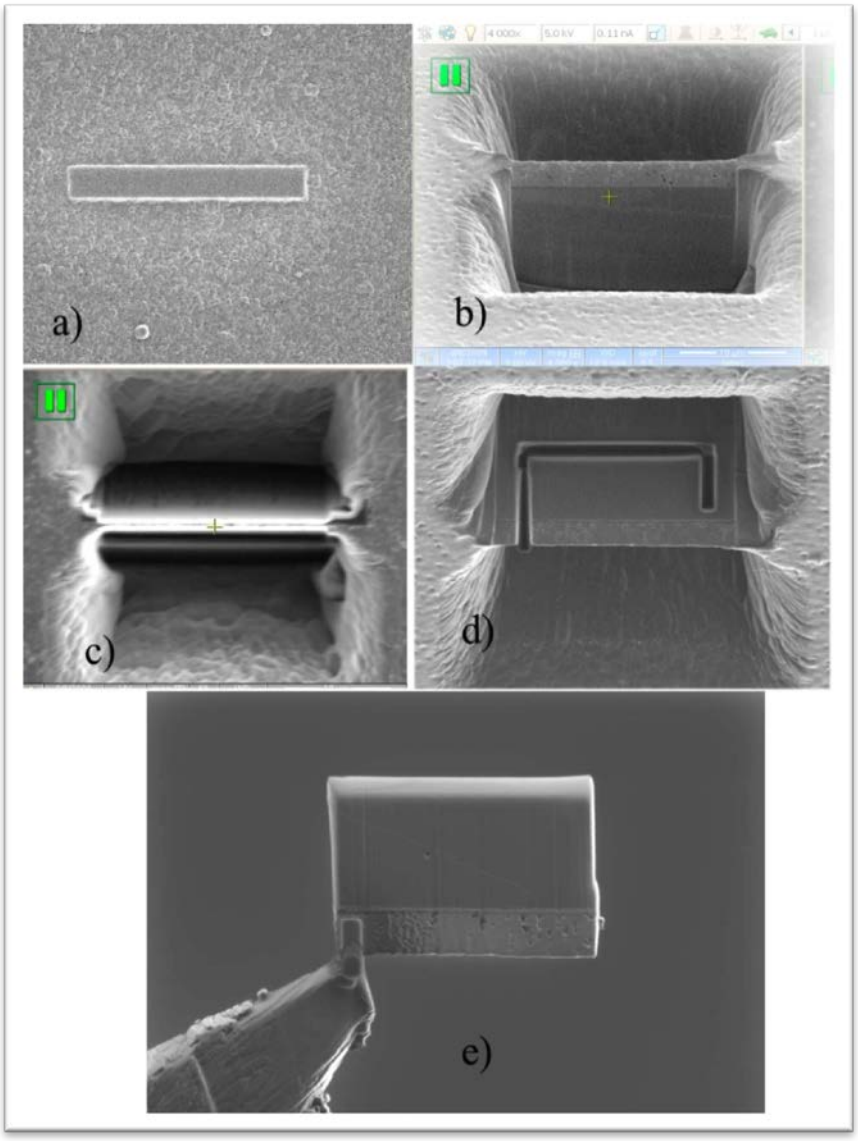

gure 3-10 FIB process; a) cover sample, b) mill sample, c) cleaning, d) cut, e) stick on a grid and then thinning

3.2 Superconducting properties analysis

3.2.1 Critical temperature (T_c) measurement

The magnetic susceptibility χ is defined as $\chi = \frac{dM}{dH}$, and describes how a specimen placed in magnetic field responds to this applied magnetic field. In our case, a superconductor

displays perfect diamagnetism with χ = -1. When a small AC magnetic field is applied to a specimen, the susceptibility will be AC susceptibility, which consists of two parts: χ' real AC susceptibility (in phase) and χ" imaginary part (out-of- phase). In this project, the AC susceptibility was measured using a Quantum Design Magnetic Property Measurement System (MPMS-XL5) in the Physics Department, with frequencies from 0.1 Hz to 1 KHz, which has a sensitivity of 2 x 10^{-8} emu at 0 T and temperature accuracy of 0.1 %. So the temperature dependence of AC susceptibility which results in T_c value has error of 0.1%.

Fundamentally, a sample is centred in two coils; the driving coil carrying an AC current (generating an AC field) and the pick-up coil detecting the signal from the sample. The time-dependent field induces a current in the pick-up coil allowing the measurement without sample movement. To determine T_c, the temperature dependence of $\chi = \chi' - i\chi''$ was registered. Normally, the minimum excitation field of the MPMS system of 0.05 Oe was used to determine T_c; a higher excitation field results in an underestimated T_c due to a higher probing current. A typical example is shown in Figure 3-11.

In fact, both χ' and χ" depend not only on temperature and AC amplitude, but also on AC frequency (especially in higher fields where thermally-activated flux creep is time-dependent). As will be described in section 3.2.3., from the frequency and field dependence of χ", the critical current density can be determined

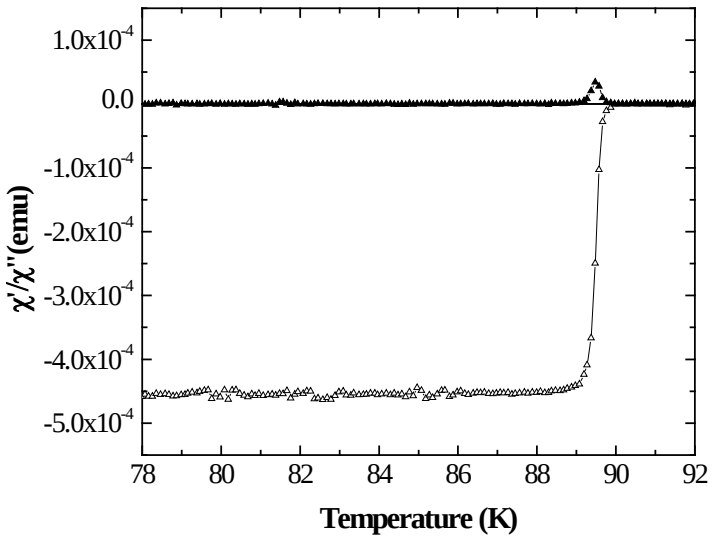

Figure 3-11 An example of determination of T_c in a YBCO thin film determined from χ vs. T measurement ($\chi' < 0$) ($\chi'' > 0$)

3.2.2 Critical current density measurement by DC magnetisation loop

Critical current density (J_c) of a sample can be easily estimated from the DC magnetisation loops. Unlike the four-point probe transport measurement, the magnetisation loop method is contactless and much easier, and based on a critical state model introduced by C. P. Bean [3]. The critical state model (Bean model) assumes that the current flowing in the sample is either the critical current J_c or zero. MPMS XL system as shown in Figure 3-12 was used to measure magnetisation loops of all samples grown on STO. The film surface (superconducting a-b planes) is normal to the applied magnetic field. The samples prepared on Ni:5W substrates could not be measured by this method due to the very strong ferromagnetic signal of the Ni:5W substrate. Transport measurements and AC susceptibility were carried out to calculate J_c of the sample on Ni:5W substrates. Most of samples on STO substrate were 5 x 5 mm and in this case, J_c was calculated as

$$J_c = \frac{6m}{a^3 d} \quad (3.1)$$

where m is the irreversible magnetic moment, or half of the width of the magnetisation loop. In some cases, samples were accidently broken while taking out from the heater, and the broken samples were polished in rectangular shape with dimensions a and b (a < b). For such rectangular samples, J_c was estimated from

$$J_c = \frac{4m}{a^2 bd(1-\frac{a}{3b})}. \quad (3.2)$$

where d is film thickness. The formulae (3.1) and (3.2) are not applicable below a characteristic magnetic field B_c [4], which is a function of J_c. In our films at 77.3 K B_c does not exceed 0.1 T. In magnetic field below B_c, whenever it was necessary, J_c was determined by an exponential approximation from J_c at higher fields.

Figure 3-12 MPMS system used in this project, with DC magnetic field up to 6 T

The MPMS superconducting magnets have high field homogeneity (0.01%) within the measuring region and the accuracy of 0.03%.

Measurement error of J_c comes from magnetic moment m of MPMS system, thickness d of the sample and size of the sample a. By using standard deviations, one can calculate error for J_c from equation (3.1) for square sample as $\left(\left(\frac{dJ_c}{J_c}\right)^2 = 6\left(\frac{dm}{m}\right)^2 + 3\left(\frac{da}{a}\right)^2 + \left(\frac{dd}{d}\right)^2\right)$ (3.3). Normally, error for thickness d and size a are ±0.1 and the magnetic moment has accuracy of 0.03%. For example, the error of J_c = 1.3x10^6 A/cm^2 of a sample with standard size 5x5 mm and thickness of 2 μm is 0.08x10^6 by using equation (3.3). So J_c can be rewritten as J_c = (1.3 ± 0.08)x10^6 A/cm^2.

3.2.3 Critical current density measured by AC susceptibility

The critical current density can also be calculated from AC susceptibility while a DC field is applied to the sample (or zero DC applied field at temperatures close to T_c). The dependence of J_c on DC field, temperature and AC frequency can be determined from AC susceptibility measurement. By installing the AC measurement system (ACMS) option from Physical property measurement system (PPMS), the dependence of χ' and χ" on AC frequency and DC applied field, at fixed temperatures, could be measured. The fundamental frequency components of the AC susceptibility have clear physical meanings: χ' measures the shielding effect of super-currents and χ" measures the hysteretic energy loss per cycle per unit volume [5, 6]. Brandt [7] has demonstrated that, for flat superconductors (films) in perpendicular fields,

$$J_c = \frac{H_m}{\alpha.d} \quad (3.4)$$

where H_m is the AC field amplitude at which χ" has a maximum, d is the film thickness of the sample, and $\alpha = 0.8 – 1.0$ is a coefficient slightly depending on geometry of sample. Typical results are shown in Figure 3-13.

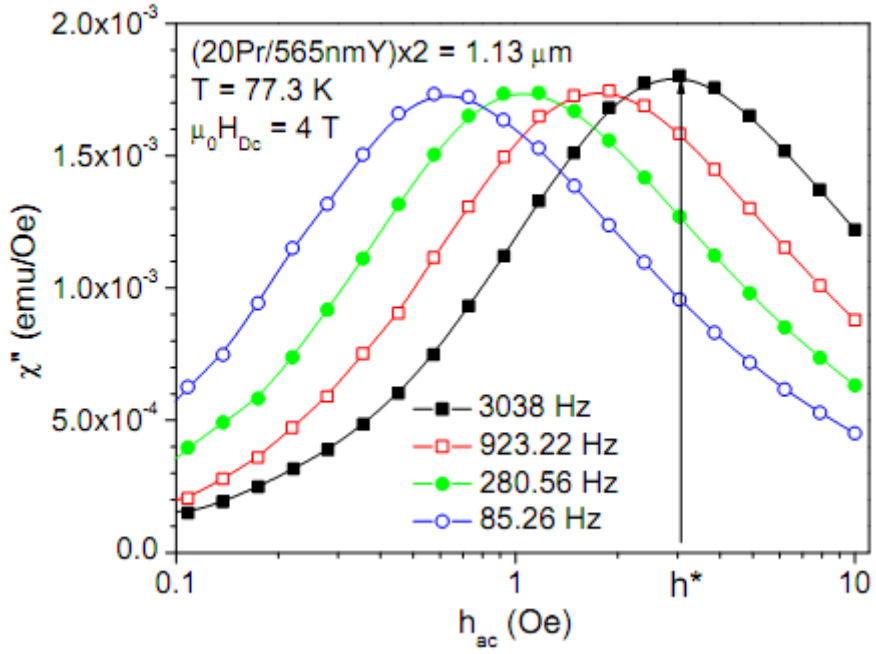

Figure 3-13 Example of AC field dependence of χ" at various frequencies, at 77.3 K and in 4 T, of PBCO/YBCO multilayer [8] where $h^* = H_m$ in eq 3.4

3.2.4 Transport measurement

To estimate the anisotropy of critical current and to determine the type of artificial pinning centres, the angular-dependent critical current density transport measurements are needed. The transport measurements were carried out using the PPMS system with Electronic Transport option inserted. The patterned sample was connected with the sample holder by indium solder through gold wires as shown in Figure 3-14 and Figure 3-15. In the beginning of the project, Ag paint was used for contact in transport measurement, but it was not very successful as the contact is not stable and not as good as indium.

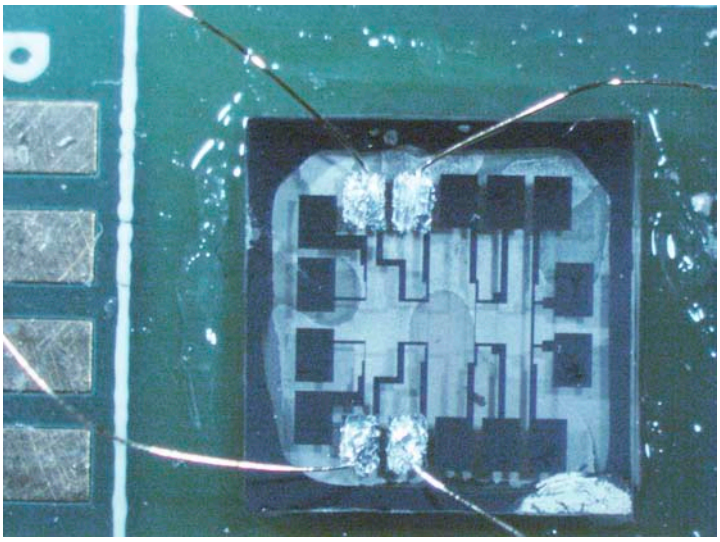

Figure 3-14 Patterned sample with 4 wires connection on sample broad

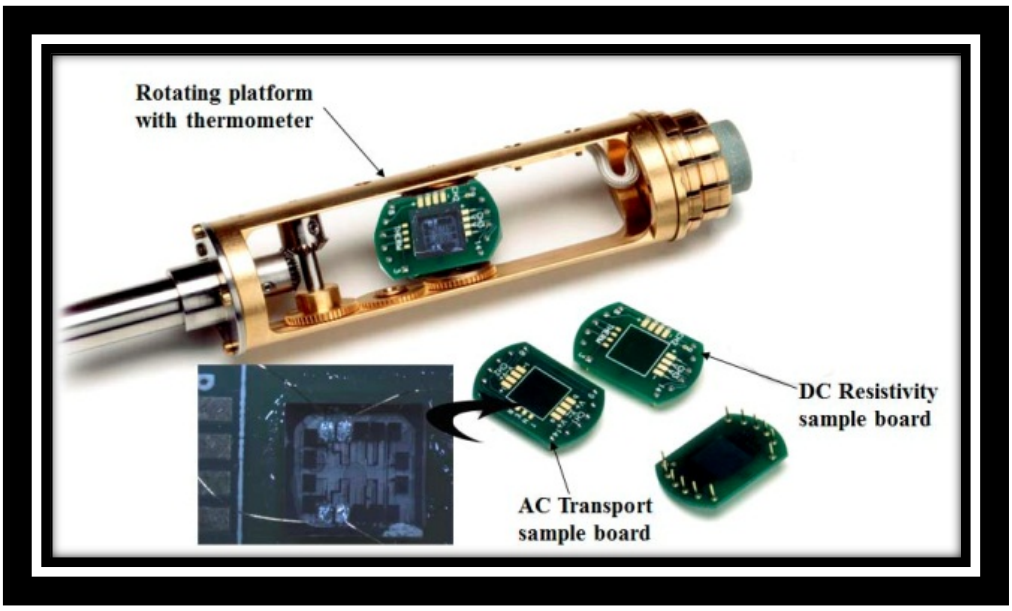

Figure 3-15 Rotator part of the PPMS with transport option

The angular range was from -10 to 370^{o} and a maximum applied field of 6 T was used. With transport measurement as shown in Figure 3-16, not only the angle between applied field and the c-axis of the sample (θ) can be changed but also applied field (B) and temperature (T) can be controlled, so $J_c(\theta, B, T)$ was determined. Depending on the size of the bridges, various field criterions down to 1 μV/cm were used.

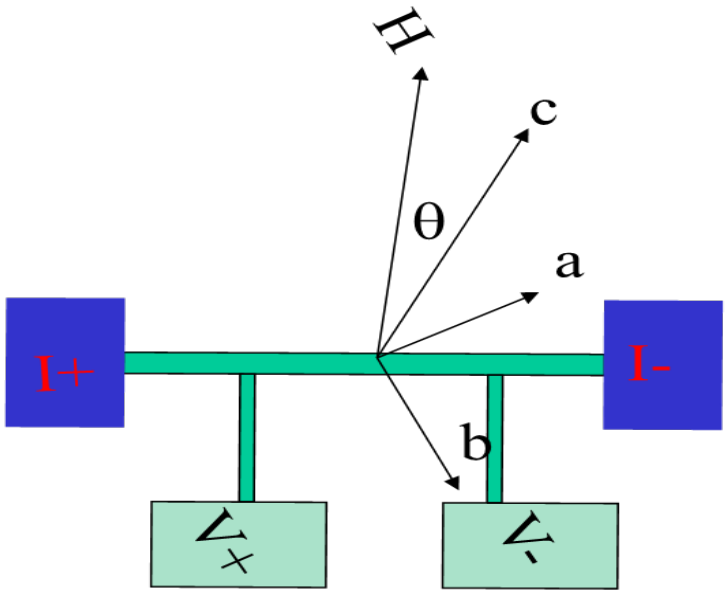

Figure 3-16 Scheme of rotation measurement of YBCO bridge

3.3 Morphological characterisation

3.3.1 Scanning electron microscopy (SEM)

The surface morphology of the films was characterised by SEM. The surface of the YBCO films, as well as of doped YBCO films, does not have a smooth surface, containing pores and precipitates. Knowing the surface characteristics is one of the key points to study the pinning mechanism of the YBCO films.

The Jeol JSM-7000F SEM, as shown in Figure 3-17, was used in this work, with different magnifications. Most of measurements were taken under the accelerating voltage of 20 kV and probe current of about 120 μA.

Figure 3-17 Jeol JSM-7000F FE-SEM with Schottky emitter equipped with EBSD, EDS option in the Centre for Electron Microscopy, School of Metallurgy and Materials

The Jeol JSM-7000F SEM is equipped with X-ray, Energy dispersive spectroscopy (EDS) and Electron backscattered diffraction (EBSD) detectors. In this thesis EBSD was used to analyse crystallographic information of the Ni:5W substrate.

3.3.2 Atomic force microscopy (AFM)

Atomic force microscopy (AFM) is commonly used in investigating sample surfaces at the nano scale, in addition to SEM, and can be used in ambient atmosphere on a variety of samples, from organic to metals. The Veeco Multimode AFM was used in this project to analyse topography of nano-particles (Ag, PBCO) grown on substrates for the substrate decoration approach. Figure 3-18 describes the operation of a basic AFM. Sample is positioned on a piezoelectric ceramic transducer (PZT) actuator and under a probe (tip). A low power laser is directed to the top of the cantilever and, when the tip moves in contact with sample and a small force acts on the tip, the reflected laser will be changed. By recording the change of reflected laser beam, the 3D topography of the sample can be recorded at the nano

scale. However, for higher resolution images necessary for our substrates decorated with nano-dots, tapping mode is usually used. A super-sharp tip (smaller than 10 nm diameter, normally 1 nm) was used in this project. The tapping mode means the tip is approached very close to contact with the sample surface and then lifted off the surface to avoid dragging the tip across the sample surface. The cantilever is excited in vibration with a frequency near to the resonant frequency of the tip. The vibrated cantilever is maintained during tapping operation. The images then were re-analysed by WSxM 5.0 free software [9] and Imagetool software.

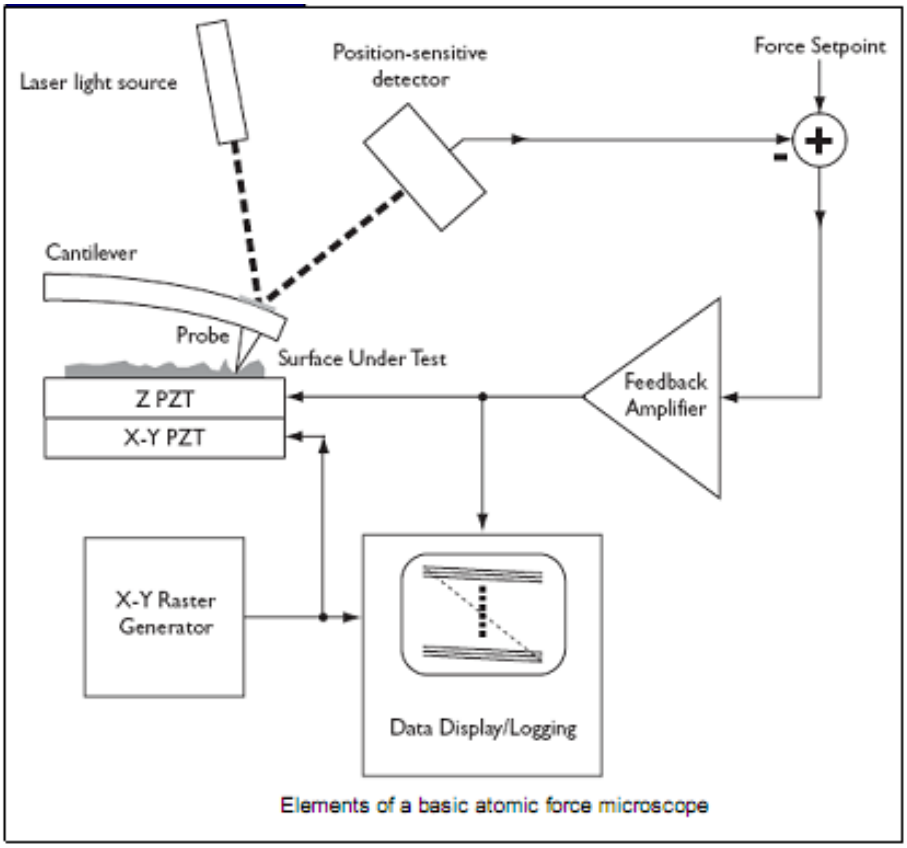

Figure 3-18 Schematic of AFM

3.3.3 Transmission electron microscopy (TEM)

Films were also analysed in cross-section using Transmission electron microscopy (TEM). The cross section images of the samples were taken by a Jeol JEM 2100 TEM (Figure 3-19) using Lanthanum hexaboride (LaB_6) crystal thermionic electron source. The TEM was operated at 200 kV and magnification up to 200,000 times. The Tecnai F20 TEM using field emission electron source was also used in this thesis. Due to the field emitter gun the Tecnai F20 was equipped with Scanning transmission electron microscopy (STEM) and Oxford EDS system. High resolution images can be obtained by the Tecnai F20 (HRTEM) and element mapping was also analysed in the STEM mode by the EDS system. Bright field image with (001) zone axis was selected in most of the TEM images in this project.

Figure 3-20 New Jeol JEM 2100 LaB6 TEM (photo from: http://www.cem.bham.ac.uk/jeol_2100.shtml)

3.4 Thickness measurement

If deposition condition is maintained, the thickness of the films is almost linear with the number of laser pulses, if the same target is used. To measure the thickness of the samples, the films were broken by hand then polished with diamond paper. The cross section was then observed by SEM or Optical microscope. An example is shown in Figure 3-21.

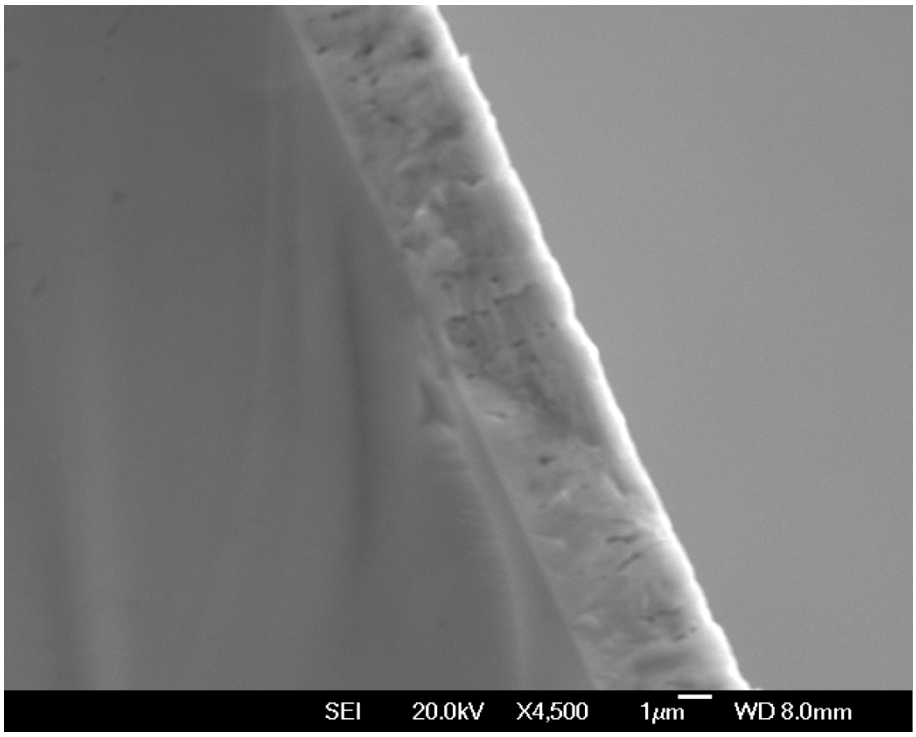

Figure 3-21 Cross section of a YBCO films with average thickness of 3.7 μm

The thickness was measured several times along the sample and then the average thickness was calculated. The films with the thickness larger than 1 μm were measured by Polarised optical microscopy (POM) while the thinner films were measured by SEM with higher resolution. Typical examples of thickness as a function of pulses are shown in Figure 3-22 (YBCO) and Figure 3-23 (BZO-doped YBCO).

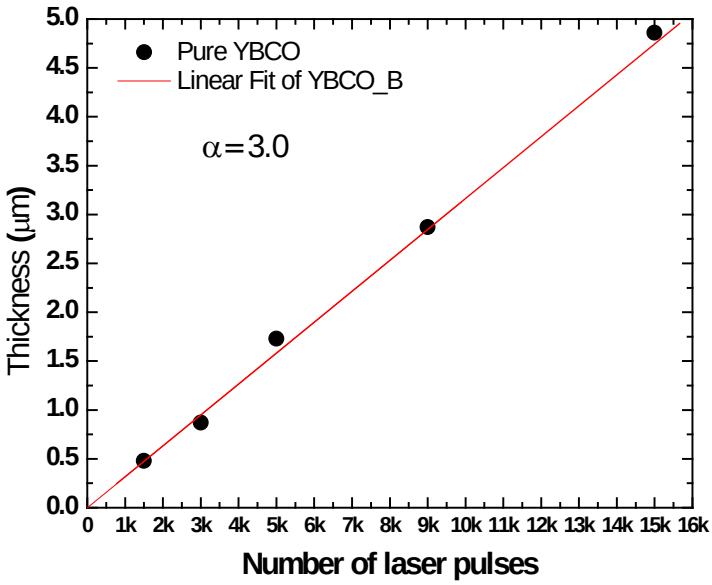

Figure 3-22 Linear dependence of thickness of YBCO films on the number of laser pulses with a coefficient of about 3

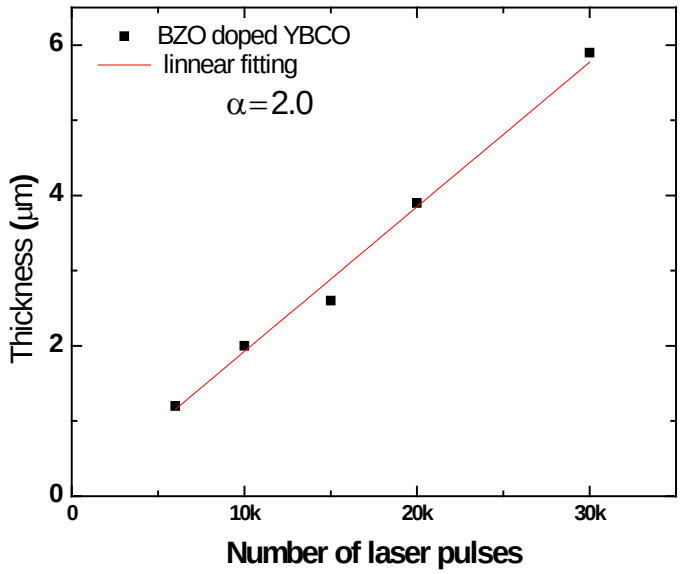

Figure 3-23 Dependence of the thickness of BZO-doped YBCO film on the number of laser pulses; the coefficient is smaller than for the YBCO film.

References

[1] N. Khare, Handbook of High-Temperature Superconductor Electronics

Marcel Dekker, Inc (2003).

[2] C.B.C. David B. Williams, Transmission Electron Microscopy: A Textbook for Materials Science, vol 1 (2004) Springer

[3] C.P. Bean, Reviews of Modern Physics 36/1P1 (1964) 31.

[4] D.V. Shantsev, Y.M. Galperin, T.H. Johansen, Physical Review B 61/14 (2000) 9699.

[5] W. Xing, B. Heinrich, H. Zhou, A.A. Fife, R.A. Cragg, Ieee Transactions on Applied Superconductivity 5/2 (1995) 1420.

[6] J.R. Clem, A. Sanchez, Physical Review B 50/13 (1994) 9355.

[7] E.H. Brandt, Physical Review B 49/13 (1994) 9024.

[8] A. Crisan, V.S. Dang, P. Mikheenko, Y.Y. Tse, A. Sarkar, J. Bowen, J.S. Abell, Physica C-Superconductivity and Its Applications 470/1 (2010) 55.

[9] I. Horcas, R. Fernandez, J.M. Gomez-Rodriguez, J. Colchero, J. Gomez-Herrero, A.M. Baro, Review of Scientific Instruments 78/1 (2007).

Chapter 4. **Results and discussion on nano-dots materials and multilayer architecture of YBCO films**

4.1 Optimisation of nano-dot materials

4.1.1 Dependence of silver nano-dots morphology on the deposition temperature

Deposition parameters such as; temperature, gas pressure, laser energy etc., affect the formation of nano-particles. In this section, Ag nano particles were grown on substrates by PLD under the conditions presented in Chapter 3, at different substrate temperatures, with a constant total number of 15 laser pulses on Ag target. For comparison, the image of a bare STO substrate was taken by AFM as show in Figure 4-1. There are some bright spots on the STO substrate, which may reflect a not very clean substrate since the AFM image was taken in the air.

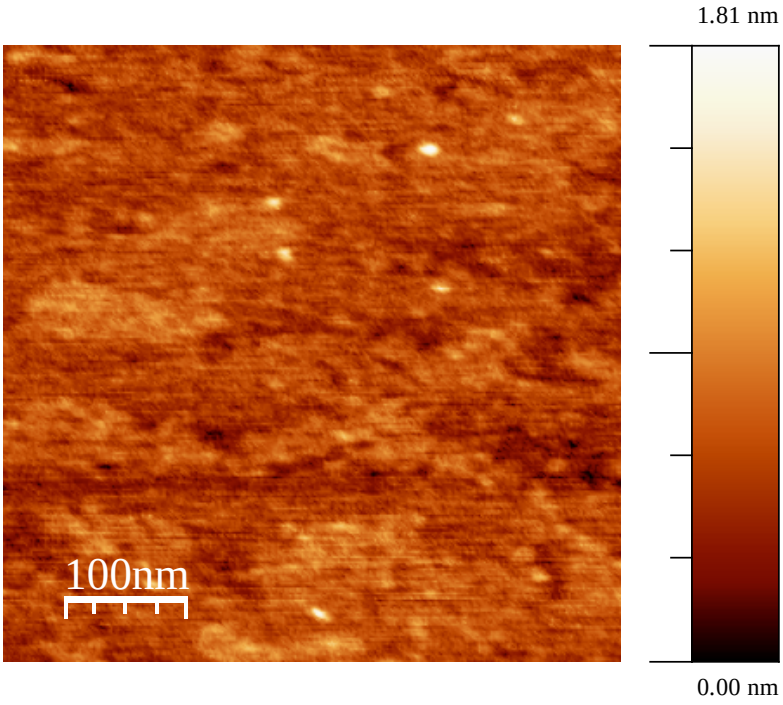

Figure 4-1 AFM image of bare STO substrate, there is no other particles on the STO surface.

The AFM images of Ag nano-dots grown by 15 laser pulses, at different substrate temperatures from 780^{o} C (which is the temperature of YBCO deposition) to room temperature and in vacuum are shown in Figure 4-2 to Figure 4-17.

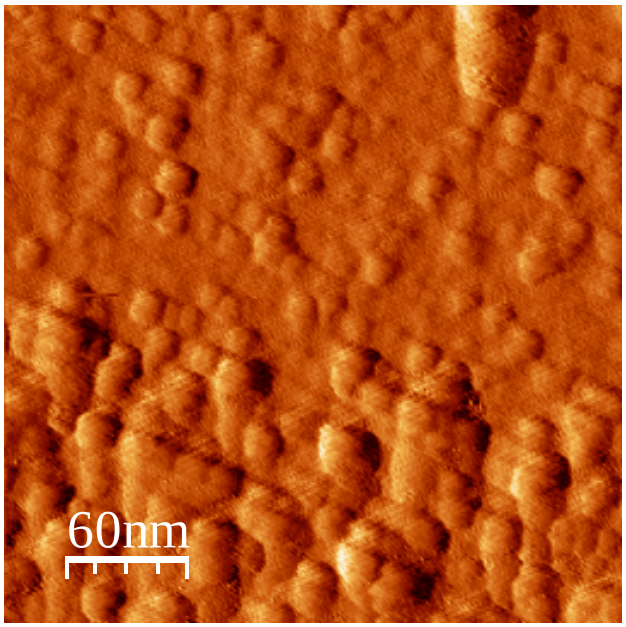

Figure 4-2 The AFM images of Ag nano particles deposited at 780^{o} C (reflected image).

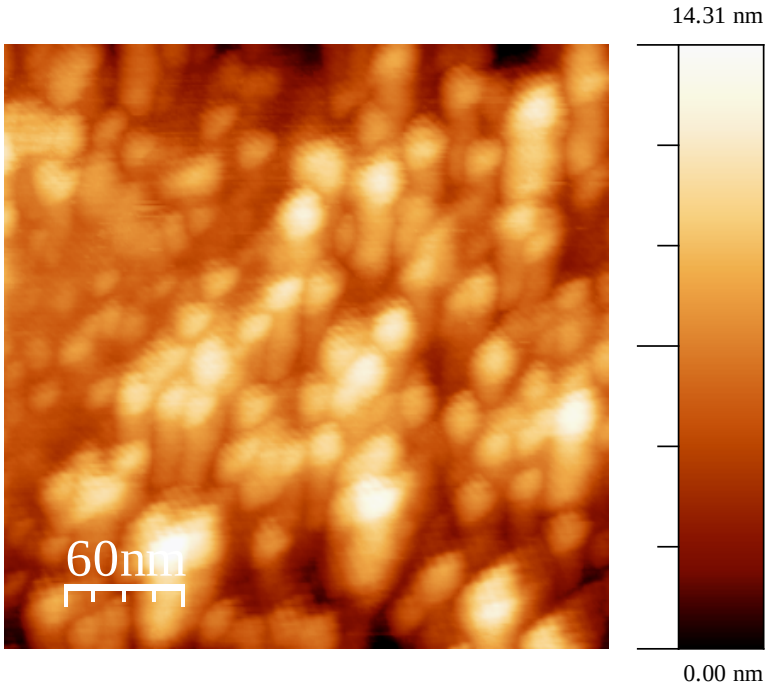

Figure 4-3 The AFM images of Ag nano particles deposited at 780 ^{o}C.

Figure 4-2 and Figure 4-3 show the distribution of the Ag nano particles deposited at a temperature of 780^{o} C by 15 laser pulses on the Ag target. Dense and irregular distributions are observed, with nano particles of about 20 nm diameter and 6 nm in height. However, in other parts of the STO surface, the Ag nano particles were not well distributed, forming a big cluster as shown in Figure 4-4.

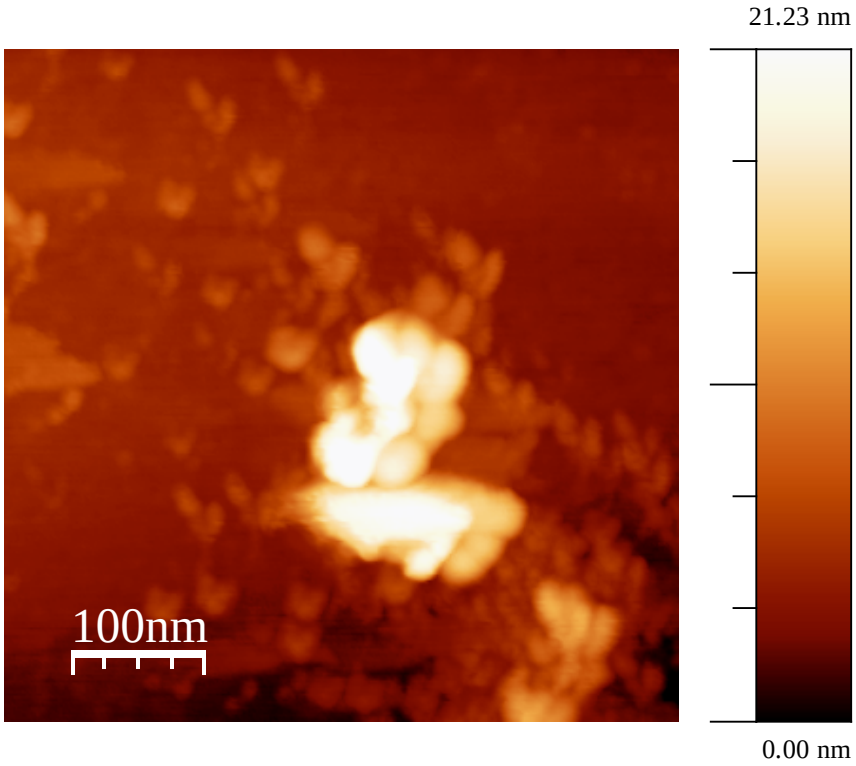

Figure 4-4 Formation of the Ag nano cluster in others parts of the STO substrate, for 780 ^{o}C deposition temperature.

The formation of big nano clusters on the STO surface is not suitable to grow YBCO films with artificial pinning centres as it may reduce the critical current density of the YBCO film. This aspect will be mentioned in the next section.

The height histogram data was obtained using WSxM 5.0 software. The AFM topography images show the real signal obtained as the amplitude of the cantilever in the tapping mode.

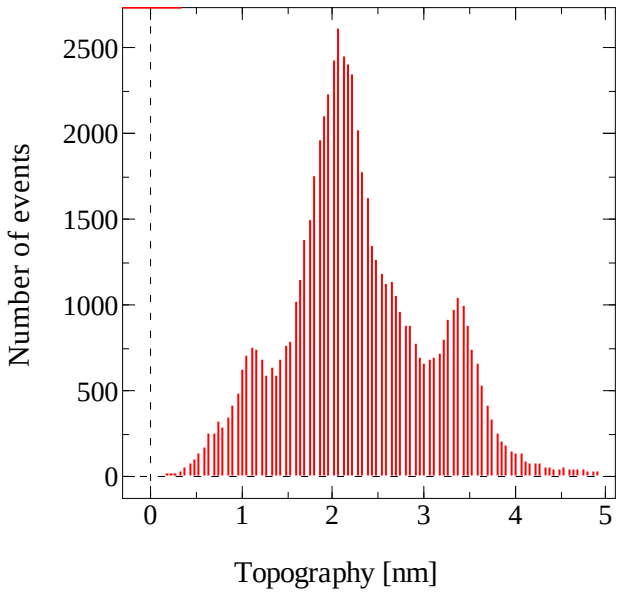

Figure 4-5 Height histogram of Ag nanodots deposited at 780^{o} C with 15 laser pulses, the histogram data was obtained from Figure 4-2

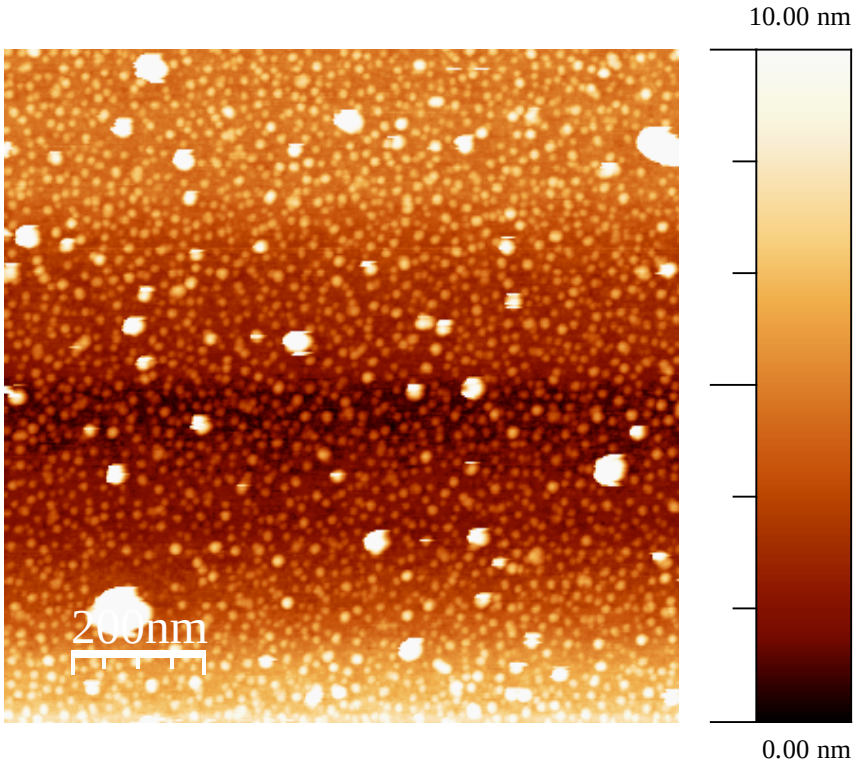

Figure 4-6 Distribution of the Ag nano particles deposited at 400^{o} C by 15 laser pulses

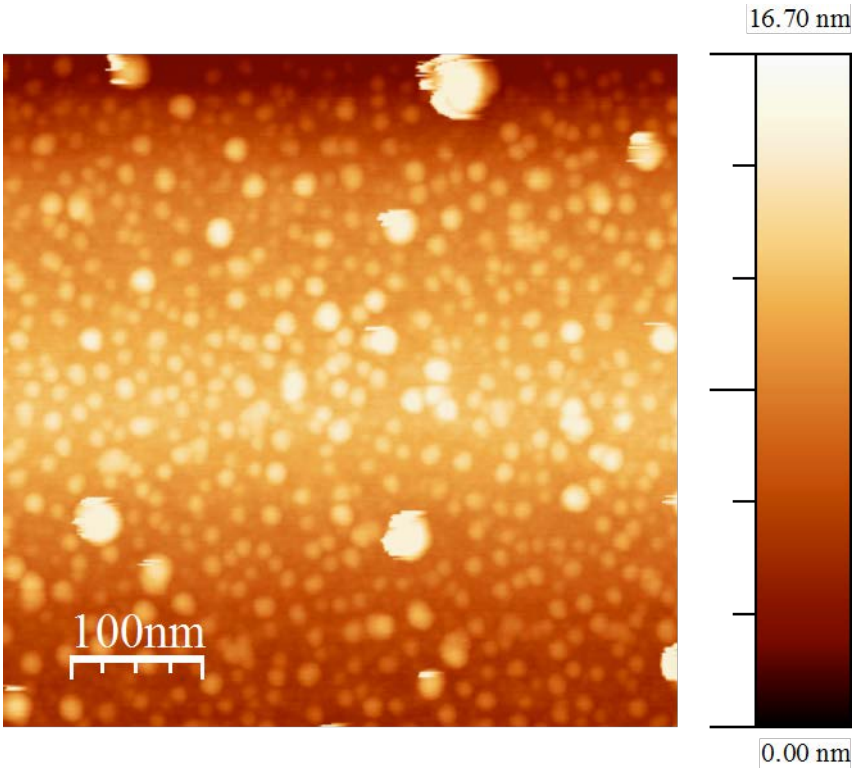

Figure 4-7 Higher resolution image of the sample in Fig. 4-6

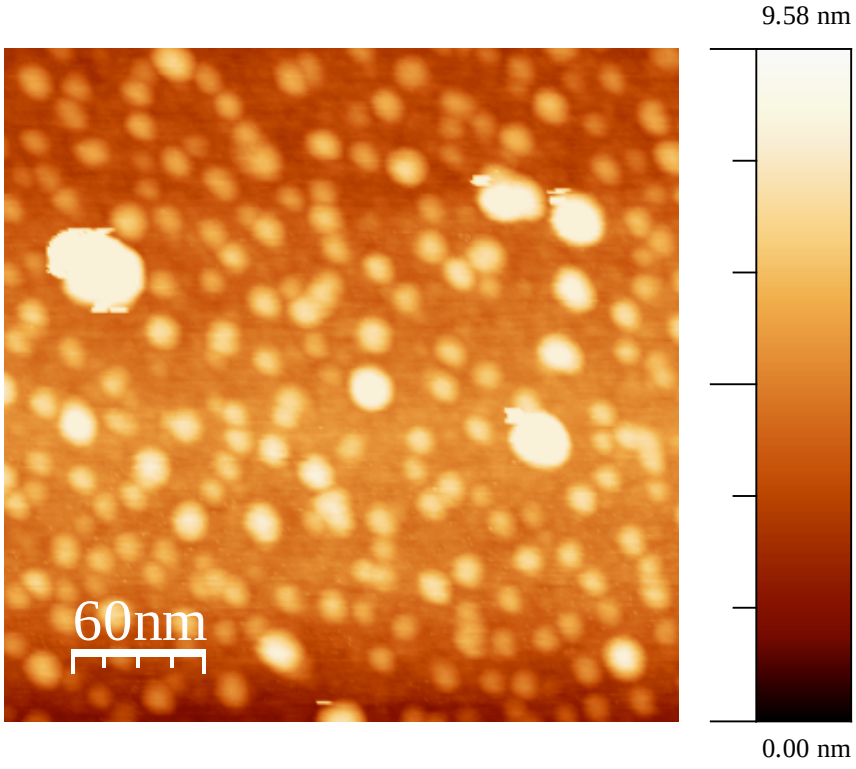

Figure 4-8 Higher resolution image of the sample in Figs. 4-6 and 4-7

Figure 4-6 to Figure 4-8 show the AFM images of Ag nano-dots obtained by 15 laser pulses at 400^{o} C substrate temperature. The effect of deposition temperature can be easily observed. At deposition temperature of 400^{o} C, regularly dense distribution of Ag nano-particles can be observed. Also the height distribution is different from the case of the samples deposited at 780^{o} C, as shown in Figure 4-9. Nano clusters were not observed in this case.

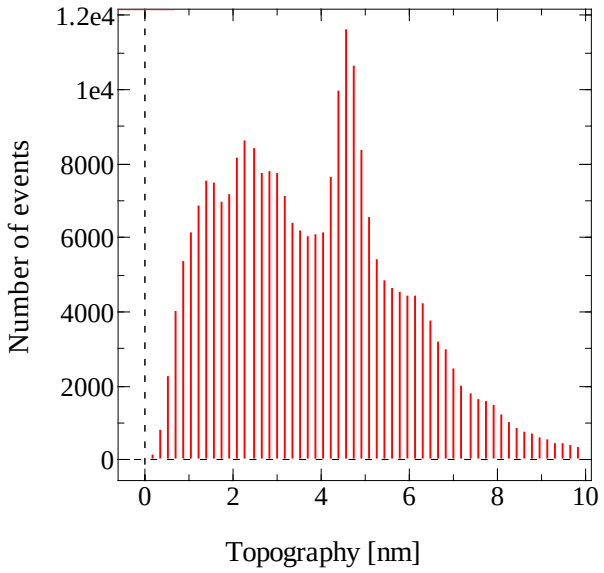

Figure 4-9 Height histogram of Ag nanodots deposited at 400^{o} C with 15 laser pulses, the histogram data was obtained from Figure 4-2

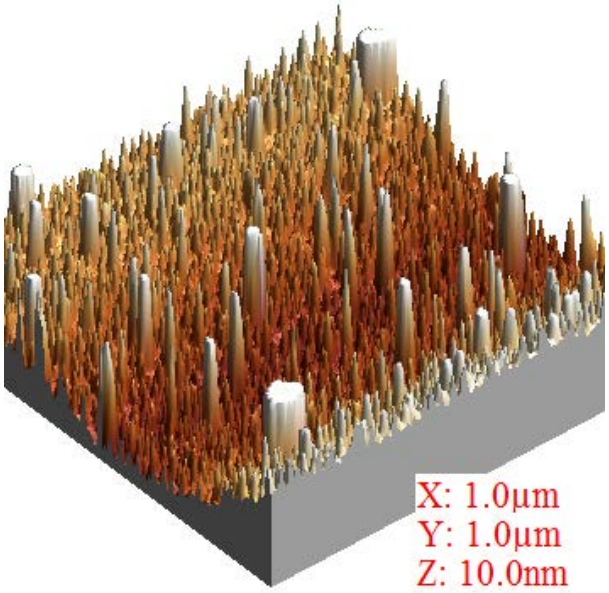

Figure 4-10 3D view of Figure 4-6

Figure 4-11 to Figure 4-14 show the AFM image of Ag nano-dots obtained by 15 laser pulses at 200^{o} C

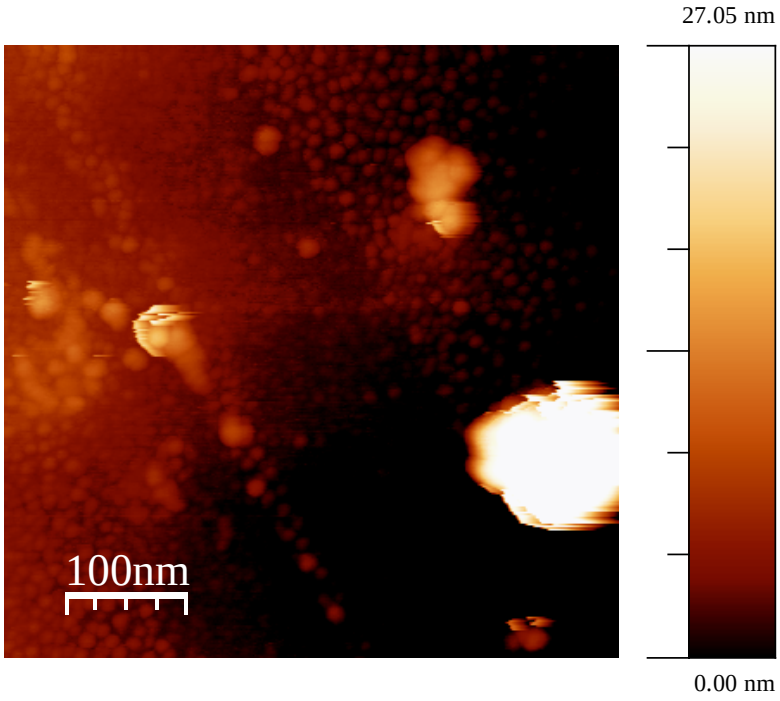

Figure 4-11 Nano clusters of Ag appear again at 200^{o} C, but not as large as in Figure 4-4

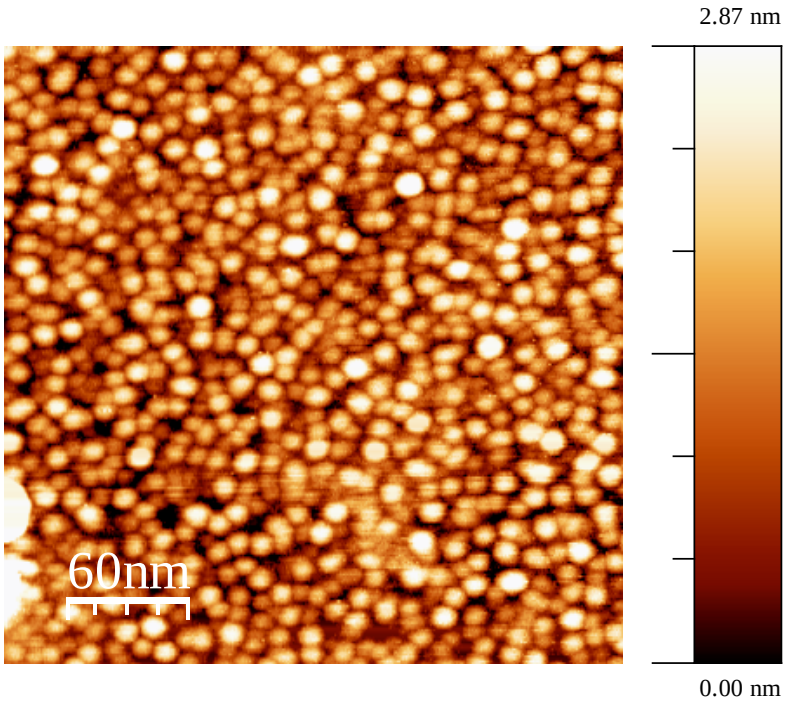

Figure 4-12 Regular distribution of Ag nano-dots deposited at 200^{o} C in a different place on the STO substrate

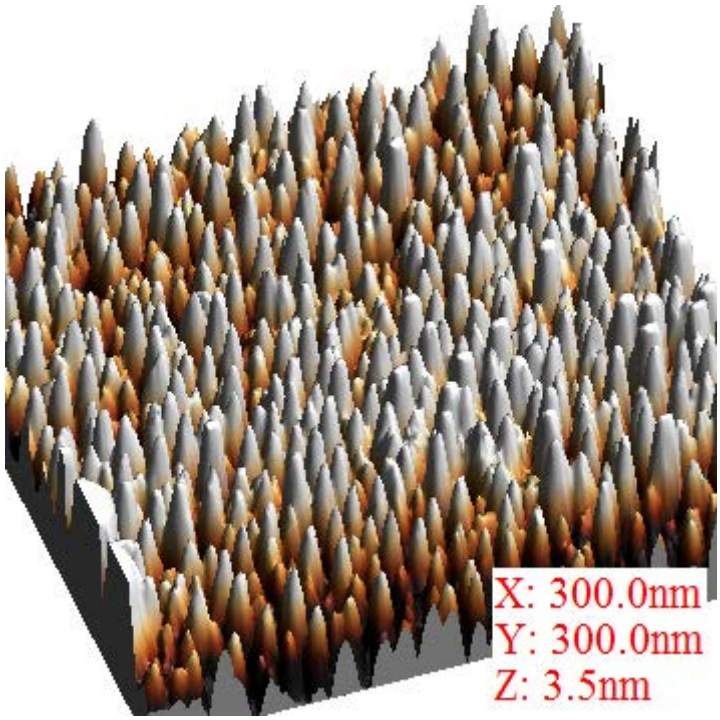

Figure 4-13 3D image taken from Figure 4-12

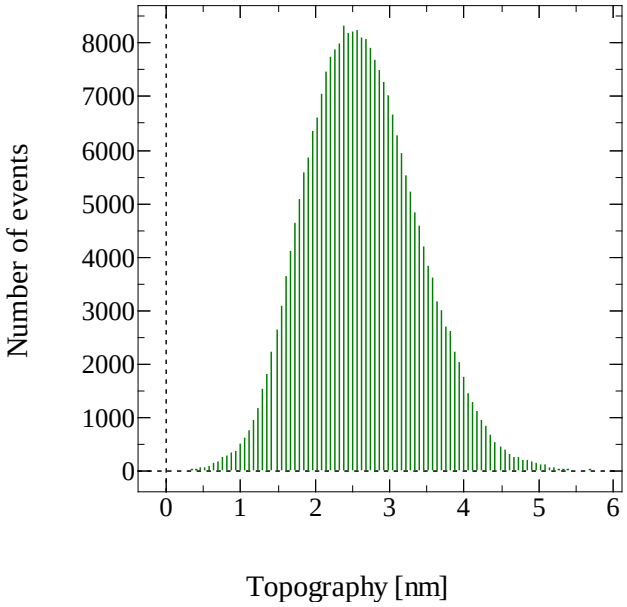

Figure 4-14 Height histogram of Ag nanodots deposited at 200^{o} C with 15 laser pulses, the histogram data was obtained from Figure 4-12

By reducing deposition temperature from 400 to 200^{o} C, Ag nano-clusters appear again as in the case of high temperature deposition shown in Figure 4-4, but less frequent and smaller.

Similar Ag clusters appear in room temperature (RT) deposition as shown below

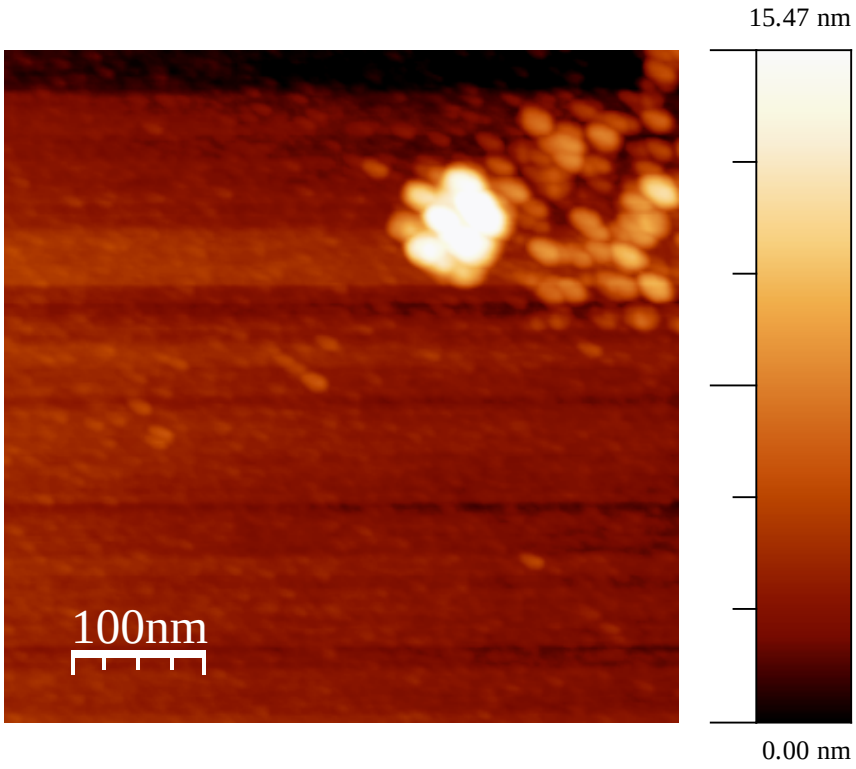

Figure 4-15 Irregularly distribution of the Ag nano particles deposited at RT

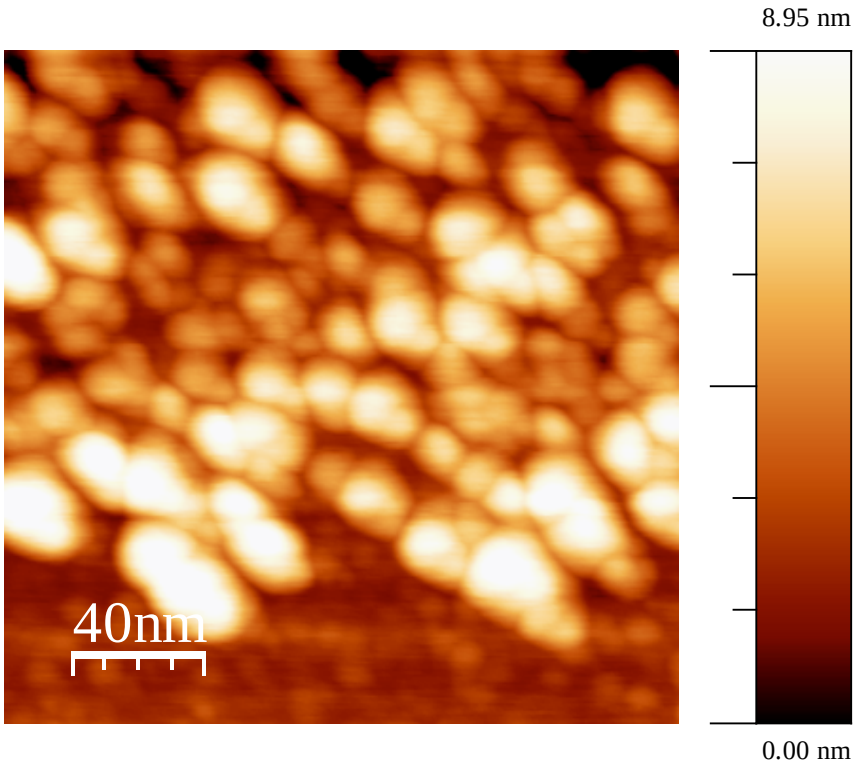

Figure 4-16 Zoom in on Figure 4-15

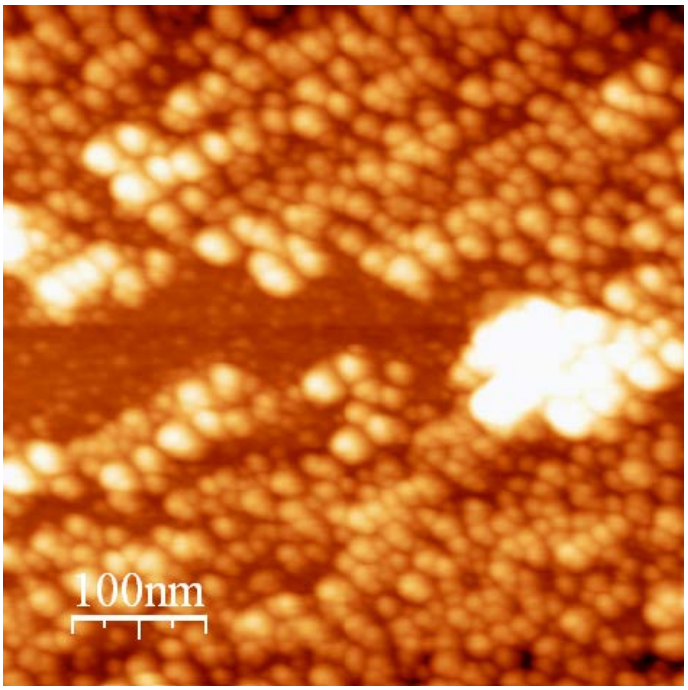

Figure 4-17 Ag nano-dots grown by 15 laser pulses at RT in a different place on the STO substrate

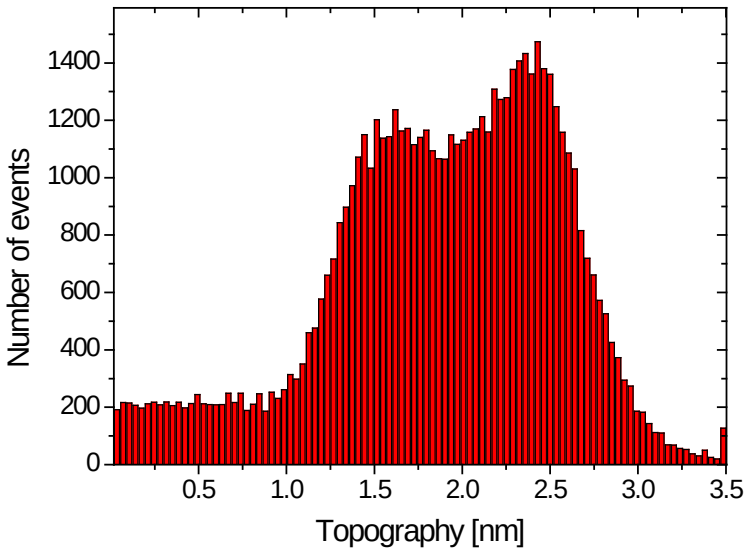

Figure 4-18 Height histogram of Ag nano particles deposited at RT

By changing the deposition temperature, the distribution and average height of the Ag nano particles are changed. At RT and high temperature (780^{o} C) deposition, the distribution of the Ag dots is irregular and large nano clusters appear, while at an intermediate temperature of 400^{o} C the distribution of Ag nano-dots is rather regular and denser.

Figure 4-19 shows a linear dependence of average height of the Ag nano dots on the deposition temperature.

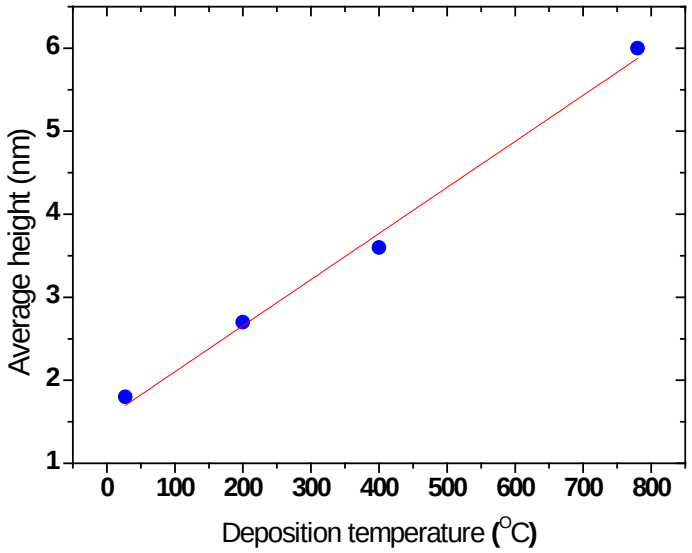

Figure 4-19 Dependence of the average height of the Ag nano-dots on the deposition temperature, the red line is a linear fit

4.1.2 Dependence of average size of the Ag nano-particles on the number of laser pulses

Based on the results shown in section 4.1.1, a deposition temperature of 400^{o} C is chosen, but in this section the number of laser pulses on the Ag target is changed from 5 laser pulses to 30 pulses. The results show that not only the average height of the Ag nano-dots is changed but also the diameter of the Ag nano-dots is different. Of course, the surface density (number of Ag nano-dots in a given surface) depends strongly on the number of laser pulses.

As can be seen in Figure 4-20 and Figure 4-21, by reducing the number of laser pulses to 5, only few Ag particles can be observed in an area of 0.25 μm^2. This is easy to understand: smaller the number of laser pulses hitting the Ag target, a smaller amount of Ag is ablated and deposited on the substrate.

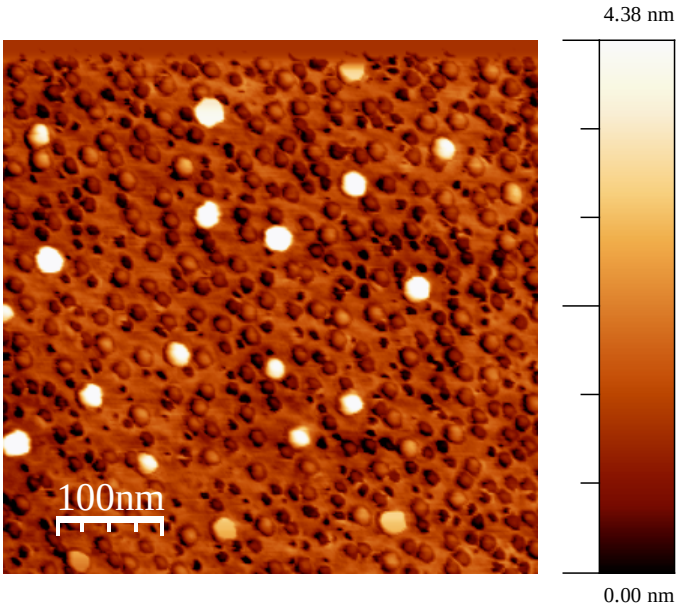

Figure 4-20 Sparse distribution of the Ag nano particles on the STO substrate deposited by 5 laser pulses

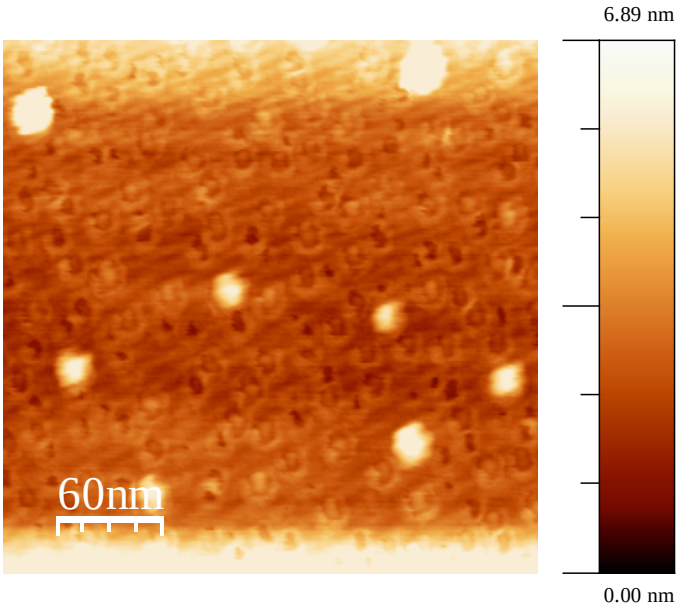

Figure 4-21 Zoom in Figure 4-20

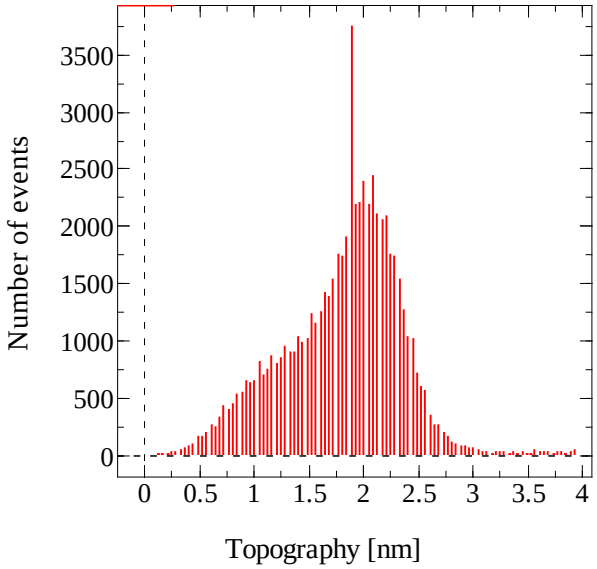

Figure 4-22 Height histogram of Ag nanodots deposited at 400^{o} C with 5 laser pulses, the histogram data was obtained from Figure 4-20

Figure 4-23 shows the histogram of diameters of Ag nano particles deposited by 15 laser pulses at 400^{o} C, "manually" estimated from Figure 4-7 in section 4.1.1

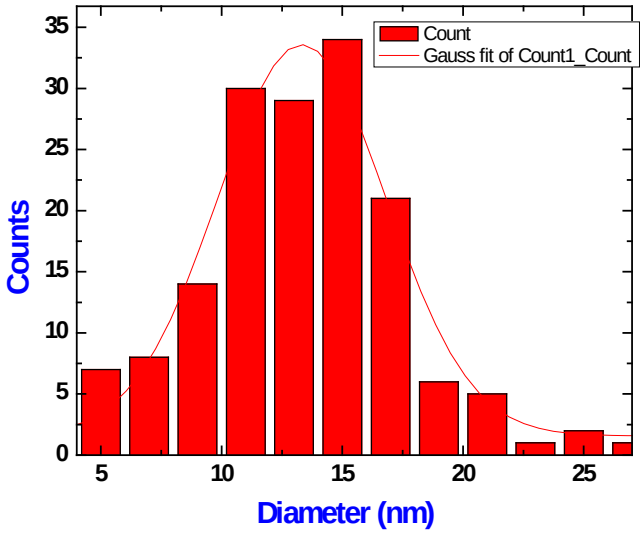

Figure 4-23 Histogram of the diameter of Ag nano particles deposited by 15 laser pulses at 400^{o} C, solid line is Gaussian fit

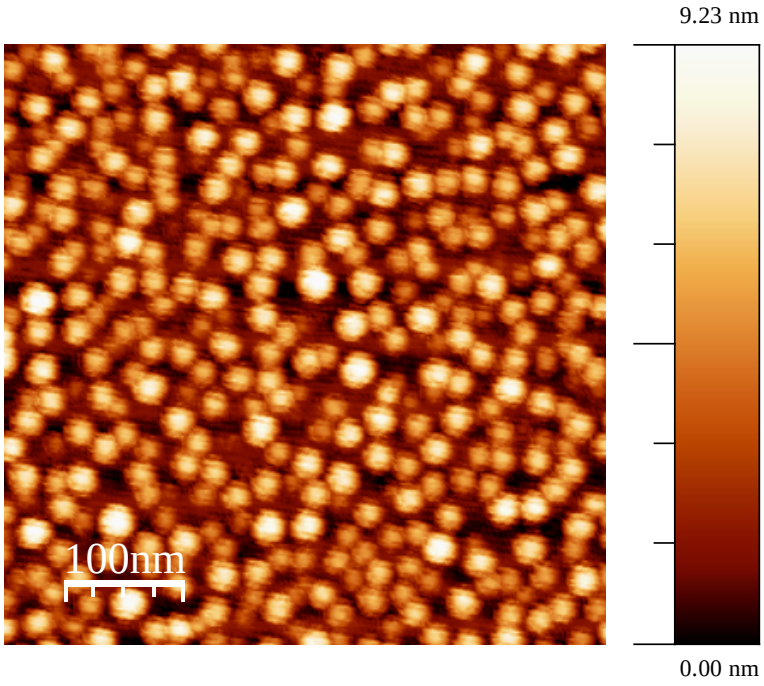

Figure 4-24 AFM image of the STO covered by Ag nano-dots grown by 30 laser pulses at 400^{o} C

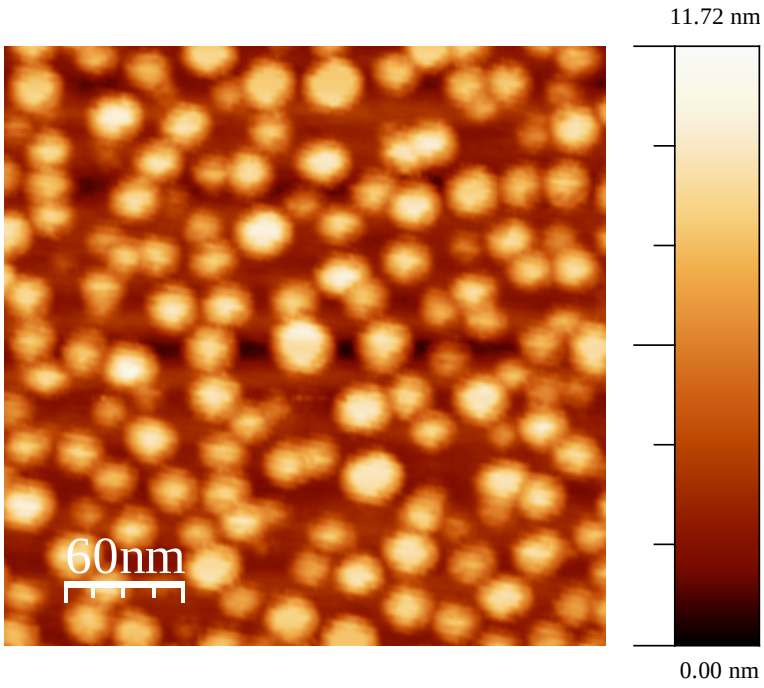

Figure 4-25 Different scale and place for the same sample as in Figure 4-24

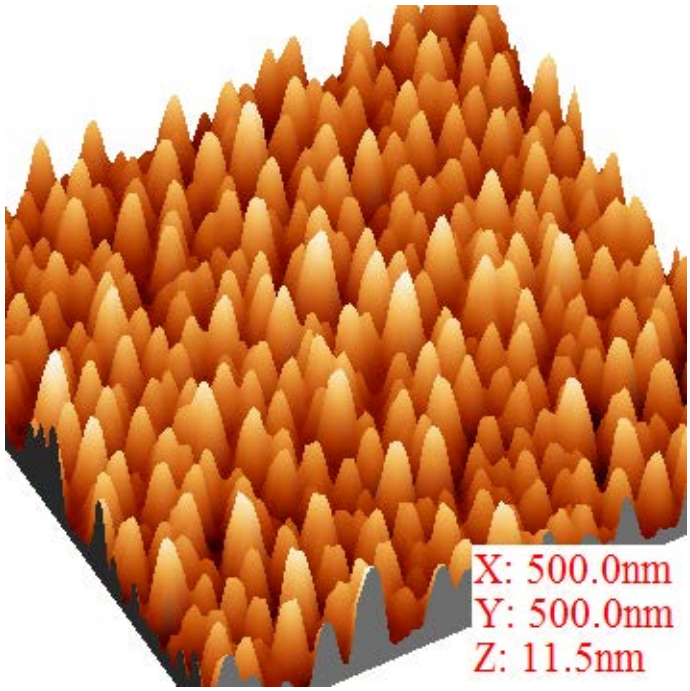

Figure 4-26 3D view of Figure 4-25

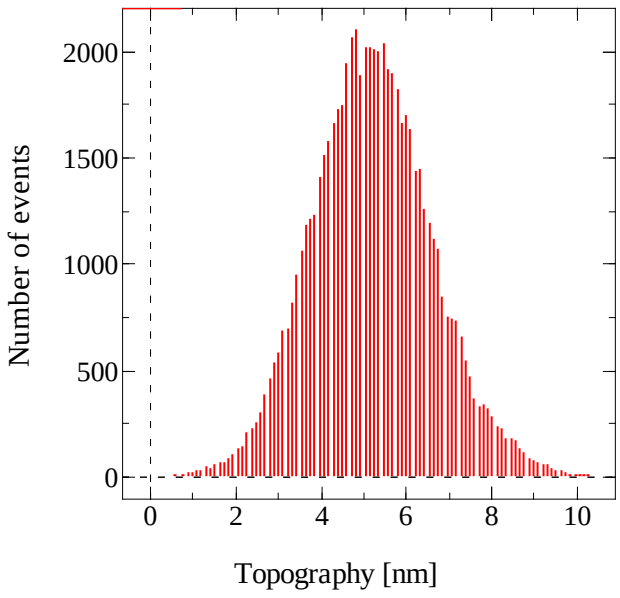

Figure 4-27 Height histogram of Ag nano-particles deposited by 30 laser pulses at temperature of 400^{o} C, data obtained from Figure 4-24

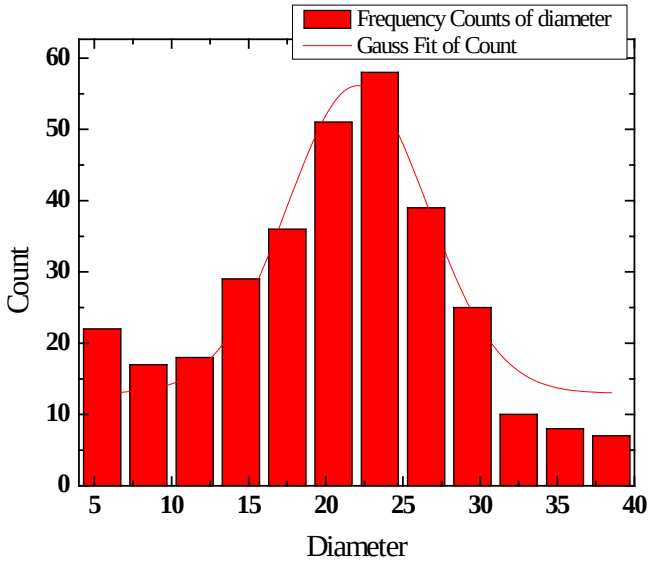

Figure 4-28 Histogram of the diameter of Ag nano particles deposited by 30 laser pulses at 400^{o} C, solid line is Gaussian fit

Figure 4-24 to Figure 4-26 show AFM images of Ag nano-dots deposited at 400^{o} C by 30 laser pulses, one can see that the distribution of Ag nano dots in this case is denser than in Figure 4-7 and Figure 4-20. The average height of the Ag nano particles is 4 nm as shown in Figure 4-27. Figure 4-28 shows a histogram of diameter of Ag nano dots which was obtained from Figure 4-24, solid line is Gaussian fit of the data in which the maximum is average diameter.

Figure 4-29 and Figure 4-30 summarise geometrical parameters: average height and diameter of the Ag nano dots deposited at 400^{o} C. As can be seen, the average height and diameter depend linearly on the number of laser pulses.

Higher numbers of laser pulses resulted in a very high surface density of Ag particles in which separate nano-dots cannot be distinguished and a thin layer of Ag is formed, as shown in Figure 4-31 for the case of 40 laser pulses. The upper limit of Ag amount which can form separate Ag nano-dots was found to be that resulted from 30 laser pulses. The optimum

temperature which can easily create uniform and well separated Ag nano-particles is about 400^{o} C.

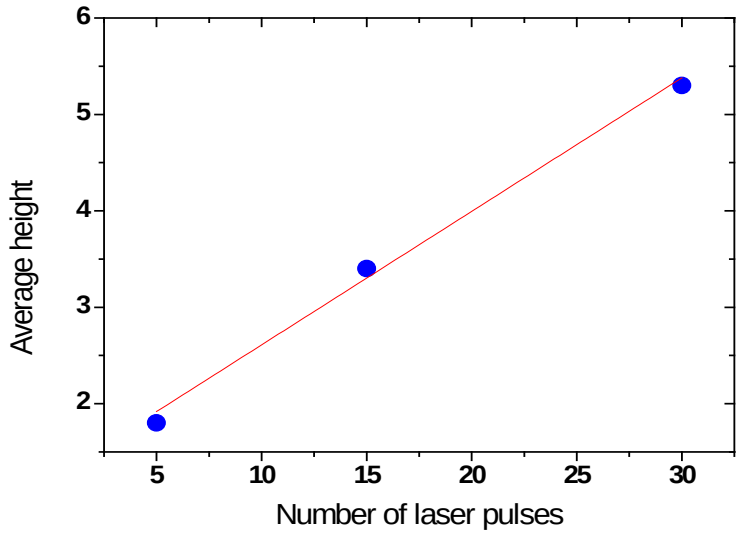

Figure 4-29 Average height of Ag nano dots deposited at 400^{o} C as a function of number of laser pulses, red line is linear fit

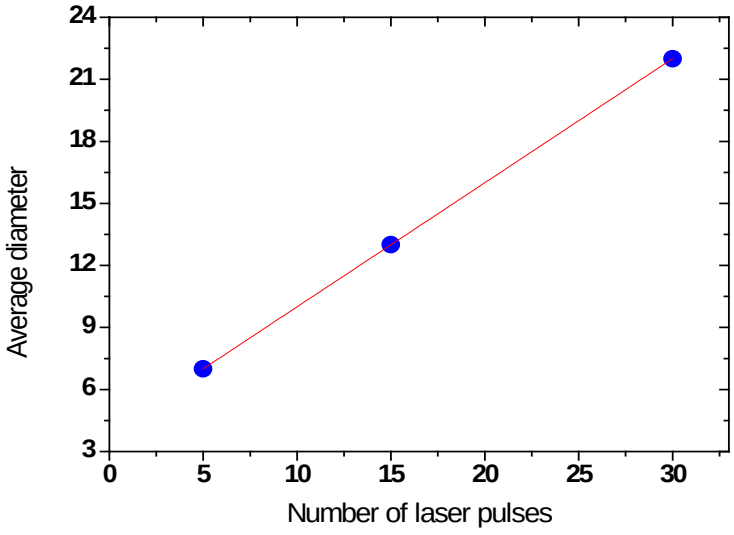

Figure 4-30 Average diameter of Ag nano dots deposited at 400^{o} C as a function of number of laser pulses, red line is linear fit

The optimum parameters for Ag deposition which led to the largest increase of critical current density of YBCO films is found to be 15 laser pulses and a deposition temperature of 400^{o}C, details will be discussed in the section devoted to the critical current.

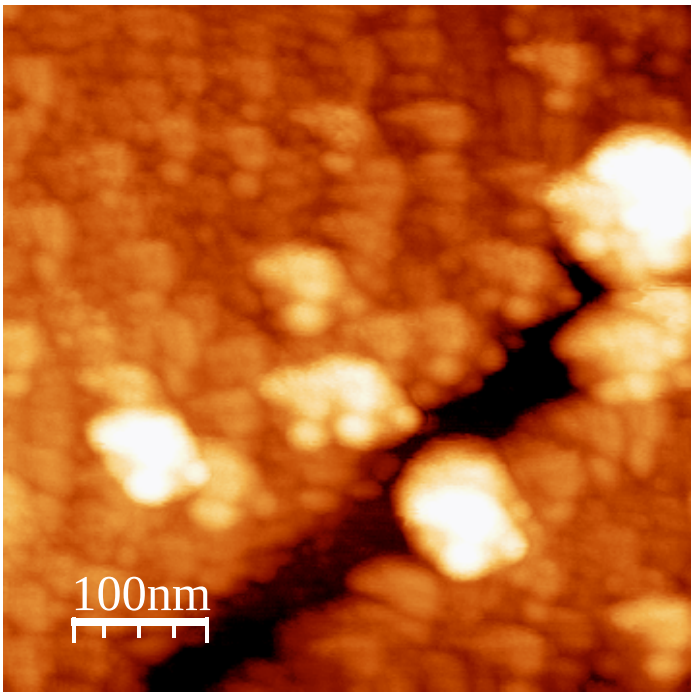

Figure 4-31 Thin layer of Ag was formed with 40 Ag laser pulses deposited at 400^{o} C

4.1.3 Nano dots of $PrBa_2Cu_3O_7$ (PBCO)

PBCO was also tested in this project as a nano-dots material, using the deposition conditions as described in section 4.1.1 and 4.1.2, i.e., 15 laser pulses on PBCO target, at substrate temperature of 400^{o} C, in vacuum.

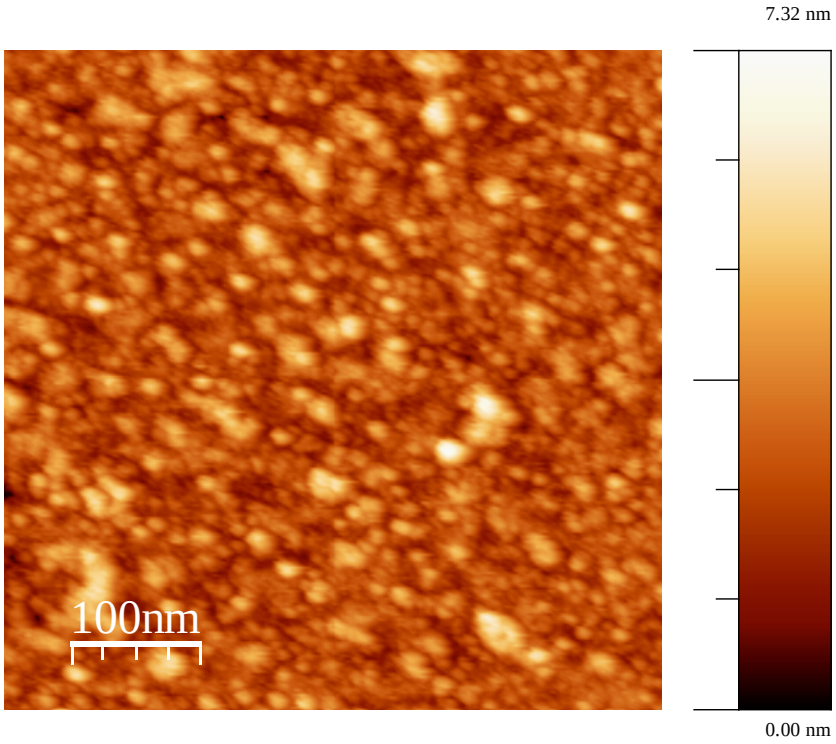

Figure 4-32 AFM image of STO substrate covered with PBCO nano-dots obtained from 15 laser pulses at temperature of 400^{o} C

On the STO substrates, 15 laser pulses on PBCO target at a deposition temperature of 400^{o} C led to the growth of a high number density of nano-dots, the substrate being almost entirely covered, as shown in Figure 4-32 and Figure 4-33. As can be seen, the substrate is almost entirely covered with PBCO nano-dots with various diameters, from few nm up to 20–30 nm, and various heights, the average height being 2.7 nm as shown in Figure 4-34. The J_c of the films grown on PBCO nano dots will be discussed in section 4.5.

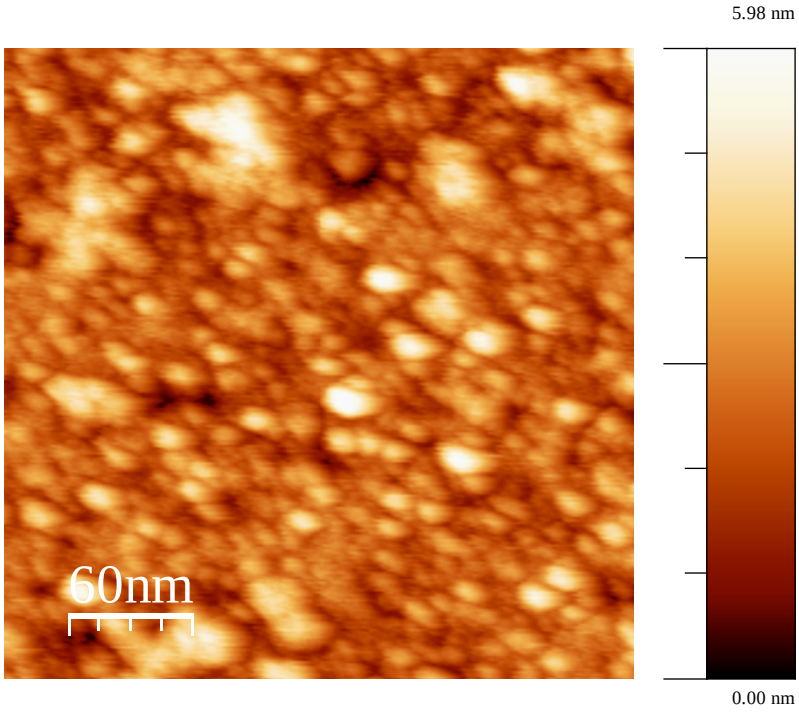

Figure 4-33 Higher magnification image of the sample as in Figure 4-32

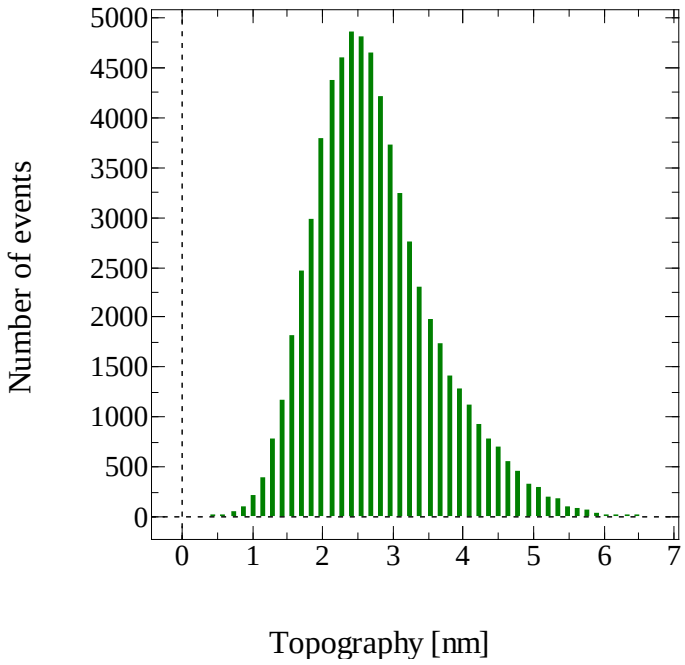

Figure 4-34 Height histogram of PBCO nano-dots taken from Figure 4-33

4.2 Growing YBCO films

4.2.1 Optimisation of T_c and J_c

YBCO films prepared by PLD are normally deposited at high substrate temperature from 650 to 800^o C [1] depending on the intended purposes of the film. The aim is to obtain high quality YBCO film on STO substrate with sharp transition, high T_c and high J_c in applied fields.

As shown in Figure 4-35, the sharpest transition is for the film deposited at a temperature of 780^o C, but the highest T_c of 90.7 K is obtained for the film deposited at a higher temperature of 800^o C. In this thesis T_c is defined as the peak of the imaginary part (out-of-phase) of the AC susceptibility, χ", and ΔT is defined as the width of the χ" peak. In some papers, T_c is defined as $T_{c\ onset}$ as shown in Figure 4-35. The other parameters such as O_2 pressure, laser energy, etc also affect the epitaxial growth of the film. In this project, those parameters were optimised as mentioned in Chapter 3. Substrate temperature of 780 ^{o}C during YBCO deposition was selected due to the highest in-field J_c of the film, as shown in Figure 4-36. As can be seen, the film deposited at 800^o C shows higher J_c in zero field but lower in all applied fields.

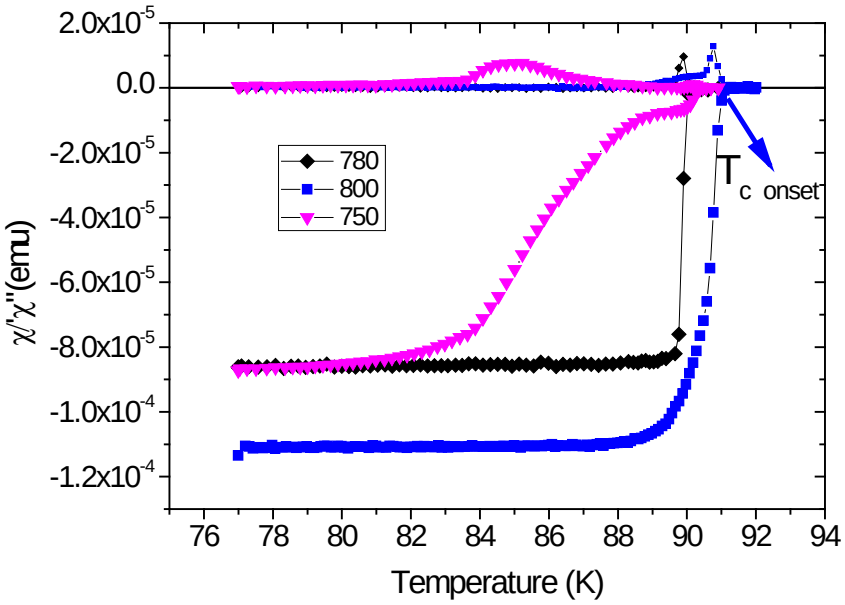

Figure 4-35 Temperature dependence of the AC susceptibility for films grown on single crystal STO substrate at 750, 780 and 800 ^{o}C, dependence of T_c on the deposition temperature of the YBCO film can be seen as the position of the peak in χ" or of the transition on-set.

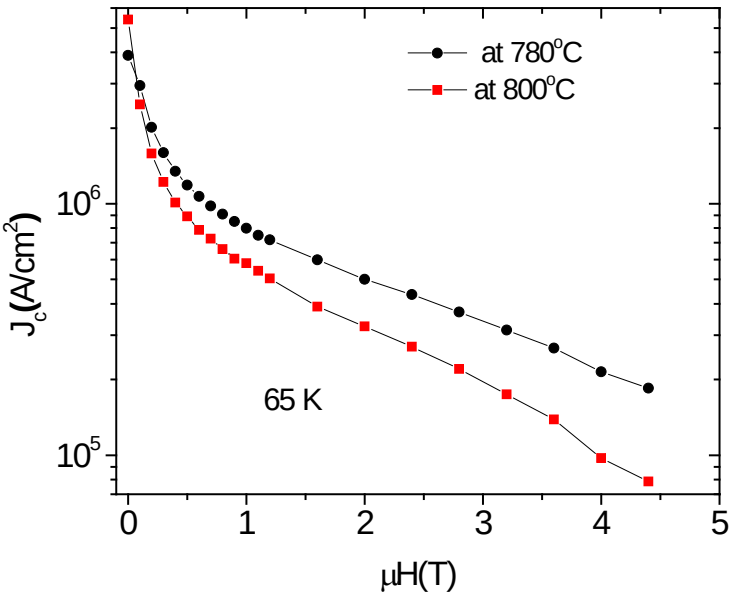

Figure 4-36 Applied magnetic field dependence of J_c at 65 K for 2 μm-thick films deposited on single crystal STO substrate and at substrate temperatures of 780^{o} C and 800^{o} C

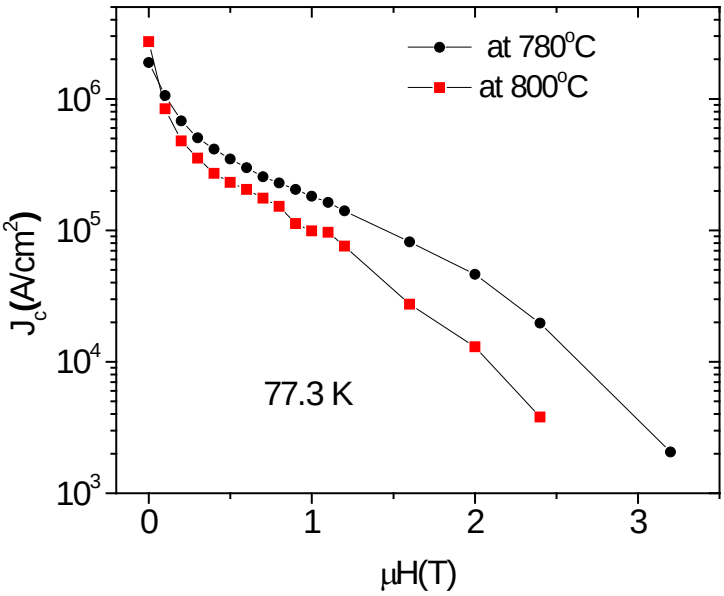

Figure 4-37 Applied magnetic field dependence of J_c at 77.3 K for the same films as in Fig. 4-46.

For the quite thick (2 μm) YBCO films high J_c at 77.3 K and in zero field was obtained: 2.7 MA/cm^2 and 1.8 MA/cm^2 for the films deposited at 800 and 780^o C, respectively. These are quite high values in comparison with recent reports on films of similar thickness [2] and much higher than for the films prepared by other methods [3] being on the trend of the best YBCO on STO substrates reviewed by Foltyn et al in Nature Materials [4]

4.2.2 STO and MgO single crystal substrates

MgO and $SrTiO_3$ (STO) single crystals are most popular substrates for YBCO deposition of due to their good lattice mismatch. While MgO is normally used in high frequency (microwave) applications, YBCO films grown on STO have higher J_c than the films grown on MgO in the same optimum growth conditions because the lattice mismatch between STO and YBCO is better than between MgO and YBCO [5].

Figure 4-38 shows the temperature dependence of AC susceptibility of two YBCO films grown on STO (black squares) and MgO substrate (red circles), respectively. T_c of the film grown on MgO substrate (89.3 K) is a little lower than T_c of the film grown on STO substrate (90.7K).

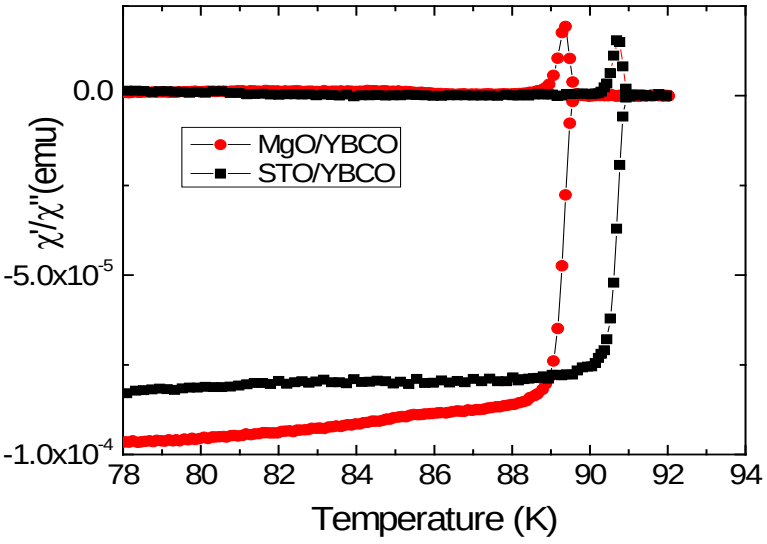

Figure 4-38 Temperature dependence of AC susceptibility of YBCO films deposited on STO and MgO substrates.

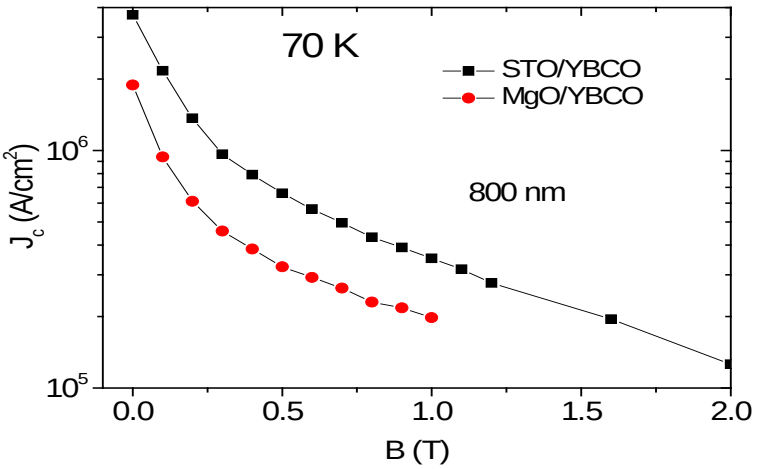

Figure 4-39 Field dependence of J_c at 70 K of YBCO films deposited on STO and MgO substrates.

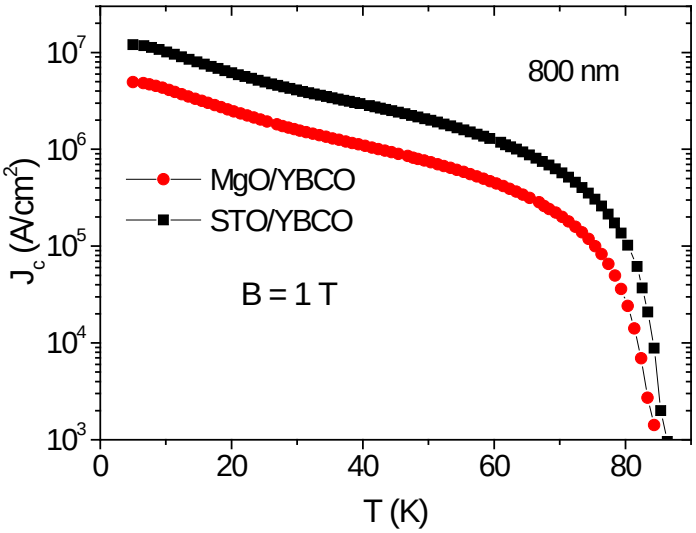

Figure 4-40 Temperature dependence of J_c of YBCO films deposited on MgO and STO (legend on the figure) in an applied field of 1 T.

Figure 4-39 and Figure 4-40 show field dependence at 70 K and temperature dependence in 1 T of the critical current density J_c of the films deposited on STO and MgO, respectively. For the same film thickness, J_c of the film grown on STO is larger than the one grown on MgO by about 100% and the difference is higher in higher applied fields. Temperature dependence of J_c in 1T shows that at all temperatures from 5 K to 90 K, J_c of the film grown on STO is higher than those of the film grown on STO but the absolute gap is smaller at higher temperatures.

4.2.3 X-ray diffraction pattern of optimum YBCO film

X-ray diffraction pattern of the YBCO film deposited at 780^o C shows very good epitaxial growth, with (00l) peaks only as shown in Figure 4-41.

Oxygen content is an important factor controlling superconducting properties of $YBa_2Cu_3O_{7-\delta}$. For a good quality film, the oxygen deficiency δ has to be smaller than 0.07 [6]. By investigating the ratios between intensities of various (00l) peaks the oxygen deficiency of

the YBCO film can be calculated as was shown in Ref. [6]. The (006) and (005) peaks are the strongest peaks of YBCO films deposited on the STO substrate but their ratio cannot be used for this purpose since the (006) YBCO peak is overlapped with the (002) peak of STO. The ratio of intensities of (005)/(004) peaks can be used to determine δ. As shown in Figure 4-41, ratio I(005)/I(004) = 13, this value is smaller than 20 (which correspond to δ as small as about 0.1).

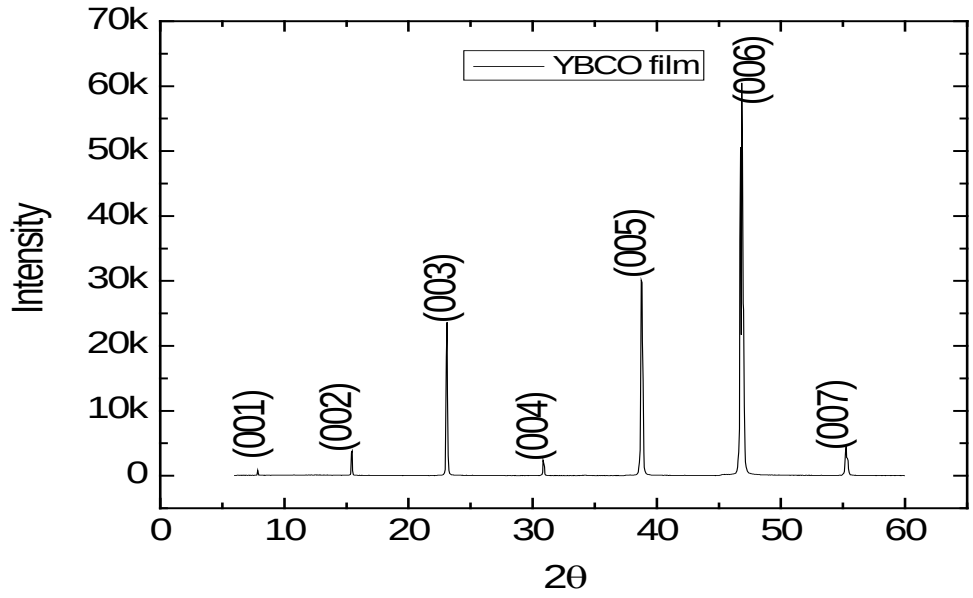

Figure 4-41 X-ray diffraction pattern of YBCO film.

4.2.4 SEM and AFM of the optimum YBCO film

For comparison with nanostructured films, the standard (optimum conditions) YBCO film was investigated by SEM and AFM, as shown in Figure 4-42 and Figure 4-43.

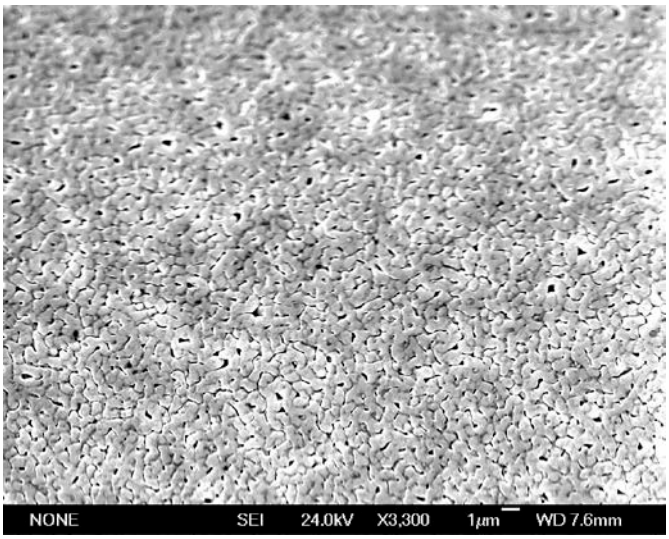

Figure 4-42 Low resolution image of standard YBCO on STO film.

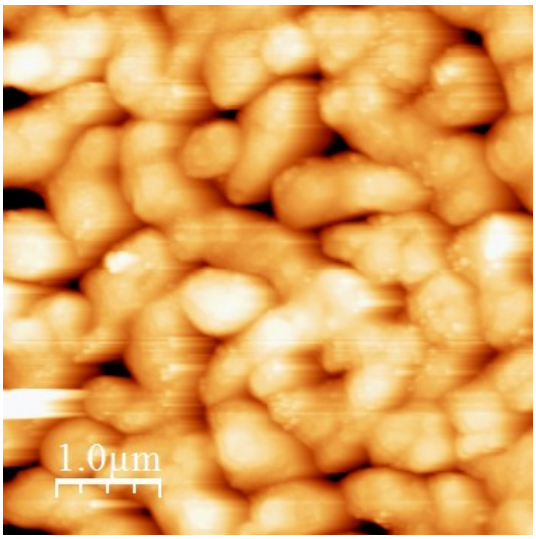

Figure 4-43 AFM of the same YBCO sample as in Figure 4-42.

The YBCO film with the thickness of 1.2 μm was chosen as a standard sample for reference. SEM and AFM images of the sample show a typical surface of the YBCO film with pores and particulates on the film's surface. The AFM image shows RMS roughness of the film of about 30 nm.

4.3 YBCO films on substrates decorated with Ag nano-dots

4.3.1 Optimisation of J_c of YBCO films on substrates decorated with Ag nano-dots

4.3.1.1 Dependence of $J_c(H)$ on the number of laser pulses on Ag target

As mentioned in section 4.1, the architecture of Ag nano dots was changed by changing the number of laser pulses on the Ag target, and, as expected affected the J_c of the YBCO films deposited on decorated substrates. The change of J_c is demonstrated in Figure 4-44, which shows J_c as function of the number of laser pulses on the Ag target, N, for 1.0 μm thick YBCO films deposited on Ag-decorated substrates, in zero magnetic field (a) and in magnetic fields of 0.5 and 1 T (b),. In all three fields, the maximum of J_c occurs for N = 15. This optimum Ag-substrate decoration increases J_c in zero field by about 30% in comparison with reference YBCO films (grown in the same conditions on bare substrate) of the same thickness and up to 600% in 2 T as shown in Figure 4-45. It is obvious that the distribution and size of the Ag nano-dots plays the most important role in promoting columnar growth and defects which acts as pinning centres in the YBCO film.

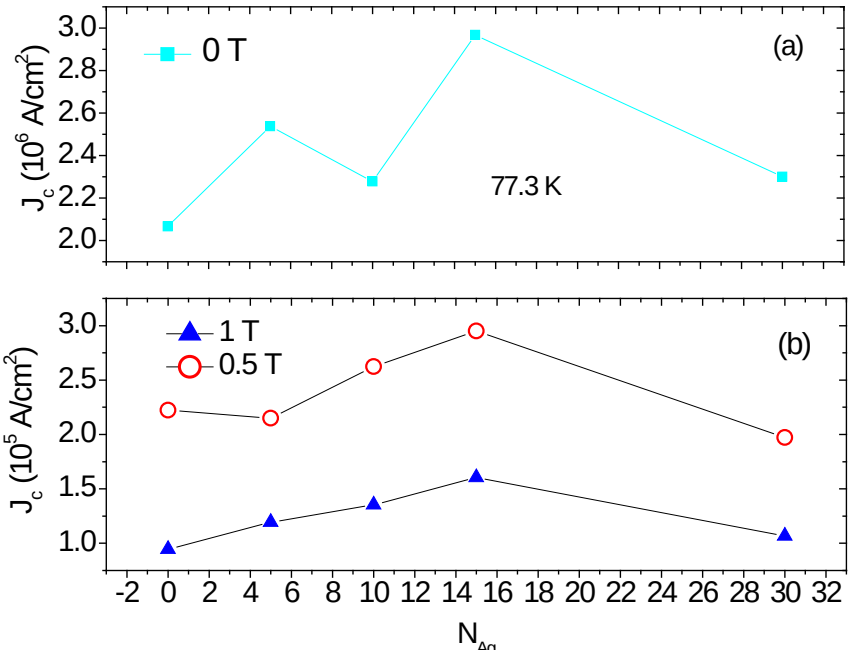

Figure 4-44 Critical current density at 77.3 K as function of the number of laser pulses in 1.0 μm thick YBCO films deposited on Ag-decorated substrates in zero magnetic field (a) and in magnetic fields of 0.5 and 1 T (b). The optimum number of laser pulses is 15.

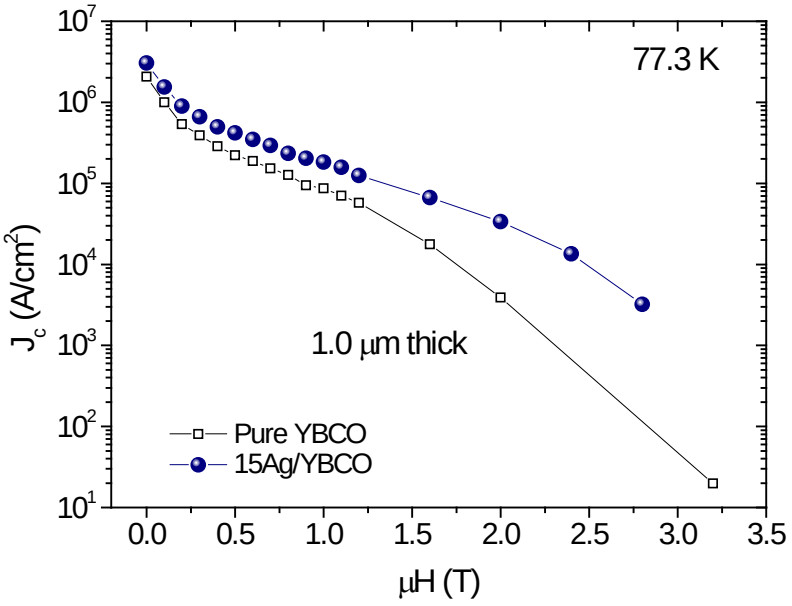

Figure 4-45 Field dependence of critical current density at 77.3 K of pure YBCO film (open squares) and of the film grown on substrate decorated with 15 laser pulses substrate (full circles).

4.3.1.2 Dependence of J_c (H) on the deposition temperature of Ag nano-dots

To investigate the effect of deposition temperature of Ag nano-dots on J_c of the films, 15 laser pulses on Ag target were used to grow Ag nano-dots at various temperature substrates 27 (Room Temperature, RT) to 780^o C, prior to depositions (at 780^o C) of YBCO films with the same thickness of 1 μm. Figure 4-46 shows the field dependence of J_c at 77.3K of the YBCO films grown on substrates decorated with 15 laser pulses on Ag target at various temperatures, and, for comparison, of the reference sample. Figure 4-47 show the dependence of J_c (77.3K) in 0, 0.5 and 1 T, on the temperature used for the growth of Ag nano-dots. As can be seen, the optimum J_c is obtained for the Ag-deposition temperature of 400^o C.

Theoretically, best pinning in the case of nanoinclusions occurs when their dimension is of the same order of magnitude as the coherence length (which is about 3 nm). In our case, for Ag nano-dots grown using optimum conditions (largest increase in J_c) their mean diameter is 14.1 nm and the average height is 3.47 nm. These values are a bit different in comparison with other results, for example Ag nano-island with diameter of about 100 – 500 nm [7], 20 nm for Hf nano-dots [8], 150 nm for Ir nano-dots [9], 50 nm [10], 40 nm [11], 23 – 25 nm [12] and less than 10 nm [13] for Y_2O_3 nano-dots, or 80 – 100 nm for $Nd_{1/3}Eu_{1/3}Gd_{1/3}Ba_2Cu_3O_x$ (NEG) [14], 15 – 30 nm [15], 15 – 20 nm [16] for BZO nanoparticles. Such large differences in diameter of various nano-dots is not clearly understood, it may relate to different free energies of various materials in comparison with the free energy of the substrate, and by differences in the deposition method and conditions.

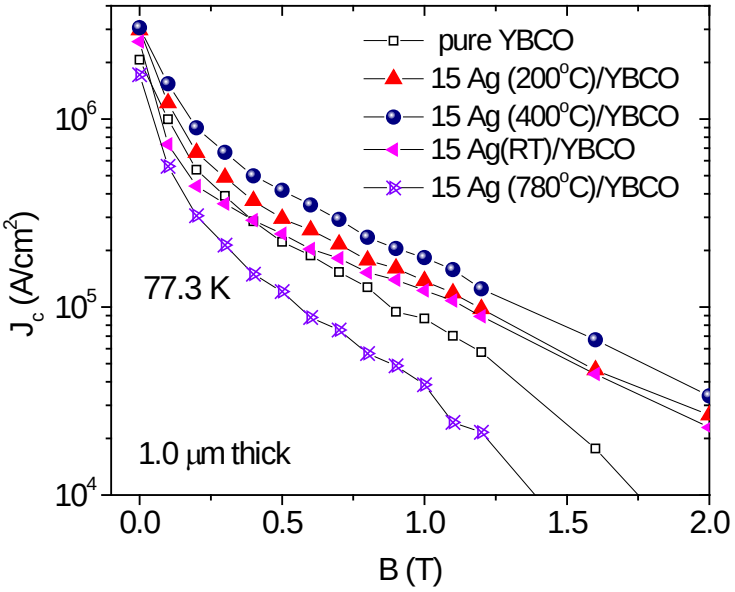

Figure 4-46 Field dependence of J_c at 77.3 K of pure YBCO (open squares), and of YBCO films grown on substrates decorated (15 laser pulses on Ag target) at substrate temperatures of 200°C (triangles), 400° C (circles) RT (stars), and 780° C (crossed triangles), for the same YBCO film thickness of 1 μm.

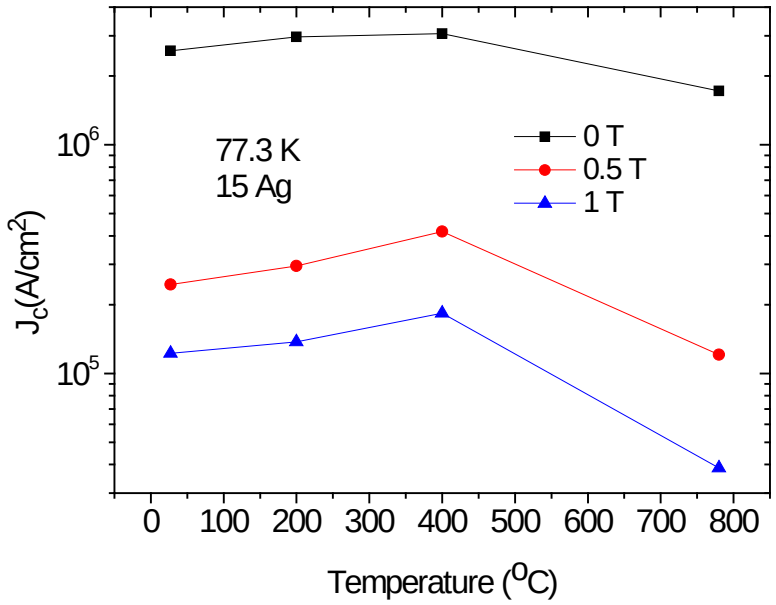

Figure 4-47 Critical current density of YBCO films at 77.3 K as a function of Ag deposition temperature for magnetic fields of zero (black), 0.5 (red) and 1 T (blue). The optimum deposition temperature for Ag nano-dots is 400 °C.

4.3.1.3 YBCO films on MgO substrates decorated with Ag nano-dots and STO substrate

At mentioned in section 4.2.2, J_c of YBCO films grown on MgO is lower than for the films grown on STO. This comparison is now extended to the case of Ag-decorated substrates, in which the same optimum conditions (400 °C, 15 laser pulses) were used to decorate MgO and STO, prior to the growth of 800 nm thick YBCO films. Figure 4-48 shows the field dependence of J_c at 77.3 K of such films grown on bare MgO and on Ag-decorated MgO and STO.

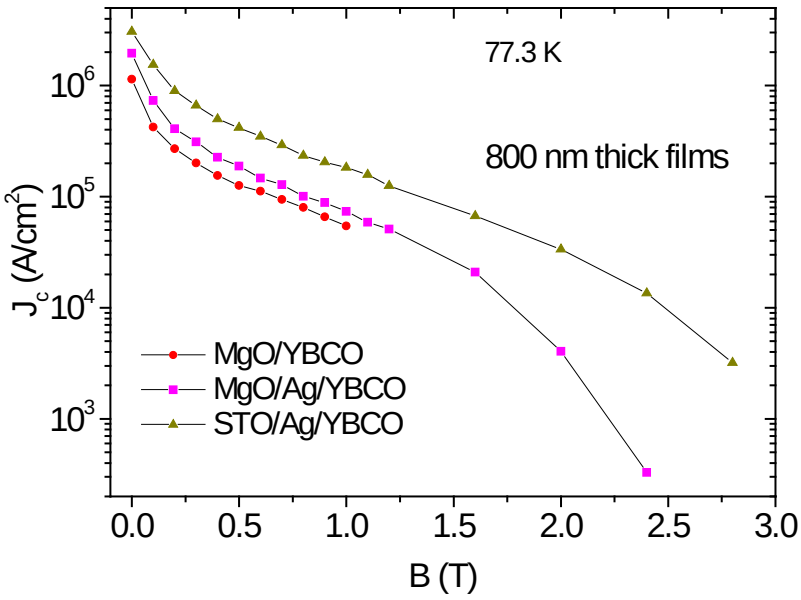

Figure 4-48 Field dependence of J_c at 77.3 K of YBCO films grown on MgO, and on MgO and STO decorated with Ag nano-dots.

An improvement in J_c due to Ag nano-dots is observed for the films grown on MgO substrates, but J_c is still much smaller than of the films grown on Ag-decorated STO substrates,.

The temperature dependence of J_c in 1T of the films grown on Ag-decorated MgO and STO substrates are shown in Figure 4-49. At all temperatures from 5K to 90K, J_c of YBCO on Ag-decorated MgO is below J_c of YBCO on Ag-decorated STO substrate. For this reason, for further investigations of nanostructured superconducting films in this project, MgO substrates were discarded.

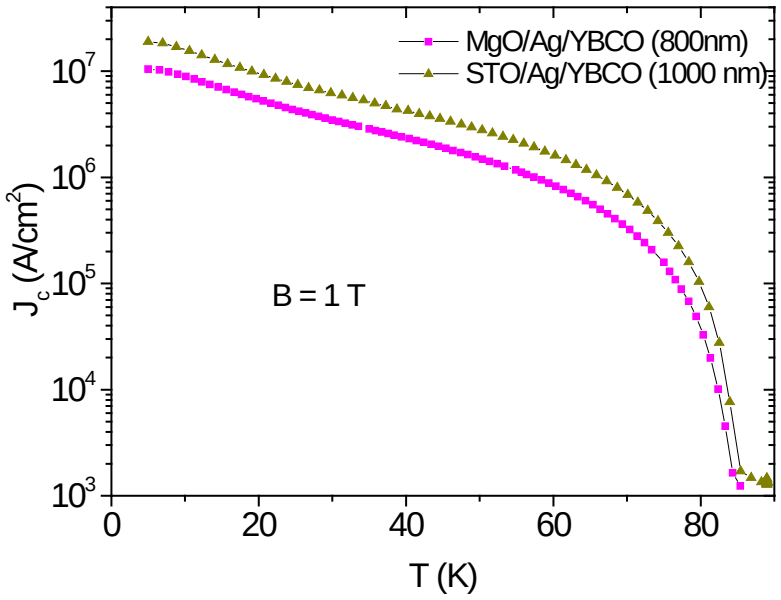

Figure 4-49 Temperature dependence of J_c in 1 T of YBCO films grown on Ag-decorated MgO (squares) and on Ag-decorated STO (triangles).

4.3.2 Superconducting transitions and critical temperatures of YBCO films grown on Ag-decorated substrates

Figure 4-50, Figure 4-51, and Figure 4-52 show the temperature dependence of AC susceptibility of 1 μm-thick YBCO films grown on STO substrates decorated with 15 laser pulses on Ag target (named 15Ag/YBCO), at different temperatures of Ag deposition: room temperature (RT), 200 and 400^o C, respectively. The YBCO was deposited at the standard temperature of 780^o C.

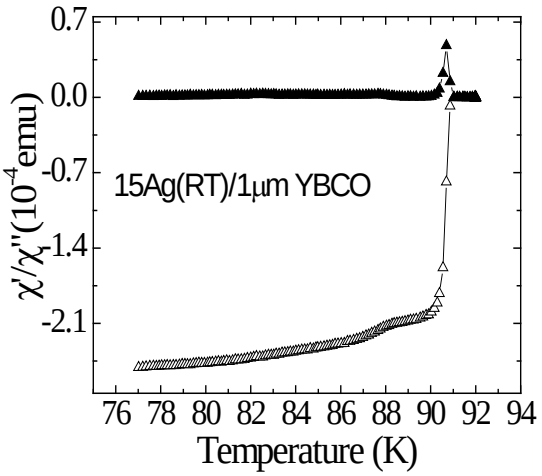

Figure 4-50 Temperature dependence of susceptibility in 15Ag/YBCO (1μm) film in which Ag was deposited on STO at RT.

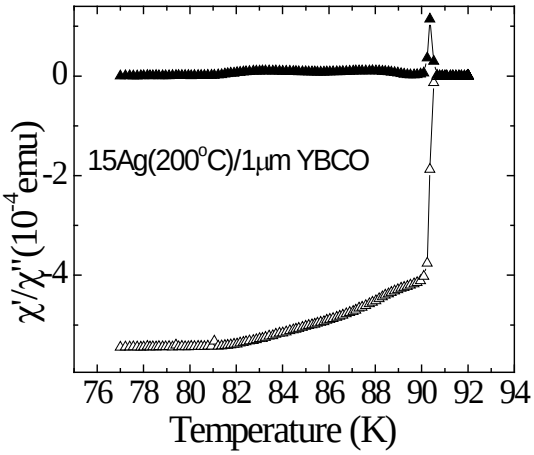

Figure 4-51 Temperature dependence of susceptibility in 15Ag/YBCO (1μm) film in which Ag was deposited on STO at 200°C.

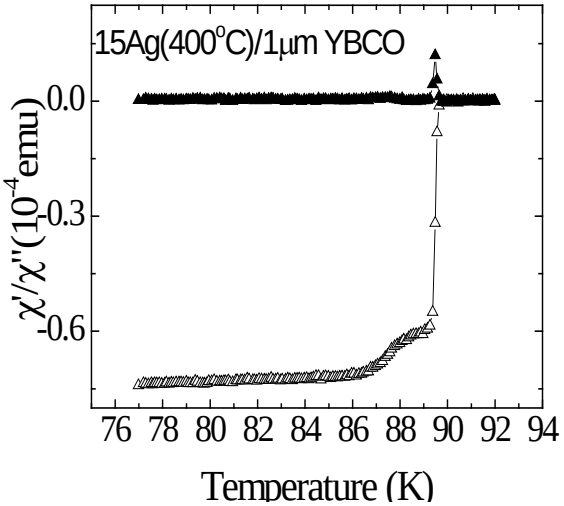

Figure 4-52 Temperature dependence of susceptibility in 15Ag/YBCO (1μm) film in which Ag was deposited on STO at 400°C.

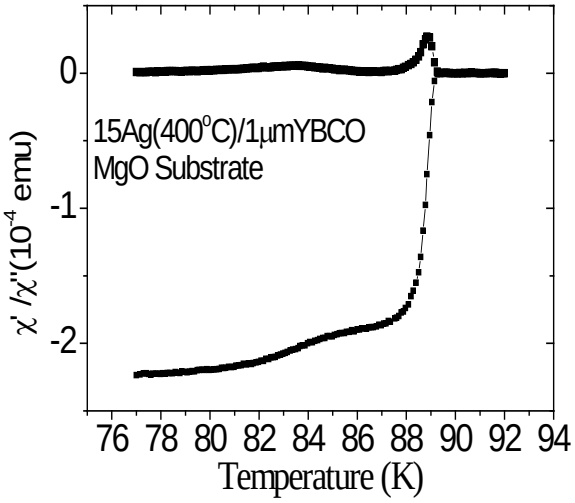

Figure 4-53 Temperature dependence of susceptibility in 15Ag/YBCO (1μm) film in which Ag was deposited on MgO at 400°C.

As can be seen, the transition temperature decreases with increasing the deposition temperature of Ag from 90.7 K (RT deposition), to 90.3 K (200° C) and, finally, to 89.7 K (400°C). It can be see that the in-phase (real) AC susceptibility in all samples is not very flat,

meaning that the films have a secondary phase caused by Ag nano particles, most likely having slightly smaller T_c (delta-T_c pinning centres) which does not appear in pure YBCO films as shown in Figure 4-35

Figure 4-53 shows the temperature dependence of AC susceptibility of 1 μm-thick YBCO film grown on MgO substrates decorated with 15 laser pulses on Ag target at 400^o C. The YBCO was deposited at the standard temperature of 780^o C. As can be seen, T_c of the film is about 88.5 K which is equal to T_c of YBCO film deposited on MgO without Ag decoration. However, the superconducting transition of the film without Ag decoration is a sharper T_c than in the case of the film with Ag decoration.

4.3.3 Thickness dependence of critical current density of YBCO films on Ag-decorated STO substrates

Normally, as shown in Chapter 2, J_c decreases sharply with increasing the thickness of pure YBCO films, (for thickness higher than few hundred nm).

By using Ag-decorated substrates, we can improve J_c for increasing thickness up to about 1 μm, as can be seen in Figure 4-54. Unfortunately, J_c decreases for the films thicker than 1.5 μm.

Figure 4-55 shows the thickness dependence of J_c for YBCO films deposited on Ag-decorated STO substrates; the optimum thickness is about 1 μm for which J_c reaches its maximum of 3.05 MA/cm^2 in self-field. This value is 30% higher than for the film of the same thickness grown on bare STO (stars in Figure 4-55). For very thin films (few hundred nm), YBCO grown on bare substrates have higher J_c than the films of same thickness grown on Ag-decorated substrates, which can be explained by the poor epitaxial growth of the YBCO layer nearest to the substrate due to Ag nano-dots.

Figure 4-56 shows the temperature dependence of J_c for a 480 nm-thick film (triangles) and of a 1.0 μm-thick film (sphere), both grown on Ag-decorated STO in the same optimum condition (15 pulses on Ag target at 400^o C), in an applied field of 1 T. Unlike the case of films grown on bare STO (in which J_c of a 0.5 μm-thick film is higher than of a 1 μm-thick film) , for substrates decorated with Ag nano-dots, the thicker YBCO film has higher J_c than the thinner one, at all temperatures.

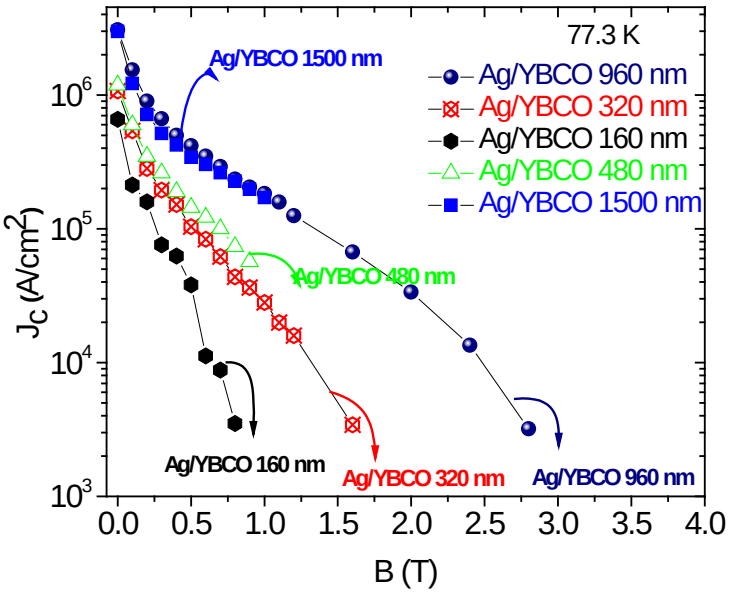

Figure 4-54 Field dependence of J_c of YBCO films with different thickness, grown on Ag-decorated STO.

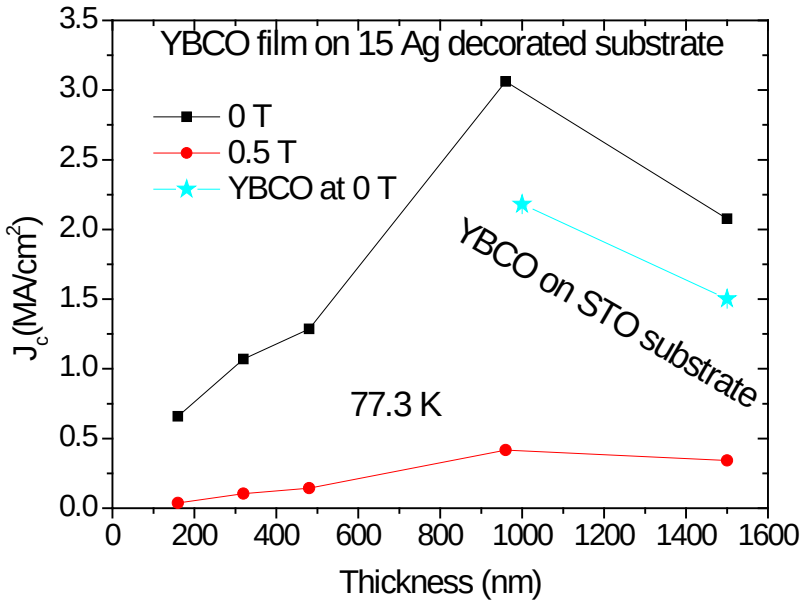

Figure 4-55 Thickness dependence of J_c for YBCO films grown on Ag-decorated STO, substrates, and, for comparison, for YBCO on single crystal STO (blue stars).

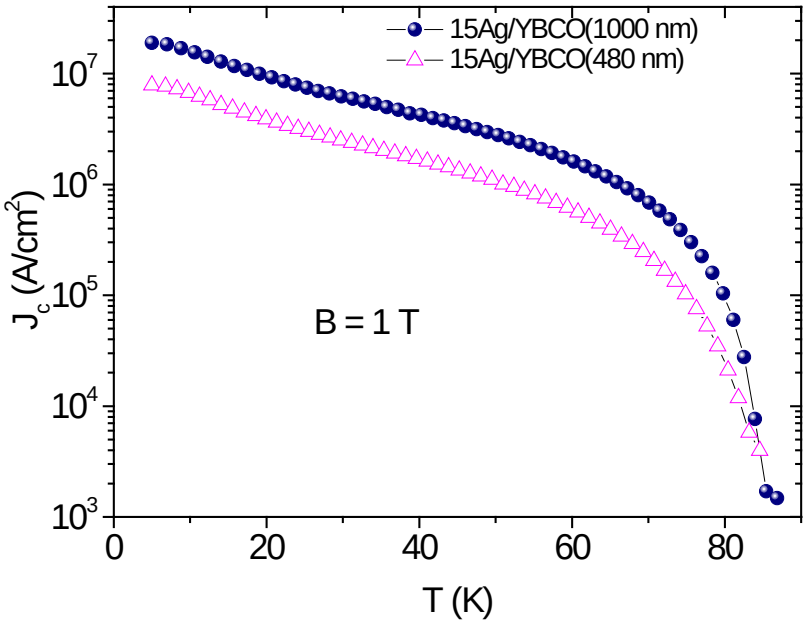

Figure 4-56 Temperature dependence of J_c for a 480 nm-thick film (triangles) and of a 1.0 μm-thick film (sphere), both grown on Ag-decorated STO in the same optimum condition (15 pulses on Ag target at 400^o C), in an applied field of 1 T.

4.3.4 Microstructure of YBCO films grown on substrates decorated with Ag nanodots

Figure 4-57 and Figure 4-58 show the AFM images of surface morphology of 1 μm-thick YBCO film grown on STO and, respectively, on STO decorated with 15 laser pulses on Ag target. A characteristic of AFM images for both films is the island structure, with an island diameter of hundreds nm, the islands being separated by trenches consisting of nanosized pores. However, the islands structure of the film on Ag-decorated substrate is not as uniform as of the film on bare substrate, many small islands with diameters between 100 to 400 nm appeared. The higher number of islands (grains) with different sizes, in the film grown on Ag-decorated STO may imply additional linear/columnar defects acting as effective flux pinning centres which improve J_c of films in comparison with films grown on undecorated substrate.

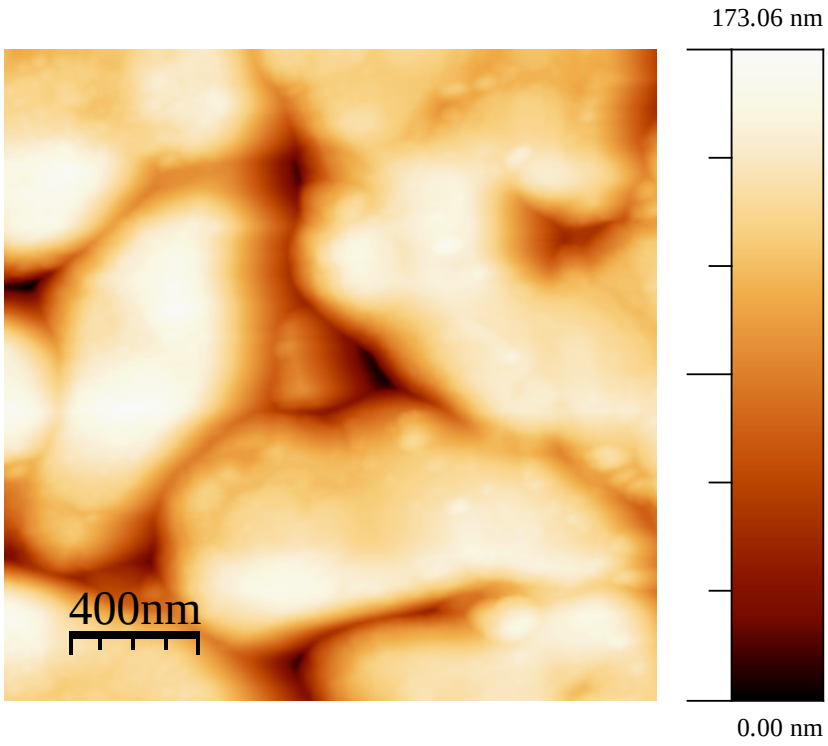

Figure 4-57 AFM image of 1 μm-thick YBCO film grown on bare substrate

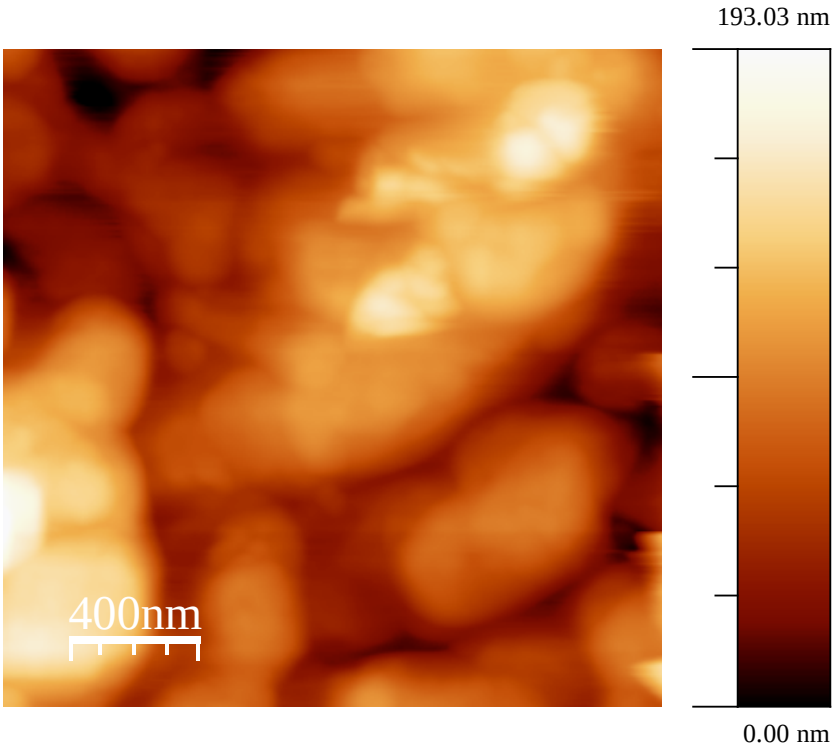

Figure 4-58 AFM image of 1 μm-thick YBCO film grown on Ag-decorated substrate (optimum conditions for Ag growth).

X-ray diffraction results are presented in Figure 4-59. XRD pattern of a STO substrate decorated with Ag nano-dots is shown in Fig. 4-69a. As can be seen, small peaks of Ag appear in the figure alongside the dominant STO peaks.

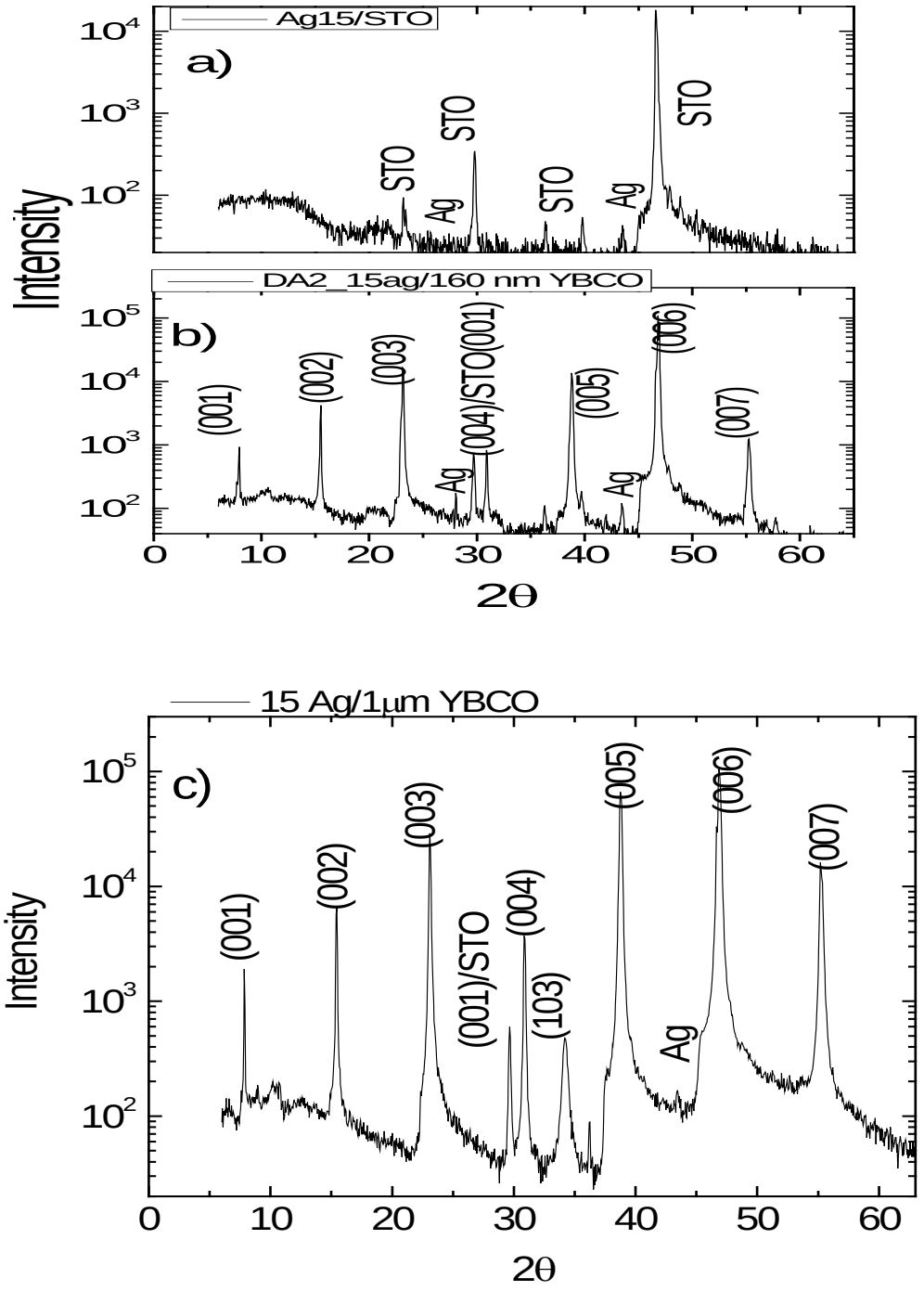

Figure 4-59 2θ scan of the following samples: 15Ag/STO (a), 160nmYBCO/15Ag/STO (b) and 1000nmYBCO/15Ag /STO (c)

Figure 4-59b and c show XRD of YBCO films grown on Ag-decorated substrates, with very different thickness of 160 nm and 1000 nm, respectively. All XRD patterns show strong (00*l*) peaks indicating strong out-of-plane (c-axis) orientation, hence very good epitaxy. However, the (103) peak appears in thicker film due to the misalignment of a few grains. The additional peak normally appears in films with thickness of several μm [17], leading to degeneration of J_c in thicker films. In contrast, "small enough" misalignment due to Ag nano-dots may enhance J_c due to additional pinning centres, as seems to be the case in our 1 μm-thick film grown on Ag-decorated substrate.

4.4 Ag/YBCO quasi-multilayer films

4.4.1 Quasi-multilayer architecture and improvement of J_c

It is known from the literature review (Chapter 2) that J_c rapidly decreases with increasing of film thickness. In order to obtain high critical current per cm-width (I_c), ideally over 1000 A/cm, increasing the film thickness without decreasing too much J_c is required. In this section is discussed the quasi-multilayer architecture, composed of quasi-layers of Ag (grown by 15 laser pulses on Ag target) interspaced with layers of YBCO with a certain thickness, the sequence repeating several times (N). These samples are denoted by (15Ag/mYBCO)xN, where m is the thickness of each of YBCO layers and N is the number of sequences.

4.4.1.1 Quasi-multilayers architecture of (15Ag/1.5μmYBCO)xN

In this section, incomplete layers of Ag nano-particles (formed from 15 laser pulses) were interspaced with 1.5 μm-thick YBCO layers, the sequence being multiplied by N = 1, 2, 3 and 4; leading to a total film thickness of 1.5 μm, 3.0 μm, 4.5 μm and 6.0 μm, respectively. As shown in section 4.3.3, of the film grown on Ag-decorated substrate 15Ag/1.5μmYBCO has a high J_c of about 2 MA/cm^2 in self-field. If this high J_c can be maintained for two or more layers, the critical current of such thick films can be very high.

Temperature dependence of susceptibility in (15Ag/1.5μmYBCO)xN thick films is shown in Figure 4-60, the measurements being performed with an AC field amplitude of 0.05 Oe. The critical temperature T_c, determined from the peak of imaginary (out-of-phase) susceptibility in samples with N = 1, 2, 3 and 4, is 89.3 K, 89.8 K, 89.8 K and 89.5 K, respectively.

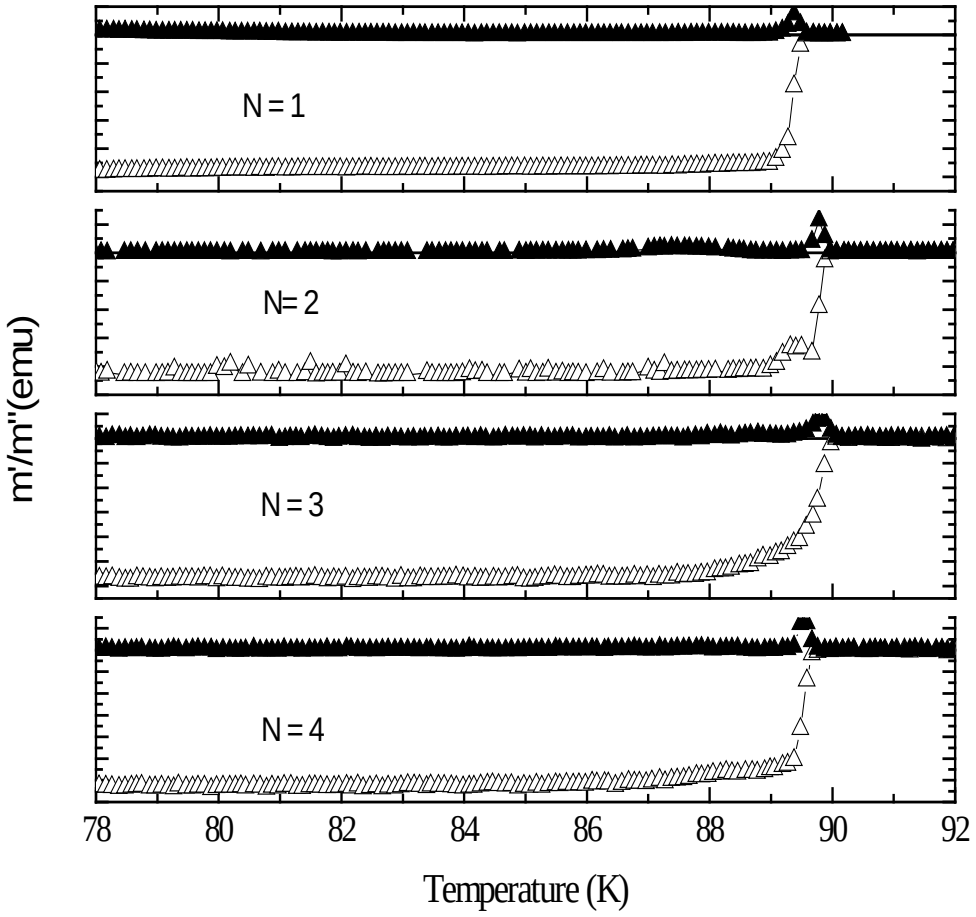

Figure 4-60 Temperature dependence of susceptibility in (15Ag/1.5μmYBCO)xN thick films

The T_c values are very close to each other, even for the 6 μm thick film (N = 4), and δT < 0.5 K for all films. High T_c in such thick films shows good, homogeneous superconducting properties. However, J_c values depend very much on the film thickness (on number N of sequences.

Figure 4-61 shows the field dependence of critical current density, at 77.3 K, for the four quasi-multilayer samples (with N = 1, 2, 3 and 4) and, for comparison, of a 2 μm - thick YBCO reference sample.

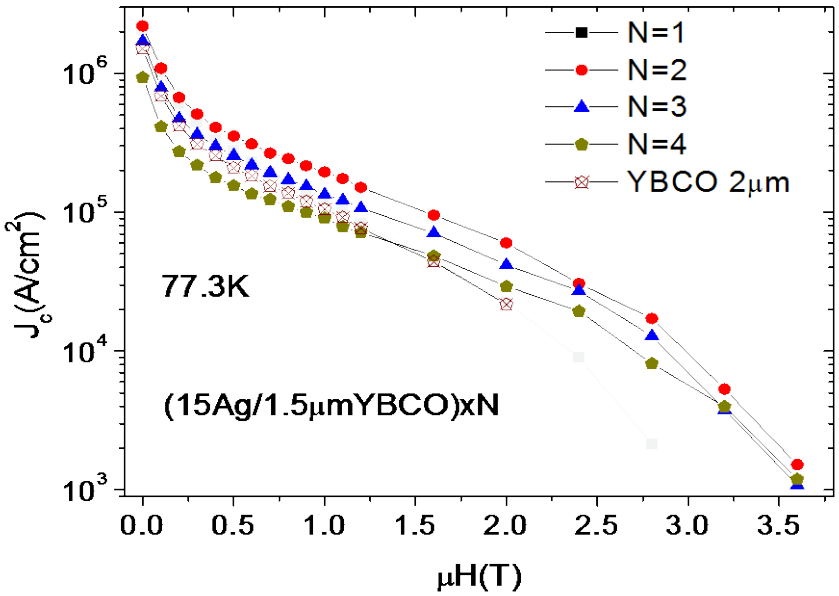

Figure 4-61 Field dependence of J_c of (15Ag/1.5μmYBCO)xN multilayer films at 77.3 K

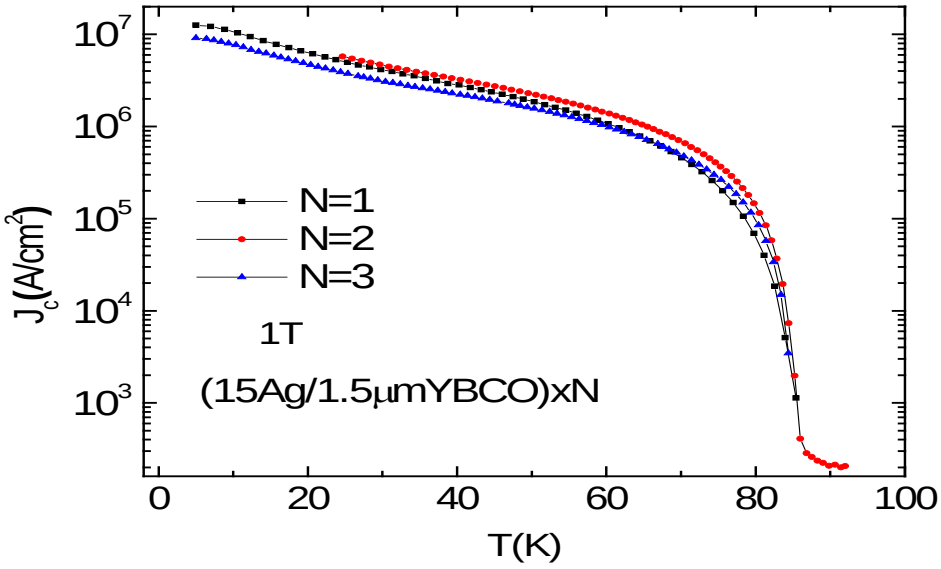

Figure 4-62 Temperature dependence of J_c of (15Ag/1.5μmYBCO)xN multilayer films in 1 T

As can be seen, the 3.0 μm-thick (15Ag/1.5μmYBCO)x2 and 4.5 μm-thick (15Ag/1.5μmYBCO)x3 samples have higher critical current densities than the 2.0 μm thick

reference YBCO sample in all fields (except the self-field value in the case of the 3-layers sample). Normally, a 2 μm thick YBCO film should have a higher J_c than 3 or 4 μm-thick pure YBCO films, so choosing a 2 μm-thick pure YBCO film for comparison is reasonable. The much thicker (6 μm) (15Ag/1.5μYBCO)x4 quasi-multilayer has a smaller J_c than the reference film in self-field and moderate fields. However, in fields higher than 1.5 T, even the thicker sample has a higher J_c than the reference sample. The self-field J_c of our 3 μm – thick Ag/YBCO quasi-multilayer is comparable with best YBCO films of similar thickness, doped with barium zirconate + yttrium oxide [18]. Table 4-1 summarizes the values of J_c of the films at 77.3 K, in self-field and 1 T.

As can be seen in Figure 4-62, in 1T the 3 μm – thick Ag/YBCO quasi-multilayer (N =2) has higher J_c than the other two films (with N = 1 and 3) at all temperatures from 20 to 90 K.

Table 4-1 J_c values of the films at 77.3K, in self-field and in 1T, taken from Figure 4-61.

N (layers)	J_c(0T)	J_c (1T)
1	2. 04 (MA/cm^2)	0.12 (MA/cm^2)
2	2.2 (MA/cm^2)	0.2 (MA/cm^2)
3	1.71 (MA/cm^2)	0.13 (MA/cm^2)
4	0.94 (MA/cm^2)	0.09 (MA/cm^2)

The very significant improvement of J_c of (15Ag/1.5μmYBCO)x2 (N = 2) film is more visible at temperature of 70 K as shown in Figure 4-63.

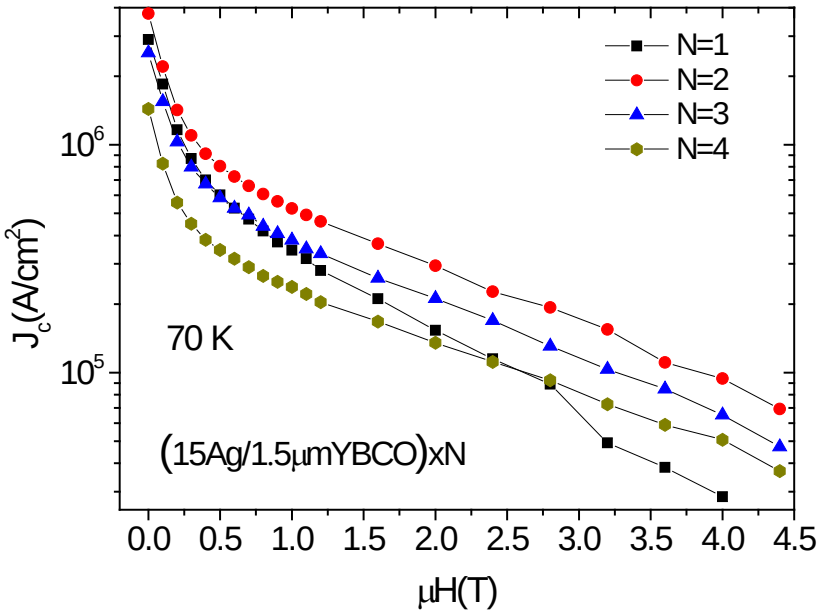

Figure 4-63 Field dependence of J_c of (15Ag/1.5μmYBCO)xN films at 70 K.

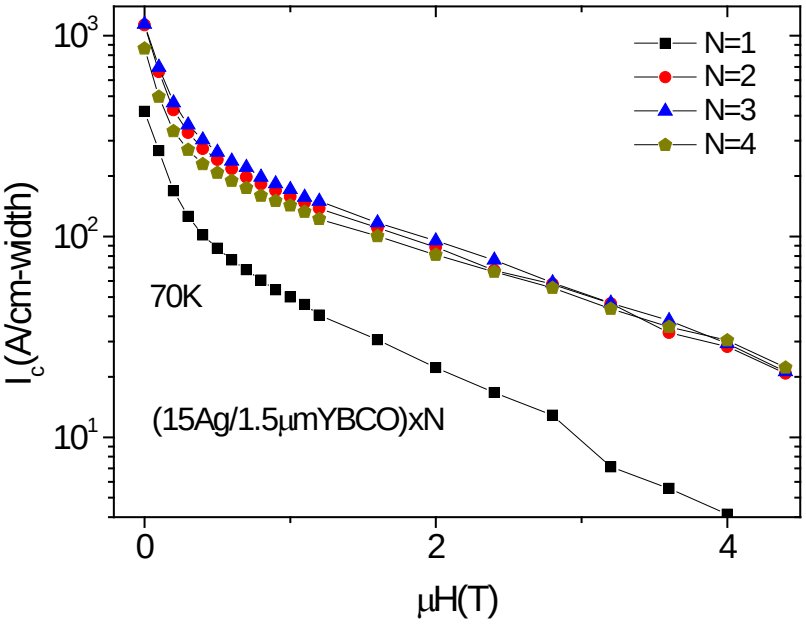

Figure 4-64 Field dependence of I_c of (15Ag/1.5μmYBCO)xN films at 70 K.

At 70 K in self-field, J_c is 2.9 MA/cm^2, 3.76 MA/cm^2, 2.54 MA/cm^2 and 1.44 (MA/cm^2) for films with N = 1, 2, 3 and 4, respectively. Field dependence of critical current of the films at 70 K is shown in Figure 4-64, the highest I_c being achieved in the film with N = 3 (4.5 μm) in all applied fields up to 4 T.

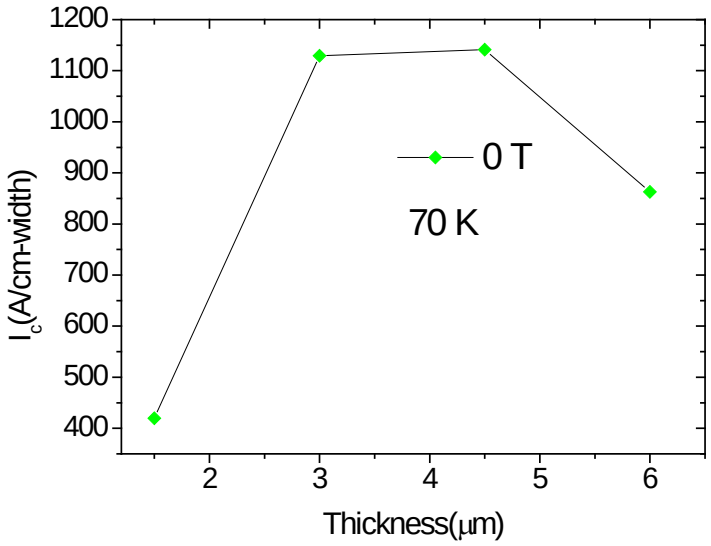

Figure 4-65 Thickness dependence of critical current per cm (I_c) of (15Ag/1.5μmYBCO)xN films in self-field and at 70 K.

The values of critical current in self-field and at 70 K of the films are shown in Figure 4-65. The I_c values increase with increasing N from 1 to 3, with 1141 A/cm-width being the highest I_c, for the film with N = 3. The I_c then decreases to 842 A/cm for the thicker film with N = 4, similar to the decrease in J_c for the same film, as shown in Figure 4-61.

4.4.1.2 Quasi-multilayers architecture of (15Ag/450nmYBCO)xN

Quasi-multilayers composed of Ag nano-dots (15 laser pulses) and thinner, 450nm, YBCO films were also investigated. For sequence repetition numbers N = 1, 3, 4, 5 and 10, the resulting quasi-multilayers have thicknesses of 0.45 μm, 1.35 μm, 1.8 μm, 2.25 μm and

4.5 μm, respectively. Figure 4-66 shows temperature dependence of AC susceptibility of (15Ag/ 450nmYBCO)xN films with N = 1, 3, 5 and 10.

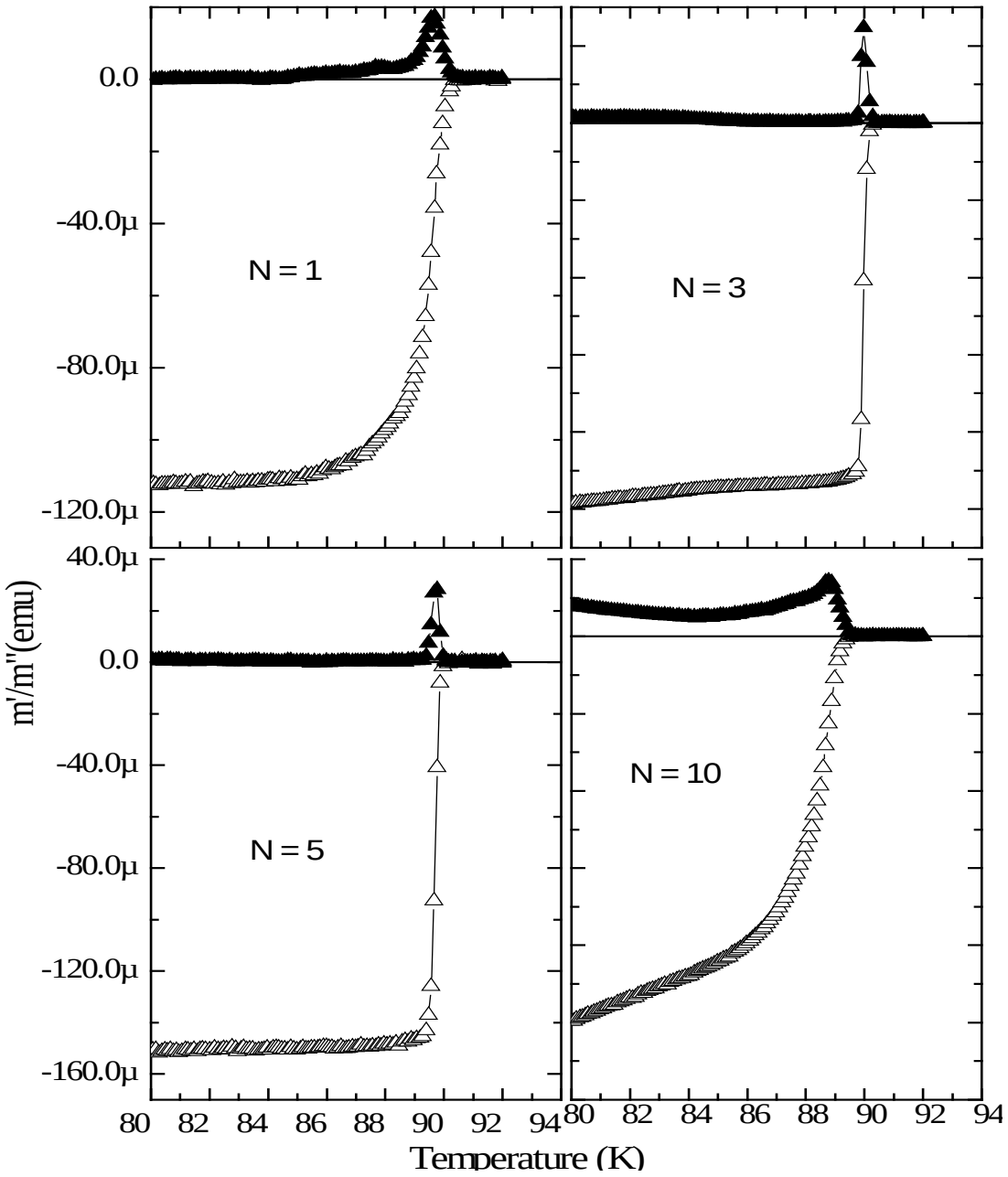

Figure 4-66 Temperature dependence of AC susceptibility of (15Ag/450nmYBCO)xN

As can be seen, for the films with N = 3 and 5, T_c is about 89.7 K and 89.9 K), respectively, with ΔT_c smaller than 0.5 K, while for the thinner film (N=1) and the very thick film (N=10), the superconducting transition is broader. For the very thin film, the broader

transition is related to the low J_c of the very thin film on Ag-decorated STO as mentioned in 4.3.3, and is due to imperfections of the YBCO layer near the substrate caused by Ag nano-particles. The structural quality of YBCO in thicker films is much better than in the very thin film, as proved by much sharper superconducting transitions due to long enough deposition time at the high temperature of 780^o C and oxygen environment. It takes about 6 minutes to deposit single-layer film (N = 1), 80 minutes for tri-layer film (N = 3) and much longer (about 260 minutes) for ten-layer film (N = 10) due to excursions between the two the different deposition temperatures of Ag (400^{o}C) and YBCO (780^o C). However, a too long deposition time (the film with N=10) is not good for such multilayered YBCO film as indicated by the broader transition and a smaller T_c of 88.7 K as compared with 89.9 K for the N = 5 film.

Figure 4-67 shows the temperature dependence of critical current density of (15Ag/450nmYBCO)xN films (N = 3, 4, 5 and 10) in 1 T.

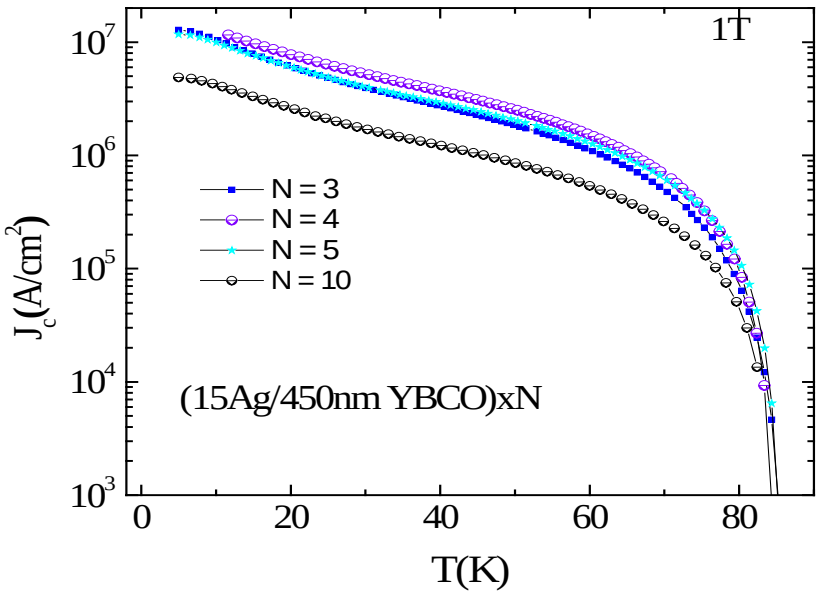

Figure 4-67 Temperature dependence of J_c of (15Ag/450nmYBCO)xN films in 1 T.

In all temperature range from 5 to 90 K, J_c of the film with N = 10 is much lower than other ones, which is correlated with its broader transition, which is due to in-homogeneities induced by the very long deposition time. For temperatures below 65 K, J_c of the film with N = 4 is highest, while for higher temperatures the J_c of the film with N = 5 has the highest value.

Field dependence of J_c at 77.3 K of the (15Ag/450nmYBCO)xN films is shown in Figure 4-68.

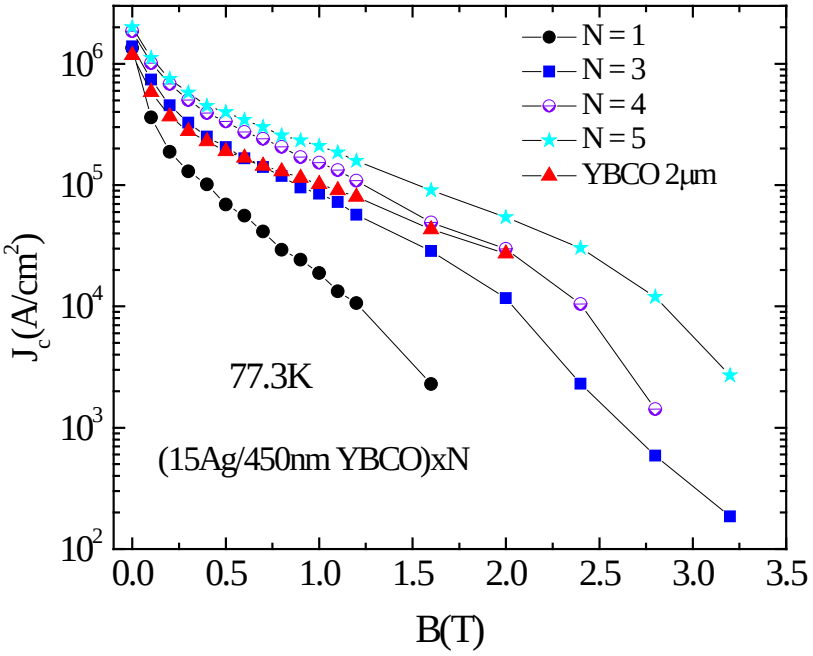

Figure 4-68 Field dependence of J_c at 77.3 K of the (15Ag/450nmYBCO)xN quasi-multilayers, and, for comparison, of a 2 μm-thick pure YBCO film.

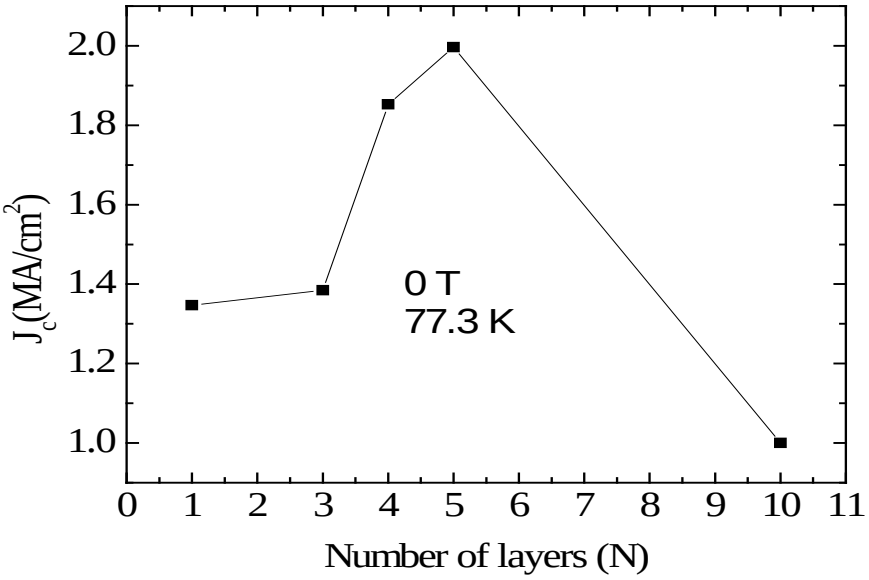

Figure 4-69 J_c at 77.3 K in self-field vs. number of sequences.

As can be seen, J_c at 77 K of the nanostructured film with N = 5 is the highest in all applied fields. The lowest J_c is for the thinnest film (N = 1). For comparison, J_c of the 2 μm-thick pure YBCO film is displayed in the figure as red triangles. The quasi-multilayers films with N = 4 and 5, with thickness of 1.8 and 2.25 μm, respectively, have higher J_c than that of the YBCO reference film in all magnetic fields. The higher value of J_c for the films with N = 4 and 5 is a good evidence that Ag nano-dots induce efficient pinning centres that improve J_c of the films in the case of optimized architectures architecture. The values of J_c in self-field for the nanostructured films with N = 1, 3, 4, 5 and 10 at 0 T are shown in Figure 4-69. The highest value is 2.02 MA/cm^2 for the film with 5 layers and thickness of 2.25 μm. However, this thickness and this J_c are not high enough to obtain a critical current I_c higher than 1000 MA/cm, which is the case of the (15Ag/1.5μmYBCO)x N architecture, as shown in section 4.4.1.1.

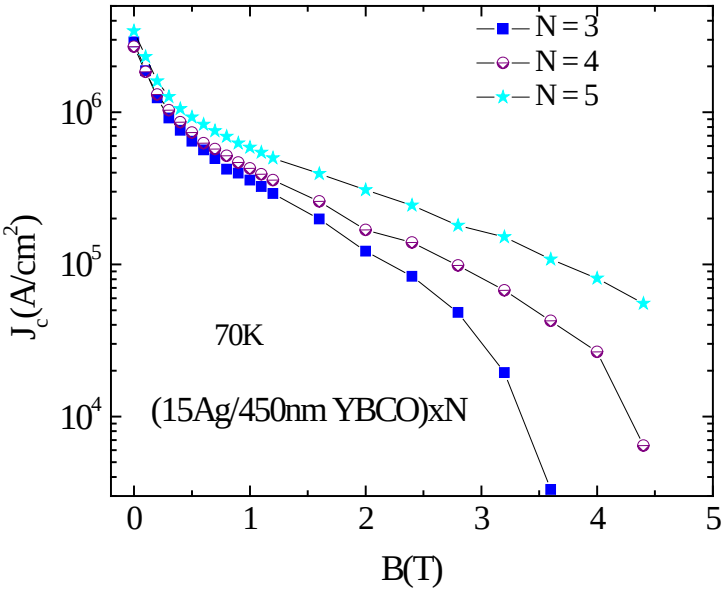

Figure 4-70 Field dependence of J_c of 3 best samples with N = 3, 4 and 5 at 70 K

Figure 4-70 shows the field dependence of J_c at 70 K of the samples with N = 3, 4 and 5. The self-field values of J_c are 2.9 MA/cm^2, 2.7 MA/cm^2 and 3.4 MA/cm^2, respectively. However, the film thickness of the sample with N = 5 is only 2.25 μm, which leads to the critical current of 767 A/cm-width at 70 K. This value is lower than 1141 A/cm-width for the film with thickness of 4.5 μm presented in section 4.4.1.1 due to lower thickness. Unfortunately, we could not obtained good films with higher thickness in this configuration due to the too long deposition time at high temperature.

4.4.2 Critical current density of quasi-multilayer films from AC susceptibility measurements

Critical current density and pinning strength can be determined from transport measurements (I–V curves), from DC magnetization loops, or from frequency-dependent AC susceptibility. In the latter case, from calculations of Brandt [19] on the flux penetration in

superconductors with one dimension much smaller than the other two (disks, squares, stripes) in a perpendicular configuration (suitable for thin films with magnetic field perpendicular to the film surface), it was shown that the position h^* of the maximum in the AC field amplitude dependence of the out-of-phase susceptibility $\chi''(h_{ac})$ is related to J_c by the equation (3.3). In practice, for a fixed temperature and DC applied field, the out-of-phase susceptibility is measured as a function of the amplitude h_{ac} of the AC field, at various AC field frequencies f. An example of such measurements is shown in Figure 4-71 for (15Ag/1.5μmYBCO)x2 quasi-multilayer, at 77.3 K and in 4 T. The position h^* of the maximum is used to calculate the $J_c(T,H,f)$. Figure 4-72, Figure 4-73 and Figure 4-74 show the frequency dependence of J_c (double logarithmic scale), at 77.3 K and few applied DC fields (shown in the figures) of (15Ag/1.5μmYBCO)x2, (15Ag/1.5μmYBCO)x3 and (15Ag/450 nmYBCO)x5, respectively.

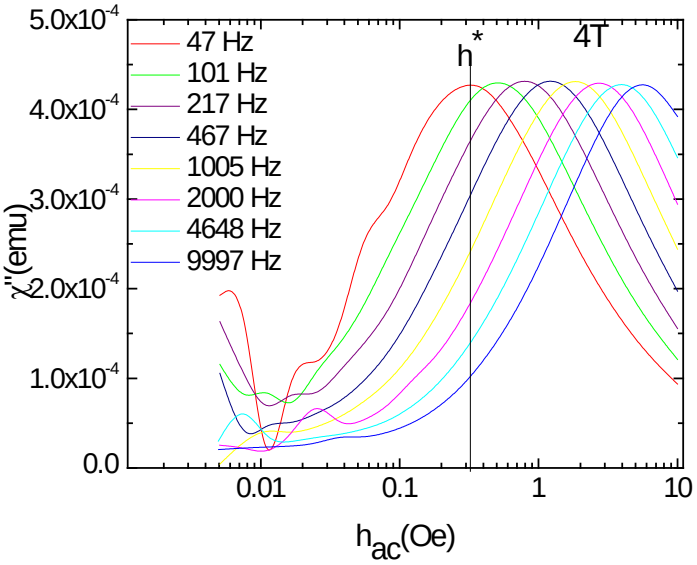

Figure 4-71 Field dependence of out-of-phase AC susceptibility of multilayer film (15Ag/1.5 μmYBCO)x2 at 77.3 K and in DC applied field of 4 T, with different AC frequencies from 47 to 9997 Hz (legend in the figure).

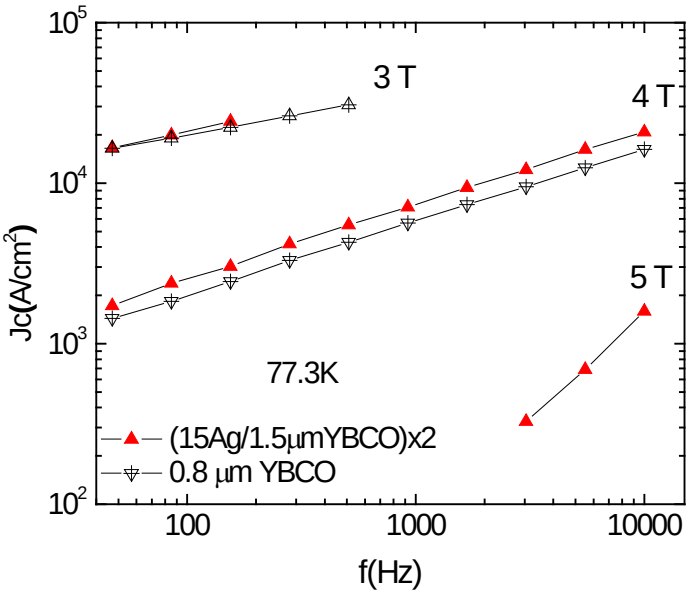

Figure 4-72 Frequency dependence of J_c of (15Ag/1.5 μm YBCO)x2 sample (red triangles) at 77.3 K, in DC applied fields of 3, 4 and 5 T in comparison with the values for a thin 0.8 μm YBCO film in the same conditions.

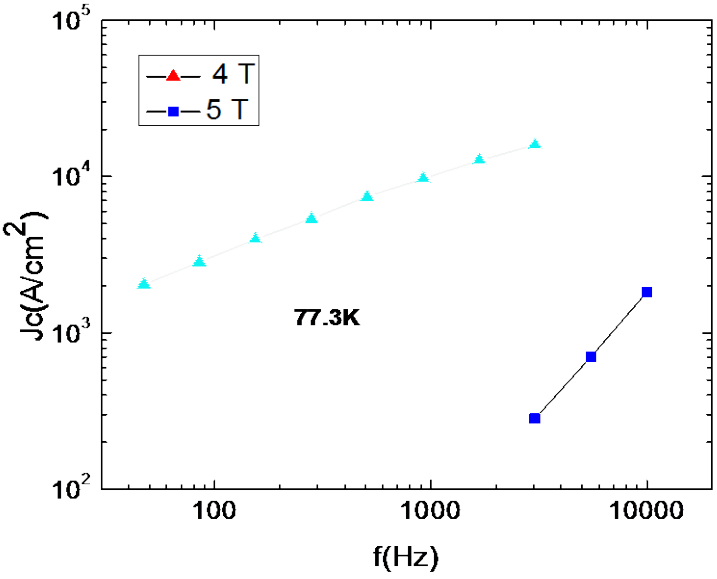

Figure 4-73 Frequency dependence of J_c of (15Ag/1.5 μmYBCO)x3 sample at 77.3 K and in DC applied fields of 4 and 5 T.

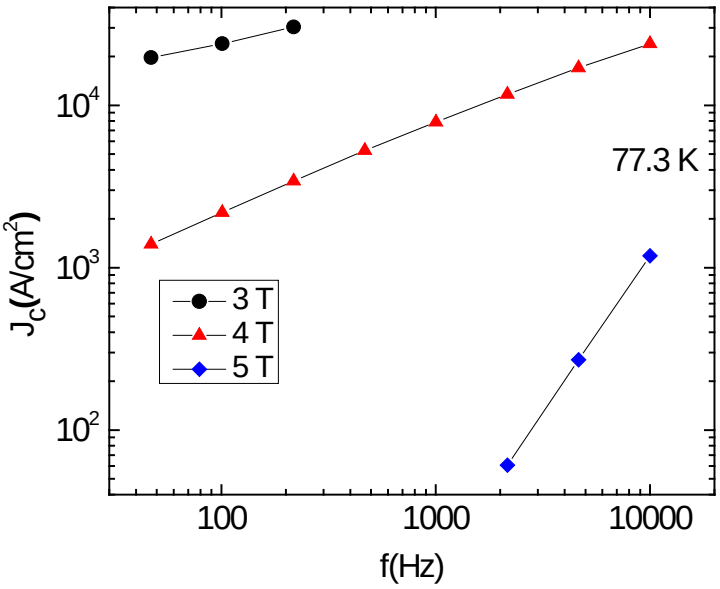

Figure 4-74 Frequency dependence of J_c of (15Ag/450 nm YBCO)x5 sample at 77.3 K in DC applied fields of 3, 4 and 5 T.

It should be noted that the experimental window (T, H) in which this method can be used is limited by the film thickness and by the values of critical current density in the respective conditions. In all the above figures the data in double - logarithmic plot are well described by straight lines. Frequency (time)-dependence of J_c can be explained by the different timescale of the thermally activated flux creep. Figure 4-72 clearly shows that J_c of the multilayer film is higher than that of the pure YBCO, which is also closer to the optimum thickness.

For all the measured films, and in all *T* and *H* conditions, the frequency dependence of J_c (in double logarithmic scale) is very well fitted by a straight line $y = a - b*x$, where $y = ln(J_c)$ and $x = ln(f_0/f)$. Such examples are shown in Figure 4-75, Figure 4-76 and Figure 4-77, with a and b values of linear fitting being shown in Table 4-2

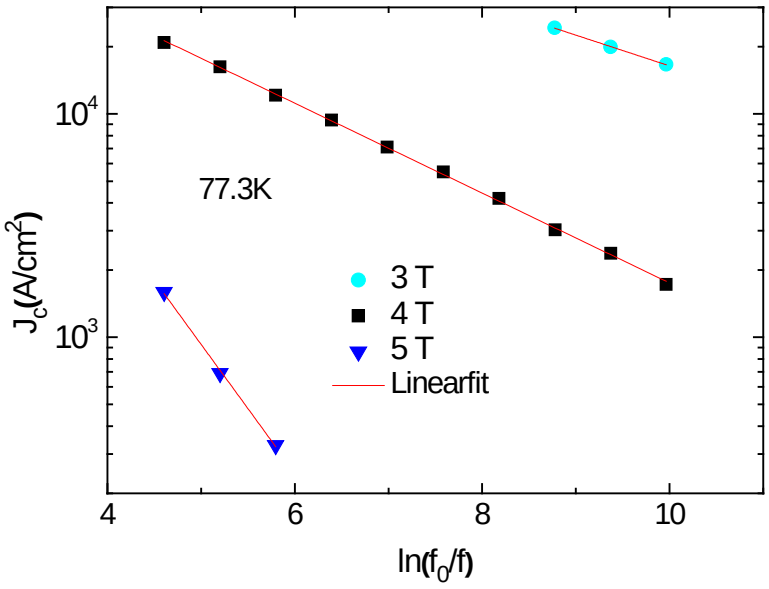

Figure 4-75 Frequency dependence of J_c of (15Ag/1.5 μmYBCO)x2 film in different fields

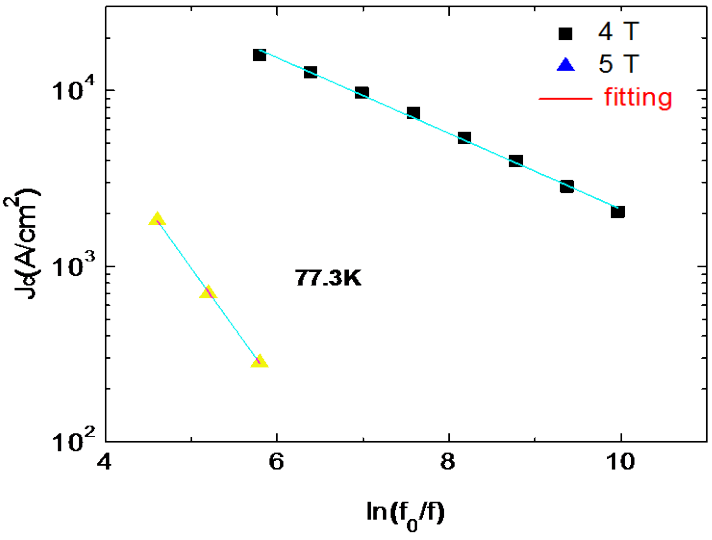

Figure 4-76 Frequency dependence of J_c of (15Ag/1.5 μm YBCO)x3 film at different fields

From the frequency (time) dependence of critical current density one can estimate the pinning potential U_0. Our attempts to describe the experimental data by the power-law current

density dependence of the pinning potential from the weak collective pinning theory [20] or by the linear Anderson–Kim (AK) model [21] were unsuccessful. A comparison of different models is given in Figure 4-78 for (15Ag/1.5 μmYBCO)x2 sample at 77.3 K and in 4 T. The unsuccessful fit of J_c vs. f with collective pinning model $J_c \approx \frac{k_B T}{U_0}\left(ln\frac{f_0}{f}\right)^{-1/\mu}$ or the Anderson-Kim model $J_c \approx \ln\left(f_0/f\right)$, where f_0 is a macroscopic attempt of about 10^6 Hz [22] is obvious. Instead, as can be seen in Figure 4-75 to Figure 4-78, our data is very well described by a straight line in double logarithmic plot: $lnJ_c = a - b\left(ln\left(\frac{f_0}{f}\right)\right)$ (4.1)

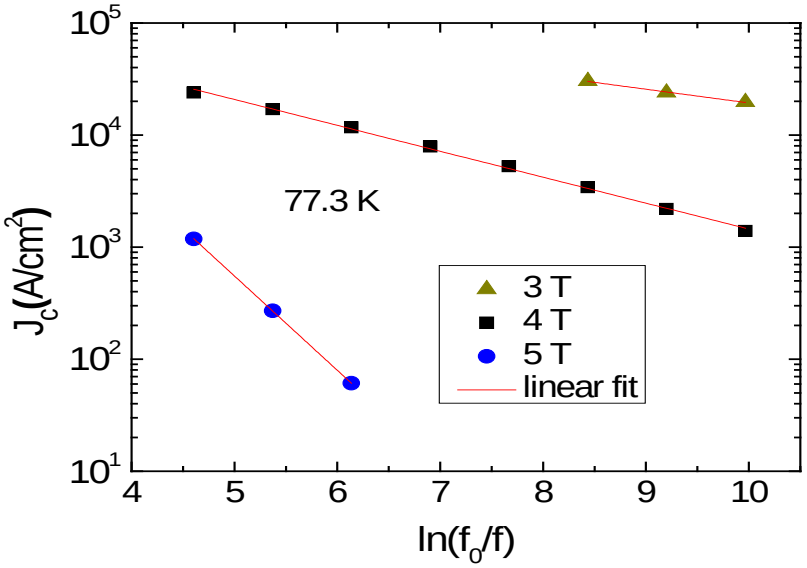

Figure 4-77 Frequency dependence of J_c of (15Ag/450 nm YBCO)x5 film at different fields

Table 4-2 a and b values resulting from the linear fitting of data from Figure 4-75 to Figure 4-77

Samples	*a*			*b*		
	3 T	4 T	5 T	3 T	4 T	5 T
(15Ag/1.5μmYBCO)x2	5.6	5.3	5.8	0.1	0.2	0.6
(15Ag/1.5μmYBCO)x3	na	5.5	6.4	na	0.2	0.7
(15Ag/450 nmYBCO)x5	5.5	5.5	6.9	0.1	0.2	0.8

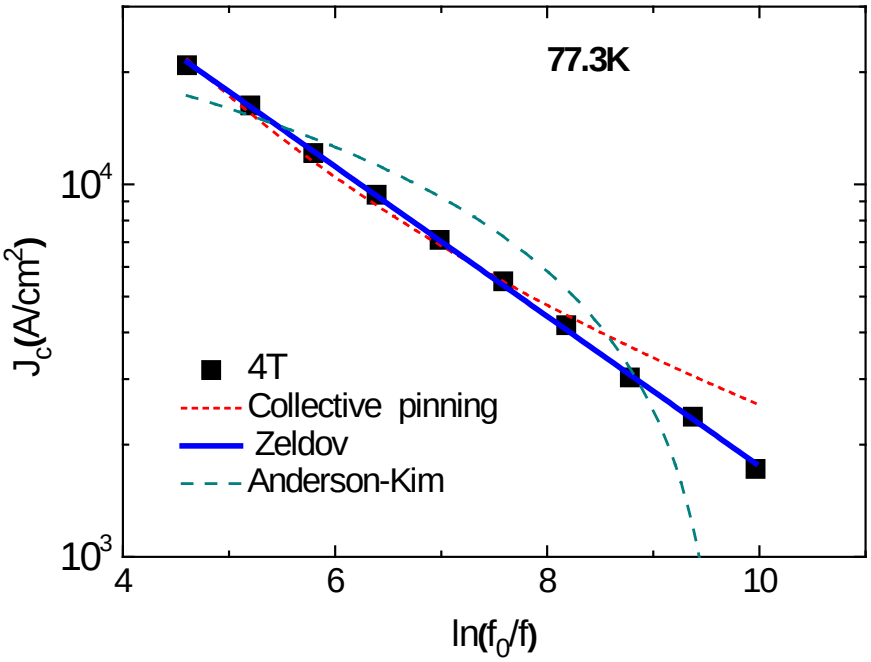

Figure 4-78 Frequency dependence of critical current density of the (15Ag/1.5μmYBCO)x2 multilayer, at 77.3 K and in 4 T. Dotted line (dark cyan) is the fit of the data with the Anderson–Kim model, red dotted line is the fit of the data with the collective pinning model, and full line is the fit of the data with equation 4.1.

The equation 4.1 is consistent with a logarithmic dependence of the effective pinning potential on the current density: $U_{eff} = U_0 ln\left(\frac{J^*}{J}\right)$ (4.2)

where J^* is a critical current density at which the effective pinning potential U_{eff} approaches zero (cross-over between flux creep and flux flow). This dependence was proposed by Zeldov and co-workers based on magneto-resistivity [23] and current-voltage characteristic measurements on YBCO thin films, and explained theoretically [24, 25] by a potential well having a cone-like structure exhibiting a cusp at its minimum and a broad logarithmic decay with the distance. It can be shown that, by using equation (4.2) for the current dependence of the effective pinning potential, U_0 can be related to the slope b in equation (4.1) of our experimental data $U_0 = k_B T \left(1 + \frac{1}{b}\right)$ (4.3).

Equation (4.3) can be derived in the by following way, from equation (4.1) can be rewritten as $\ln J = \ln J_0 - b ln\left(\frac{t}{t_0}\right)$, where $t = f^{-1}$, $t_0 = f_0^{-1}$ and J_0 is the critical current density in the absence of thermally-activated flux creep (T = 0 K) or, by using the properties of logarithm function,

$$J = J_0 \left(\frac{t}{t_0}\right)^{-b} \quad (4.4).$$

In an inductive circuit, the voltage V is proportional to the time derivative of the current and, from Eq. (4.4) , it is given by

$$V \propto \frac{dJ}{dt} = -bJ_0 t_0^{-1} \left(\frac{t}{t_0}\right)^{-(b+1)} \quad (4.5)$$

In thermally activated flux creep regime, the dissipation (voltage) is proportional to the probability of flux jumping over the pinning barrier:

$$V \propto e^{\left(\frac{-U_{eff}}{k_B T}\right)} \quad (4.6)$$

From Eqs. (4.5) and (4.6) and replacing U_{eff} from (4.3), one has:

$$-bJ_0 t_0^{-1} \left(\frac{t}{t_0}\right)^{-(b+1)} = Ce^{\left(\frac{-U_{eff}}{k_B T}\right)} = Ce^{\left(\frac{-U_0}{k_B T}\right) ln\left(\frac{J^*}{J}\right)} = C\left(\frac{J^*}{J}\right)^{\frac{-U_0}{k_B T}} \quad (4.7)$$

By introducing the current density J from Eq. (4.4), the Eq. (4.7) can be rewrite as

$$-bJ_0 t_0^{-1}\left(\frac{t}{t_0}\right)^{-(b+1)} = C\left(\frac{J^*}{J_0}\right)^{\frac{-U_0}{k_B T}}\left(\frac{t}{t_0}\right)^{\frac{-bU_0}{k_B T}} \quad (4.8)$$

For Eq. (4.7) to hold for any value of the variable time, it is necessary that the exponents of (t/t0) in both sides are equal, hence $-(b+1) = -b\frac{U_0}{k_B T}$ or

$$U_0 = k_B T\left(1+\frac{1}{b}\right) \quad (4.9) \quad [26]$$

By replacing the slopes b (listed in Table 4-2 into) Eq.(4.9), U_0 can be calculated for the analysed samples. The values of the pinning potential are listed in Table 4-3. It can be seen that the average pinning potentials in the multilayer films are much higher than in pure thin YBCO films, leading to a lower dissipation caused by thermally activated flux creep in Ag/YBCO multilayer films with artificial pinning centres induced by Ag nano-dots, and, consequently, to a higher in-field J_c in comparison with pure YBCO films.

Table 4-3 Pinning potential calculated from experimental data in DC fields of 3, 4 and 5 T of 3 multilayer samples, in K,(k_B = 1)

Samples	U_0(K)			*b*		
	3 T	4 T	5 T	3 T	4 T	5 T
(15Ag/1.5 μm YBCO)x2	629	464	211	0.1	0.2	0.6
(15Ag/1.5 μm YBCO)x3	NA	429	191	NA	0.2	0.7
(15Ag/450 nm YBCO)x5	644	413	169	0.1	0.2	0.8
YBCO 0.96 μm	360	248	142	0.2	0.5	1.2

4.4.3 Pinning force and pinning mechanisms in Ag/YBCO films

Apart from critical current density, from DC magnetization loops one can also determine the bulk (total) pinning force $F_p = B \times J_c$. In order to understand pinning mechanisms, the Dew-Hughes [27] model of flux pinning mechanisms in type II superconductors was used to

analyze our data for pure YBCO films and Ag/YBCO multilayer films. According to Dew-Hughes, the pinning centres are of two types: "$\Delta\kappa$ pinning" due to small differences in κ, arising from changes in the normal state resistivity due to composition fluctuations, or non-uniform distributions of dislocations and "normal pinning" due to non-superconducting particles, which may be normal metal, insulator or void. In addition, pinning centres can be point pins, surface pins and volume pins, in relation with the number of their respective dimensions (1,2 or 3) that are large compared with the inter-flux-line spacing d $\left(=1.07(\Phi_0/B)^{0.5}\right)$ where Φ_0 denotes the flux quanta.

In Dew-Hughes model, the field dependence of the normalised pinning force F is $F_p/F_{pmax} = h^p(1\text{-}h^q)$ where $h = B/B_{irr}$, while p and q values depend on the types of pinning centres. The values of p and q for the pinning centres of interest are given by Dew-Hughes, and will be addressed later. When there are several types of pinning centres in the same sample, the normalised pinning force can be described by:

$$F = Ah^{p1}(1-h)^{q1} + Bh^{p2}(1-h)^{q2} + Ch^{p3}(1-h)^{q3} + \cdots \quad (4.10)$$

In Dew-Hughes original paper, 6 terms were taken into account; in the following, only 3 terms (at most) were needed for fitting our data.

Figure 4-79 shows the field dependence of the normalized pinning force at 77.3 K, of a 2 μm-thick pure YBCO film, from $J_c(H)$ data of the same film as in Figure 4-61. The normalising irreversibility field of the x axis (B_{irr}) is determined by using the criterion of 10^3 A/cm^3 which, in this case, extrapolated to B_{irr} = 3.75 T. The y axis (pinning force) is normalised dividing $F_p(h)$ by its maximum value F_p^{max}.

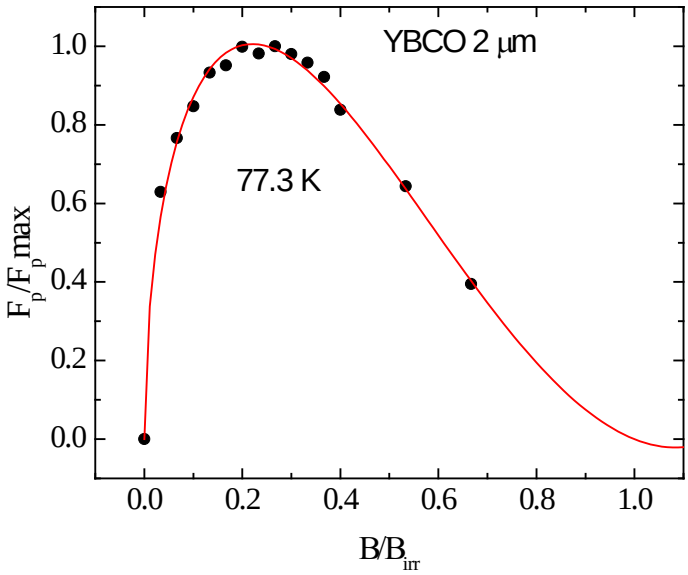

Figure 4-79 Field dependence of the normalized pinning force at 77.3 K, of a 2 μm-thick pure YBCO film., The red solid line is the fitting curve with Eq.(4.10), using two terms, with $p1 = 0.5$, $q1 = 2$, and $p2 = 1$, $q2 = 1$, and A and B free parameters.

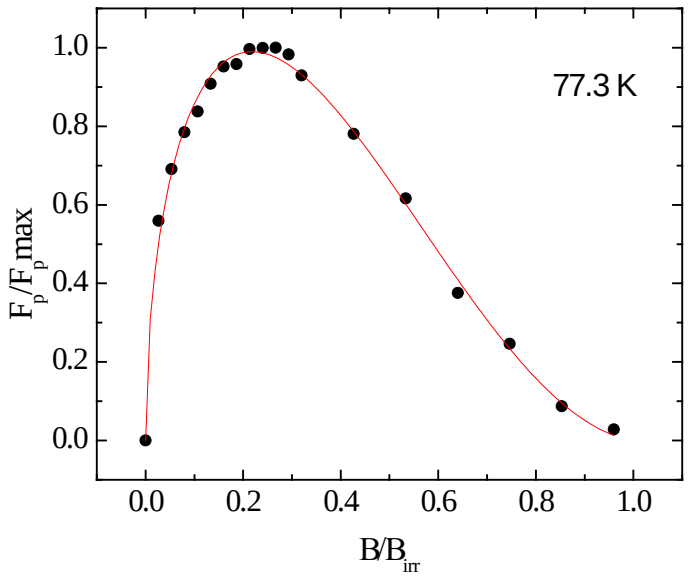

Figure 4-80 Field dependence of the normalised pinning force at 77.3 K of (15Ag/1.5μmYBCO)x2 film. The red solid line is the fitting curve with Eq.(4.10), using three terms with $p1 = 0.5$, $q1 = 2$; $p2 = 1$, $q2 = 2$; and $p3 = 1.5$ and $q3 = 1$.

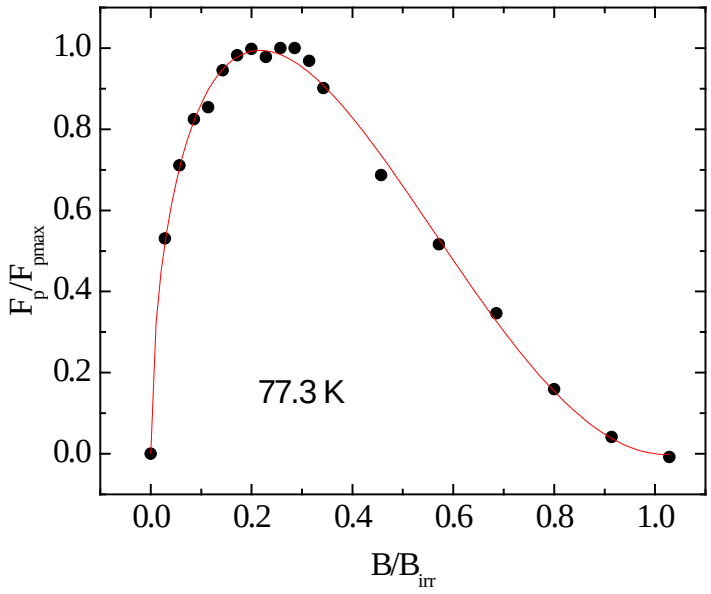

Figure 4-81 Field dependence of the normalised pinning force at 77.3 K of (15Ag/450nmYBCO)x5 film. The red solid line is the fitting curve with Eq.(4.10), using three terms with $p1 = 0.5$, $q1 = 2$; $p2 = 1$, $q2 = 2$; and $p3 = 1.5$ and $q3 = 1$.

The experimental data are very well fitted with Eq.(4.10) with $A = 3.23$, $B = 0.50$, $C = 0$ (negligible third term), $p1 = 0.5$, $q1 = 2$, $p2 = 1$ and $q2 = 1$. The exponents p and q that allowed a good fit imply that, according to the classification in [27], the main pinning centres in the pure YBCO film are normal-core surface pins ($p = 0.5$, $q = 2$) (with 87% contribution to the pinning force), with 13% contribution due to Δκ- core volume ($p = 1$, $q = 1$).

Figure 4-80 shows the field dependence of the normalized pinning force at 77.3 K of (15Ag/1.5 μmYBCO)x2, which could be well fitted using three terms.

Like the case of pure YBCO, in the (15Ag/1.5 μmYBCO)x2 multi-layer the largest majority of pinning centres (of about 80%) is the normal-core surface with $A = 3.15$, $p1 = 0.5$ and $q1 = 2$. In this multilayer film, two more types of pinning centres are found with $B = 0.57$, $p2 = 1$ and $q2 = 2$ which is normal-core point, and with $C = 0.19$, $p3 = 1.5$ and $q3 = 1$ which is

Δκ- core surface. The contributions of the normal-core point and the Δκ- core surface in the total of pinning centres are about 15% and 5%, respectively.

Figure 4-82 shows the field dependence of the normalized pinning force at 77.3 K of (15Ag/450nmYBCO)x5. The data of the 5-layered film could also be well described using three terms, and, as expected, the same types of pinning centres were found, with a very little difference in the contributions of the normal-core surface, the normal-core point and the Δκ- core surface pinning centres: 81%, 15% and 4%, respectively.

From this analysis, the conclusion is that the largest numbers of pinning centres are two-dimensional (surface) normal-core pinning, most likely dislocations and pinning centres related to inter-grain boundaries, in all samples. In pure YBCO, additional 3D-like Δκ- core pinning centres. By adding Ag nanoparticles, more pinning centres have been created, most of them the same type as the major part of pinning centres in pure YBCO films (2D normal-core dislocations). In addition, instead of a minor contribution of Δκ- core volume pinning, we found minor contributions due to normal-core point and Δκ- core surface pinning centres, of about 15% and 5%, respectively.

Table 4-4 summarizes the types of pinning centres and their contributions to the normalized pinning force in the three samples analysed above.

Table 4-4 Exponents, types of pinning centres and their contribution of the three samples described in the figures above

Samples	$p1$	$q1$	Types of pinning; %	$p2$	$q2$	Types of pinning; %	$p3$	$q3$	Type of pinning; %
2 μm YBCO	0.5	2	normal-surface 87%	1	1	Δκ-volume 13%	-	-	-
(15Ag/1.5 μmYBCO)x2	0.5	2	normal-surface 80%	1	2	normal-point 15%	1.5	1	Δκ– surface 5%
(15Ag/450nmYBCO)x5	0.5	2	normal-surface 81%	1	2	normal-point 15%	1.5	1	Δκ– surface 4%

4.4.4 Angle-dependent transport measurements of critical current density of Ag/YBCO multilayer films

4.4.4.1 Transport measurements of (15Ag/450nm YBCO)x1

The most accurate measurement of the critical current density, which does not imply any theoretical model like in the case of magnetic measurements, is the transport measurement, which is a contact measurement. For this method, a narrow bridge needs to be etched, as described in Chapter 3, and contacts need to be prepared and connected to a current source and a digital voltmeter. In our case, the transport measurements are integrated in the Quantum Design PPMS with the transport option set. Moreover, by transport measurement, one can determine J_c at different angles θ between the film surface and applied magnetic fields. Critical current density is automatically determined by the PPMS software from the current-

voltage characteristics, using usually a voltage criterion of 1 μV/cm. For example, the angle dependence of J_c in an applied field of 1 T, at various temperatures from 77.3 K to 83 K, for a substrate-decorated film (15Ag/450nmYBCO)x1 is shown in Figure 4-83 In these rotating scans, angles $\theta = 0^o$, 180^o and 360^o correspond to the direction of magnetic field along the c-axis of the sample while the angles at $\theta = 90^o$ and 270^o corresponding to the direction of magnetic field along the ab-plane of the sample (film surface). It can be seen that the values of J_c along the ab-plane are maximum at all temperatures. The temperature dependence of J_c in 1 T, along the c-axis and in the ab-plane, is shown in Figure 4-84. While the temperature dependence of their ratio, J_c^{ab}/J_c^{c}, is shown in Figure 4-85. It can be seen that at temperatures higher than 84 K, this ratio is close to 1.

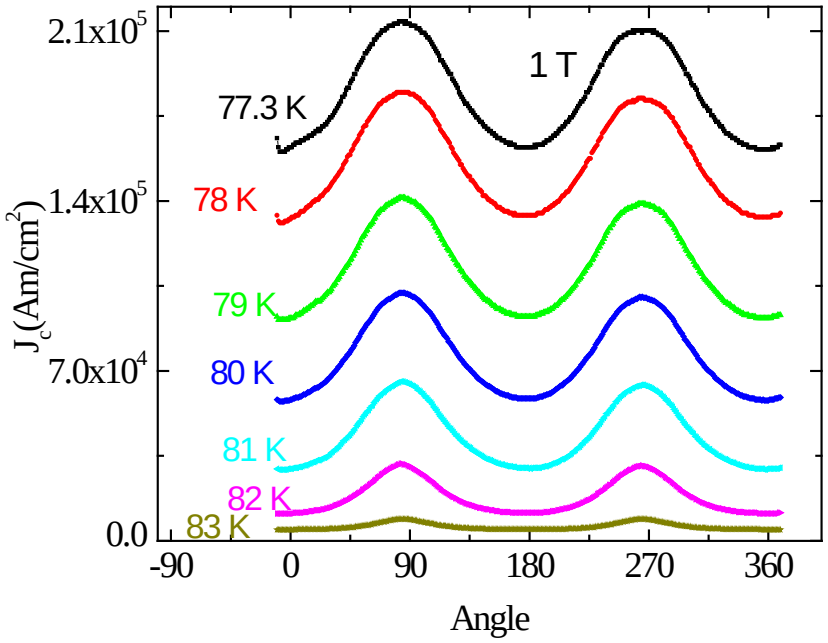

Figure 4-83 Angle-dependent critical current density of (15Ag/ 450 nmYBCO)x1 in 1 T and at different temperatures from 77.3 to 83 K.

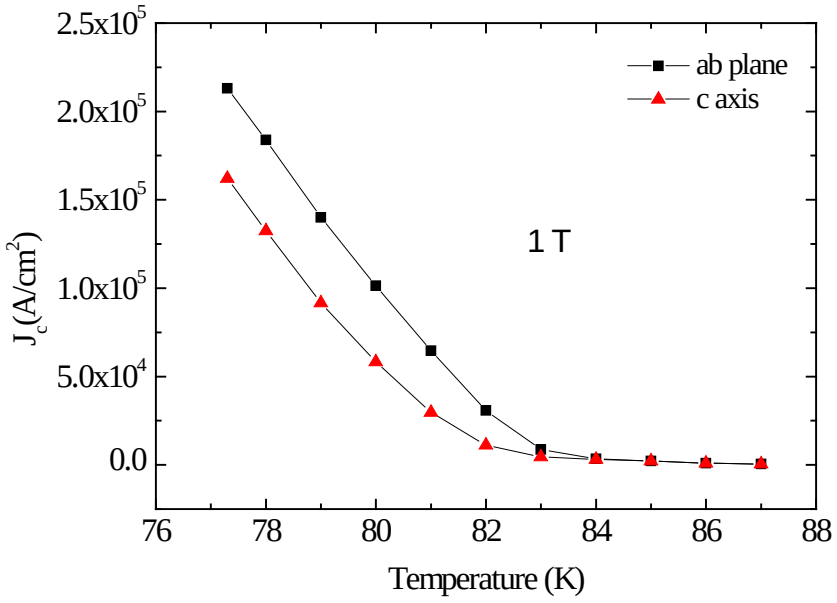

Figure 4-84 Temperature dependence of J_c^{ab} and J_c^{c} in 1T for the same sample

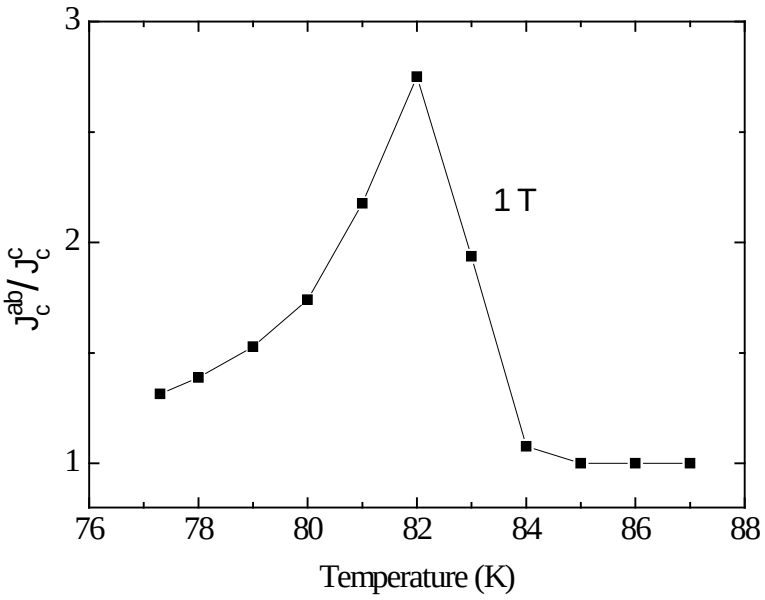

Figure 4-85 Temperature dependence of the ratio J_c^{ab}/J_c^{c} in 1 T of the same sample

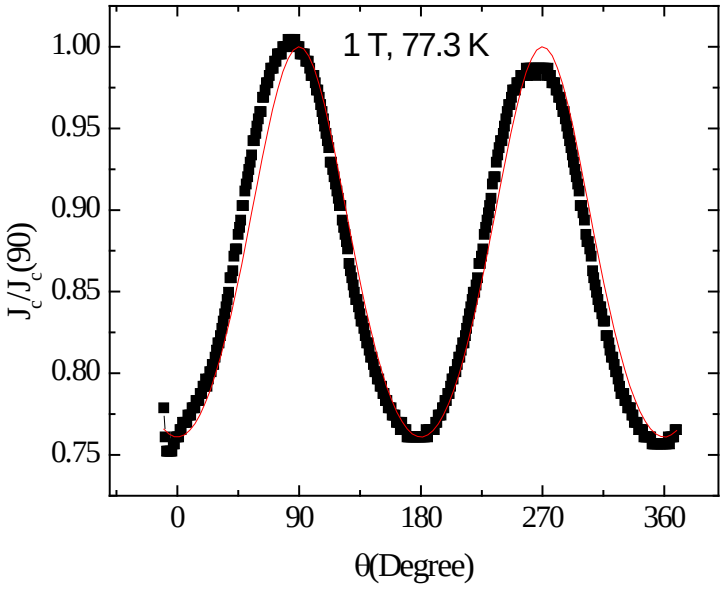

Figure 4-86 Angle dependence of normalised critical current density $J_c/J_c(90°)$ of the same film, at 77.3 K and 1 T. The full red line is the fit with the theoretical dependence in Blatter scaling approach, with fitting parameter $\gamma = 1.6$.

For this sample, the $J_c(\theta)$ shown in Figure 4-83 are very well fitted by Blatter scaling approach [28] as mentioned in Chapter 2, $J_c(\theta)/J_c(90) = (\sin^2\theta + \gamma^2\cos 2\theta)^{-1/2}$, where γ is the anisotropy of critical current density, which, for samples with artificially-induced pinning centres, is not the same with the effective mass anisotropy in the Ginzburg-Landau theory. One example is shown in Figure 4-86 for 77.3 K, where the full red line is the one-parameter fit (γ = 1.6) with the Blatter formula. The angle-dependent J_c of this sample (15Ag/450nmYBCO)x1 shows no secondary peak along the c-axis indicating that the majority of artificially-induced defects are not c-axis extended pins.

4.4.4.2 Transport measurements of (15Ag/450 nmYBCO)x10 film

J_c of the (15Ag/450nmYBCO)x10 quasi-multilayer film as a function of θ, in several fields at a temperature of 82 K, is plotted in Figure 4-87. Overall, the curves in the figure look quite similar to those of the YBCO grown on Ag-decorated substrate shown in Figure 4-83.

However, a closer look at the curves in high fields from 3 to 6 T show some small additional peaks along the c-axis at 0 ^{o} and 180^o, which were not observed in Figure 4-83 for single layer film in 1 T. The first conclusion that can be drawn is that angular dependence of J_c of multilayer films can give additional information on the nature of pinning centres.

In Figure 4-88 is shown the field dependence of J_c^{ab} and J_c^{c} at 82 K. It can be seen that $J_c^{ab} > J_c^{c}$. As can be deduced from the figure, the ratio between J_c^{ab} and J_c^{c} depends on the value of the field.

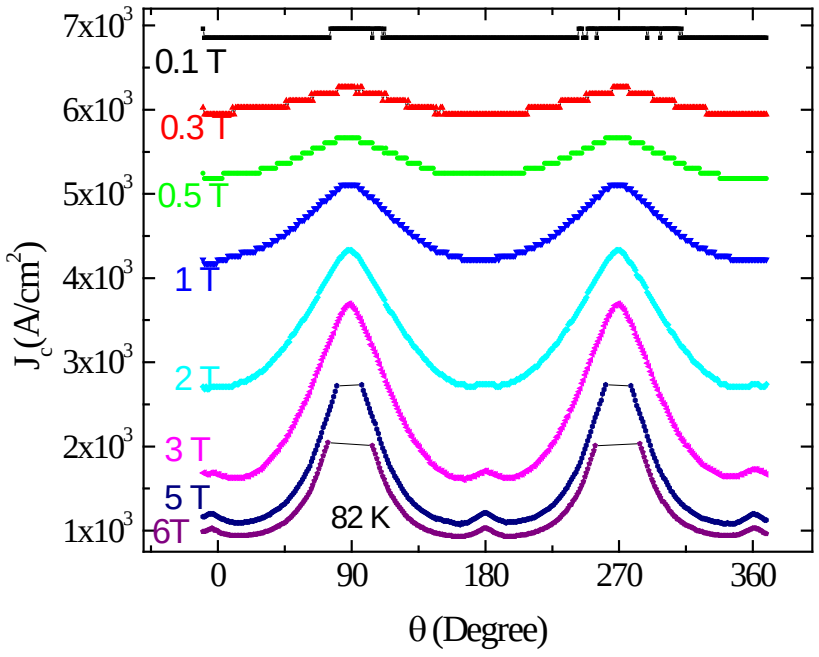

Figure 4-87 Angular dependence of J_c at several fields at T = 82 K for (15Ag/450 nm YBCO) x 10 multilayer film, applied fields are legend on the left hand side of each curve.

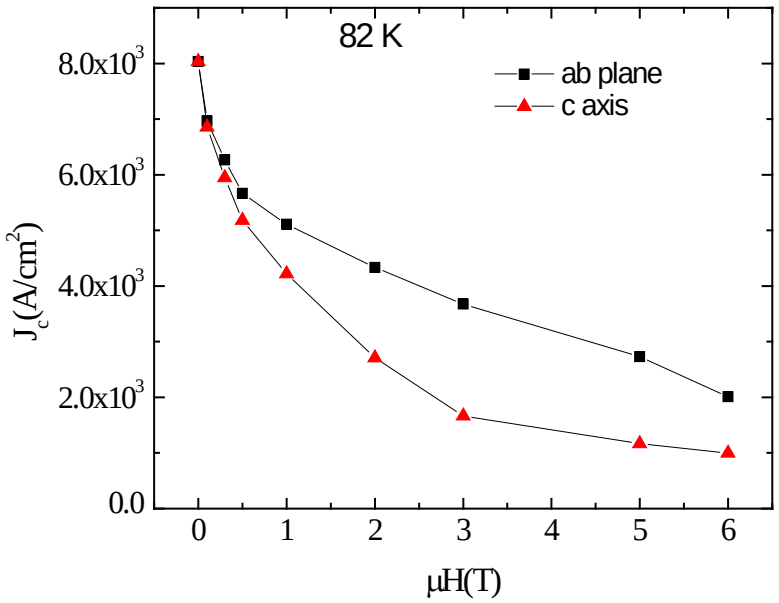

Figure 4-88 Field dependence of J_c along the c-axis (red triangles) and the ab-plane (black square) at 82 K of (15Ag/450 nmYBCO)x10 film.

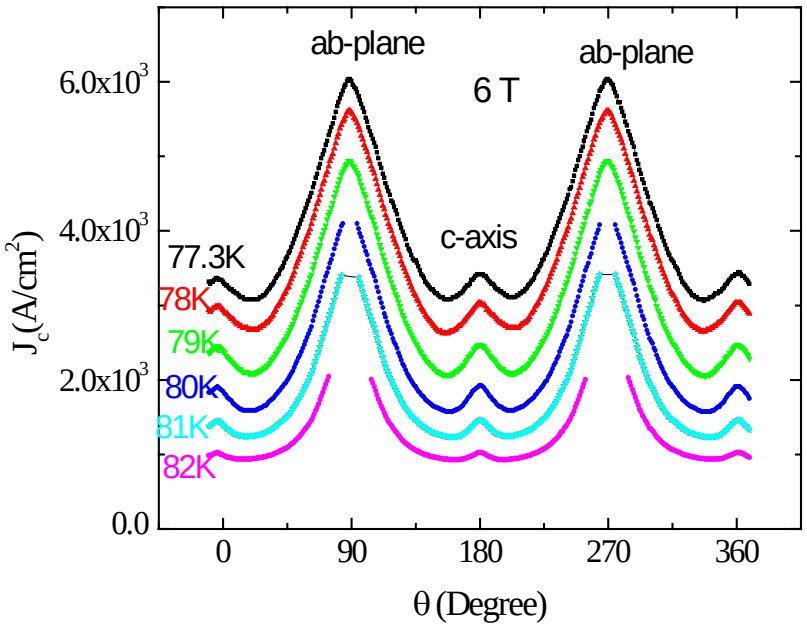

Figure 4-89 Angular dependence of J_c at several temperatures in 6 T for (15Ag/450nmYBCO)x10 multilayer film.

In high field of 6T, the secondary peak along the c-axis appears at all temperatures from 77.3 K to 82 K, as shown in Figure 4-89. This secondary peak is attributed to c-axis correlated extended defects created by Ag nanodots.

The isotropic or anisotropic nature of pinning centres created by Ag quasi-layers can be clarified by scaling the angle dependence of critical current density $J_c(\theta,H)$. One of the approaches uses direct Blatter's et al. scaling based on the anisotropic Ginzburg-Landau theory. In this approach, which was first proposed by Civale et al. [29], the isotropic and anisotropic pinning centres can be identified from a plot of J_c versus effective magnetic field $H_{eff} = \varepsilon(\theta)H$, where $\varepsilon^2(\theta) = \cos^2\theta + \gamma^{-2}\sin^2\theta$, γ is the anisotropy factor, (γ = 5-7 for YBCO single crystal), and θ is the angle between the magnetic field and *c*-axis of YBCO. However, later it was shown that, in YBCO films with artificial pinning centres, the parameter γ in the scaling is not the effective mass anisotropy.

The plot of $J_c(\theta)$ and the rescaled plot $J_c(H_{eff})$ of (15Ag/450nmYBCO)x10 multilayer film at 77.3 K and in 6 T are shown in Figure 4-90. The points A and B help to visualise how the various angular regions are transformed by the rescaling. In Figure 4-90 a the full line represent the one-parameter fit with Blatter's formula for the parameter $\gamma = 3$. The plot is repeated for every field for several parameters γ and the rescaled curves are plotted in the same graph, until the right parameter γ is found in which all data collapse onto a single smooth decreasing curve, except for those points corresponding to the angular regions close to *H*//*ab* (*B*) and *H*//*c* (*A*) for each field, as shown in Figure 4-91. We find that by using the effective mass anisotropy γ=7, the curves do not collapse (Figure 4-91 a), while for γ = 3 (Figure 4-91 b) the best collapse of the curves is achieved. This value is smaller than that in the pure YBCO film.

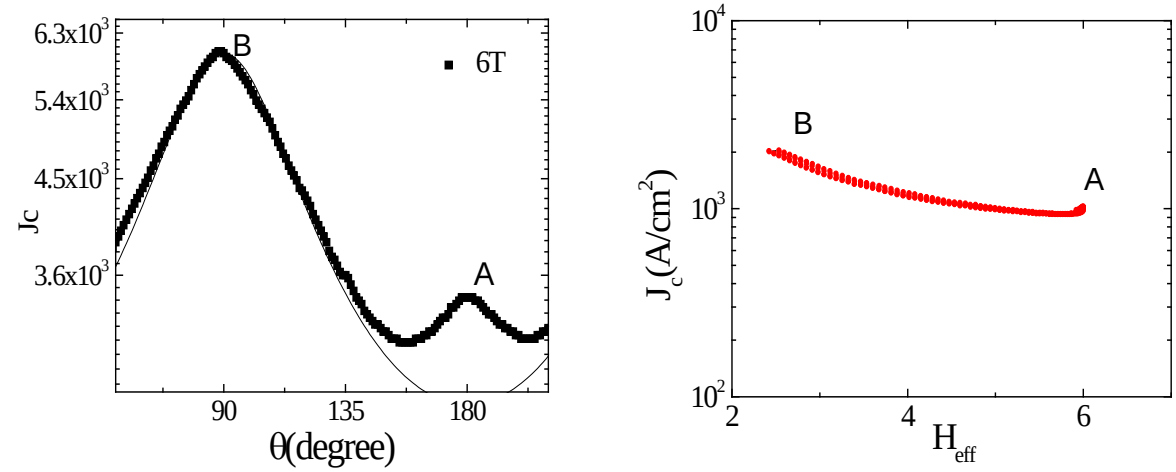

Figure 4-90 Angular dependence of J_c of (15Ag/450nmYBCO)x10 multilayer film at 77.3 K and in 6 T, A and B indicate the peaks for $H//c$ and ab, respectively (a); and J_c as a function of H_{eff} for the same data, with $\gamma = 3$ used to calculate H_{eff}

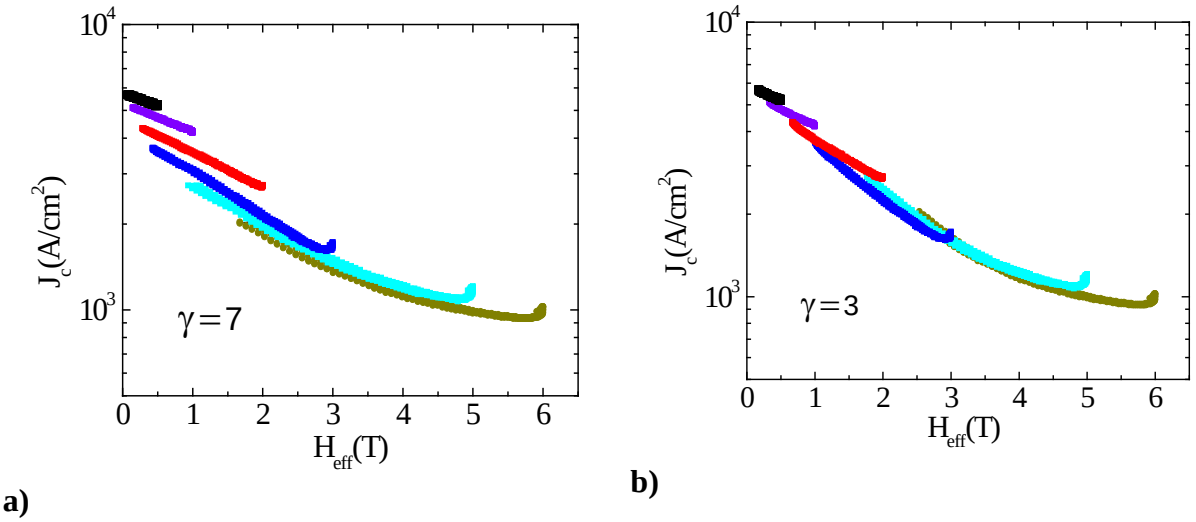

Figure 4-91 J_c as a function of H_{eff} for all applied fields, with H_{eff} calculated using $\gamma = 7$ (effective mass anisotropy of YBCO) the data $J_c(H_{eff})$ do not collapse in a single curve (a), while with H_{eff} calculated using $\gamma = 3$, the data of $J_c(H_{eff})$ collapsed quite well in a single curve (b).

The peak at $H//ab$ represent the intrinsic pinning contribution, which arises mainly from the modulation of the superconducting order parameter along the *c* direction, as *a*

consequence of the layered crystallographic structure and of course, it can also include the contribution of other correlated structures parallel to the ab-planes. The weaker peak at *H*//*c* is due to correlated disorder along the *c-axis*, such as twin boundaries, linear and columnar defect.

4.4.4.3 Transport measurements of J_c of (15Ag/1.5 μmYBCO)x1

Similar features in angle-dependent transport measurements are found also for the film grown on a decorated substrate, (15Ag/1.5μmYBCO)x1. Figure 4-92 show such data at 77.3 K, in applied fields between 3 and 6 T.

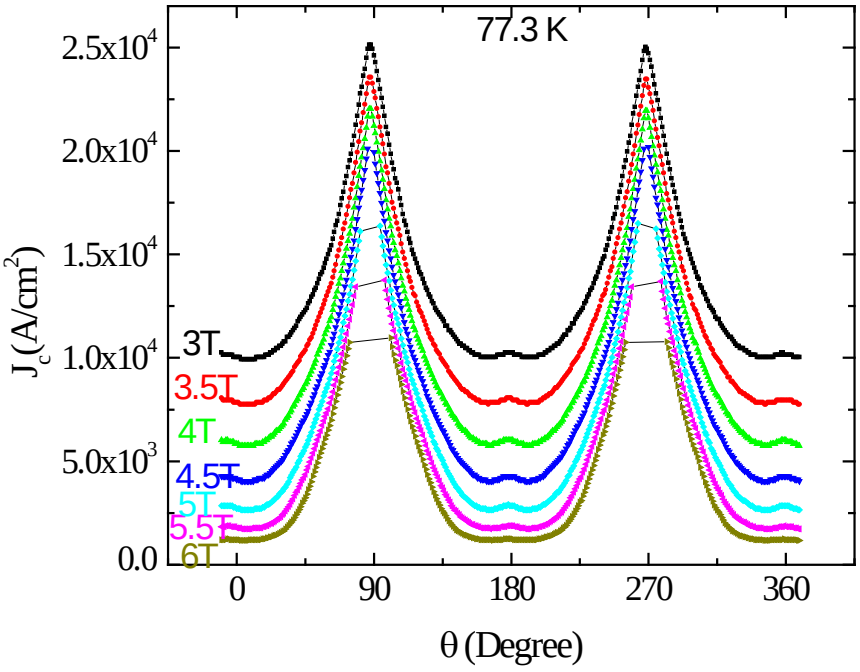

Figure 4-92 Angular dependence of J_c for (15Ag/1.5μmYBCO) sample, at temperature of 77.3 K and in applied fields from 3 T to 6 T as indicated on the left hand side of each curve

Again, $J_c(\theta)$ curves show a dominant peak at *H*//*ab* and a secondary weak peak at *H*//*c*. However, at 77.3 K, the weak peak along the c-axis appears only for applied fields from 3 T and disappears at 6 T. The same Blatter rescaling procedure was used for the collapse of

$J_c(H_{eff})$ curves. The best collapse of rescaled data was obtained, for this sample, by using the H_{eff} given by $\gamma = 3.5$, as shown in Figure 4-93. This value is a bit higher than the value $\gamma = 3$ which was obtained for the multilayered film described in the previous section.

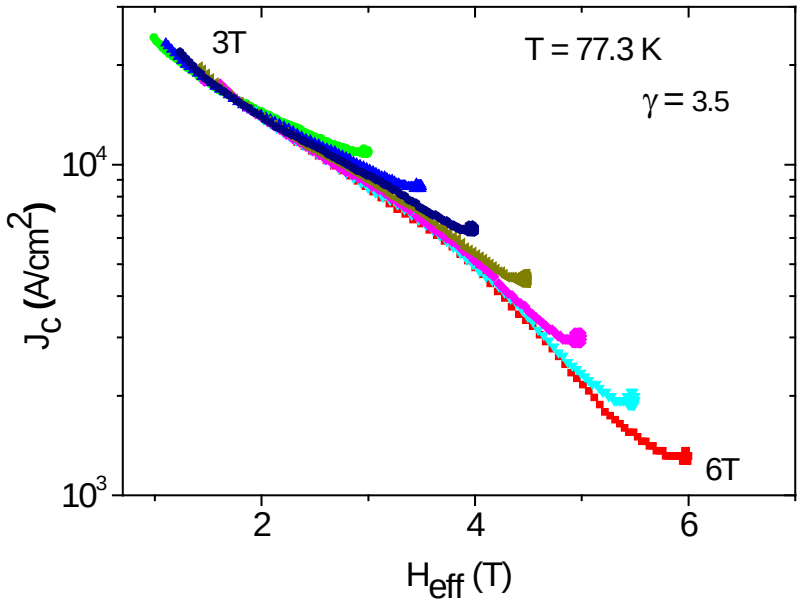

Figure 4-93 J_c as a function of H_{eff} for all applied fields, with H_{eff} calculated using $\gamma = 3.5$, which gave the best collapse.

Figure 4-94 shows the field dependence of J_c^{ab} and J_c^{c} of the (15Ag/1.5μmYBCO) film at 77.3 K, as resulted from transport measurements. The curves are very well described by exponential decay $y = ae^{\frac{x}{t}}$, where y is either J_c^{ab} or J_c^{c}, x is the field, and, as resulted from the fit, t = -2.15 for the J_c along the *c-axis* and t = -4.55 for the J_c along the ab-plane as shown in Figure 4-94.

Figure 4-95 and Figure 4-96 show the angular dependence of J_c of this sample in low fields and higher temperatures of 80 K and 85 K, respectively. The applied fields are shown on the left hand side of each figure.

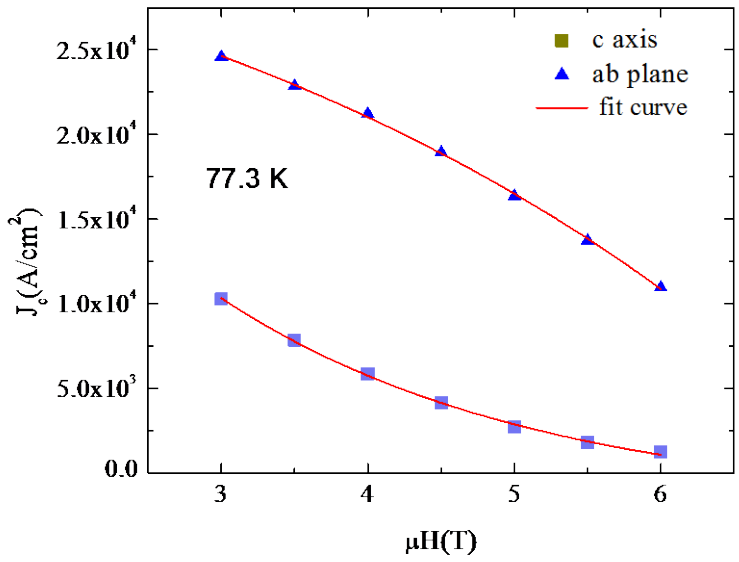

Figure 4-94 Field dependence of J_c^{ab} and J_c^{c} of the (15Ag/1.5μm YBCO) sample determined from transport measurement, solid lines represent fits with the exponential decay function.

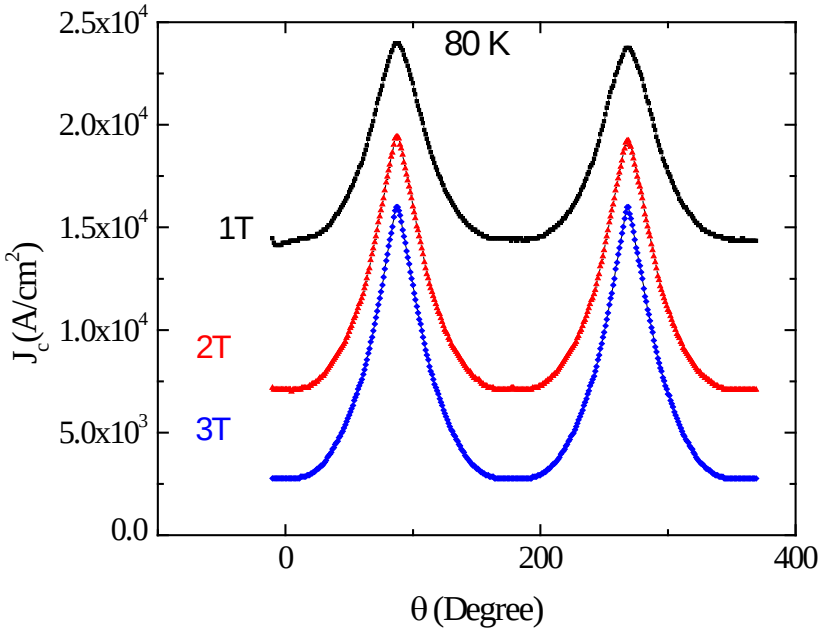

Figure 4-95 Angular dependence of J_c of the same sample at 80 K and in applied fields of 1, 2 and 3 T.

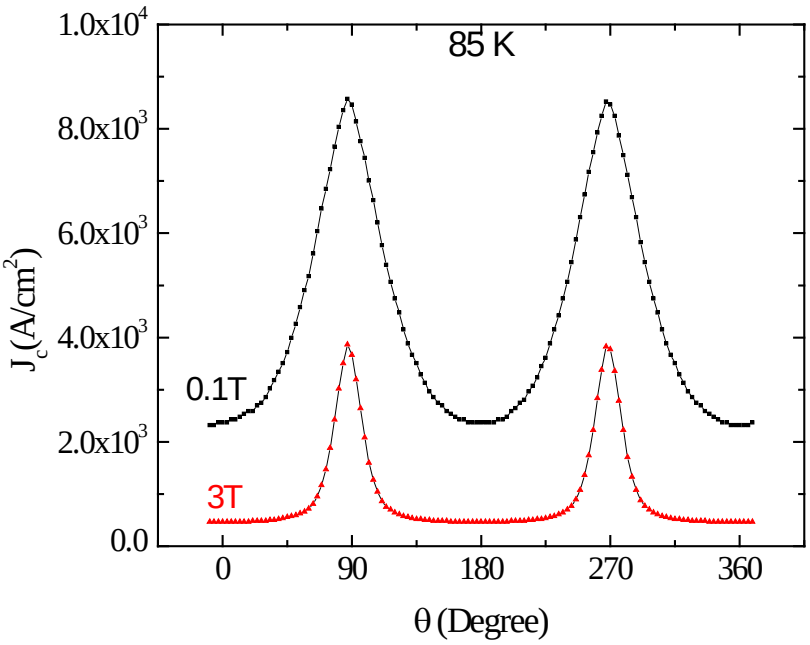

Figure 4-96 Angular dependence of J_c of the same sample at 85 K and in applied fields of 0.1 and 3 T.

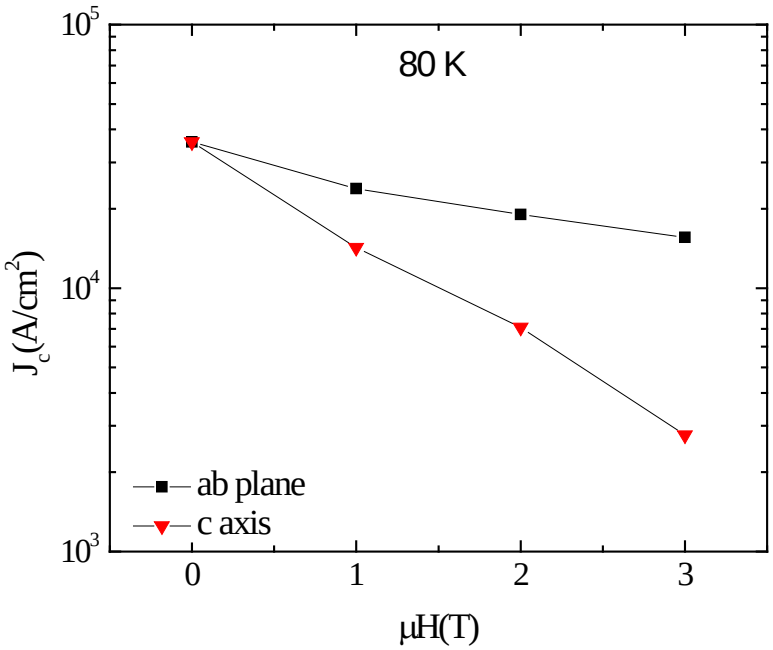

Figure 4-97 Field dependence of J_c of (15Ag/1.5μm YBCO) sample at *H//ab* plane (red triangles) and *H//c-axis* (black squares) at 77.3 K measured by transport measurement.

Due to the limitation of the PPMS we could not measure the angular dependence of J_c of the film at low field and low temperature (77.3 K), where the critical current densities are too high. No evidence of the peak along the c-axis is observed. This implies that the c-axis extended defects due to Ag nanoparticles have a significant effect on the angle-dependence of critical current in certain limited ranges of temperature and field. Figure 4-97 shows the field dependence of J_c^{ab} and J_c^{c} of the same film at 80 K.

4.4.5 Microstructure of quasi-multilayer films

4.4.5.1 X-ray diffraction pattern of Ag/YBCO multilayers

Figure 4-98 shows the X-ray diffraction pattern of the (15Ag/450nmYBCO)x5 film in comparison with a pure 1.5 μm-thick YBCO film.

In thin YBCO films only (00*l*) peaks appear. However, as shown in Figure 4-98, in both 1.5 μm-thick pure YBCO and multilayer (15Ag/450nm YBCO)x5 film, apart from the (00*l*) peaks, the (103) peak is observed. However, the (103) peak (due to some grains with a different orientation) does not influence in a negative way the J_c of the film; as shown in section 4.4.2, the J_c of the multilayer is higher than that of pure YBCO.

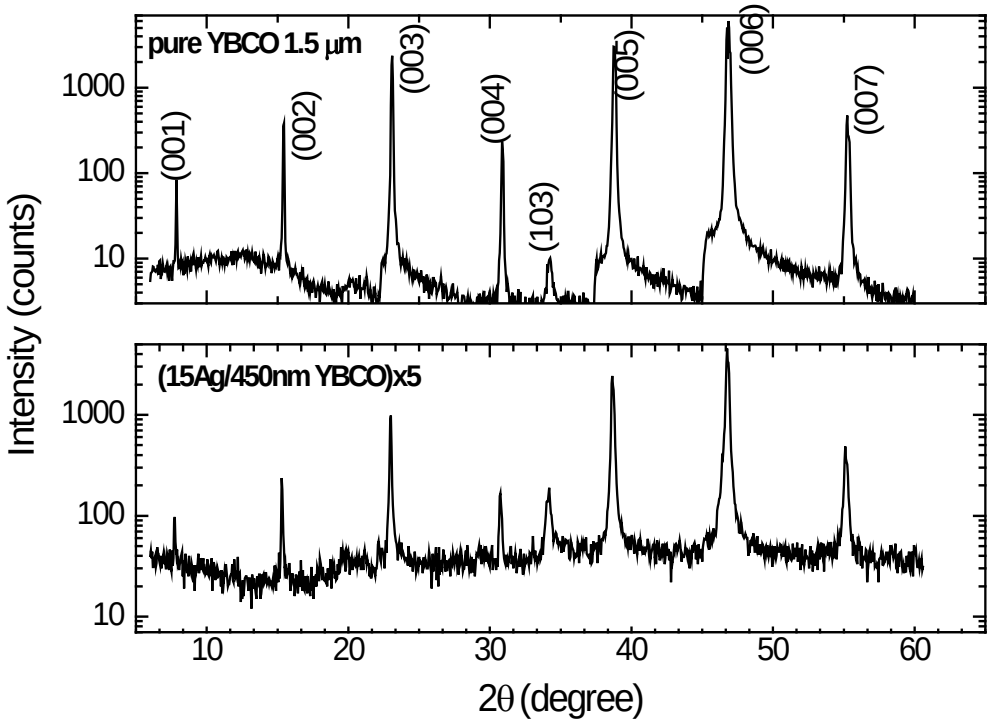

Figure 4-98 XRD of multilayer film (15Ag/450nm YBCO)x5 in comparison with 1.5 μm thick YBCO film.

4.4.5.2 AFM images of Ag/YBCO multilayer

Figure 4-99 and Figure 4-100 show AFM images of the (15Ag/450nmYBCO)x5 and (15Ag/450nmYBCO)x10 quasi-multilayers, respectively.

Similar surface morphology as in the case of thin YBCO films and of YBCO films on Ag-decorated substrate is observed in these quasi-multilayers, with characteristic big islands of several hundred nanometres and pores. However, in these thick multilayer films, the pores almost disappeared, only a few of them can be seen.

The AFM image of the polished surface of the (15Ag/1.5μmYBCO)x2 film is shown in Figure 4-101

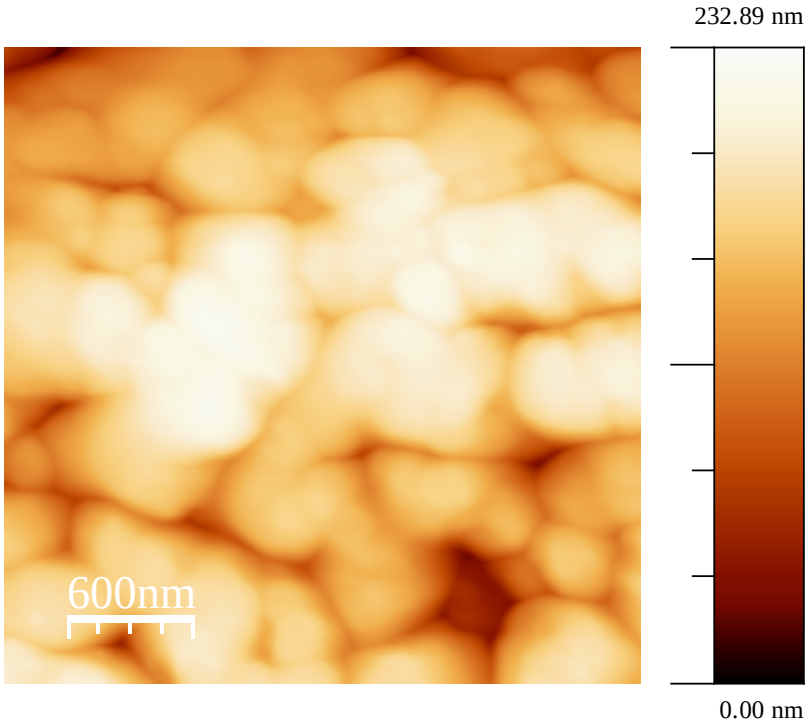

Figure 4-99 AFM image of (15Ag/450nmYBCO)x5 film showing a RMS roughness of about 36 nm.

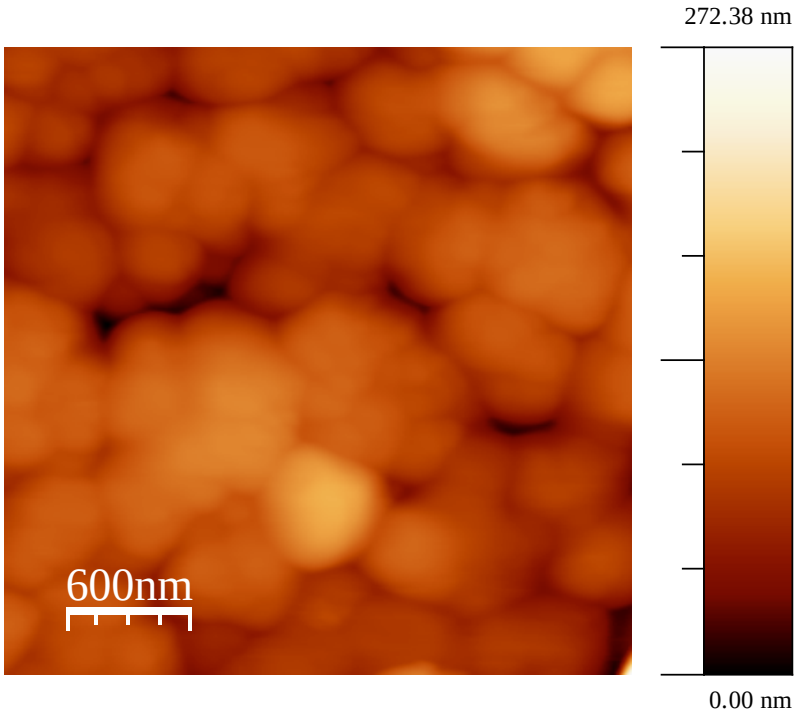

Figure 4-100 AFM image of (15Ag/450nm YBCO)x10 film showing a RMS roughness of about 26 nm.

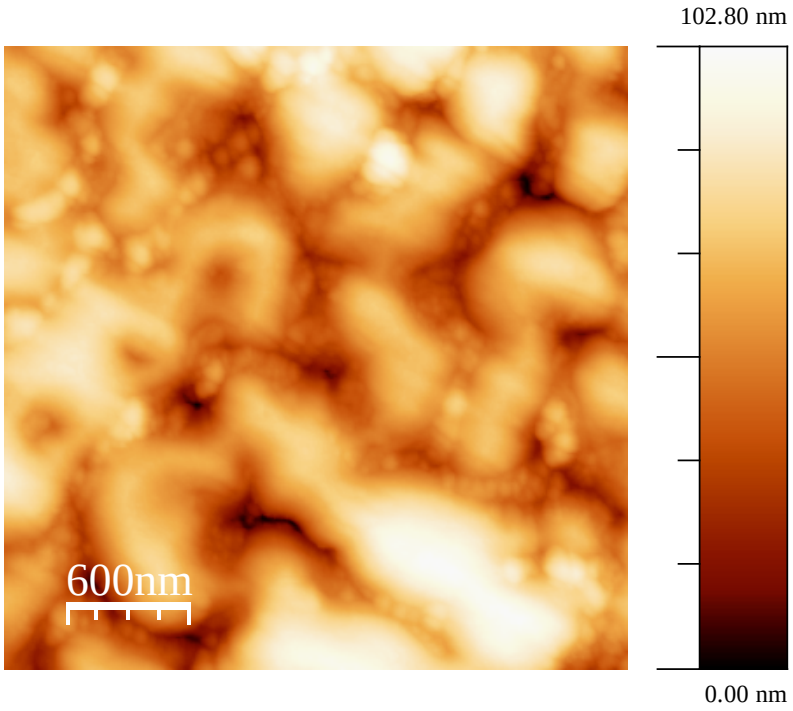

Figure 4-101 AFM image of (15Ag/1.5μm YBCO)x2 the polished surface

There is a difference from the image of the unpolished surface, namely the presence of nano precipitates, which were also observed in thin YBCO film as shown in section 4.3.4. The nano precipitates could be off-stoichiometry grains, such as Y-rich or Cu-rich phases, which were also observed in TEM images. However, it is important to note that these nano-grains of a slightly different phase do not necessarily decrease J_c. On the contrary, such nano-particles may be efficient pinning centres.

4.4.5.3 TEM images of Ag/YBCO multilayer

The (15Ag/1.5μmYBCO)x2 film is chosen for TEM investigations. Figure 4-102 shows a typical plan view TEM image of this film.

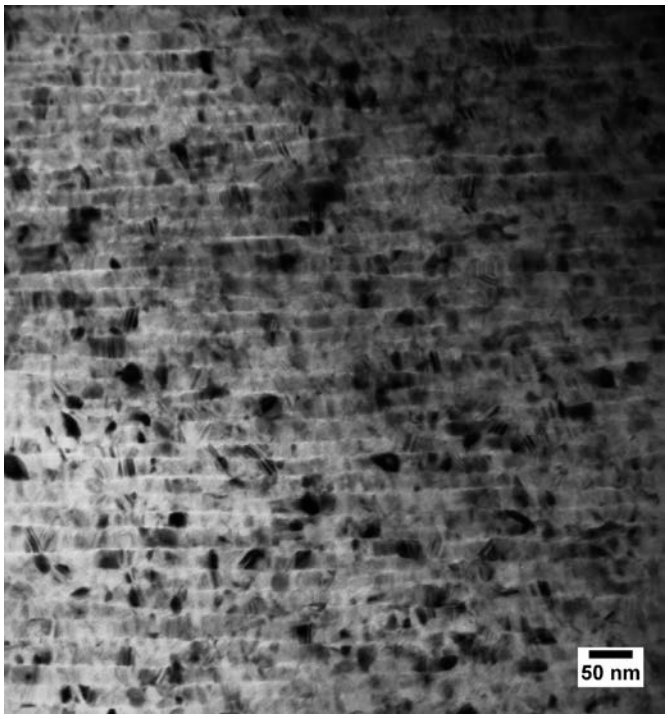

Figure 4-102 Plane view of (15Ag/1.5 μmYBCO)x2 film

A very high density of small precipitates is clearly visible, with diameters between 7-40 nm. Such precipitates were also observed by Solovyov et al.[30] and Yamasaki et al.[31], who claimed to be Y-rich phase (Y_2O_3). Together with twin boundaries, as shown in the figure, the nanoscale Y_2O_3 precipitates are candidates for strong flux pinning centres in the Ag/YBCO multilayer film.

The nano-precipitates are also observed in the low magnification cross-sectional TEM images as shown in Figure 4-103 and Figure 4-104, where some of the Y_2O_3 nano-particles are marked by arrows.

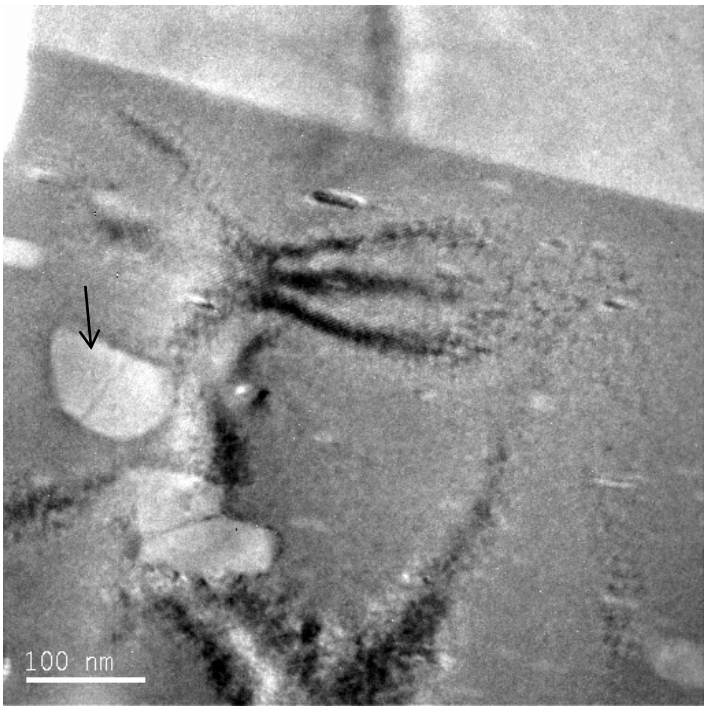

Figure 4-103 Low magnification cross-sectional TEM in the middle of the film. Arrow indicate a Y_2O_3 nano-particles.

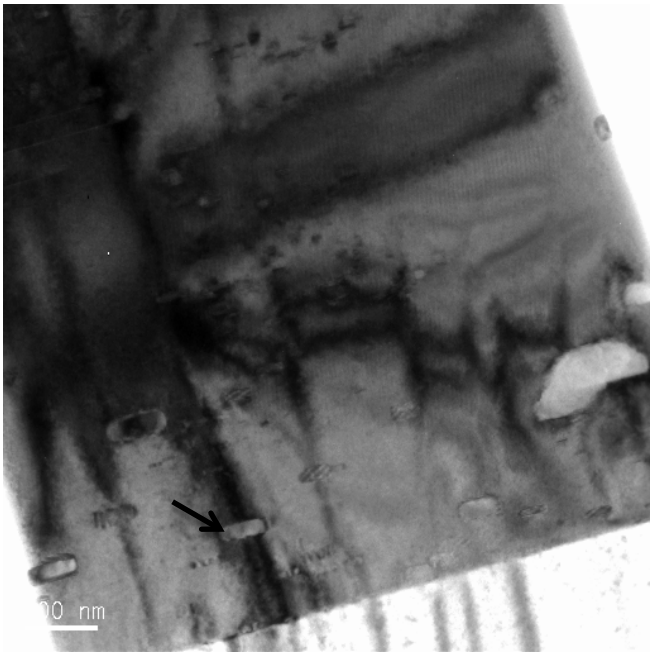

Figure 4-104 Low magnification cross-sectional TEM near the substrate. Arrow indicate a Y_2O_3 nano-particles.

A higher magnification cross-sectional TEM image is shown in Figure 4-105.

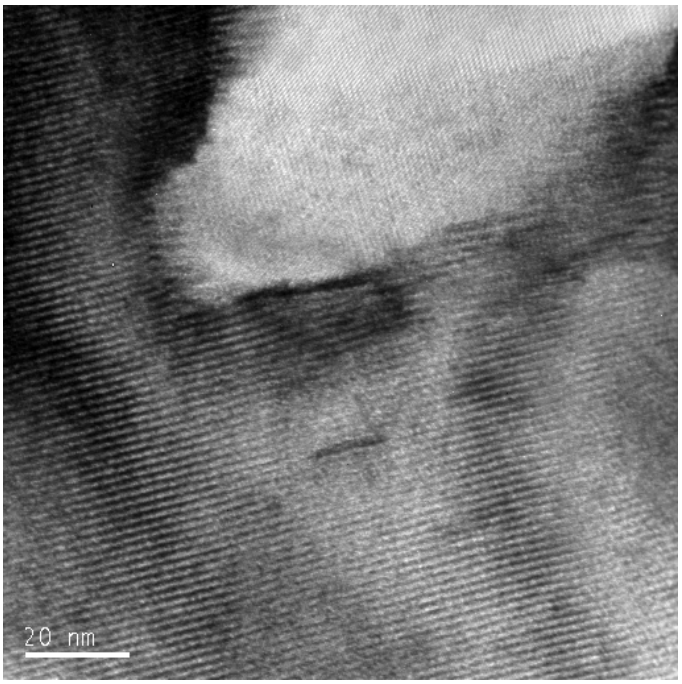

Figure 4-105 4-106 High magnification cross-sectional TEM in the film. A large Y_2O_3 particle with diameter of about 40 nm is clearly visible.

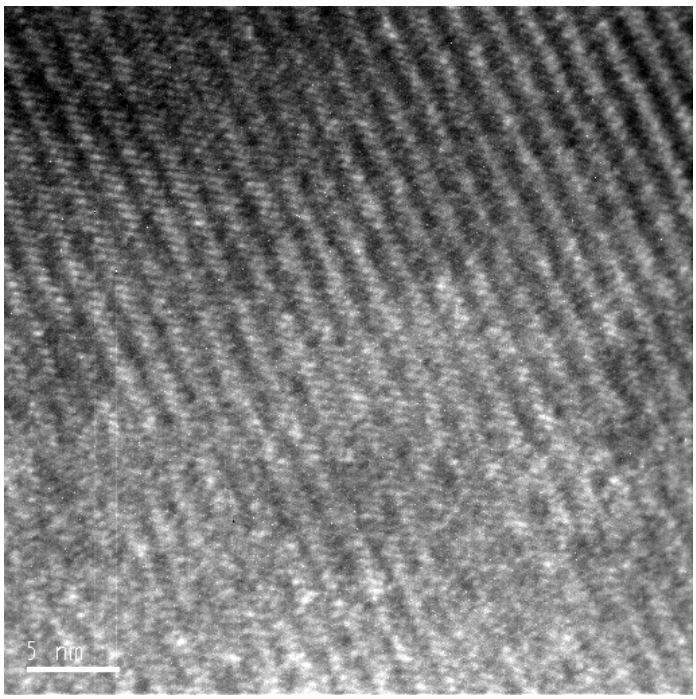

Figure 4-107 4-108 Higher magnification cross-sectional TEM in the film Cu-O_2 layered structure of YBCO can be clearly seen.

A clearly visible Y_2O_3 particle with diameter about 40 nm is observed in this figure. These nano-scale particles formed in YBCO matrix are in fact the strong, isotropic pinning centres in such Ag/YBCO quasi-multilayers, while the small secondary peak of J_c along the c-axis is most likely caused by nano columnar defects, due to the Ag-induced columnar growth of YBCO or other types of c-axis correlated defects, which can be seen in Figure 4-109 and Figure 4-114.

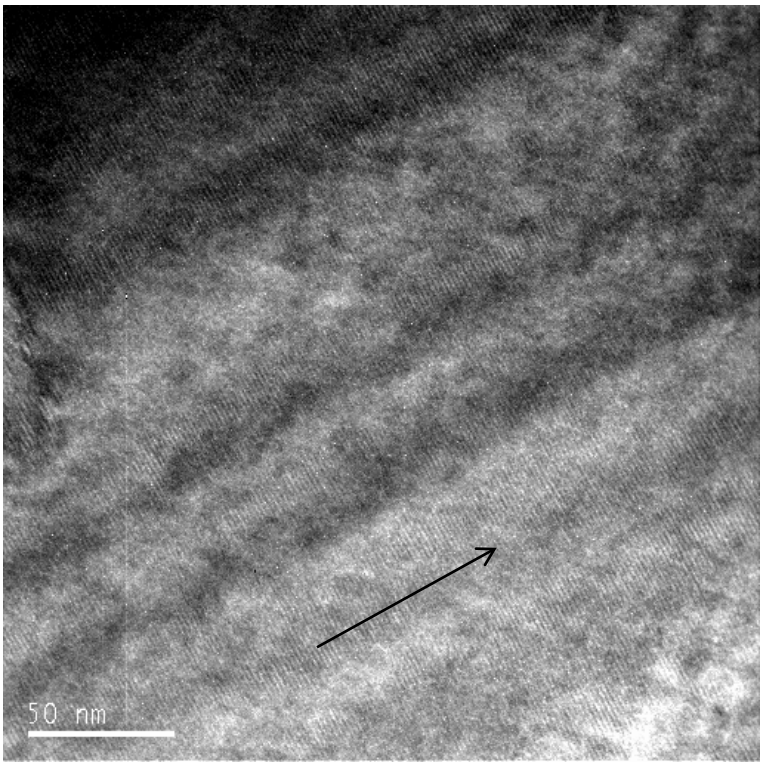

Figure 4-109 Cross-sectional TEM image, showing c-axis correlated defects, arrow indicates c-axis.

Figure 4-107 and Figure 4-110 show high resolution cross-sectional TEM images of the (Ag/YBCO) multilayer film. In both of them, a high density of stacking faults is observed.. Figure 4-110 is a TEM image at the boundary between the STO substrate and the YBCO film. No evidence of Ag nano-particles can be observed in this figure, indicating that the Ag nano-particles move from the substrate during the film growth or may not be present in this small viewed area.

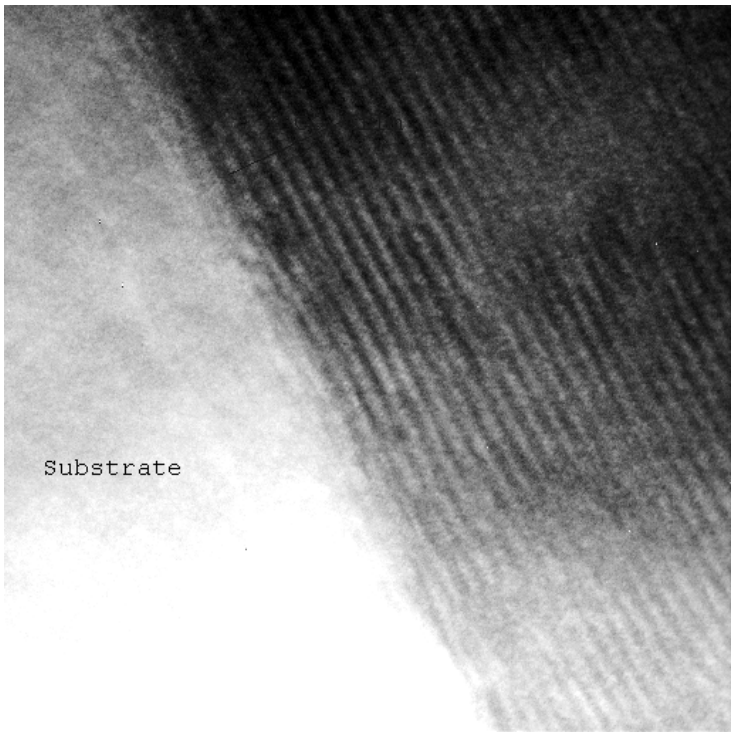

Figure 4-110 High-resolution cross-sectional TEM image of the substrate-film boundary, (with the same scale as of Figure 4-111).

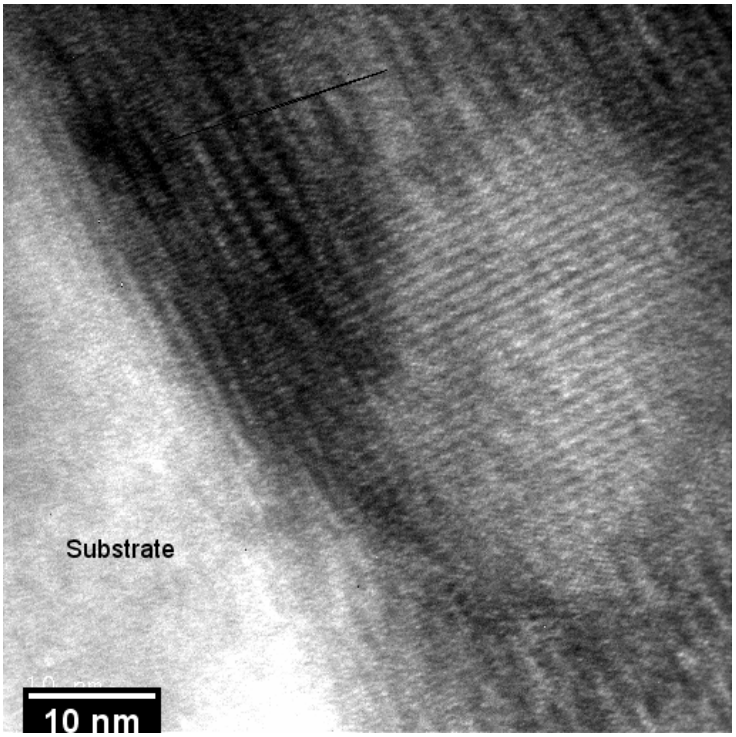

Figure 4-112 High-resolution cross-sectional TEM image of the substrate-film boundary. A nano-particle can be seen near the substrate

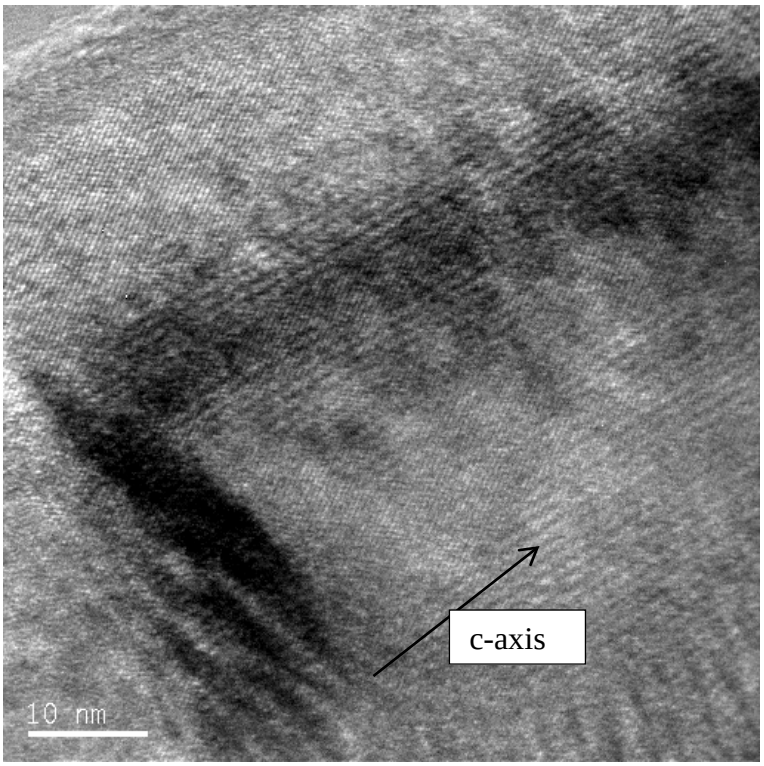

Figure 4-113 Mis-orientation in the boundary area

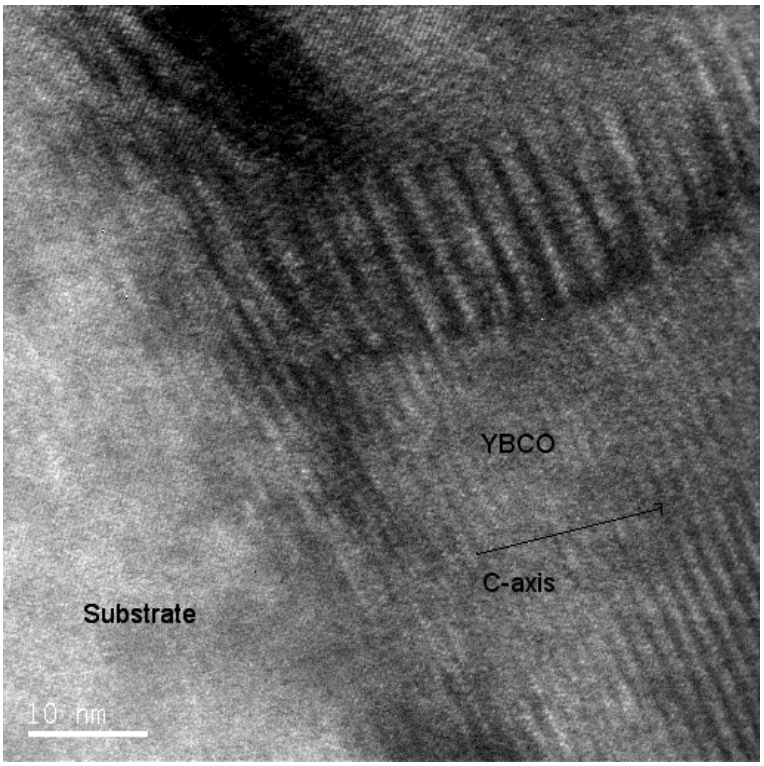

Figure 4-114 Columnar structure formed from the substrate

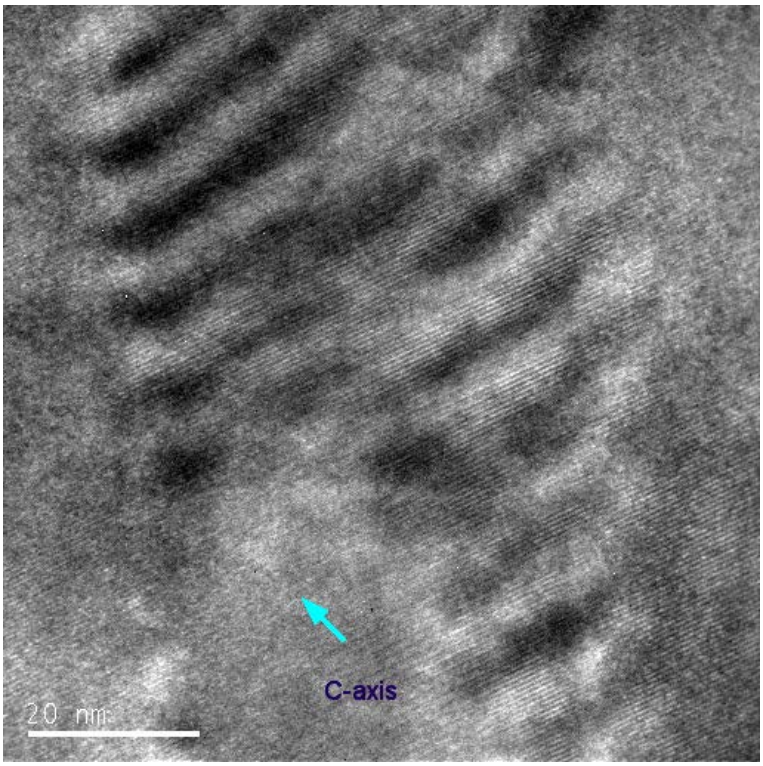

Figure 4-115 Columnar structure

A nano-particle of Y-rich phase or Y_2O_3 is also observed in the boundary area of the film (near the substrate) as shown in Figure 4-112.

Figure 4-113 shows another TEM cross section image of the boundary area between the STO substrate and Ag/YBCO film. In this area, one can see mis-orientations of the Cu-O planes which (the ab-plane), which may be caused by Ag nano-particles around this area.

Figure 4-114 shows clearly a columnar structure of YBCO growing from the STO substrate. This type of columnar defect was also recognised in recent publication in BZO-doped films as referred in Chapter 2. Higher resolution image of the columnar structure is shown in Figure 4-115.

Further chemical analysis of the Ag/YBCO multilayer film was done by scanning transmission electron microscopy (STEM) mapping as shown in Figure 4-116. The substrate

can be seen (Figure 4-116 a) in the bottom-left hand side of the image. Unfortunately, we are unable to detect any Ag nano-in the boundary region between the STO substrate and the YBCO film.

Figure 4-116 b shows the mapping of O_2 which is present all over the film and the STO substrate. Sr is very clearly seen in Figure 4-116 c in the substrate area (and not in the YBCO film), however, Ag is detected in the whole sample which is not possible since Ag nano dots were added on the STO substrate and in the YBCO film at a certain distance from the substrate;, the signal detected in Figure 4-116 d may be just noise. Cu and Y mapping are presented in Figure 4-116 e and f, respectively, and they are distributed, as expected, only in the YBCO film. One can see some small brighter spots in Figure 4-116 f (marked by surrounding red circles), which is a clear evidence of nano-grains of Y rich phase (Y_2O_3) as those observed in TEM images.

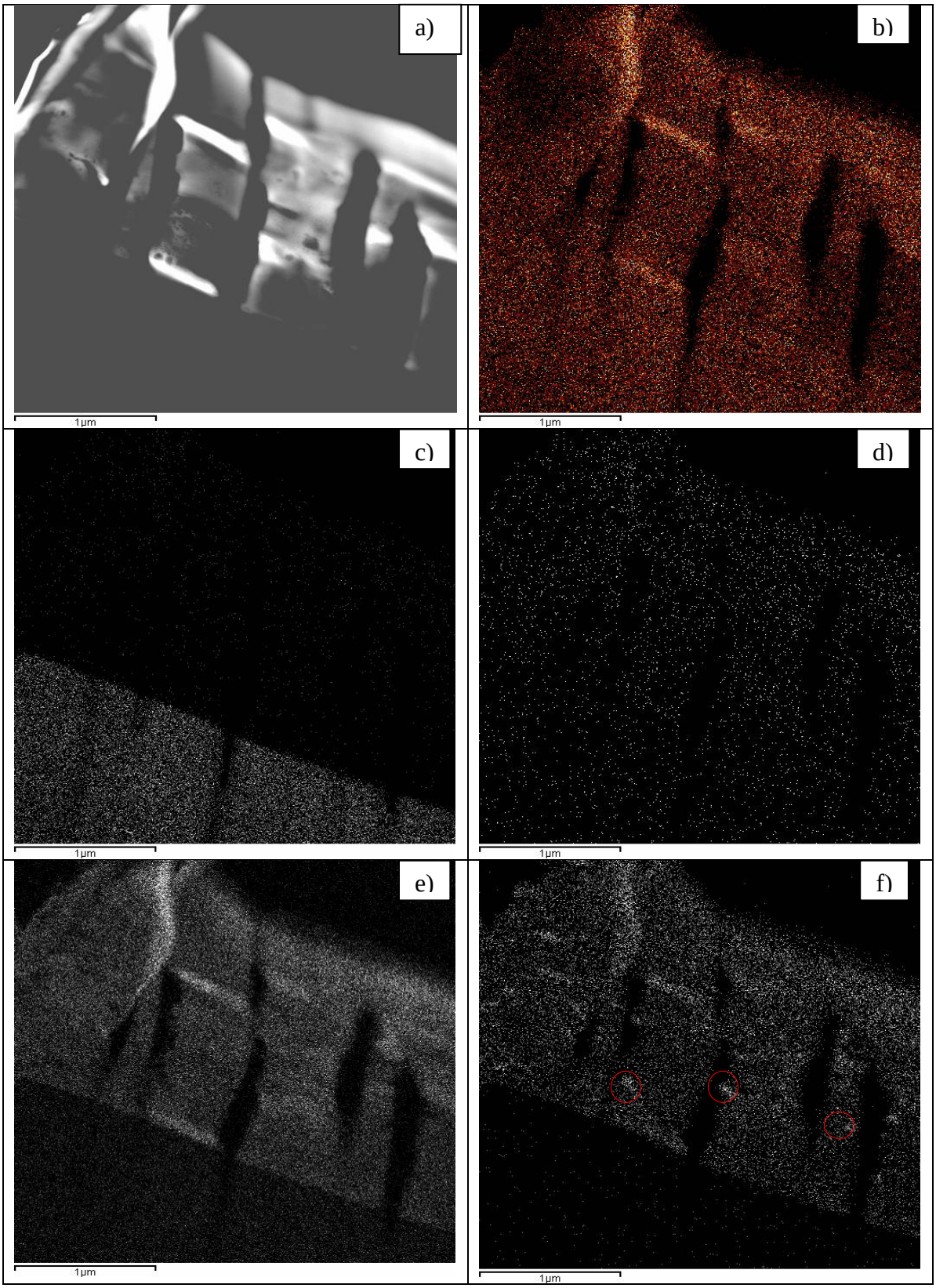

Figure 4-116 a) STEM image and element mapping of b) O_2, c) Sr, d) Ag, e) Cu, f) Y

4.5 PBCO/YBCO quasi-multilayer films

$PrBa_2Cu_3O_7$ (PBCO) was also used as nano-dots material for substrate decoration techniques (with 15 laser pulses) and for quasi-multilayers architecture with different thickness of YBCO layers.

4.5.1 Quasi-multilayer architecture of (15PBCO/0.5μm YBCO)xN

Superconducting transitions of the films are investigated by AC susceptibility measurements as shown in Figure 4-117. Critical temperatures T_c of the films are 90.4 K, 90.0 K, 89.2 K and 89.2 K, for the quasi-multilayers with N = 2, 3, 4 and 5. It can also be seen that transition width (ΔK) of films with N = 4 and 5 is larger than those of thinner films with N= 2 and 3, which indicate that the superconducting properties of the films degrade when the film thickness increase too much. The same conclusion can be drawn from Figure 4-118 and Figure 4-119, where it can be seen that J_c of the films with N = 4 and 5 is lower than the J_c of the other (thinner) films.

Figure 4-118 shows the field dependence of J_c at 65 K of the multilayer films with N = 2, 3, 4 and 5, with thickness of 1 μm, 1.5 μm, 2 μm and 2.5 μm, respectively. As can be seen, J_c of the films with N = 2 and 3 have a J_c higher than that of the films with N = 4 and 5 in all applied fields. A quite unusual field dependence of J_c occurs in the sample with N = 5, as it is higher than J_c of the film with N = 4 film in self-field, but also in applied fields higher than 1 T.

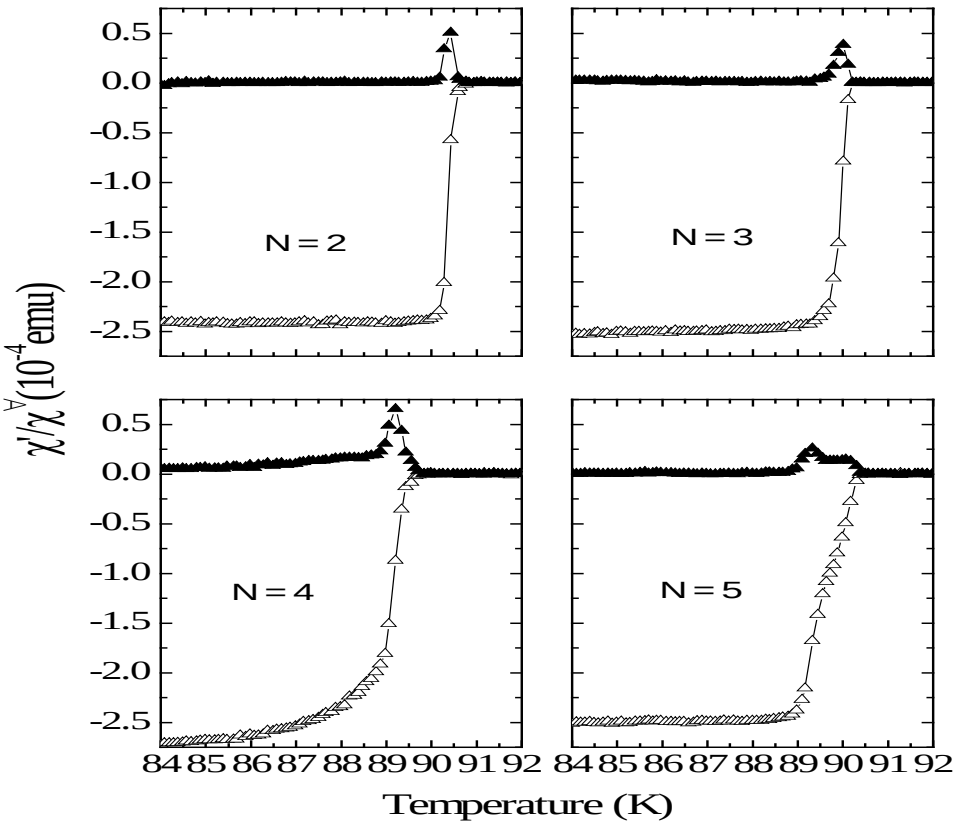

Figure 4-117 Temperature dependence of AC susceptibility of (15PBCO/0.5mm YBCO)xN, N value is shown in the figure.

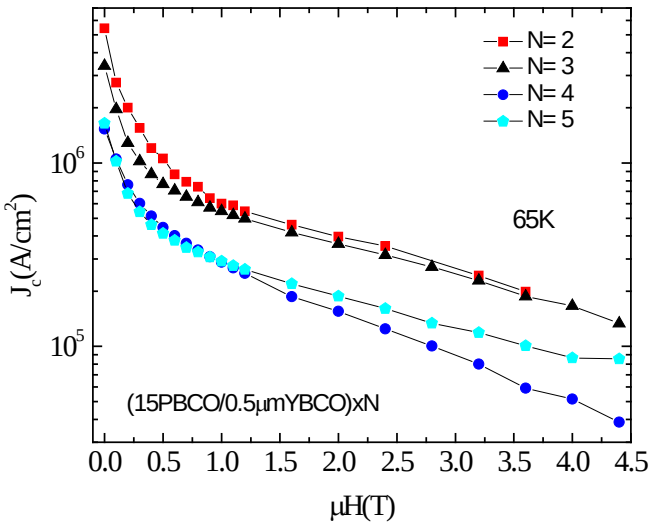

Figure 4-118 Field dependence of J_c of the (15PBCO/0.5μm YBCO)xN films with N = 2, 3, 4 and 5,at 65 K.

The field dependence of J_c of the films at a higher temperature of 77.3 K is shown in Figure 4-119, in comparison with J_c of a 2 μm-thick pure YBCO film. The multilayer film with N = 4 which has the same thickness of 2 μm as the pure YBCO has lower J_c than the reference film. In this multilayer architecture of PBCO/YBCO, J_c does not improve, but gets worse than the J_c of the reference film.

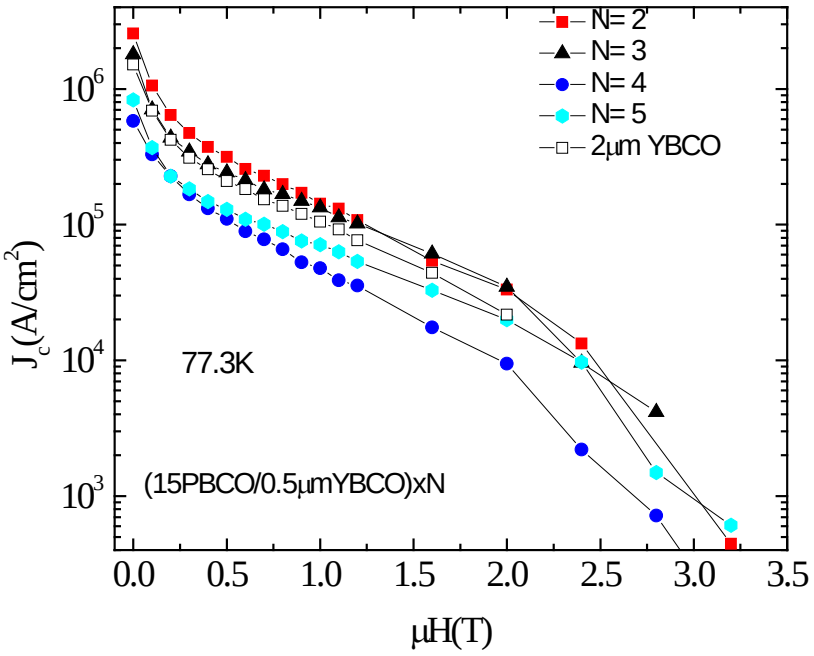

Figure 4-119 Field dependence of J_c of the (15PBCO/0.5μm YBCO)xN with N = 2, 3, 4 and 5, at 77.3 K, in comparison with J_c of 2μm pure YBCO film.

4.5.2 Other multilayer architectures of PBCO/YBCO

As shown above, the multilayer architecture (15PBCO/0.5μm YBCO)xN is not successful in improvement of J_c. Also, for high I_c, thicker (15PBCO/YBCO) films are required, which are presented in this section.

The first sample being tested has the architecture of (15PBCO/0.9μm YBCO)x3, and the field dependence of J_c at 77.3 K is shown in Figure 4-120 in comparison with a pure YBCO

film of the same thickness. As can be seen, J_c at low applied fields and in self-field of the reference sample is higher than in the multilayer film. However, in applied fields higher than 1 T, J_c of the multilayer film becomes larger than that of the pure YBCO film. This kind of architecture is quite promising for high J_c only in applied field higher than 1T.

Superconducting transition of the (15PBCO/0.9μm YBCO)x3 film is shown in Figure 4-121 with T_c of 89.9 K with ΔT_c = 0.8 K, these values being quite good in comparison with pure YBCO.

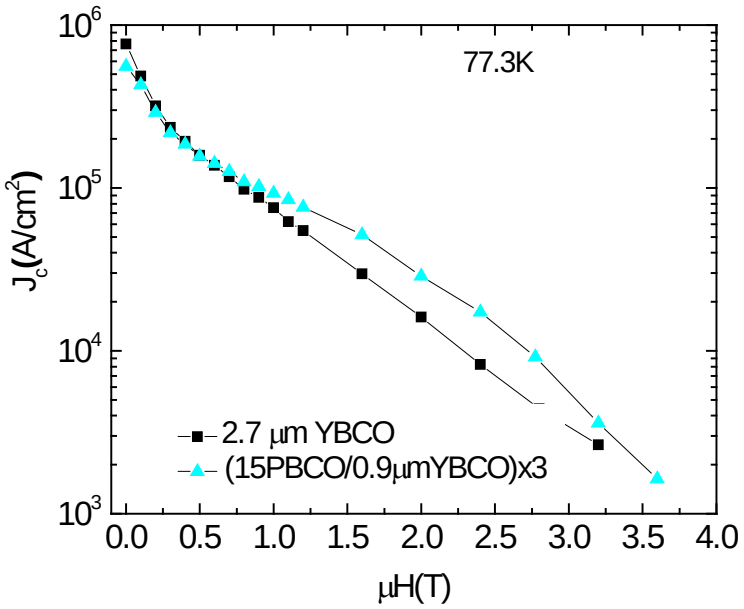

Figure 4-120 Field dependence of J_c of (15PBCO/0.9μm YBCO)x3 film at 77.3 K in comparison with pure YBCO film of the same thickness

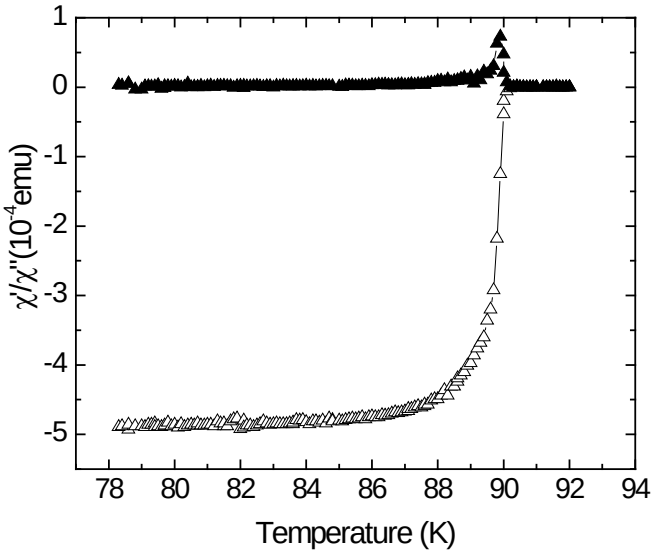

Figure 4-121 Temperature dependence of AC susceptibility of (15PBCO/0.9μm YBCO)x3 film.

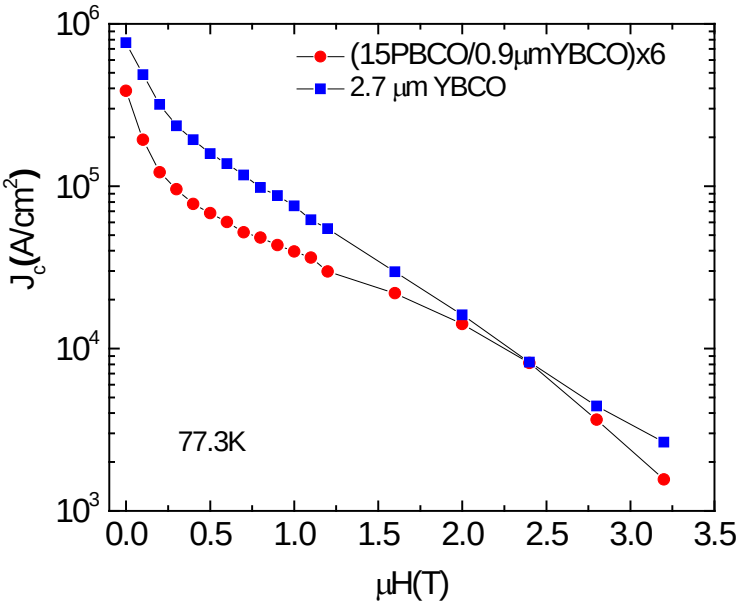

Figure 4-122 Field dependence of J_c of (15PBCO/0.9μm YBCO)x6 multilayer film in comparison with J_c of 2.7μm-thick YBCO at 77.3 K.

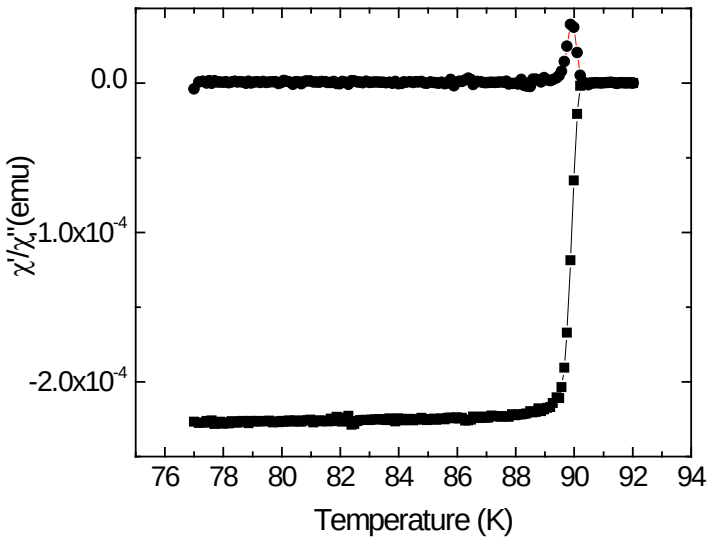

Figure 4-123 Temperature dependence of AC susceptibility of (15PBCO/0.9μm YBCO)x6 film

In order to obtain higher I_c, a 5.4 μm-thick film with the architecture (15PBCO/0.9μm YBCO)x6 was fabricated. The field dependence of J_c of the film is shown in Figure 4-122. As can be seen, J_c of this film is very low because of its large thickness; however, J_c of the multilayer film is comparable with that of the 2.7 μm-thick reference YBCO in applied fields higher than 2.4 T. The field dependence of I_c of the thick multilayer film and the thinner 2.7 μm YBCO is shown in Figure 4-124. There is not very much difference between the two critical currents in low fields, but for applied fields higher than 1.2 T, a notable increase of I_c of the thick multilayer film is observed.

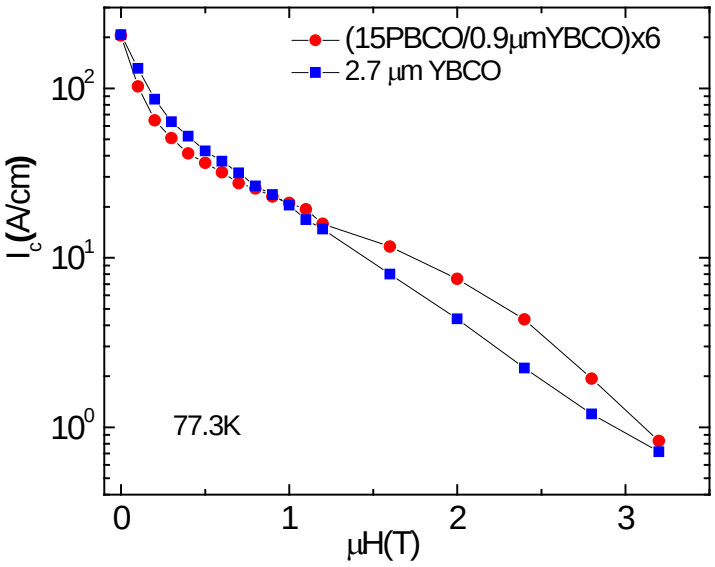

Figure 4-124 Field dependence of I_c of thick (15PBCO/0.9μm YBCO)x6 multilayer film, in comparison with a 2.7 μm-thick pure YBCO film.

Superconducting transition of the (15PBCO/0.9μm YBCO)x6 film is shown in Figure 4-123 with T_c of 89.9 K which is quite close to 88.8 K of the (15PBCO/0.9μm YBCO)x3 film. However the 6 layer film has a very sharp T_c with ΔT_c of 0.5 K which is smaller than 0.8 K for the 3 layer film.

By increasing the thickness of the film to 5.4 μm, T_c of the film is still good and the transition is sharp; however, J_c of the thick film decreases.

4.5.3 AC susceptibility measurements of (15PBCO/YBCO) quasi-multilayer films

In sections 4.5.1 and 4.5.2, the J_c of the PBCO/YBCO multilayer films is quite promising at high applied fields. To clarify the improvement of J_c in high fields, 3 samples with architecture of (15PBCO/0.5 μmYBCO)x2, (15PBCO/0.5 μmYBCO)x3 and (15PBCO/0.6 μmYBCO)x6 have been produced and investigated. Critical current densities J_c in several

high magnetic fields were determined by the AC susceptibility method and compared with a 1 μm-thick pure YBCO film, as shown in Figure 4-125, Figure 4-126 and Figure 4-127, respectively. As can be seen, J_c of all films is higher than that of the reference 1 μm-thick YBCO film in applied fields of 3, 4 and 5 T, at all frequencies in the range between 47 to 10000 Hz and at the temperature of 77.3 K.

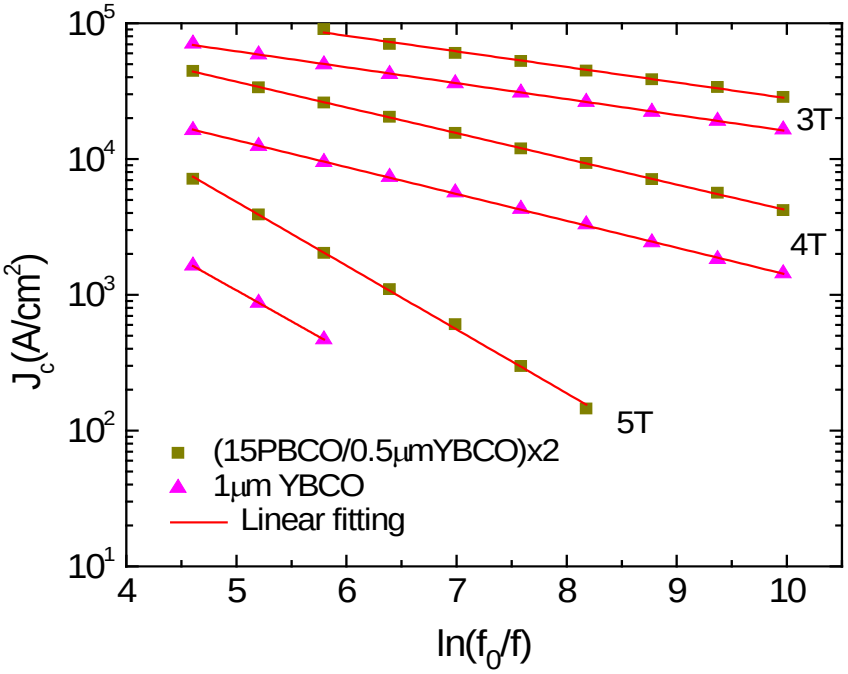

Figure 4-125 Frequency dependence of J_c at 77.3 K, in 3, 4 and 5 T of the (15PBCO/0.5μm YBCO)x2 film (squares) in double logarithmic scale, and of a pure YBCO film of the same thickness and in the same conditions (triangles), the solid line is the linear fit.

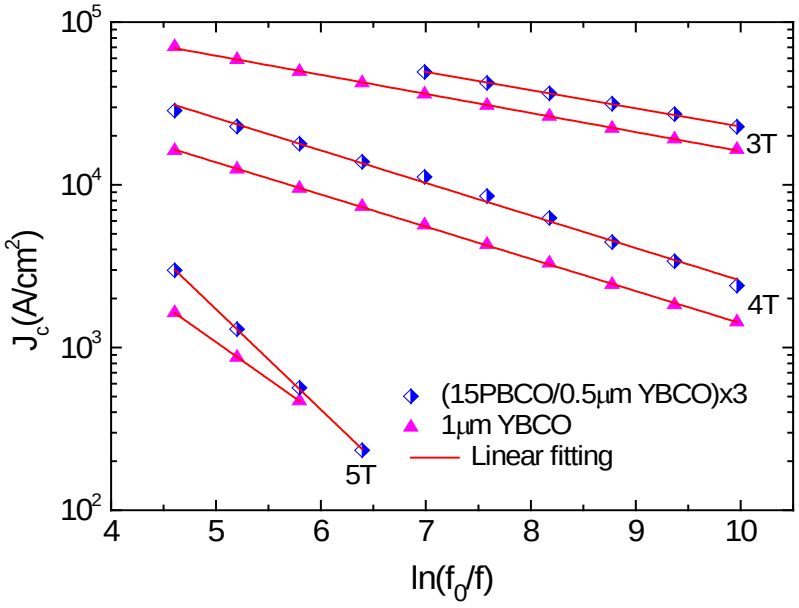

Figure 4-126 Frequency dependence of J_c at 77.3 K, in 3, 4 and 5 T of the (15PBCO/0.5μm YBCO)x3 film (diamonds) in double logarithmic scale, and of the 1μm-thick pure YBCO film in the same conditions (triangles), the solid line is the linear fit.

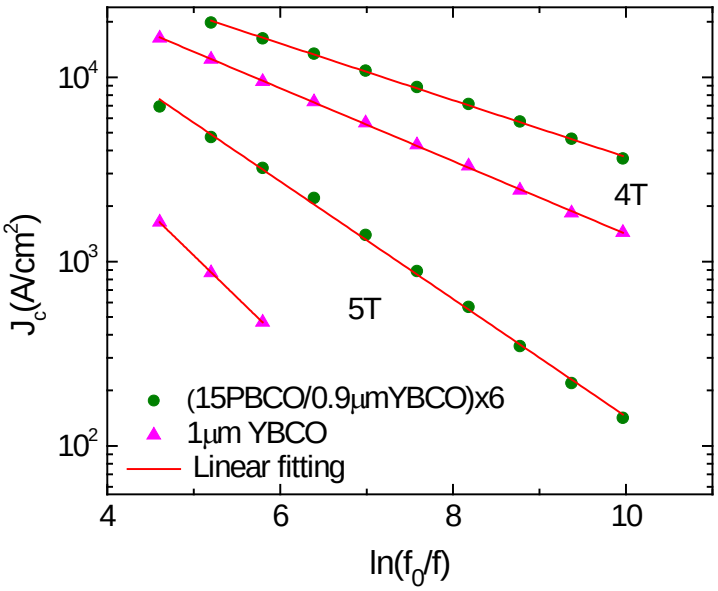

Figure 4-127 Frequency dependence of J_c at 77.3 K, in 4 and 5 T of the (15PBCO/0.9μm YBCO)x6 film (circles) in double logarithmic scale, and of the 1μm-thick pure YBCO film in the same conditions (triangles), the solid line is the linear fit.

The frequency dependence of J_c of the PBCO/YBCO multilayer films data is very well fitted with Eq. (4.1), *i.e.*, a straight line in double logarithmic scale (the red solid line in Figure 4-125, Figure 4-126 and Figure 4-127). By using the same approach as in section 4.4.2, we determined the average pinning potential of PBCO/YBCO multilayer films as shown in Table 4-5

Table 4-5 Slope value *b* from the fitting by Eq.(4.1) and the values of the pinning potential of PBCO/YBCO multilayer samples, and of the reference film.

Samples	*b*			U_0		
	3T	4T	5T	3T	4T	5T
1μm YBCO	0.27	0.46	1.1	363.6	245.3	150.9
(15PBCO/0.5μmYBCO)x2	0.26	0.44	1.1	374.6	253.1	148.9
(15PBCO/0.5μmYBCO)x3	0.26	0.46	1.4	374.6	245.3	131.7
(15PBCO/0.9μmYBCO)x6	N/A	0.35	0.7	N/A	298.2	183.2

It can be seen that the pinning potential of (15PBCO/0.5μmYBCO)x2 film is higher than that of pure YBCO film in 3 and 4 T but lower in 5 T. For (15PBCO/0.5μmYBCO)x3 film, U_0 is higher than that of the reference YBCO film in 3T, the same with that of pure YBCO in 4 T and lower in 5T. J_c data of (15PBCO/0.9μmYBCO)x6 at 3T could not be recorded due to the limitation of the experimental range of both AC field amplitudes and frequencies. The U_0 of (15PBCO/0.9μmYBCO)x6 film is significantly higher than that of pure YBCO in 4 and 5T at the temperature of 77.3 K.

4.5.4 Transport measurements of J_c of (15PBCO/0.5μm YBCO)x4 film

The angular dependence of J_c of the (15PBCO/0.5μm YBCO)x4 film at 77.3 K and in different fields from 0.1 to 6 T is shown in Figure 4-128. As can be seen, the curves show maximum J_c along the ab-plane. A small secondary peak along the c-axis can be seen at fields from 1 T to 3 T, however, it disappears at fields higher than 4 T.

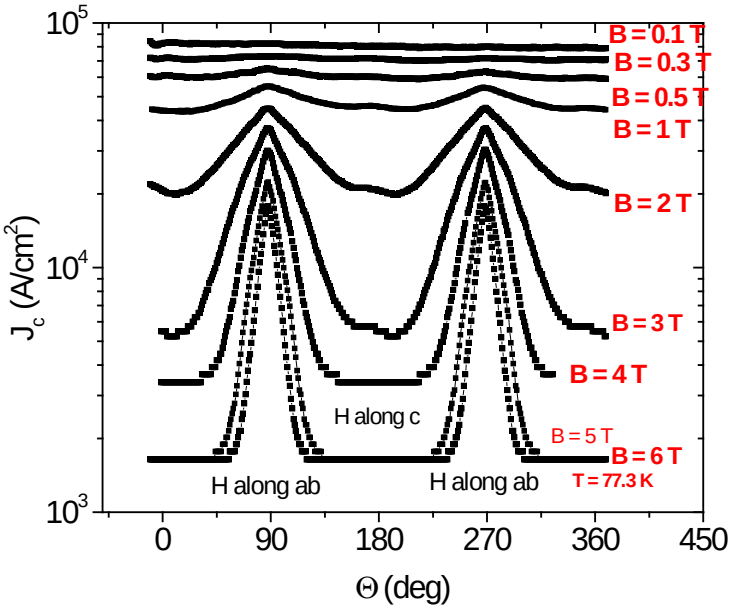

Figure 4-128 Angular dependence of J_c of the (15PBCO/0.5μmYBCO)x4 film at 77.3K and applied fields from 0.1 T to 6 T, the values of the applied magnetic fields are shown on the right hand side of the figure.

From Figure 4-128 one can see that the small, secondary peak of J_c along the c-axis is only observed in applied fields from 1 to 3T at 77.3 K. To clarify the J_c peak along the c-axis at high fields and high temperature, the angular dependence of J_c in 1T and at different temperatures from 77.3 K to 83 K has been carried out, as shown in Figure 4-129. It resulted that the peak of J_c along the c-axis in 1 T is present at all temperatures shown in the figure, but vanishes at temperature higher than 84 K.

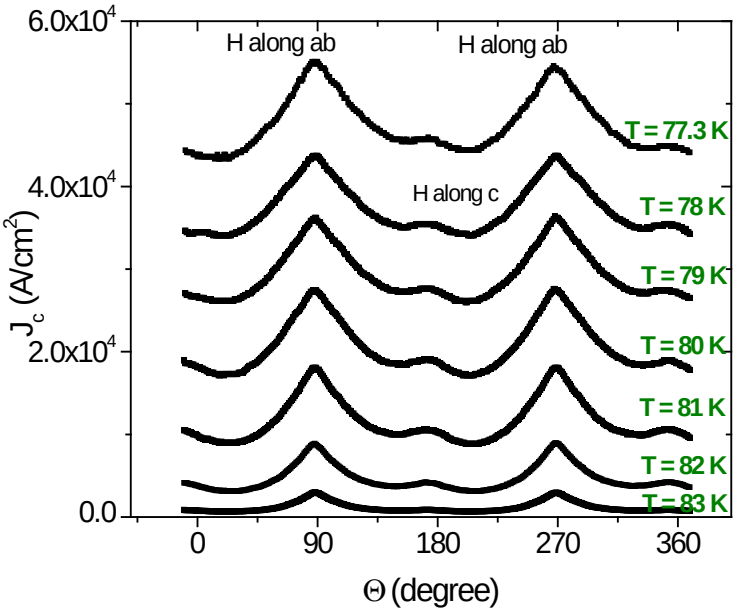

Figure 4-129 Angular dependence of J_c of the (15PBCO/0.5μmYBCO)x4 film in 1T and at different temperatures as shown on the right hand side of the figure.

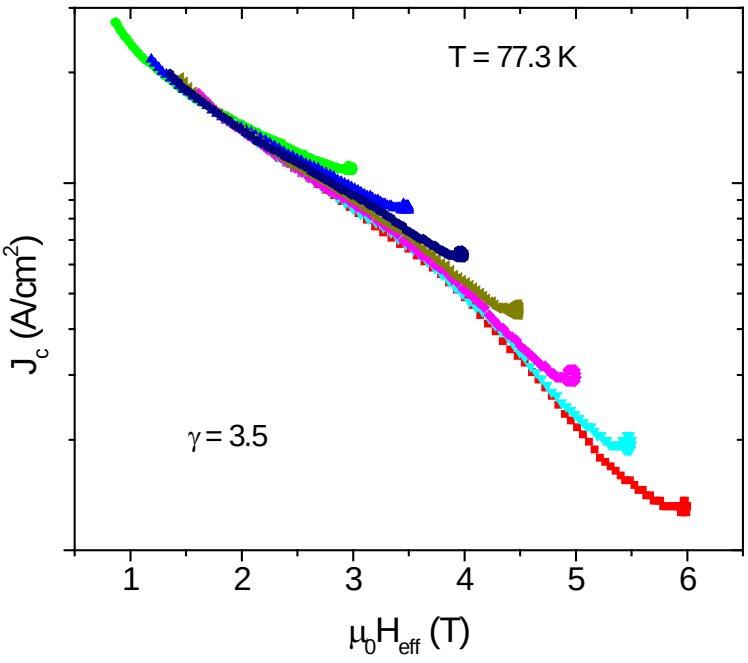

Figure 4-130 Anisotropy factor γ = 3.5 given the best fit by Blatter scaling in the (15PBCO/0.5μmYBCO)x4 film at 77.3 K

The same approach for angular dependence of J_c as performed in section 4.5.4, the Blatter scaling, is applied for this PBCO/YBCO multilayer. The same anisotropy factor of 3.5 as for Ag/YBCO multilayer is found for the PBCO/YBCO multilayer architecture at 77.3 K. However, the J_c secondary peak along the c-axis of the PBCO/YBCO multilayer film is not as strong as in the case of Ag/YBCO multilayer. This implies that there are fewer strong extended defects along the c-axis in the PBCO/YBCO multilayer films, and the vast majority of the strong pinning centres are isotropic. TEM images in the next section will confirm this.

4.5.5 Microstructure of PBCO/YBCO multilayer

Surface morphology of one of the PBCO/YBCO multilayer film is shown in Figure 4-131.

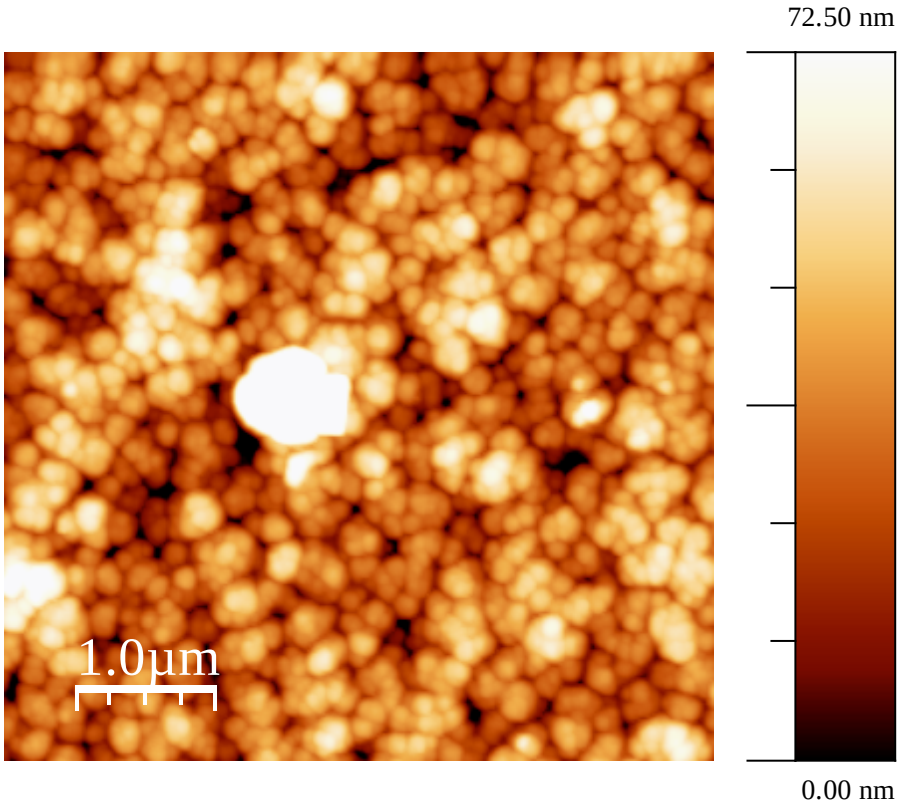

Figure 4-131 AFM of (15PBCO/0.5µmYBCO)x3 sample with RMS roughness of 20nm

The AFM image of the (15PBCO/0.5μmYBCO)x3 sample shows the same morphology as pure YBCO and Ag/YBCO multilayers, with a structure of islands and pores. However, the island's diameter of 200-300 nm of PBCO/YBCO in this image is smaller than that of pure YBCO shown in section 4.2 and Ag/YBCO shown in section 4.4. The RMS roughness of this PBCO/YBCO multilayer is about 20 nm, slightly smaller than 25-35 nm in the case of Ag/YBCO shown in section 4.4.

The microstructure of the PBCO/YBCO multilayer films was further be investigated by TEM. Figure 4-133 shows a high-resolution cross-section TEM image of the PBCO/YBCO multilayer film near the film/substrate interface. It is very difficult to see the presence of PBCO because the lattice parameter of PBCO is very close to that of YBCO, and the amount of PBCO is very small (15 laser pulses).

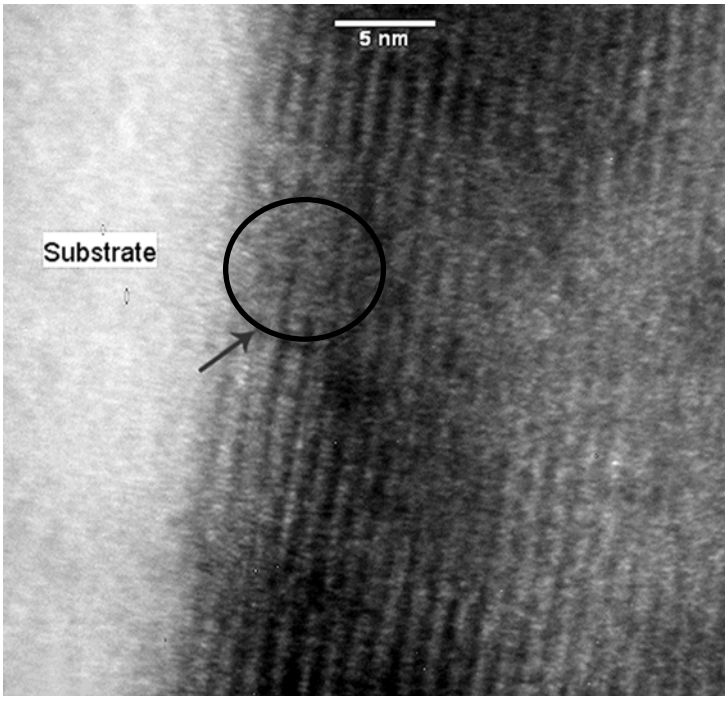

Figure 4-132 High-resolution TEM image of PBCO/YBCO multilayer near the film substrate interface, arrow and circle point to a PBCO nano-particle.

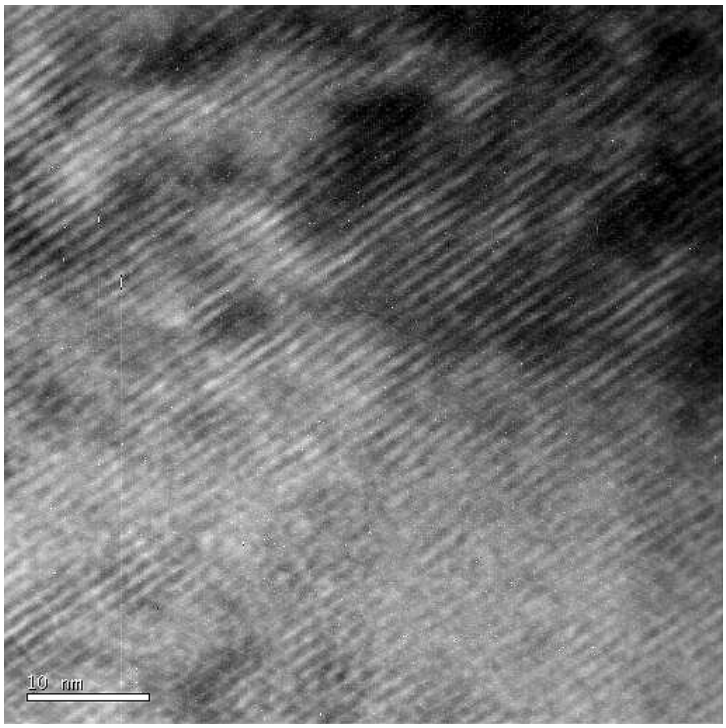

Figure 4-133 High-resolution cross TEM image in the middle of the film.

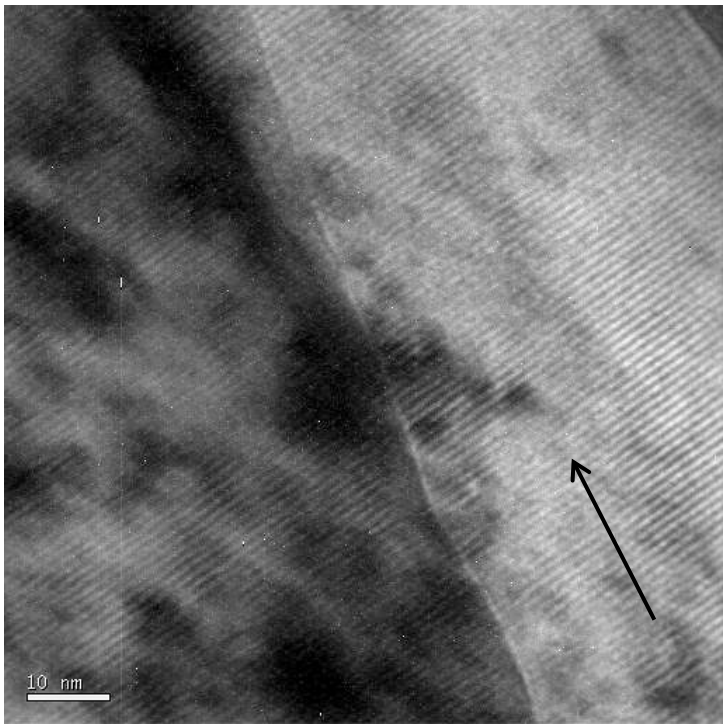

Figure 4-134 A boundary along the c-axis (arrow).

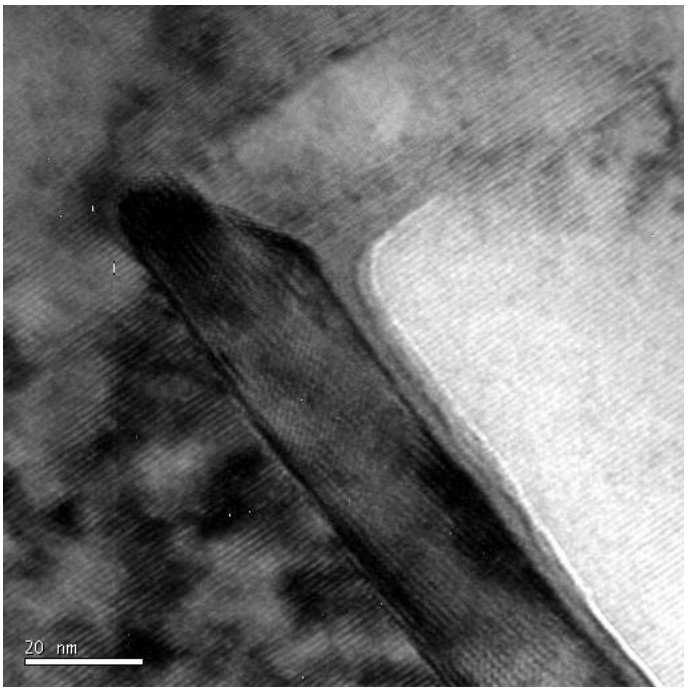

Figure 4-135 Mis-orientated grain observed in the cross section TEM image.

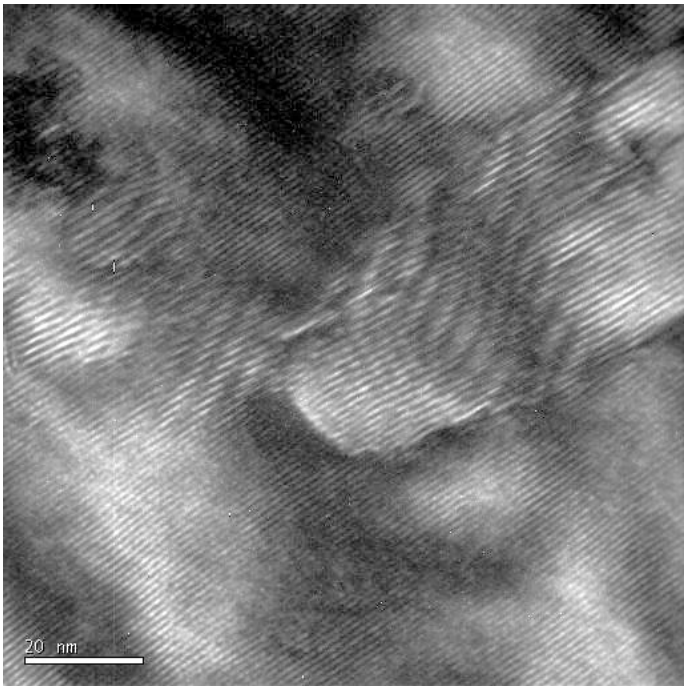

Figure 4-136 Low resolution image in the middle of the film.

One can see a PBCO nano-particle in the YBCO matrix as marked by the arrow and circle in the Figure 4-133.

Another high-resolution cross section image is shown in Figure 4-133., The Cu-O layers are clearly observed; missing layers or stacking faults can also be seen in this figure. Small dark areas appear, which may be due to thicker areas (resulting from non-uniform FIB milling) or could be other phases such as Y-rich or Cu-rich grains.

The small secondary peak in J_c along the c-axis is likely to be caused by the c-axis oriented grain boundary (twin boundary) as the one seen in Figure 4-134. Figure 4-135 shows a mis-orientated region (from the ab-plane it rotates to the c-axis direction). Such defects may also contribute to the increase in J_c.

Figure 4-136, shows the low resolution TEM image of the film taken in the middle area, indicating the presence of few spheroidal or spherical grains which may be PBCO, similar to the one seen near the substrate in Figure 4-133.

References

[1] B.L. Low, Superconductor Science and Technology 10/1 (1997) 41.

[2] R.L.S. Emergo, J.Z. Wu, T. Aytug, D.K. Christen, Applied Physics Letters 85/4 (2004) 618.

[3] S. Ghalsasi, Y.X. Zhou, J. Chen, B. Lv, K. Salama, Superconductor Science & Technology 21/4 (2008).

[4] S.R. Foltyn, L. Civale, J.L. Macmanus-Driscoll, Q.X. Jia, B. Maiorov, H. Wang, M. Maley, Nat Mater 6/9 (2007) 631.

[5] M. Hawley, I.D. Raistrick, J.G. Beery, R.J. Houlton, Science 251/5001 (1991) 1587.

[6] J. Ye, K. Nakamura, Physical Review B 48/10 (1993) 7554.

[7] A.H. Li, H.K. Liu, M. Lonescu, X.L. Wang, S.X. Dou, E.W. Collings, M.D. Sumption, M. Bhatia, Z.W. Lin, J.G. Zhu, Journal of Applied Physics 97/10 (2005).

[8] E. Backen, J. Hanisch, R. Huhne, K. Tscharntke, S. Engel, T. Thersleff, L. Schultz, B. Holzapfel, Ieee Transactions on Applied Superconductivity 17/2 (2007) 3733.

[9] M.P. Aytug. T, A. A. Gapud, S. Kang, H. M. Christen, K. J. Leonard, P. M. Martin, J. R. Thompson, and D. K. Christen, R. Meng, I. Rusakova, C. W. Chu, T. H. Johansen, Journal of Applied Physics 98 (2005) 114309.

[10] P. Mele, K. Matsumoto, T. Horide, O. Miura, A. Ichinose, M. Mukaida, Y. Yoshida, S. Horii, Physica C-Superconductivity and Its Applications 445 (2006) 648.

[11] C. Cai, J. Hanisch, R. Huhne, V. Stehr, C. Mickel, T. Gemming, B. Holzapfel, Journal of Applied Physics 98/12 (2005) 123906.

[12] K. Matsumoto, T. Horide, K. Osamura, M. Mukaida, Y. Yoshida, A. Ichinose, S. Horii, Physica C-Superconductivity and Its Applications 412-14 (2004) 1267.

[13] M. Sparing, E. Backen, T. Freudenberg, R. Huhne, B. Rellinghaus, L. Schultz, B. Holzapfel, Superconductor Science & Technology 20/9 (2007) S239.

[14] R.L. Meng, T.H. Johansen, I.A. Rusakova, A. Baikalov, D. Pham, F. Chen, Z.Y. Zuo, C.W. Chu, Physica C-Superconductivity and Its Applications 434/1 (2006) 39.

[15] J. Gutierrez, A. Llordes, J. Gazquez, M. Gibert, N. Roma, S. Ricart, A. Pomar, F. Sandiumenge, N. Mestres, T. Puig, X. Obradors, Nature Materials 6/5 (2007) 367.

[16] C.V. Varanasi, P.N. Barnes, J. Burke, Superconductor Science & Technology 20/10 (2007) 1071.

[17] J. Burke, C.V. Varanasi, L. Brunke, H. Wang, J.H. Lee, P.N. Barnes, in: U. Balachandran (Ed.), Advances in Cryogenic Engineering, vol. 1219, Amer Inst Physics, Melville, 2010, p. 355.

[18] H. Zhou, B. Maiorov, S.A. Baily, P.C. Dowden, J.A. Kennison, L. Stan, T.G. Holesinger, Q.X. Jia, S.R. Foltyn, L. Civale, Superconductor Science & Technology 22/8 (2009).

[19] E.H. Brandt, Physical Review B 49/13 (1994) 9024.

[20] M. Tihkham, Introduction to Superconductivity, Second edition (1996).

[21] P.W. Anderson, Y.B. Kim, Reviews of Modern Physics 36/1P1 (1964) 39.

[22] G. Blatter, M.V. Feigelman, V.B. Geshkenbein, A.I. Larkin, V.M. Vinokur, Reviews of Modern Physics 66/4 (1994) 1125.

[23] E. Zeldov, N.M. Amer, G. Koren, A. Gupta, R.J. Gambino, M.W. McElfresh, Physical Review Letters 62/26 (1989) 3093.

[24] E. Zeldov, Physica A 168/1 (1990) 260.

[25] E. Zeldov, N.M. Amer, G. Koren, A. Gupta, M.W. McElfresh, R.J. Gambino, Applied Physics Letters 56/7 (1990) 680.

[26] A. Crisan, V.S. Dang, P. Mikheenko, Y.Y. Tse, A. Sarkar, J. Bowen, J.S. Abell, Physica C-Superconductivity and Its Applications 470/1 (2010) 55.

[27] D. Dew-Hughes, Philosophical Magazine 30 (1974) 293.

[28] G. Blatter, V.B. Geshkenbein, A.I. Larkin, Physical Review Letters 68/6 (1992) 875.

[29] L. Civale, B. Maiorov, A. Serquis, J.O. Willis, J.Y. Coulter, H. Wang, Q.X. Jia, P.N. Arendt, M. Jaime, J.L. MacManus-Driscoll, M.P. Maley, S.R. Foltyn, Journal of Low Temperature Physics 135/1-2 (2004) 87.

[30] V.F. Solovyov, et al., Superconductor Science and Technology 20/4 (2007) L20.

[31] H. Yamasaki, et al., Superconductor Science and Technology 21/12 (2008) 125011.

[32] P. Mikheenko, A. Sarkar, V.S. Dang, J.L. Tanner, J.S. Abell, A. Crisan, Physica C-Superconductivity and Its Applications 469/14 (2009) 798.

Chapter 5. **Results and discussion on BZO-doped YBCO and multilayer architectures of BZO-doped YBCO films**

5.1 Optimisation of J_c of BZO 4wt% doped YBCO films

It recently has been reported [1] that $BaZrO_3$ (BZO)-doped YBCO is very effective in enhancement of J_c especially in high applied fields, and the optimum concentration of BZO-doped of 2 - 4wt% was found [2]. In this chapter, we have used a BZO 4wt% doped YBCO target to fabricate BZO-doped YBCO films. We define here that BZO-doped YBCO film is 4wt% BZO-doped YBCO, and unless otherwise specified all the depositions are on the $SrTiO_3$ (STO) single crystal substrates.

5.1.1 Effect of deposition temperature on J_c and T_c of BZO-doped YBCO films

For simplicity, BZO-doped YBCO was first deposited at the same temperature as pure YBCO films at 780^o C and laser frequency of 8 Hz, a massive work done on those conditions was presented in M. M. Kachick PhD thesis . The film deposited under the same conditions as pure YBCO has a sharp T_c as shown in Figure 5-1, the T_c of the film is 87.8 K with ΔT_c = 0.8 K. This value of T_c is comparable with recent publications [2, 3] with the same concentration of BZO dopant. The field dependence of J_c of the film deposited at 780^o C is shown in Figure 5-2. At 77.3 K J_c of the BZO-doped YBCO film deposited at 780^{o}C presents an improvement of J_c in applied fields higher than 1 T in comparison with pure YBCO having the same thickness. However, at 65K there is an increase of J_c for fields up to 2T but in applied fields higher than 2 T, the field dependence of J_c data of the both films is overlapped (except data at 4.2 T, which may be due to measurement error). There is no improvement of J_c of the BZO-doped film at 0T for both temperatures.

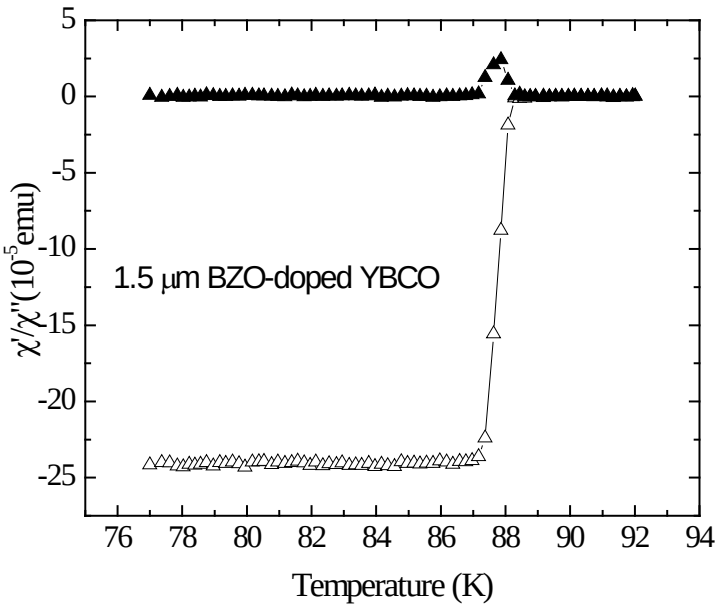

Figure 5-1 Temperature dependence of AC susceptibility of BZO-doped YBCO film fabricated at substrate temperature of 780°C and laser frequency of 8 Hz.

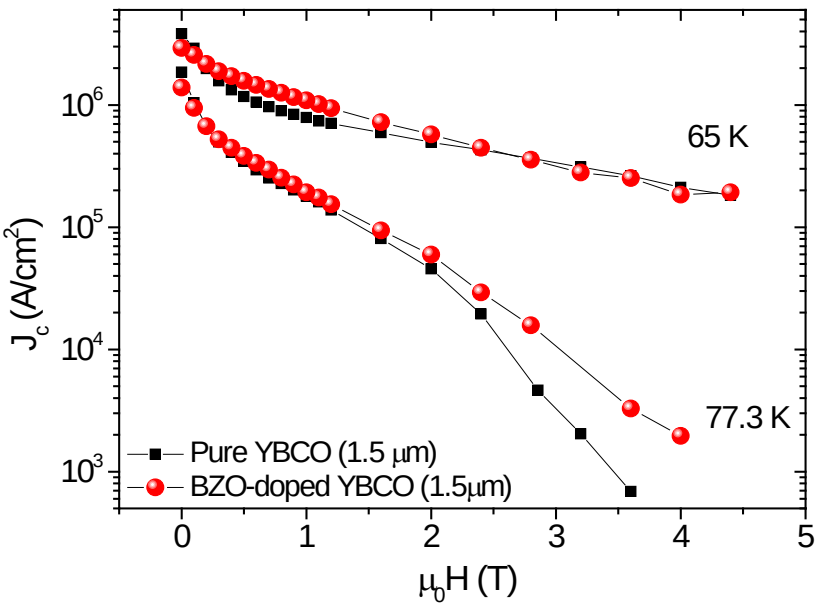

Figure 5-2 Field dependence of J_c of BZO-doped YBCO film grown at 780°C and 8 Hz in comparison with a YBCO film of the same thickness YBCO grown in the same conditions.

However, BZO-doped YBCO films deposited at substrate temperature of 800^{o} C and frequency of 3 Hz (high temperature, low frequency) demonstrates totally different properties because of the change of nano-structure of BZO in the YBCO matrix.

Figure 5-3 presents the superconducting transition of a BZO-doped YBCO film deposited at this high temperature and low frequency; T_c is about 89 K which is a bit lower than that of the best pure YBCO presented in Chapter 4, of 90.8 K and the transition is very sharp with ΔT_c < 0.5 K. This T_c value of the BZO-doped YBCO film deposited at high temperature and low frequency is 1.2 K higher than that of BZO-doped YBCO film deposited at low temperature and high frequency, and the transition width is sharper.

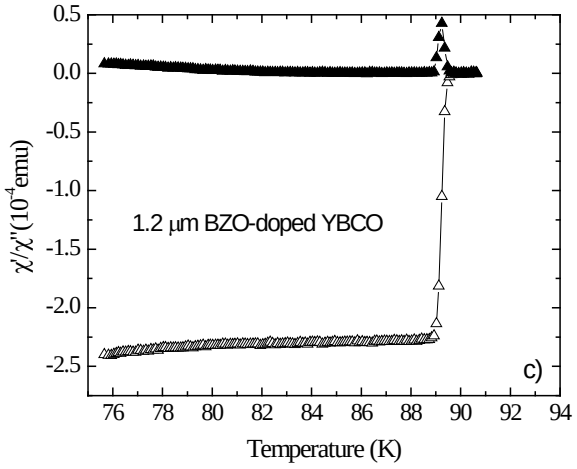

Figure 5-3 Temperature dependence of AC susceptibility of BZO-doped YBCO film deposited at substrate temperature of 800^{o}C and laser frequency of 3 Hz

The field dependence of J_c of BZO-doped YBCO films deposited at high temperature and low frequency and at lower temperature and higher frequency is shown in Figure 5-4 and Figure 5-5 at 65 K and 77.3 K, respectively, in comparison with a pure YBCO film. Legend of each curve is displayed in the figures. Despite being thicker (2 μm), the film deposited at high temperature and low frequency has J_c higher than the thinner (1.5 μm) pure YBCO and

BZO-doped YBCO deposited at low temperature and high frequency in all applied fields except at self-field, at temperatures of 65 and 77.3 K.

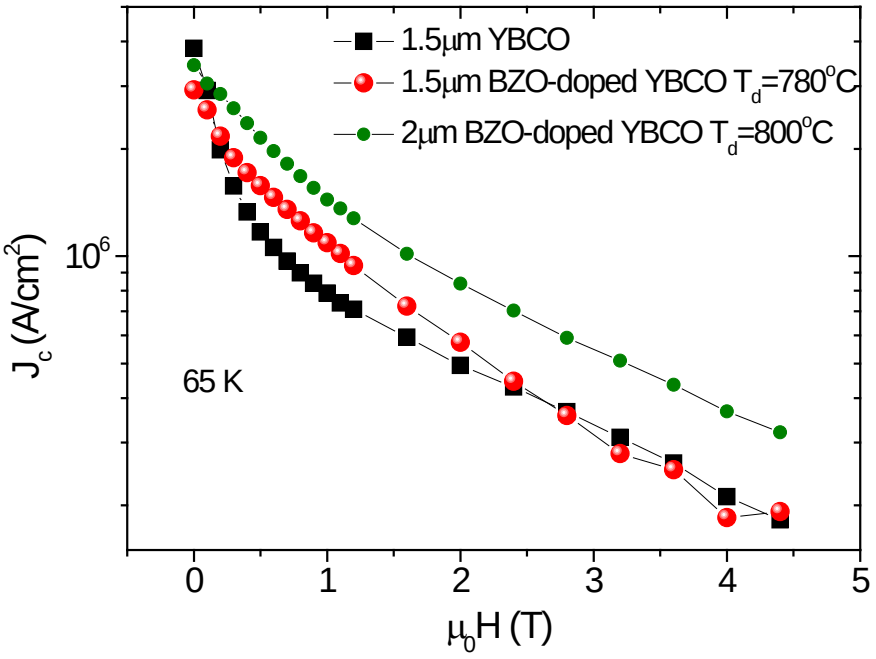

Figure 5-4 Field dependence of J_c at 65 K of BZO-doped YBCO films deposited at 780°C and 8 Hz, and at 800° C and 3 Hz in comparison with J_c of pure YBCO film grown at 780° C and 8 Hz

To get sharp transition, high T_c and high J_c at applied fields, the optimum condition to deposit BZO-doped YBCO film is at a high substrate temperature of 800°C and low laser frequency of 3 Hz (high temperature and low frequency). The reason for the higher J_c of the film deposited at high temperature and low frequency related to the formation of BZO nanorods in the YBCO matrix which will be demonstrated in section 5.1.3 by TEM images.

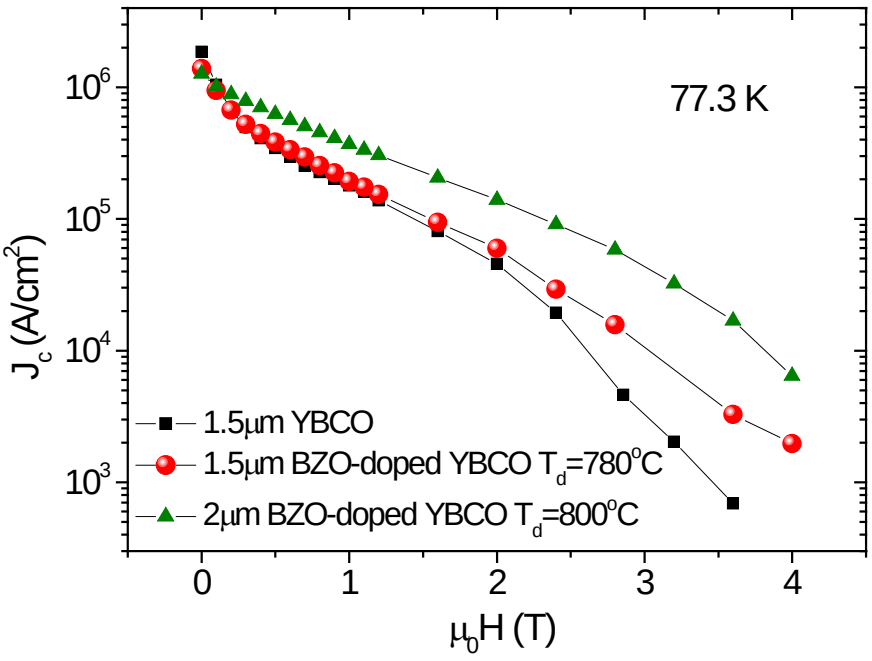

Figure 5-5 Field dependence of J_c at 77.3 K of BZO-doped YBCO film deposited at 780°C and 8 Hz and at 800° C and 3 Hz in comparison with J_c pure YBCO deposited at 780° and 8 Hz.

5.1.2 Transport measurement of J_c of BZO-doped YBCO films deposited at different temperatures

To compare the difference of J_c along the c-axis and the ab-plane of the BZO-doped YBCO film deposited at high temperature and low frequency with that of the film grown at low temperature and high frequency, the angular dependence of J_c of both films, with the same thickness of 1μm, was measured at 1 T and 77.3 K was measured, and the results are shown in Figure 5-6 and Figure 5-7.

Qualitatively, one can clearly see the difference in the peak along the ab-planes and the peak along the c-axis of the two films. While the film deposited at low temperature and high frequency shows dominance of J_c along the ab-plane, the film deposited at high temperature

and low frequency presents reverse property with supremacy of J_c along the c-axis at 1 T and 77.3 K. And hence, the ratio of J_c in-plane and out-of-plane of the two films is quite different. The ratio $J_c^c / J_c^{ab} = 1.84$ for the film deposited at high temperature and low frequency, while the ratio is only 0.91 for the film deposited at low temperature and high frequency.

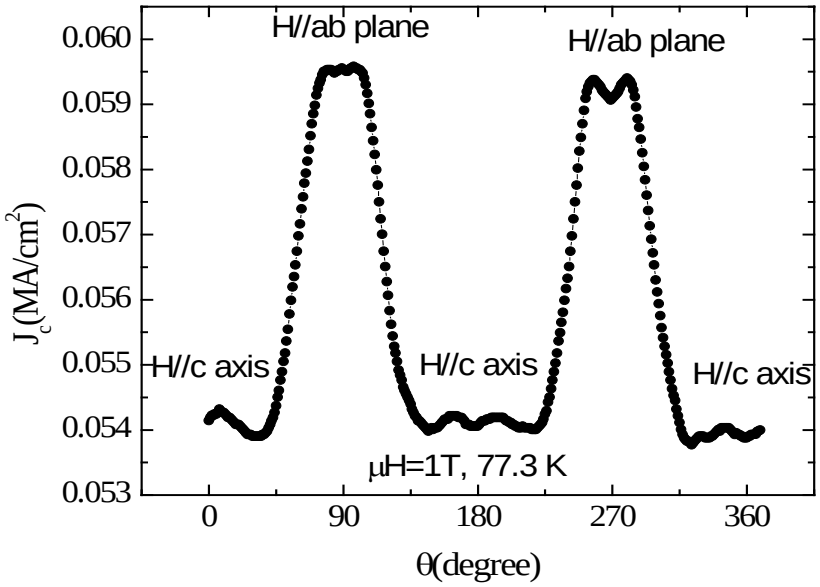

Figure 5-6 Angular dependence of J_c of BZO-doped YBCO film deposited at 780^o C and 8 Hz.

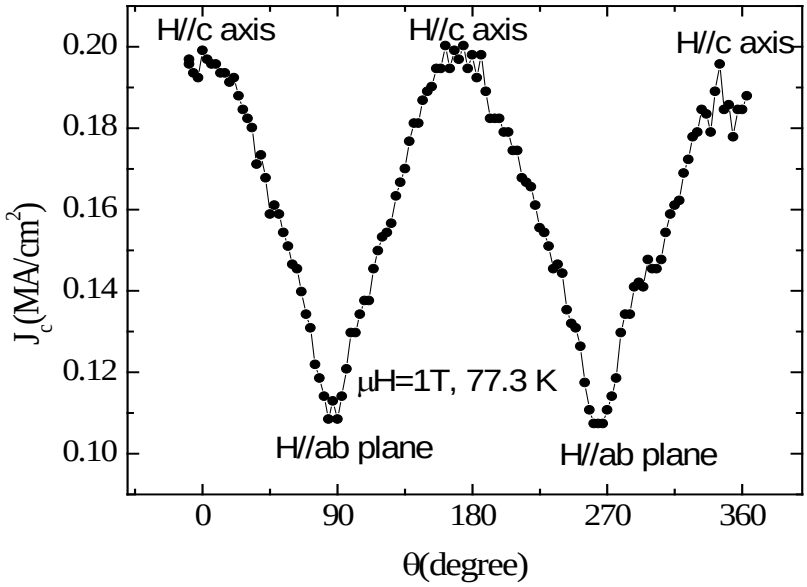

Figure 5-7 Angular dependence of J_c of BZO-doped YBCO film grown at 800^o C and 3 Hz.

The change of maximum J_c from the ab-plane for the film deposited at low temperature high frequency to the c-axis for the film deposited at high temperature and low frequency is related to the formation of BZO nano-rods in the YBCO matrix and will be discussed in the next section.

5.1.3 Microstructure of BZO-doped films deposited at different temperatures

Cross section TEM images of the films reveal a totally different formation of BZO in the YBCO matrix. For the film deposited at low temperature, as can be seen in Figure 5-8, few BZO nano-particles are present with diameter about 7-15 nm. A higher resolution image can be seen in Figure 5-9 which shows very clear Cu-O layers of the YBCO film and the BZO nano-particles marked with circles. No evidence of columnar structure is observed in this film.

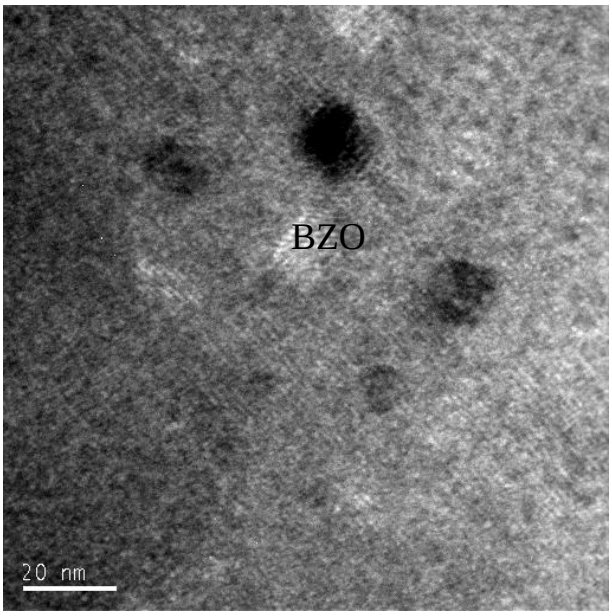

Figure 5-8 BZO nano-particles in the YBCO matrix of the film deposited at low temperature (780^{o} C)

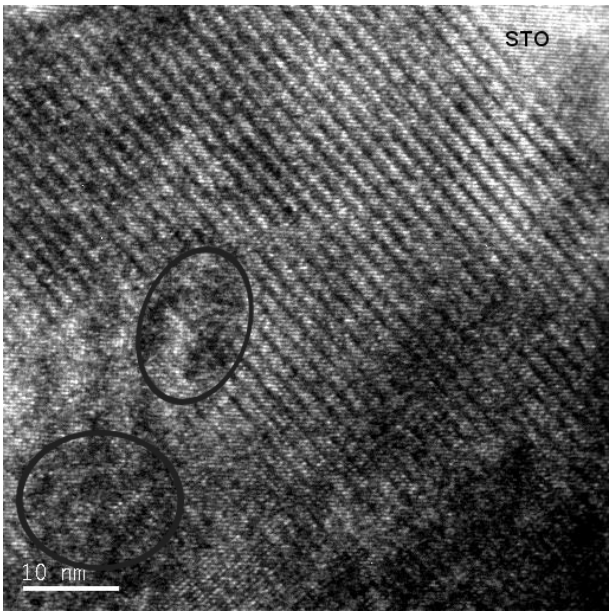

Figure 5-9 High resolution of cross section TEM image of the film deposited at low temperature, BZO nano-particles are visible, and marked by circles.

Figure 5-10 and Figure 5-11 show cross section TEM images of the BZO-doped YBCO film grown in high temperature (800^{o} C) and low frequency (3 Hz) conditions.

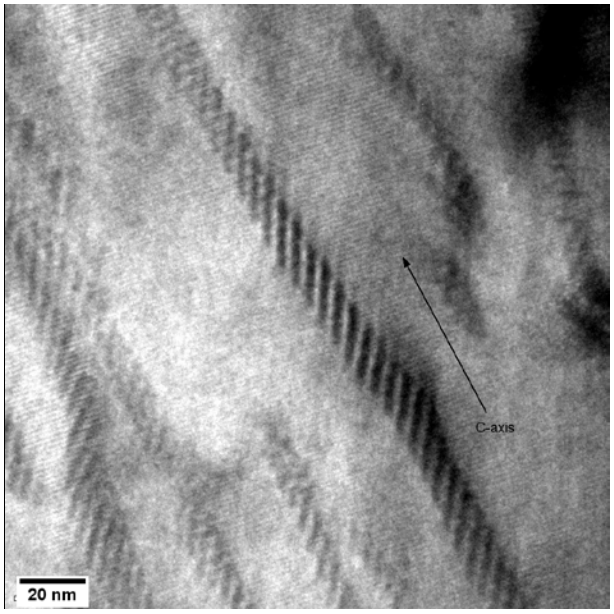

Figure 5-10 Cross section TEM image of BZO-doped YBCO film deposited at high temperature, clearly visible columnar structures (nano-rods) along the c-axis are formed.

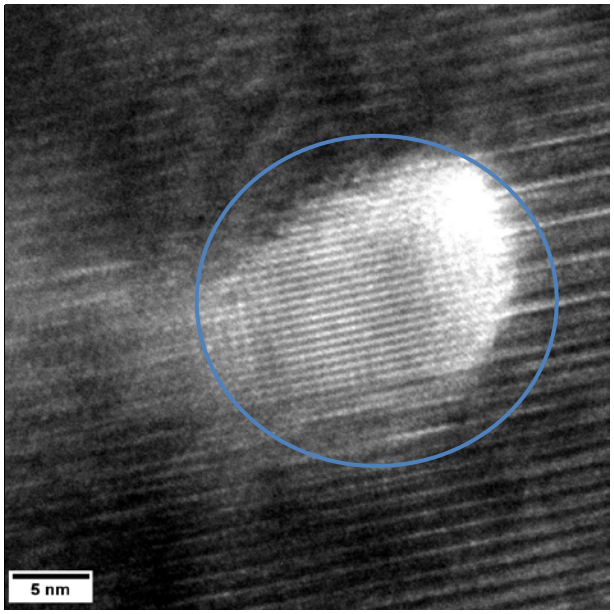

Figure 5-11 Formation of Cu-O nano-particle found in the YBCO matrix of the film deposited at high temperature.

The columnar structure formed from BZO is very clearly seen in Figure 5-10, a cross section TEM image of the film deposited at high temperature and low frequency. The columns are grown along the c-axis of the YBCO crystal with very high density. Together with the columnar defects, the BZO nano-particles are also present in the YBCO matrix of the film deposited at high temperature with diameter about 15 nm as can be seen in Figure 5-11.

By increasing deposition temperature from 780 to 800^{o} C and lowering laser frequency from 8 Hz to 3 Hz, the formation of the BZO in the YBCO matrix changed from nano-particles to columnar structure. However, nano-particles like BZO, Cu-O and Y_2O_3 are also observed in the film deposited at high temperature (details will be discussed in the next section). The formation of BZO nano-columns in the YBCO matrix of the film deposited at high temperature and low frequency is responsible for the change in ratio of J_c from the ab-plane in the film deposited at low temperature to the c-axis in the film deposited at high temperature, while the BZO nano-particles found in the YBCO matrix of the film deposited at high temperature could enhance J_c of the film in all directions.

5.2 BZO-doped YBCO films with various thickness

In this section, 4%wt.BZO-doped YBCO films with several thicknesses have been deposited. J_c of the films has been studied together with microstructure of the films with different thickness.

5.2.1 Superconducting properties of BZO-doped YBCO films

The first superconducting property of BZO-doped YBCO films was examined by AC susceptibility measurement with excitation field of 0.05 Oe as shown in Figure 5-12, a, b, c, d and e for the films with thickness of 0.4 μm, 1.0 μm, 1.2 μm, 2.0 μm and 2.5 μm, respectively. The T_c of BZO-doped YBCO films slightly decreases by 1K from 89.7 K to 88.7 K when the film thickness increases from 0.4 μm to 2.5 μm as shown in Figure 5-12 f.

The decrease of T_c with increasing of film thickness could indicate the degradation of thicker films when they are held for a longer time at the high temperature of deposition. However, a different situation was observed in Ag/YBCO films as mentioned in Chapter 4; the T_c of Ag/YBCO multilayer films remains at 90.7 K even when film thickness is increased to 4.0 μm with sharp transition widths smaller than 0.5 K.

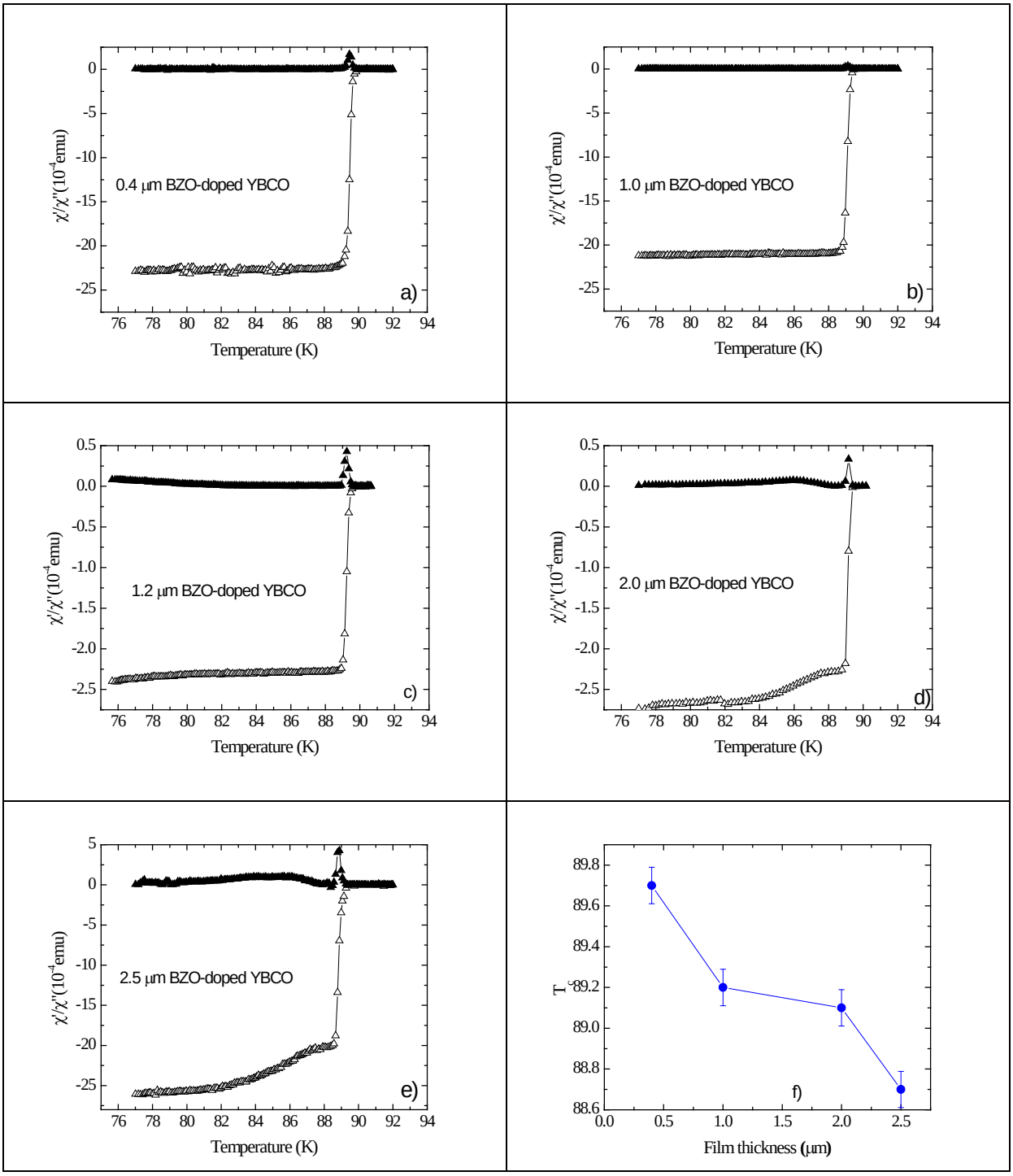

Figure 5-12 Temperature dependence of *AC* susceptibility of the BZO-doped YBCO films at various thicknesses a) 0.4 μm, b) 1.0 μm, c) 1.2 μm, d) 2.0 μm, e) 2.5 μm, f) Thickness dependence of T_c (at peak of χ") of BZO-doped YBCO films.

One can see a shoulder in the AC susceptibility measurement of BZO-doped YBCO films with the thickness of 2.0 μm and 2.5 μm as shown in Figure 5-12 d and e. The shoulder appears at temperatures from 82 to 88.2 K in the real *AC* susceptibility part (χ') and hence a little small wide peak in the imaginary part (χ"). The appearance of the shoulder in the *AC* susceptibility measurement could indicate inhomogeneity of the thicker films.

The second superconducting property of BZO-doped YBCO films with various thicknesses was measured by magnetisation measurements in which magnetic fields were applied parallel to the c-axis of the YBCO films. J_c of the film is calculated by Eq. 3.1 as mentioned in Chapter 3.

Figure 5-13 shows the temperature dependence of J_c of various thicknesses of BZO-doped YBCO film at 1 T; as can be seen, the J_c of the thin 0.4 μm film (open blue circle) is higher than that of the other thicker films. This property is observed in both pure YBCO and BZO-doped YBCO films.

Two others films with thickness of 2.0 and 2.5 μm have J_c lower than J_c of the thinner film. For comparison, the temperature dependence of J_c of a 2.4 μm pure YBCO (open square) is plotted as a reference film. One can see that, J_c the BZO-doped YBCO film with thickness of 2.5 μm which is very close to the thickness of pure YBCO film (2.4 μm) is higher than the reference film at temperatures in the range from 5 K to 82 K.

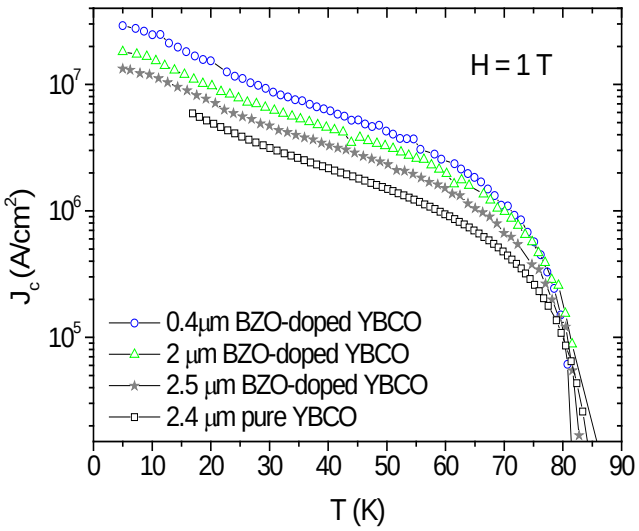

Figure 5-13 Temperature dependence of J_c of BZO-doped YBCO films with thickness of 0.4 μm, 2 μm and 2.5 μm in comparison with 2.4 μm pure YBCO films, in applied field of 1 T.

Figure 5-14 shows J_c of the BZO-doped YBCO films at 77.3 K and in applied fields in comparison with J_c of pure YBCO film.

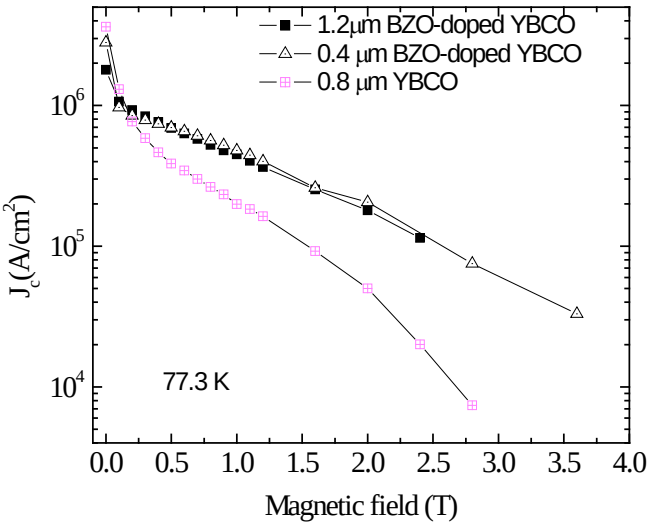

Figure 5-14 Field dependence of J_c of thin BZO-doped YBCO film with the film thickness of 0.4 and 1.2 μm in comparison with 0.8 μm pure YBCO.

The field dependences of J_c for two thin 0.4 and 1.2 μm BZO-doped YBCO films are presented in Figure 5-14 in comparison with that of a 0.8 μm pure YBCO film. The BZO-doped YBCO films have J_c higher than the reference YBCO film at all applied fields except at self-field. The same situation is observed at thicker BZO-doped YBCO films as shown in Figure 5-15 in which J_c of two BZO-doped YBCO films with thickness of 2.0 and 2.5 μm is plotted in comparison with a 1.6 μm pure YBCO film.

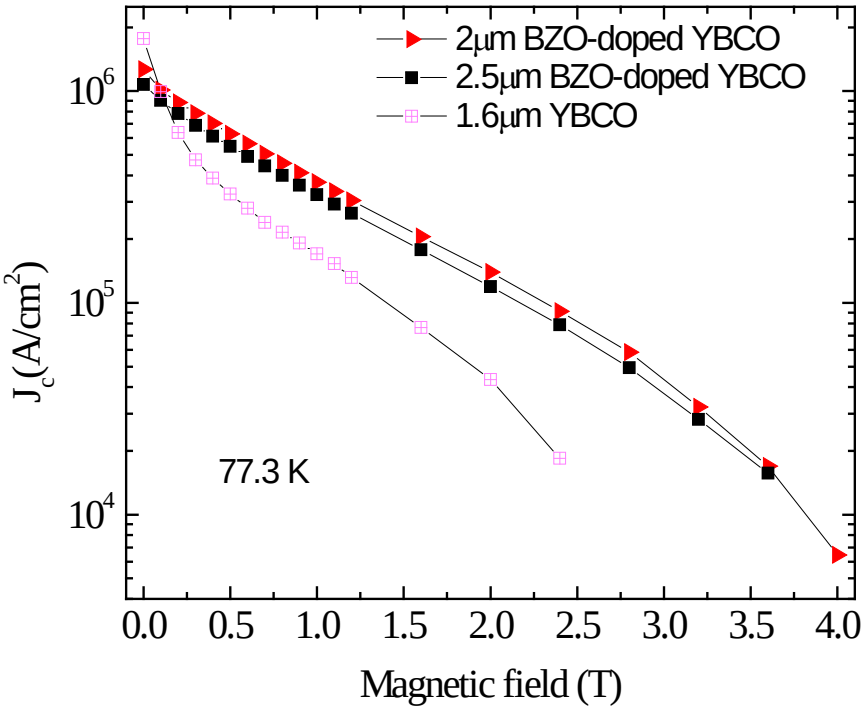

Figure 5-15 Field dependence of J_c at 77.3 K of thick BZO-doped YBCO film with the film thickness of 2.0 and 2.5 μm in comparison with 1.6 μm pure YBCO.

Figure 5-16 and Figure 5-17 show dependence of J_c on the film thickness of the BZO-doped YBCO at 77.3 K and in self-field and applied fields, respectively.

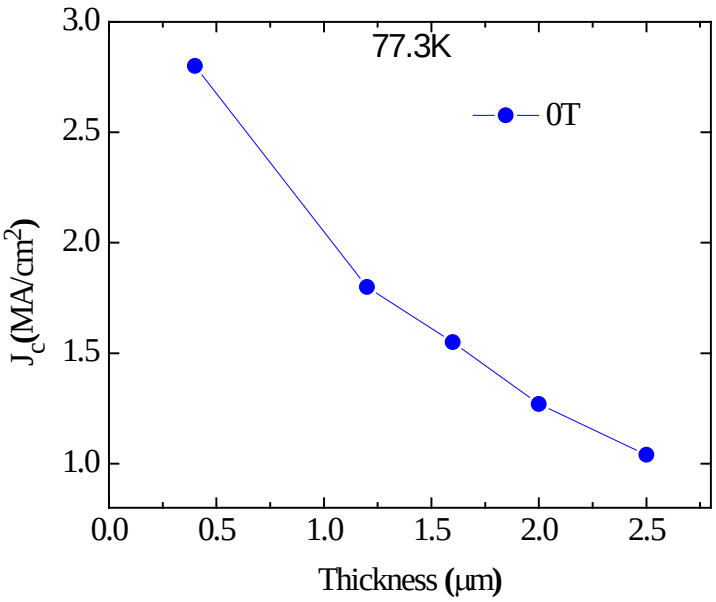

Figure 5-16 Dependence of J_c in self-field on thickness of the BZO-doped YBCO films at 77.3 K.

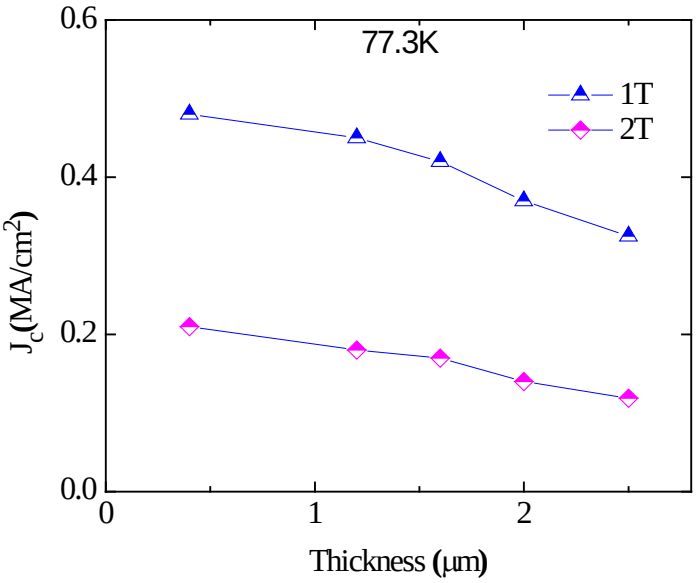

Figure 5-17 Dependence of J_c in applied fields of 1T and 2T on thickness of the BZO-doped YBCO films.

Thickness dependence of J_c of BZO-doped YBCO films at self-field is shown in Figure 5-16: as can be seen, J_c decreases with increasing film thickness. However, the J_c value at self-field of BZO-doped YBCO films is smaller than that of pure YBCO at the same thickness. Figure 5-17 shows the thickness dependence of J_c of BZO-doped YBCO films at 1 T and 2 T as legend is shown in the figure. However, at 1 T and 2 T applied fields the J_c is less dependent on the thickness than at self-field. At 0 T, J_c decreases from 2.8 MA/cm^2 at the film thickness of 0.4 μm to 1.05 MA/cm^2 at the film thickness of 2.5 μm, the decrease is about 62.5 % while at 1 T and 2 T J_c decrease from 0.48 MA/cm^2 to 0.33 MA/cm^2 (31.3%) and from 0.2 MA/cm^2 to 0.12 MA/cm^2 (40%) with the film thickness from 0.4 μm to 2.5 μm, respectively.

5.2.2 Critical current density measured by AC susceptibility

Frequency (time)-dependent J_c of a 1.2 μm thick BZO-doped YBCO film is shown in Figure 5-18 at DC applied fields of 4, 5 and 6 T. For comparison, a reference J_c of a 1 μm pure YBCO at DC applied field of 4 T is also present in Figure 5-18 (open circle). J_cs of pure YBCO film at 5 and 6 T are not displayed in the figure because of low signals from the film. As can be seen, the frequency-dependent J_c of pure YBCO at 4 T is lower than that of BZO-doped YBCO at 6 T. This is strong evidence of flux pinning centres causes by BZO nano inclusion at high applied fields. The J_c of the BZO-doped YBCO film at 4 T is limited due to the strong signal of the film; the PPMS system could not provide the peaked signal of the film at high frequency.

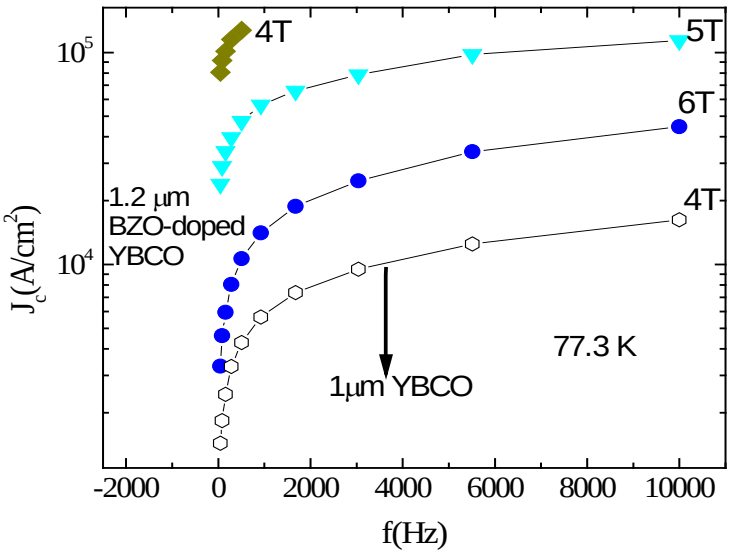

Figure 5-18 Frequency dependence of J_c measured by AC susceptibility method of 1.2 μm BZO-doped YBCO film in DC applied fields of 4, 5 and 6 T in comparison with J_c of 1 μm pure YBCO at 4 T at 77.3 K (marked by black arrow).

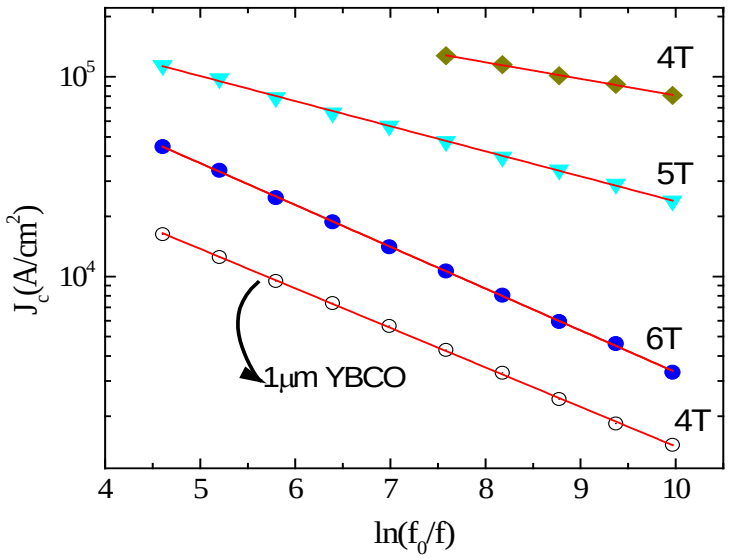

Figure 5-19 Frequency dependence of J_c of the BZO-doped YBCO film in double logarithmic scale with $f_0=10^6$ (Hz) at 4, 5 and 6 T in comparison with 1mm pure YBCO at 4 T (black sphere) at 77.3K, red solid line is linear fitting by Eq. 4.1

As mentioned in Chapter 4, the frequency dependence of J_c at 4, 5 and 6 T of BZO-doped YBCO film can be very well fitted with Eq.4.1 in a linear equation of $ln(f_0/f)$vs $ln(J_c)$ shown in Figure 5-19 with the reference pure YBCO film at 4 T; the red solid line is the linear fitting by the Microcal Origin software. From the fitting, the pinning potential U_0 of the film can be experimentally estimated by the slope of the fitting line (b) as in Eq.4.9. The pinning potential value and slope b of the fitting line is shown in Table 5-1. The value of U_0 at 4 T of BZO-doped YBCO film is almost double that of pure YBCO film as mentioned in Chapter 4, section 4.4.2 and higher than Ag/YBCO multilayer film. This confirms that BZO provides very effective pinning centres with a different pinning mechanism from that of Ag in Ag/YBCO multilayer films.

Table 5-1 Slope of the linear fitting achived from Figure 5-19 and pinning potential estimated by Eq. 4.9

Sample	slope (b)			U_0 (K)(k_B=1)		
	4T	5T	6T	4T	5T	6T
1.2μm BZO-doped YBCO	0.19	0.29	0.48	482.0	344.8	237.7

5.2.3 Transport measurement of BZO-doped YBCO film at different applied fields

5.2.3.1 Angular dependence of J_c

Angular dependence of J_c of 1μm BZO-doped YBCO films at 77.3 K at different applied fields has been measured as seen in Figure 5-20. All the curves show dominant peaks at 0, 180 and 360^o which are along the c-axis of the YBCO film. No peaks at 90 and 270^o are observed until applied fields up to 2.5 T as shown in Figure 5-21.

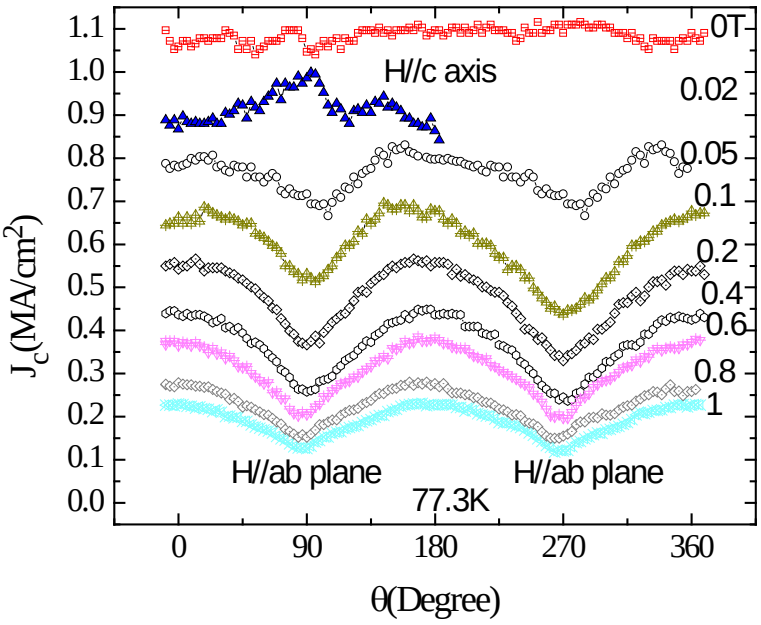

Figure 5-20 Angular dependence of J_c of 1.0 μm BZO-doped YBCO film at 77.3 K and in applied field of 0, 0.02, 0.05, 0.1, 0.2, 0.4, 0.8 and 1 T.

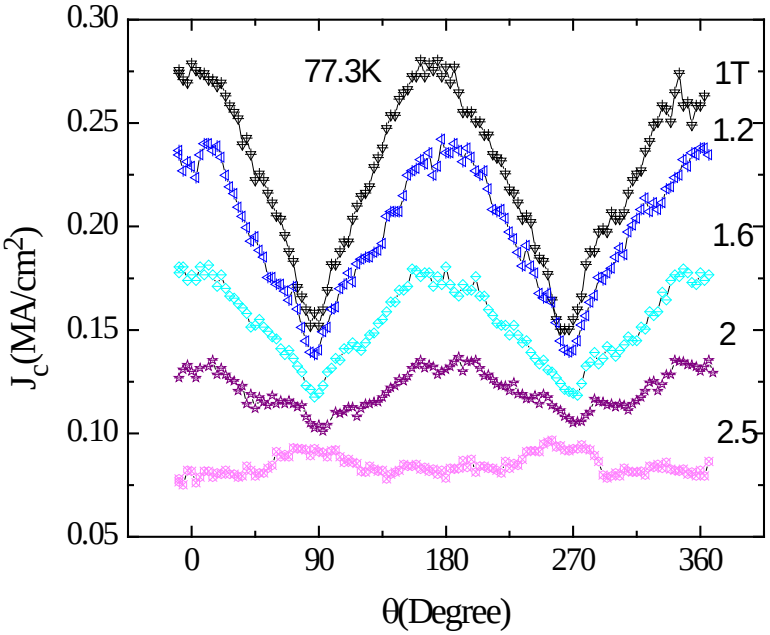

Figure 5-21 Angular dependence of J_c of 1.0 μm BZO-doped YBCO film at 77.3 K and applied field of 1, 1.2, 1.6, 2 and 2.5 T.

The dominance of peaks of J_c along the c-axis is due to the BZO columnar structure grown in the YBCO matrix which is confirmed by TEM images in the next section. However at applied fields higher than 2 T, as shown in Figure 5-22, the angular-dependent J_c shows dominant peaks at 90 and 270^o which are along the ab-plane of the YBCO matrix. There is a very smooth cross-over from the c-axis dominant to ab-plane dominant pinning at 2 to 3 T with a very small anisotropy factor which shows quite a flat curve at 2.5 T as can be seen in Figure 5-21 and Figure 5-22.

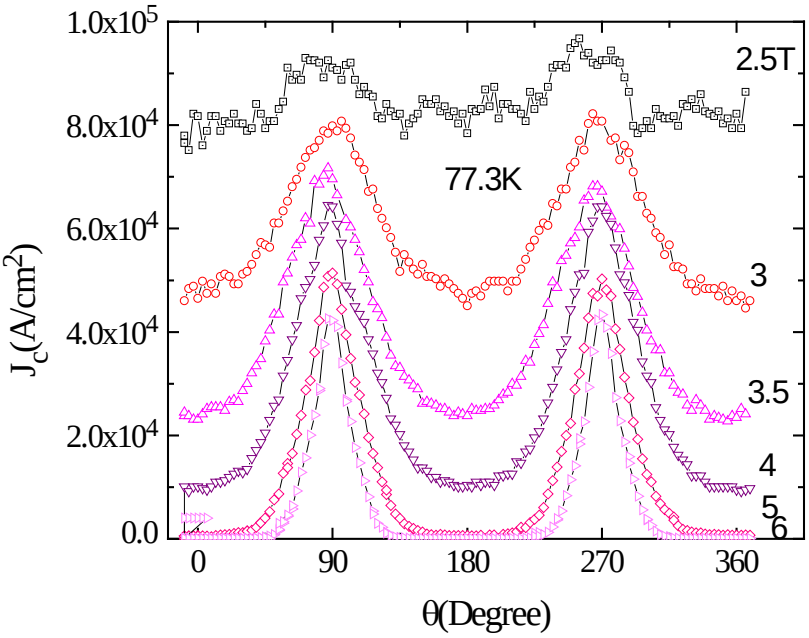

Figure 5-22 Angular dependence of J_c of 1.0 μm BZO-doped YBCO film at 77.3 K and applied field of 2.5, 3, 3.5, 4, 5 and 6 T.

The ratio of J_c^c/J_c^{ab} versus magnetic field is shown in Figure 5-23, as can be seen, the peak of the ratio is about 1.8 and at 1.2 T.

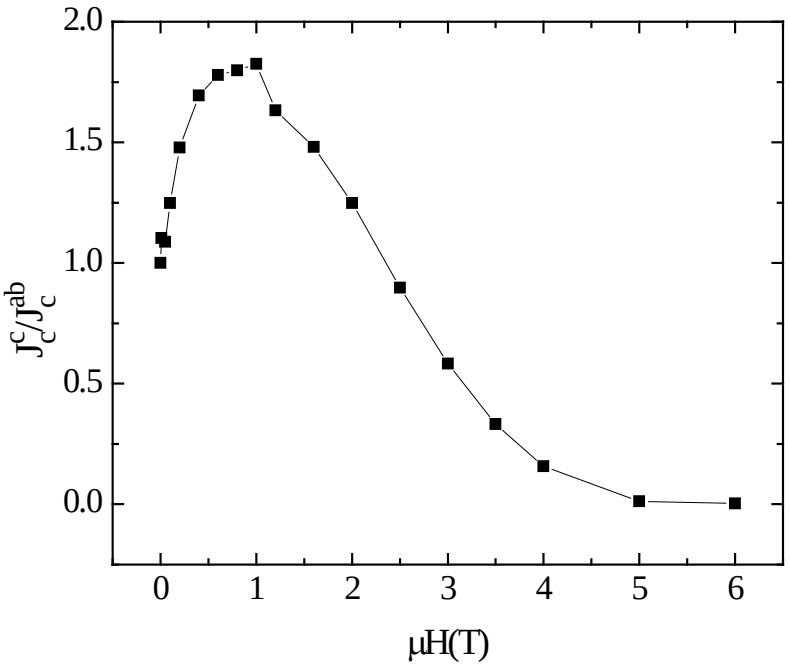

Figure 5-23 The ratio J_c^c/J_c^{ab} of the 1.0 μm BZO-doped YBCO film film at 77.3 K.

5.2.3.2 Model of angular dependence of J_c

Recently, an anisotropic scaling approach of Blatter et al has been widely used to explain isotropic point defects causing a broad peak in $J_c(\theta)$[4, 5]. However, the Blatter approach fails to fit with our data of $J_c(\theta)$ where extrinsic pinning is dominant at low applied fields as shown in Figure 5-20 and Figure 5-21.

In this section, the vortex path model developed by Long et al. [6, 7] is applied to our $J_c(\theta)$ data and there is quite a good fit with our data. The idea is that the vortex follows a path across the film, which is determined by local energy minima, but after many steps and the sum of many vortices it can be interpreted as a statistical process. The vortex path can be seen

as a random walk in the general direction of the external magnetic field. In this model, the $J_c(\theta)$ is described by Gaussian and Lorentzian statistical distributions

$$J_c(\theta) = \frac{J_c}{\Gamma_1} cosec^2\theta . exp\left(\frac{-cot^2\theta}{2\Gamma_1^2}\right) \text{ (Gaussian distribution)}$$

$$J_c(\theta) = \frac{J_2\Gamma_2}{cos^2\theta+\Gamma_2^2 sin^2\theta} \text{ (Lorentzian distribution)}$$

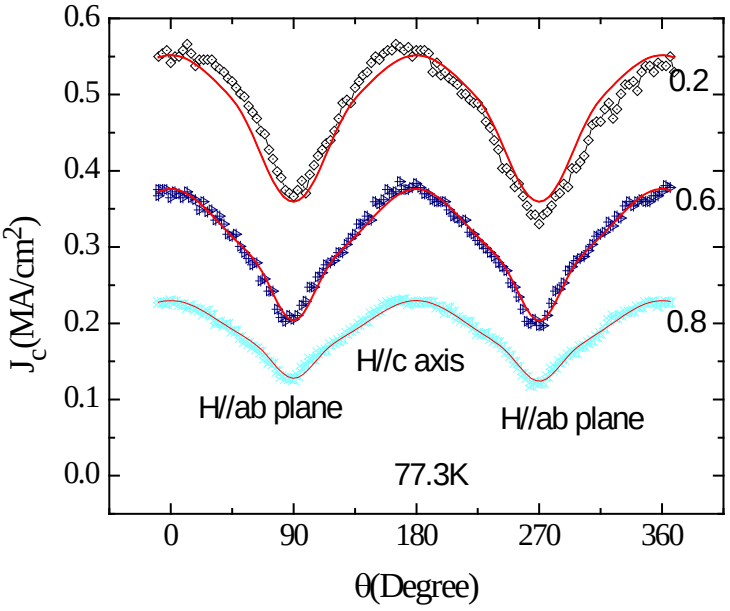

Figure 5-24 Angular dependence of J_c of BZO-doped YBCO film at applied fields of 0.2, 0.6 and 0.8 T (indicating on the right hand side of each curve), red solid line is fitting curve with vortex path model eq(5.1)

The $J_c(\theta)$ data of our sample cannot be fitted with a single function at all applied fields. A total function of Gauss and Lorentz has been used for our fitting curve by $J_c(\theta) = J\left(\frac{J_c}{\Gamma_1} cosec^2\theta . exp\left(\frac{-cot^2\theta}{2\Gamma_1^2}\right) + \frac{J_2\Gamma_2}{cos^2\theta+\Gamma_2^2 sin^2\theta}\right)$ (5.1). This equation describes well $J_c(\theta)$ of BZO-doped YBCO sample at low applied field from 0.2 T to 2.5 T as shown in Figure 5-24 and Figure 5-25 and high applied field from 2.5 to 5 T as shown in Figure 5-26 (red solid line).

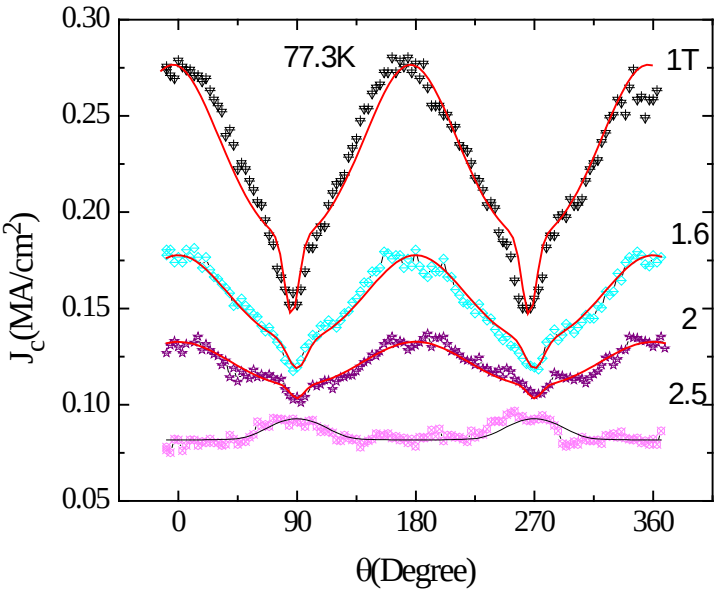

Figure 5-25 Angular dependence of J_c of BZO-doped YBCO film in applied fields of 1.0, 1.6 and 2.0 and 2.5 T (indicated on the right hand side of each curve), red solid line is fitting curve with vortex path model eq(5.1)

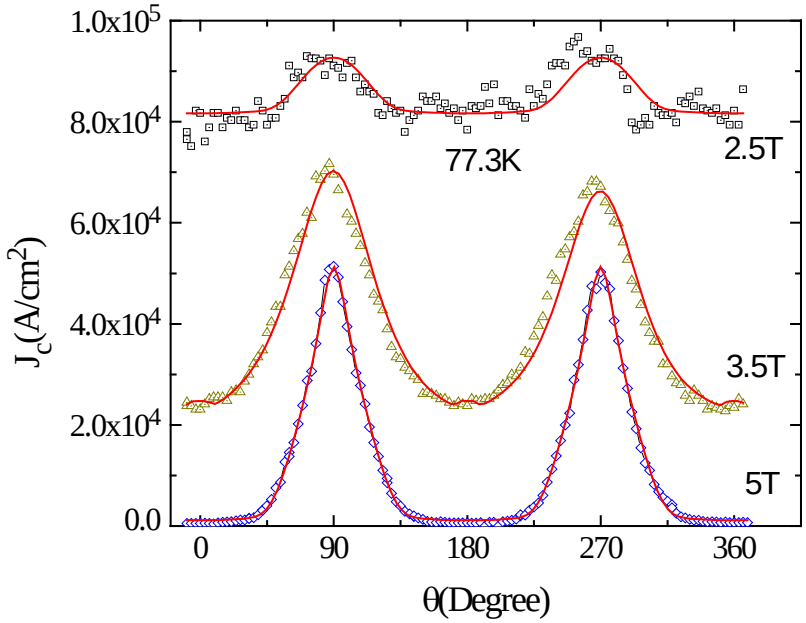

Figure 5-26 Angular dependence of J_c of BZO-doped YBCO film in applied fields of 2.5, 3.5 and 5.0 T (indicated on the right hand side of each curve), red solid line is fitting curve with vortex path model eq(5.1).

5.2.4 Irreversibility and vortex melting lines of BZO-doped YBCO films

5.2.4.1 Magneto-resistance method for irreversibility line

Aside from T_c, other important parameters of superconductors are the melting line for vortex matter $T_m(B)$, which separates the vortex-glass and vortex-liquid phase [8] and the irreversibility line which is more arbitrary depending on certain criteria. The technique used in this work to determine the irreversibility line is magneto-resistance which was used previously for un-twinned and twinned single crystals of YBCO by Kwok et al [9]. The magneto-resistance measurement of 1μm BZO-doped YBCO film was carried out using the same bridge as for the angular dependence of J_c measurement. The temperature dependence of the resistance for the BZO-doped YBCO film is shown in Figure 5-27 in applied magnetic field up to 6 T for magnetic fields perpendicular to the film surface (H//c) and Figure 5-28 for *H*//*ab*. The irreversibility temperature T_i value is identified as the peak in the derivative of the resistive transition of Figure 5-27 and Figure 5-28, an example of this is shown in Figure 5-29 at 0 T. This inflection point describes the temperature at which the slope in the resistive transition is a maximum. The width of the peak visually demonstrates the sharpness of the superconducting transition at that field.

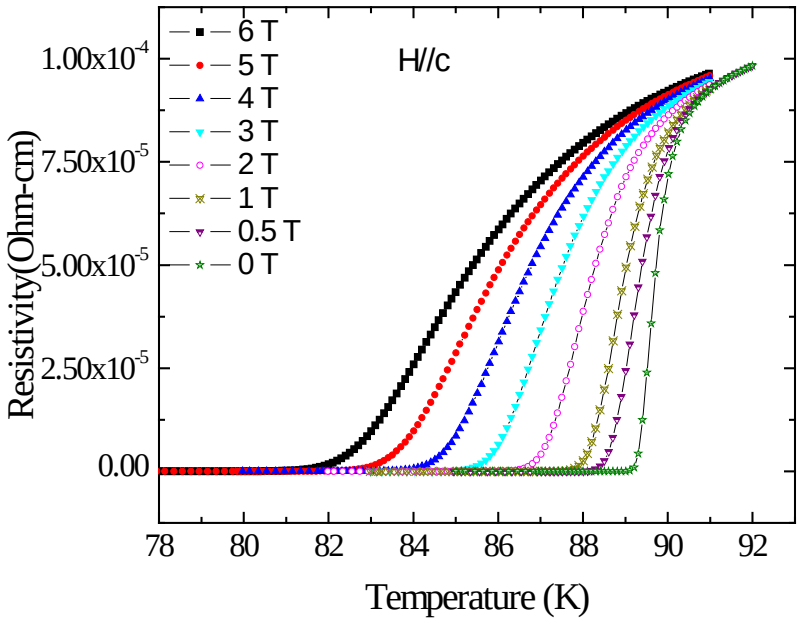

Figure 5-27 Resistivity transition of 1μm BZO-doped YBCO film in magnetic fields of 0, 0.5, 1, 2, 3, 4, 5 and 6 T with H//c

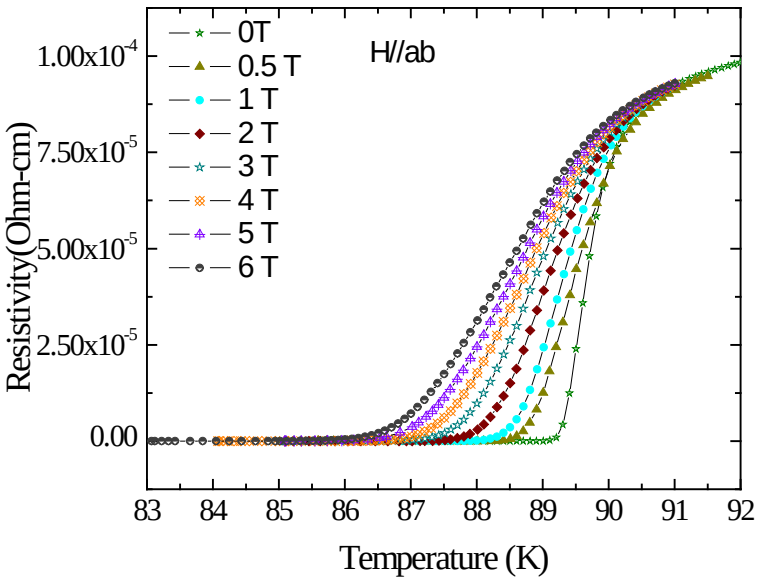

Figure 5-28 Resistivity transition of 1μm BZO-doped YBCO film in magnetic fields of 0, 0.5, 1, 2, 3, 4, 5 and 6 T with *H//ab*

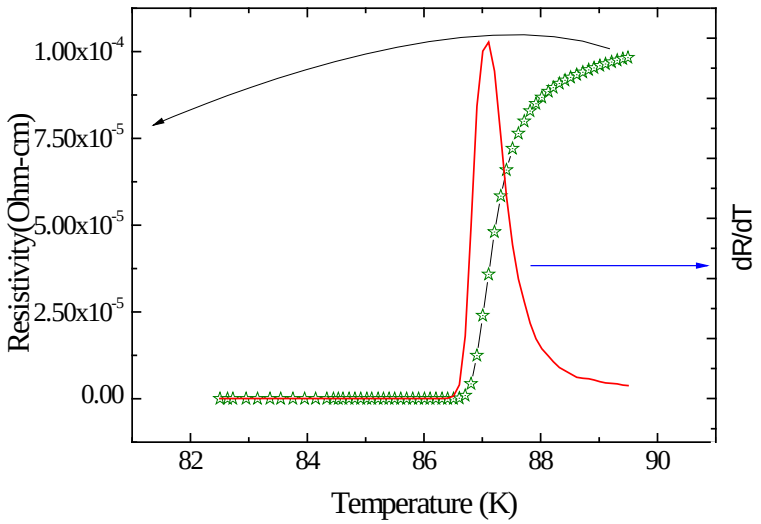

Figure 5-29 Definition of transition temperature from inflection peak of dR/dT (right *x* axis)

Figure 5-30 shows the irreversibility line of a 1μm BZO-doped YBCO film in applied fields paralleled to the c-axis and the ab-plane of the YBCO.

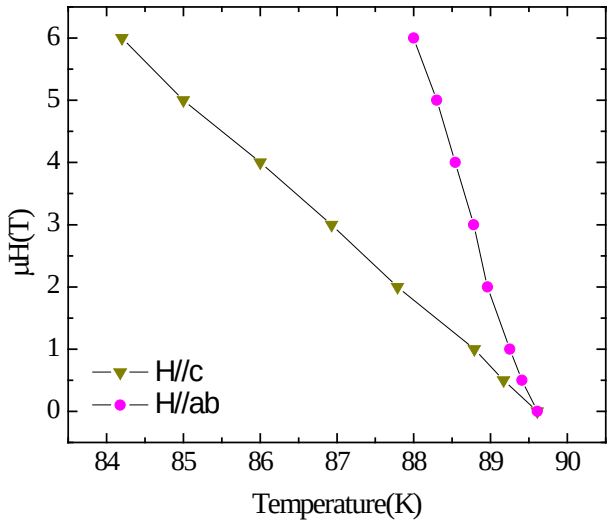

Figure 5-30 Irreversibility line of 1μm BZO-doped YBCO film for H//c and H//ab

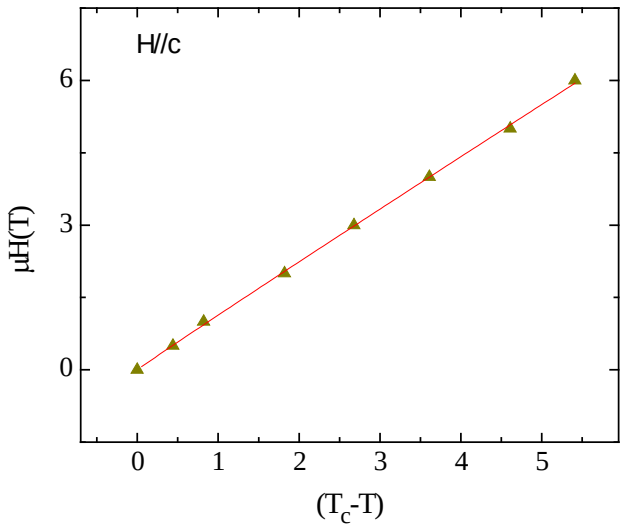

Figure 5-31 Dependence of H_i on (T_c-T), red solid line is fitting of H_i~(T_c-T)$^{\beta}$ for H//c

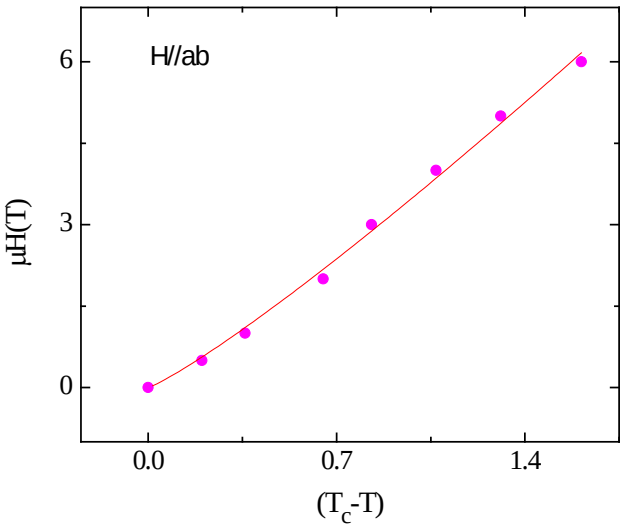

Figure 5-32 Dependence of H_i on (T_c-T), red solid line is fitting of H_i~(T_c-T)$^{\beta}$ for H//ab

The dependence of irreversibility field H_i on (T_c-T) is shown in Figure 5-31 and Figure 5-32 for H//c and H//ab, respectively. The data is then fitted with H_i~(T_c-T)$^{\beta}$, with β = 0.98 and 1.15 for H//c and H//ab, respectively. This value of β implies our H_i vs (T_c-T) is almost linear with small β of 1 which is smaller than 2 or 4/3 for pure YBCO [10].

5.2.4.2 Third-harmonic *AC* susceptibility method for votex melting line

The simplest technique to determine the melting line is by using the third-harmonic *AC* susceptibility measurement which was presented by Crisan et al [11] for $TlBa_2Ca_2Cu_3O_{10}$ superconductor. The idea is that the out-of-phase susceptibility response of a superconductor, χ", is a measure of the total dissipation, linear and nonlinear, while the third-harmonic susceptibility, χ_3, is a measure of the nonlinear dissipation only [12]. Experimentally, the vortex-glass and vortex-liquid melting transition can be examined by measuring the temperature dependence of both χ" and χ_3 in the presence of *DC* field with very low ac field amplitude. An example of such measurement is shown in Figure 5-33 for 1.2 μm thick BZO-doped YBCO film in DC magnetic field of 5 T with ac field amplitude of 0.1 Oe and AC frequency of 100 Hz. It is clearly seen that onset temperature of χ", T_1 is higher than the onset of temperature of χ_3, T_2. This means that, between T_1 and T_2, there is dissipation (χ"> 0), but it is a linear (ohmic) one since χ_3= 0. Therefore, by using low current density (low AC field amplitude), we could probe the vortex liquid phase for $T_1 < T < T_2$, and the vortex glass phase for temperature below T_2 (where $\chi_3 > 0$). The onset temperature of χ_3 was taken as the melting temperature of the vortex glass phase. Figure 5-34 shows such measurement performed at various DC fields for BZO-doped YBCO film and for YBCO film. One can see an improvement of the melting line of BZO-doped YBCO film in comparison with that of pure YBCO film.

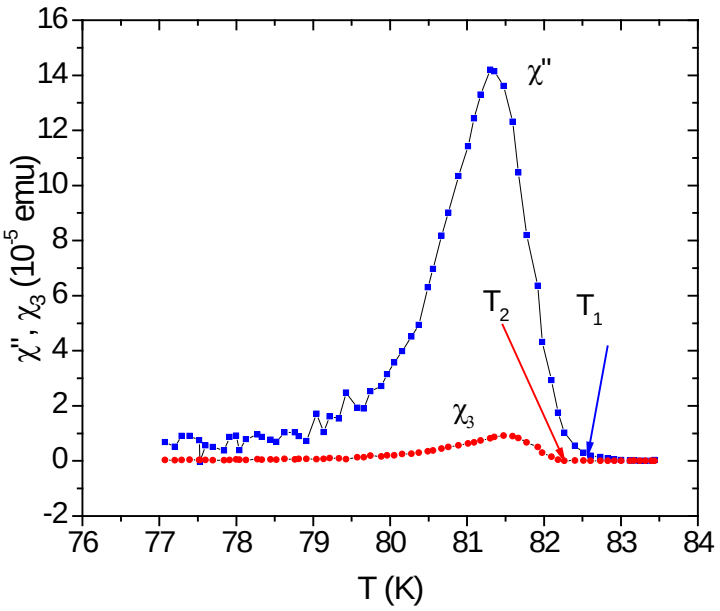

Figure 5-33 Temperature dependence of out-of-phase susceptibility and third-harmonic susceptibility of 1.2 μm BZO-doped YBCO film in a DC field of 5 T

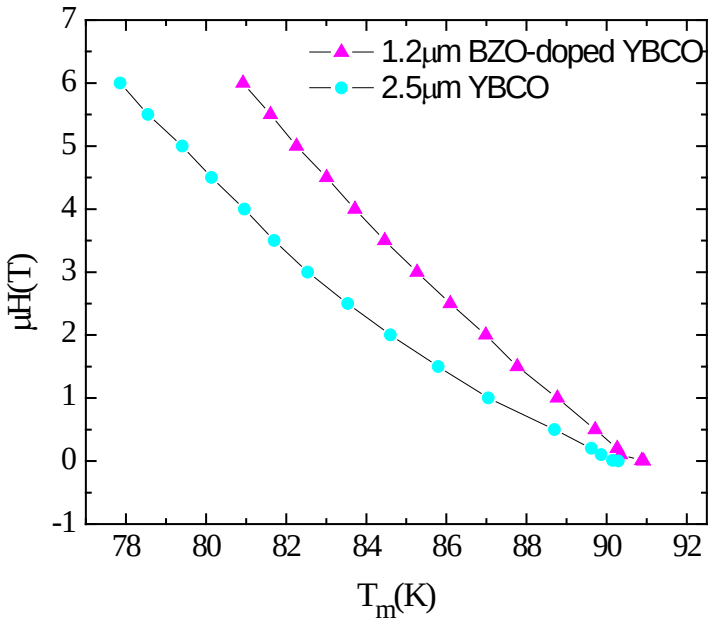

Figure 5-34 Melting line of 1.2 μm BZO-doped YBCO film (triangles) and of a 2.5 μm YBCO film.

5.2.5 Microstructure of BZO-doped YBCO films

5.2.5.1 X-ray diffraction

XRD 2θ scan of BZO-doped YBCO films with various thickness of 0.4, 2.0 and 2.5 μm is shown in Figure 5-35, Figure 5-36 and Figure 5-37, respectively. XRD of the films shows epitaxial growth with YBCO (00*l*) peaks and a BZO (002) peak. However, in the 2.5 μm thick film, as seen in Figure 5-37, instead of only (00l) peaks, one can see also the (103) peak which appeared also in thick pure YBCO films. The (103) peak in thick films implies regions mis-oriented from the c-axis to the ab-plane or it may refer to the appearance of micro-precipitates on the thick film surface.

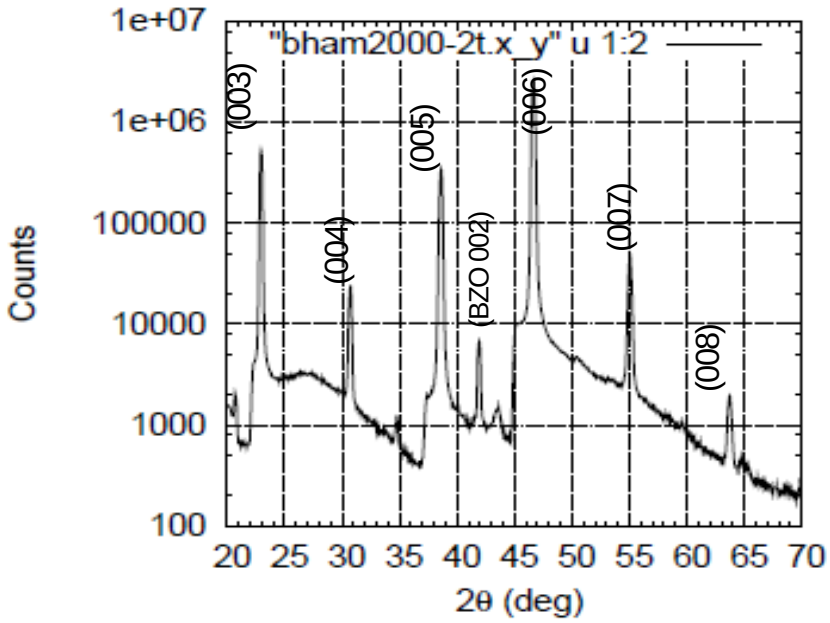

Figure 5-35 XRD pattern of 0.4μm BZO-doped YBCO film

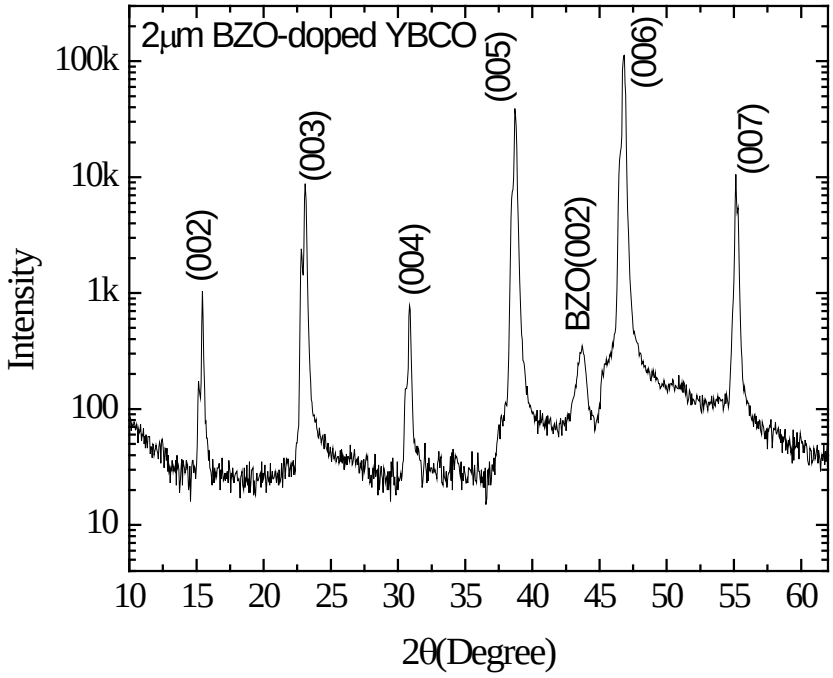

Figure 5-36 XRD pattern of 2 μm BZO-doped YBCO film

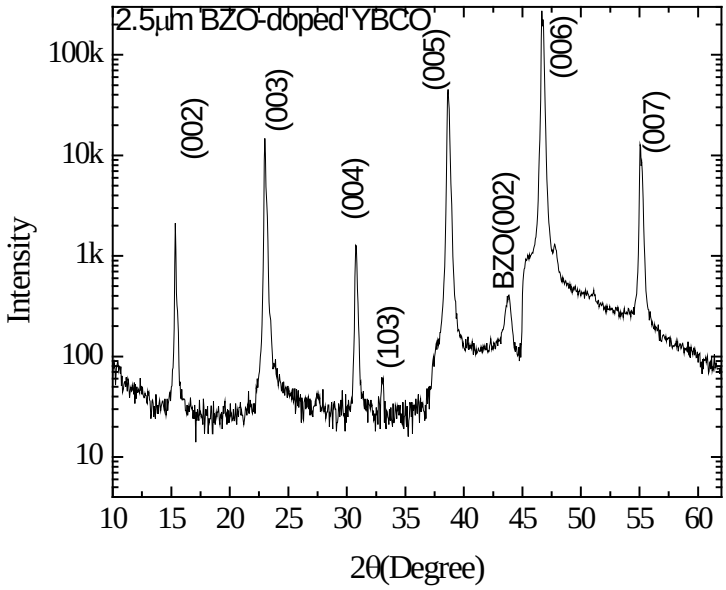

Figure 5-37 XRD pattern of 2.5 μm BZO-doped YBCO film

5.2.5.2 SEM images

A SEM image of the surface of the 0.4 μm BZO-doped YBCO film is shown in Figure 5-38; as can be seen, the surface of the film contains nano-precipitates and pores which are characteristic of YBCO films.

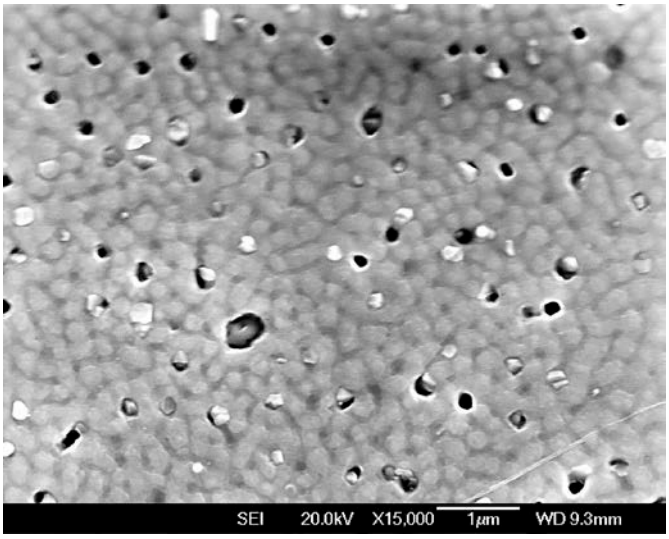

Figure 5-38 Surface SEM image of 0.4μm BZO-doped YBCO film at magnification of 15k.

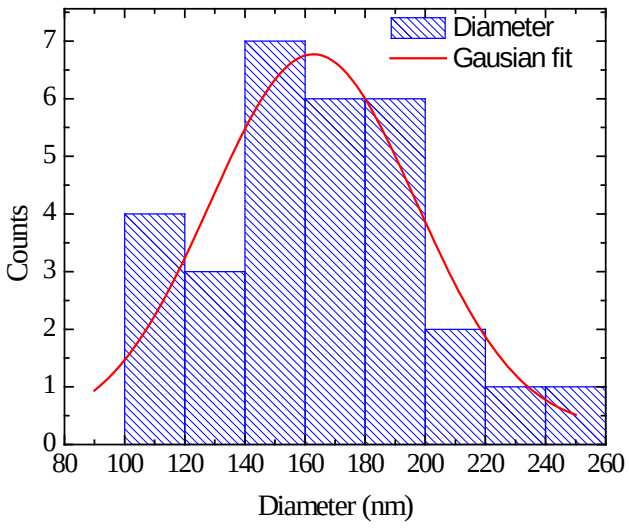

Figure 5-39 Distribution of nano- precipitates on the 0.4μm BZO-doped YBCO film surface

Figure 5-39 shows the distribution diagram of the particulates on the film surface of the 0.4 μm thick film with the average diameter of the particulates of 163 nm.

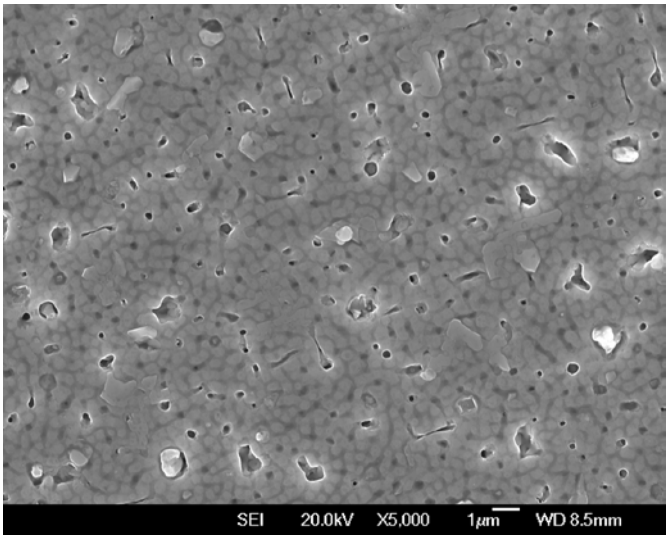

Figure 5-40 Surface SEM image of 1.2 μm BZO-doped YBCO film

By increasing the film thickness, the surface morphology is also changed as can be seen in SEM images in Figure 5-40 and Figure 5-41 of the films with the thickness of 1.2 and 2.5 μm, respectively. When the film thickness increases, the pores of the film surface decrease and the thick film surface is smoother than the thin film surface. A reverse case for particulates is observed, when the film thickness increases, the size of particulates also increases.

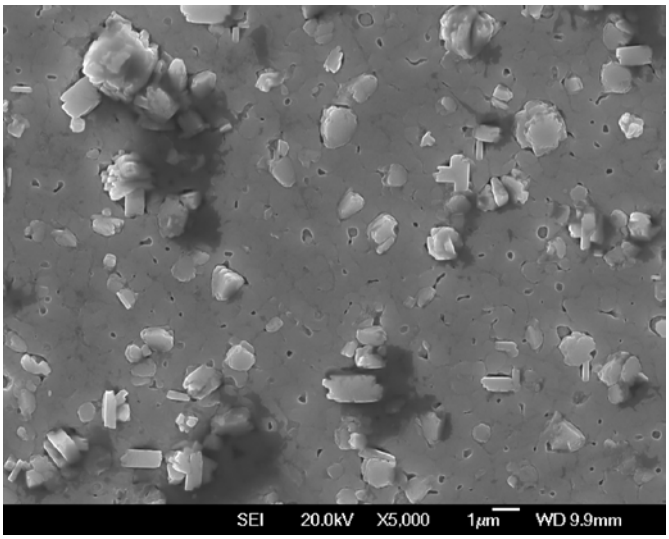

Figure 5-41 SEM image of 2.5 μm BZO-doped YBCO film

While the average diameter of the particulates of 163 nm is estimated for the 0.4 μm film, a much larger average diameter which is 990 nm of the particulates is observed for the 2.5 μm film as shown in Figure 5-42. The increase in the size of particulates and micro-pores is likely to lead to a decrease in J_c with the increase of film thickness [13].

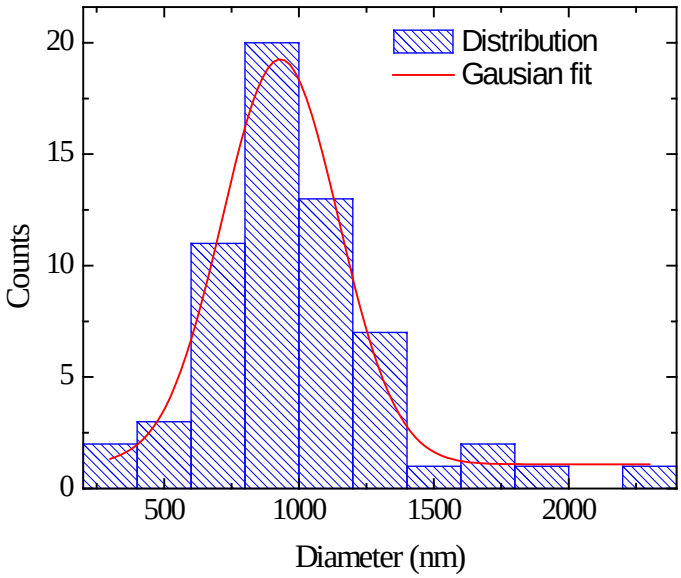

Figure 5-42 Distribution of precipitates on the 2.5 μm BZO-doped YBCO film surface, solid line is Gaussian distribution fit.

5.2.5.3 TEM images

EDX mapping was first carried out in STEM mode on cross section TEM sample to determine element mapping of the cross section of the 1.2 μm BZO-doped YBCO film. The EDX mapping of the area in the middle of the film is shown in Figure 5-43. Figure 5-43a is the STEM picture of the BZO-doped YBCO film with black and white nano-precipitations, some of them are marked by circles. The element mapping revealed that the black and white areas are Cu-rich or Y-rich phases. Figure 5-43b is the map of Ba element, area marked by circles is the Ba-deficient phase areas which are precipitates in the STEM image. Figure 5-43c and e are the maps of Cu and Y elements, respectively. There are rich Cu or Y phase marked by circles which are at the positions of the poor Ba phase. The maps of O and Zr elements are shown in Figure 5-43d and f which indicate a very homogenous distribution all over the film.

The appearance of Y- and Cu- rich phases which are possibly Y_2O_3 and CuO or CuO_2 phases together with BZO doped phase could all act as pinning centres in the film. Cross section TEM images of the film as shown in Figure 5-44 to Figure 5-52 show more clearly the presence of BZO nano-rods and precipitates of Y-rich phase or Cu-rich phase.

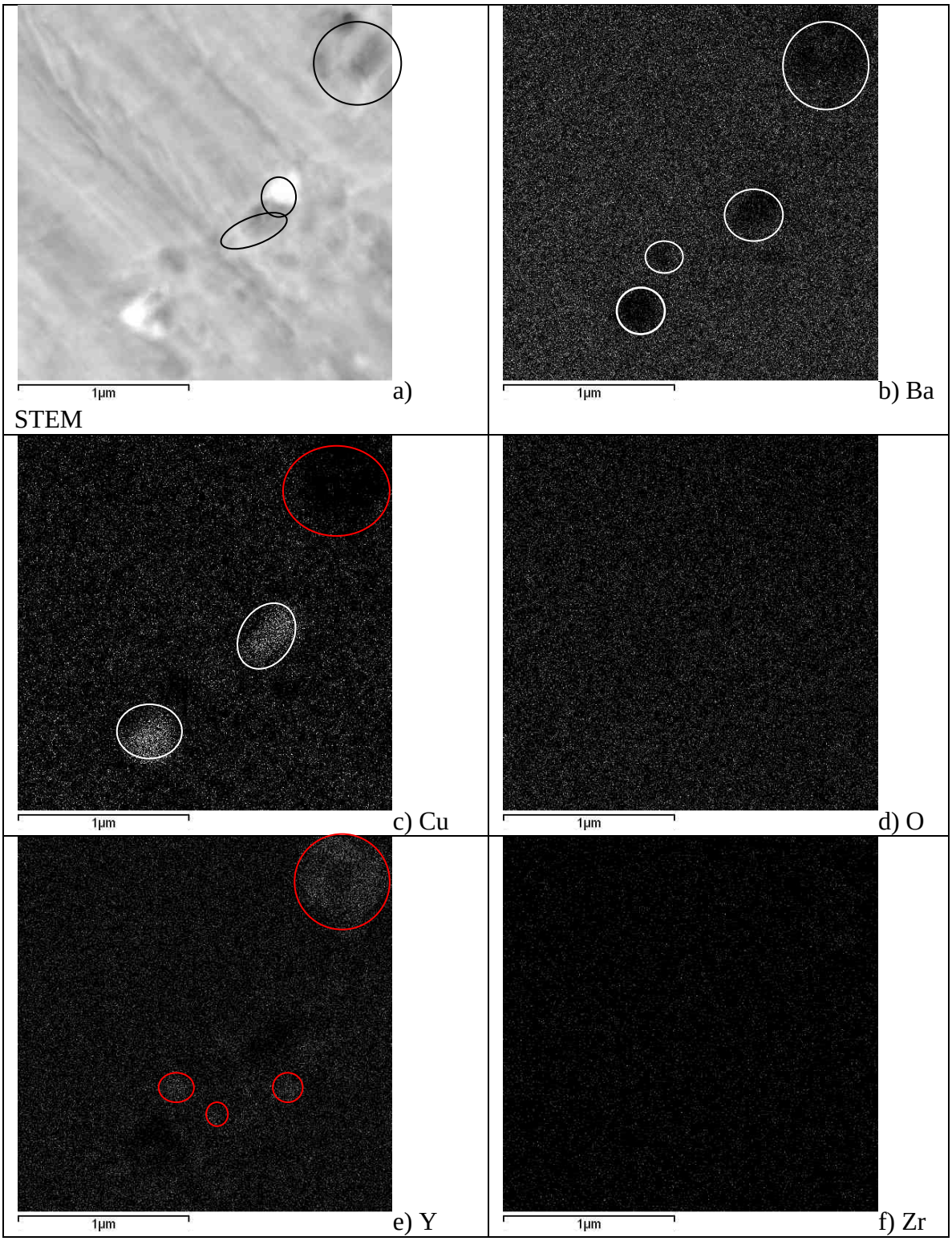

Figure 5-43 EDX mapping of the BZO-doped YBCO film using STEM mode, a) STEM image, b) mapping of Ba, c) mapping of Cu, d) mapping of O, e) mapping of Y and f) mapping of Zr

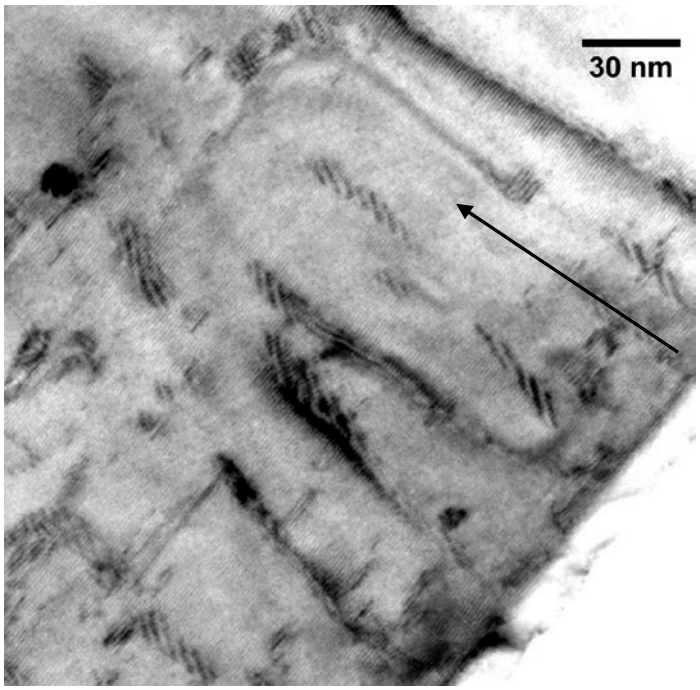

Figure 5-44 Cross section TEM image of BZO-doped YBCO film, arrow shows the c-axis of YBCO

Figure 5-44 to Figure 5-47 show cross section TEM images of the BZO-doped YBCO film. One clearly see the growth of BZO nano-rods which started growing from the STO substrate (Figure 5-44 and Figure 5-46) with length of several nanometres to hundreds nanometre. The BZO nano-rods are not only presence in the boundary area but in the whole film as shown in Figure 5-45 and Figure 5-46

Apart from the growing of BZO nano-rods, the formation of a Y_2O_3 nano-particle is also seen in Figure 5-50, which is ab-plane aligned. Y_2O_3 is naturally formed during deposition of YBCO films in our case. In a recent publication [14] Y_2O_3 was deliberately added to BZO-doped YBCO target and the combination of Y_2O_3 and BZO was shown to be very effective as pinning centres. The c-axis aligned CuO is also found in Figure 5-51 which has c lattice length of about 0.5 nm. Many more defects are also present in the film such as staking fault which is shown in Figure 5-52. Not only are those precipitates effective flux pinning centres, but they can also disrupt the YBCO matrix around them to produce even more potential

pinning centres. An example is shown in Figure 5-48, one can see the distortion of the ab-plane close to the BZO nano-rod.

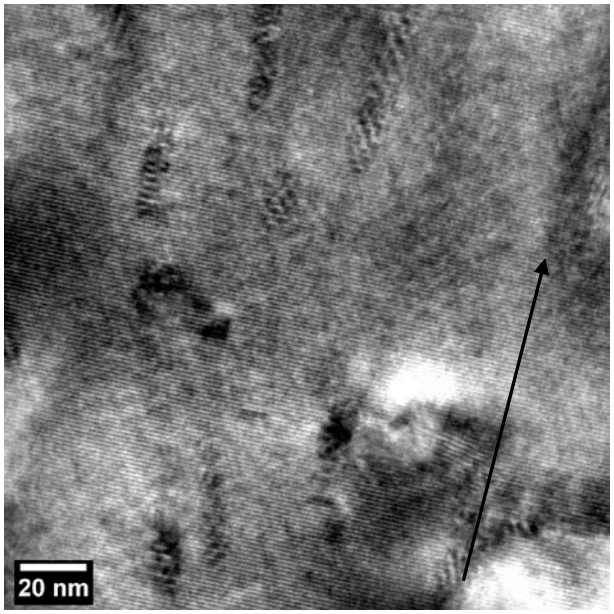

Figure 5-45 Formation of BZO nano-rods in the mildle area of the film, arrow shows c-axis.

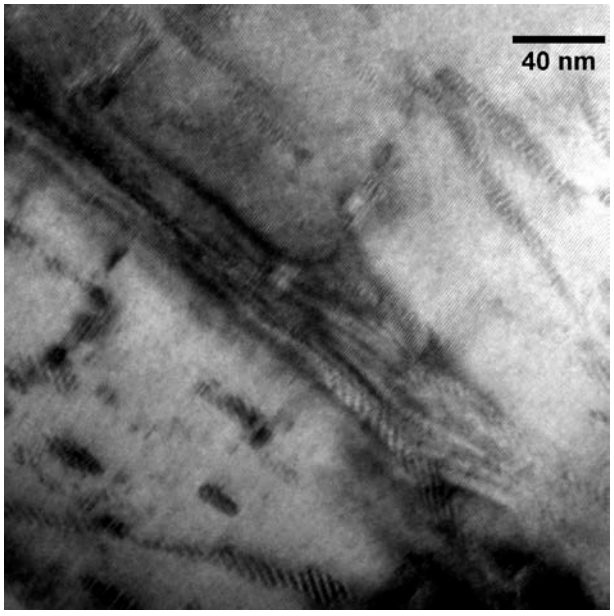

Figure 5-46 Short and long nano-rods grows together inside the YBCO matrix, along the c-axis.

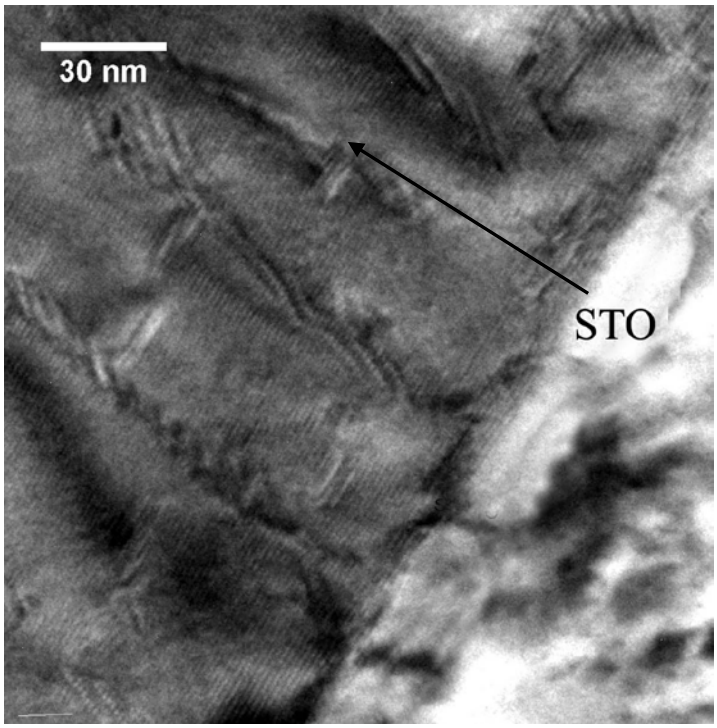

Figure 5-47 The BZO nano-rods started growing from the STO substrate, along the c-axis (arrow)

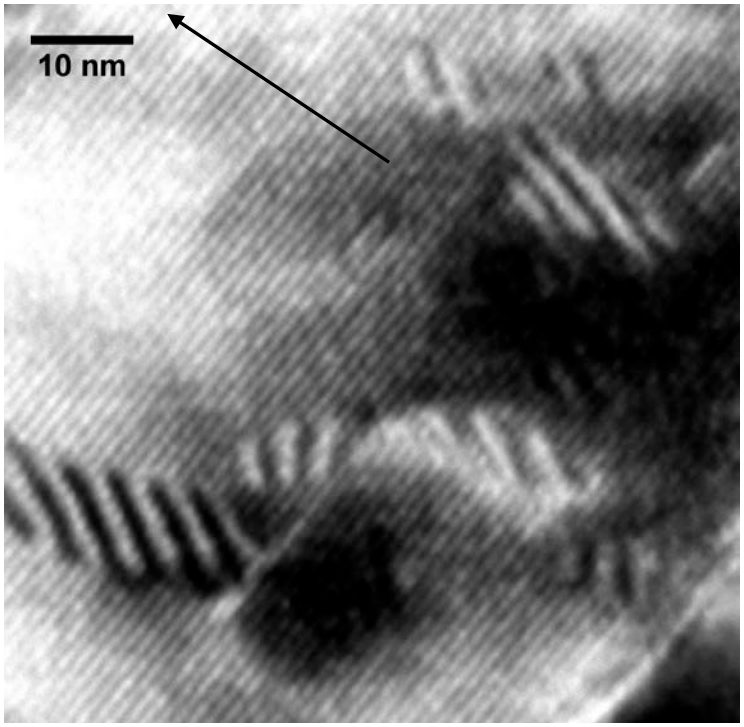

Figure 5-48 High resolution cross section TEM image

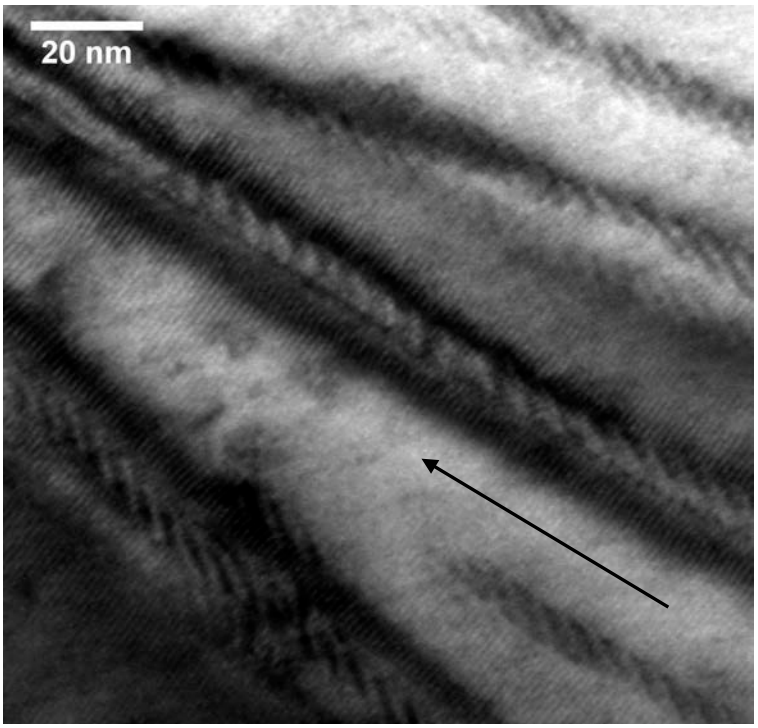

Figure 5-49 Some of the nano-rods are long, larger than the cross section of the image, arrow indicates c-axis.

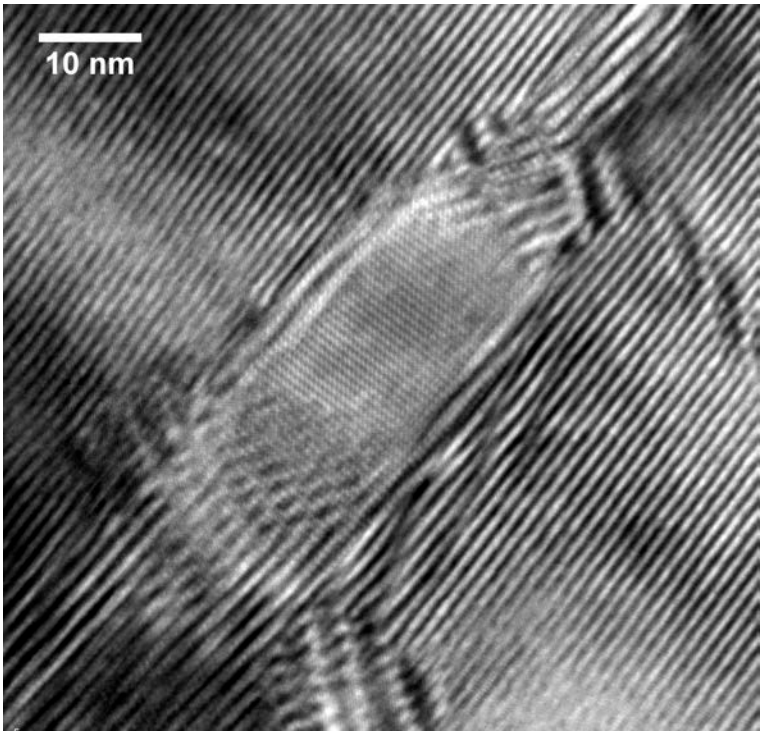

Figure 5-50 Image of a Y_2O_3 nano-particle inside the YBCO matrix.

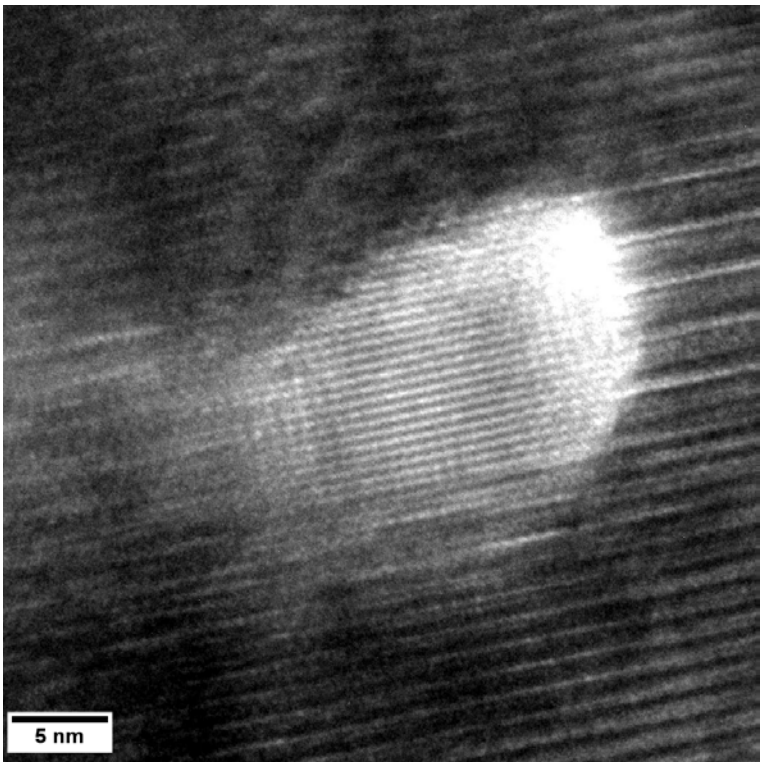

Figure 5-51 Image of CuO nano-particle inside the YBCO matrix.

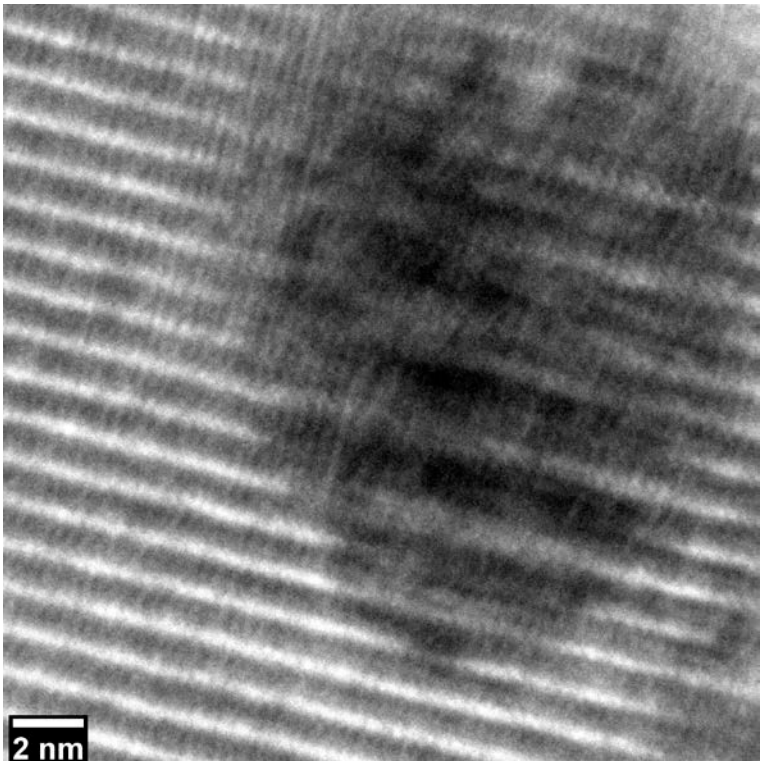

Figure 5-52 Stacking fault found in high resolution TEM image.

5.3 Combination of Ag substrate decoration and deposition of BZO-doped YBCO films

5.3.1 Optimisation of Ag nano-particles

The size of Ag nano-dots in substrate decoration mainly depends on the deposition conditions such as, substrate temperature, gas pressure and laser energy. As shown in Chapter 4, one can see that the density of Ag nano-dots increases with the increase of number of laser pulses from 5 to 45. By increasing the number of laser pulses from 15 to 30, the average diameter of Ag nanodots increases from 11 nm to 15 nm. In this section, the integration of Ag substrate decoration and BZO-doped YBCO will be investigated, Ag was deposited at 400 ^{o}C and in vacuum while BZO-doped YBCO film was deposited at the same conditions with the film in Section 5.2. As known from Chapter 4, the optimum number of laser pulses on the Ag target which leads to optimum J_c of YBCO film is 15 shots. In this section, we investigate the superconducting properties of BZO-doped YBCO films deposited on Ag decorated substrates with different number of laser shots on the Ag target.

5.3.1.1 Critical temperature of Ag decorated BZO-doped YBCO films

Critical temperature of Ag decorated films was measured by *AC* susceptibility in *AC* applied field of 0.05 Oe as shown in Figure 5-53 a, b, c, d with different number of laser shots on the Ag target of 5, 15, 30 and 40 shots, respectively. As can be seen, T_c defined as the peak of χ" is around 90K, with little dependence on different number of laser pulses of Ag. However, the sharpness of the transition changes as seen in Figure 5-54. The transition is much broader for the film on substrate decorated by 5 laser pulses of Ag and the transition is sharper when the number of Ag increases from 5 to 30 shots. The sharpest transition belongs

to the film decorated by 30 laser shots of Ag with ΔT = 0.4 K. The width of the transition is again larger when the number of laser shots of Ag increases to 40 shots with ΔT = 0.5 K.

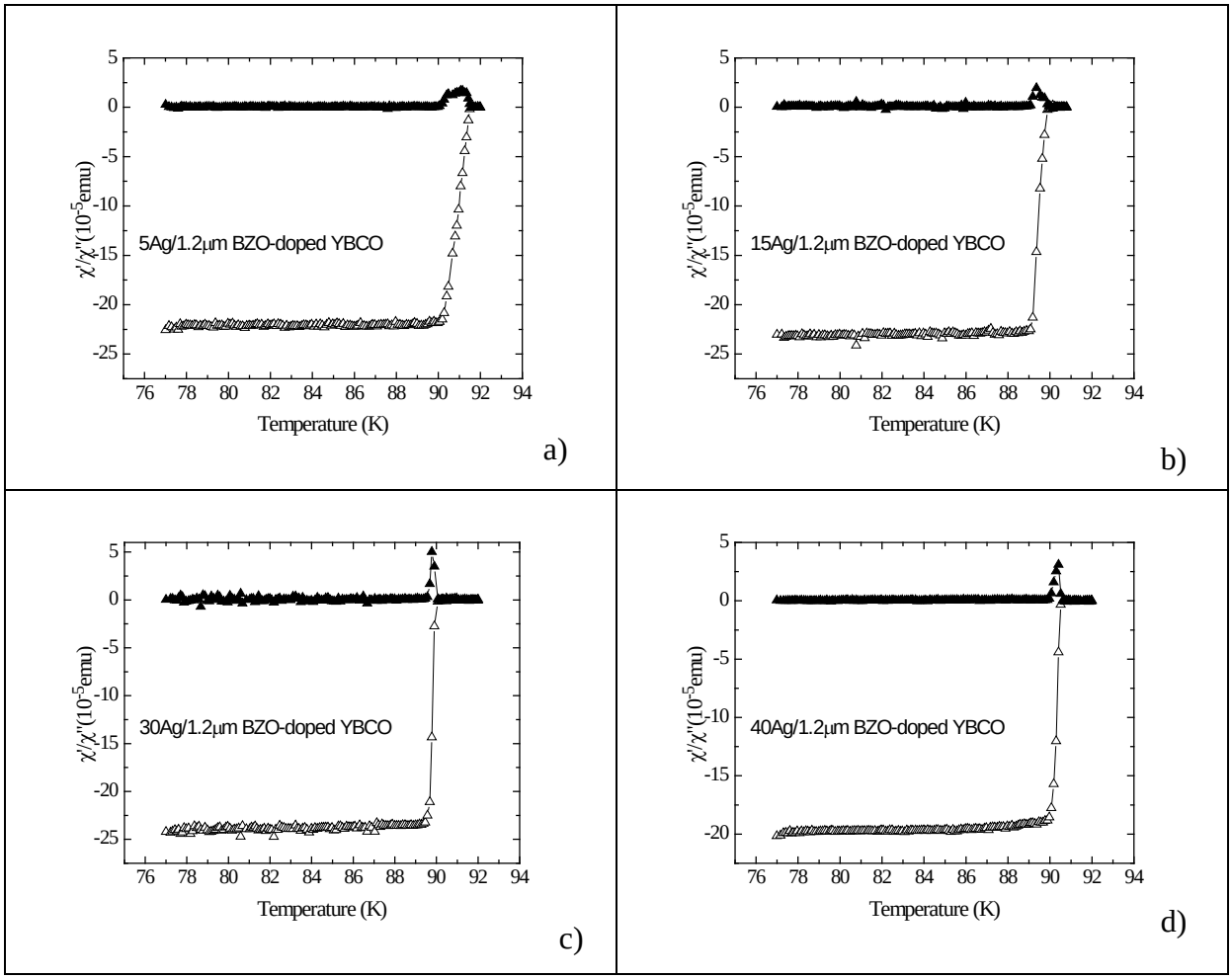

Figure 5-53 Temperature dependence of *AC* susceptibility of a) 1.2μm BZO-doped YBCO film on Ag decorated substrate with 5 laser shots on the Ag target b) with 15 laser shots on the Ag target, c)with 30 laser shots on the Ag target, d) 40 laser shots on the Ag target.

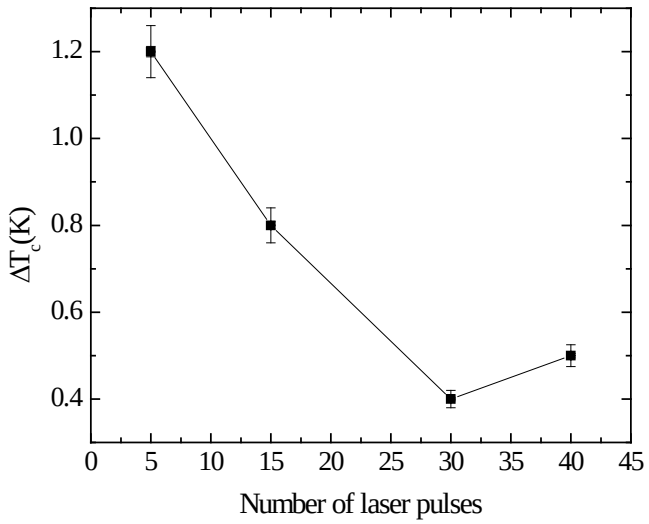

Figure 5-54 Dependence of width of T_c on number of Ag pulses on the STO substrate.

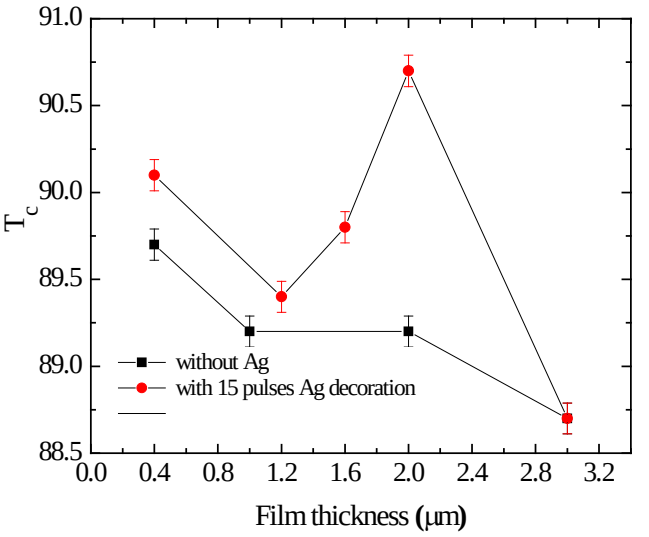

Figure 5-55 Thickness dependence of critical temperature of YBCO + 4%BZO films with (red circles) and without Ag (black squares), the substrate decoration increases T_c of the films

We also compare the value of T_c of the film with and without Ag decoration; the result is shown in Figure 5-55. As can be seen, Ag nano-dots help to retain T_c of the film close to T_c of pure YBCO film which is 90-91 K as shown in Chapter 4. The T_c of the films decorated with

15 pulses of Ag is always above that of the non-decorated films, with width of superconducting transition smaller than 1 K. The thickness dependence of T_c is also shown in Figure 5-55. The highest T_c of the Ag-decorated BZO-doped YBCO films is 90.6 K for film thickness of 2.0 μm.

5.3.1.2 Critical current density of BZO-doped YBCO film on Ag decorated substrate

We investigated the effect of the substrate decoration on J_c at 65 K measured by the magnetisation method, in which a magnetic field is applied parallels to the *c*-axis of the YBCO lattice. The dependence of J_c on the number of laser pulses on the Ag target, for the films with thickness of 1.2 μm, at different values of magnetic field (marked in the plot) is shown in Figure 5-56. As can be seen, the maximum of J_c in magnetic fields between 0 T and 1 T is given by the substrate decoration with 15 pulses (indicated by arrows), while at higher field the maximum shifts to substrate decoration with 30 pulses, which corresponds to an average diameter of Ag nano-dots of 15 nm. The field dependence of J_c of a 1.2 μm thick film with the various number of Ag pulses is shown in Figure 5-57. A significant increase in J_c in self-field and in high fields in comparison with non-decorated samples was observed for substrates decorated with 15 or 30 Ag pulses only, while J_c of the samples on substrates decorated with 5 and 45 Ag pulses is lower than in non-decorated films. It was reported in [15] that the density and mean diameter of nanoparticles play an important role in the formation of defects and enhancement of J_c. In our case, we found that the most suitable diameter of Ag nanoparticles for creating pinning centres is from 11 to 15 nm, as shown in Chapter 4.

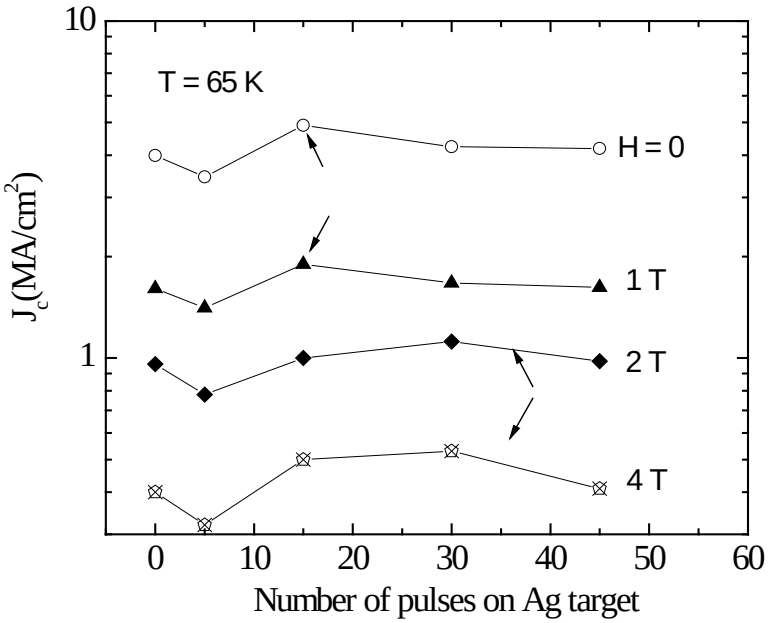

Figure 5-56 Critical current density of Ag substrate-decorated YBCO + 4%BZO films grown with different number of laser pulses on Ag target at different applied fields as marked in the plot

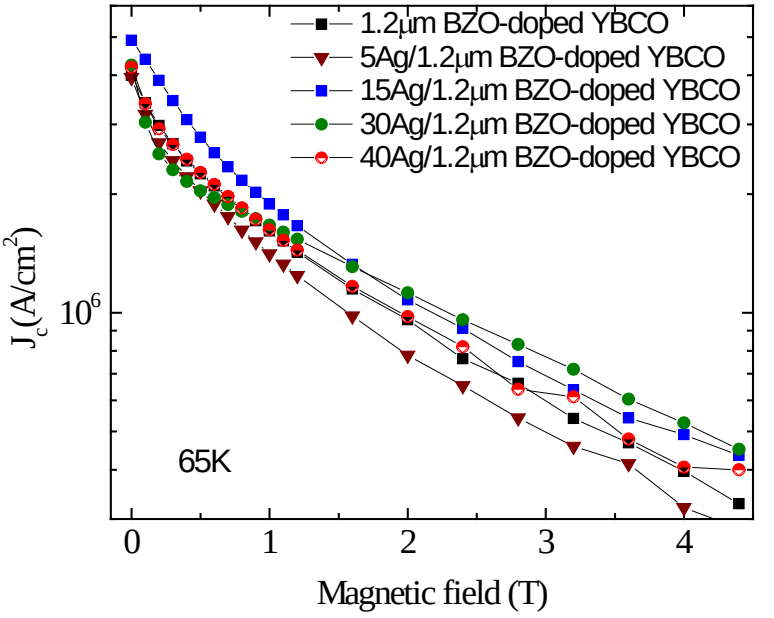

Figure 5-57 Field dependence of J_c at 65 K of Ag decorated BZO-doped YBCO films with thickness of 1.2 μm.

It is an experimental fact that J_c strongly decreases with increase of film thickness [16]. To test how this would change in the case of substrate decoration, we have chosen substrates decorated with 15 Ag pulses for the growth of YBCO + 4%BZO of different thickness from 0.4 to 3.8 μm. As can be seen in Figure 5-58, the decorated samples (black line) have J_c higher than undecorated ones (blue line) within the range of thickness from 0.4 to 3.8 μm, both at self-field and in applied field. The improvement of J_c in decorated samples in all thickness range is the evidence that Ag is effective in creating pining centres not only in thin films but also in thick films.

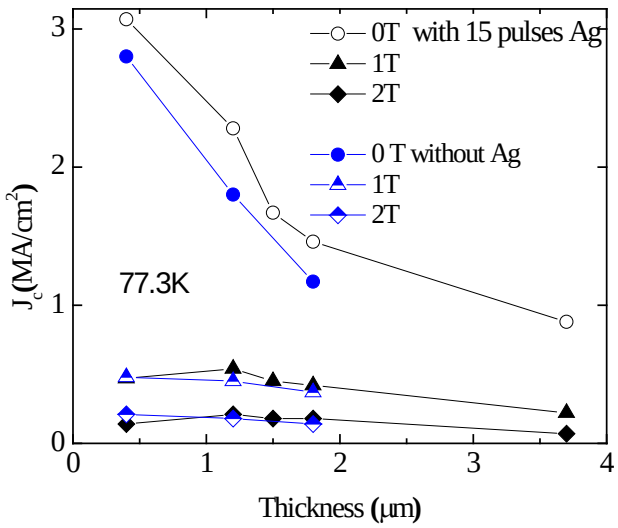

Figure 5-58 Thickness dependence of the critical current density for the films grown on substrates decorated with 15 pulses on Ag, at different applied magnetic fields from 0 to 2 T

5.3.1.3 SEM images of Ag decoration BZO-doped YBCO film

In order to investigate the effect of Ag nano-dots substrate decoration on the surface of the BZO-doped YBCO films, SEM images of two 1.2 μm BZO-doped YBCO films grown on substrates decorated by 15 laser pulses and 40 laser pulses of Ag are shown in Figure 5-59 and Figure 5-60, respectively, at the same magnification. As can be seen, the SEM images of

two films are not much different with pores and precipitates on the surface of the film. Ag nano-dots decoration does not affect the film surface as only a tiny amount of Ag is added to the surface of the STO substrate.

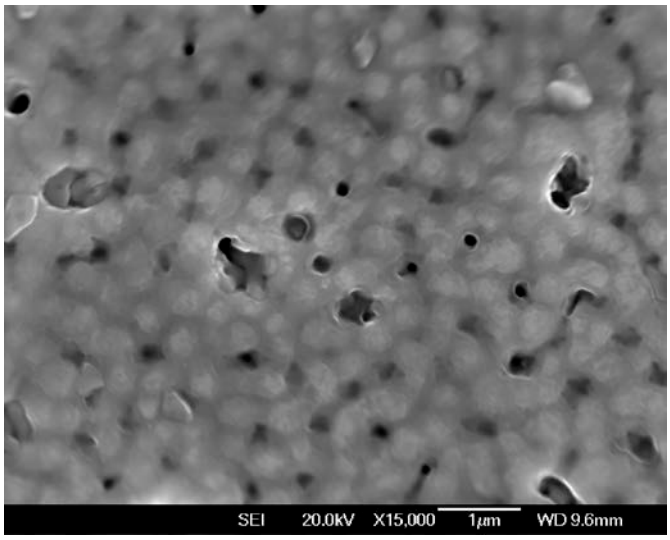

Figure 5-59 SEM image of 1.2μm BZO-doped YBCO film deposited on the STO substrate decorated with 15 laser pulses of Ag.

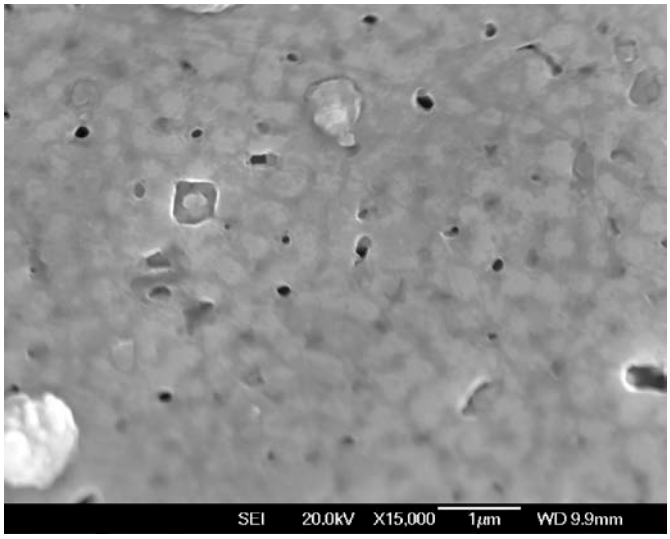

Figure 5-60 SEM image of 1.2μm BZO-doped YBCO film deposited on the STO substrate decorated with 40 laser pulses of Ag.

5.3.2 Properties of a 15Ag/BZO-doped YBCO single layer

As mentioned above, the optimum number of Ag laser pulses is about 15 for enhancement of J_c at low applied field and 30 for enhancing of J_c in higher applied field. In this section we focus on the properties of a single layer of BZO-doped YBCO film grown on 15 Ag decorated STO substrate.

5.3.2.1 Critical current density of 15Ag/BZO-doped YBCO film

As mention above, by decorating with 15 laser pulses of Ag on the STO substrate, T_c and J_c of the BZO-doped YBCO films increase a little bit in comparison with un-decorated films. In this section, the dependence of J_c on applied magnetic fields which are parallel to the *c-axis* of the YBCO matrix at temperatures of 65 K and 77.3 K is discussed for different film thickness.

Figure 5-61 to Figure 5-64 show dependence of J_c in applied fields of the BZO-doped YBCO films of different thicknesses as a function of temperature.

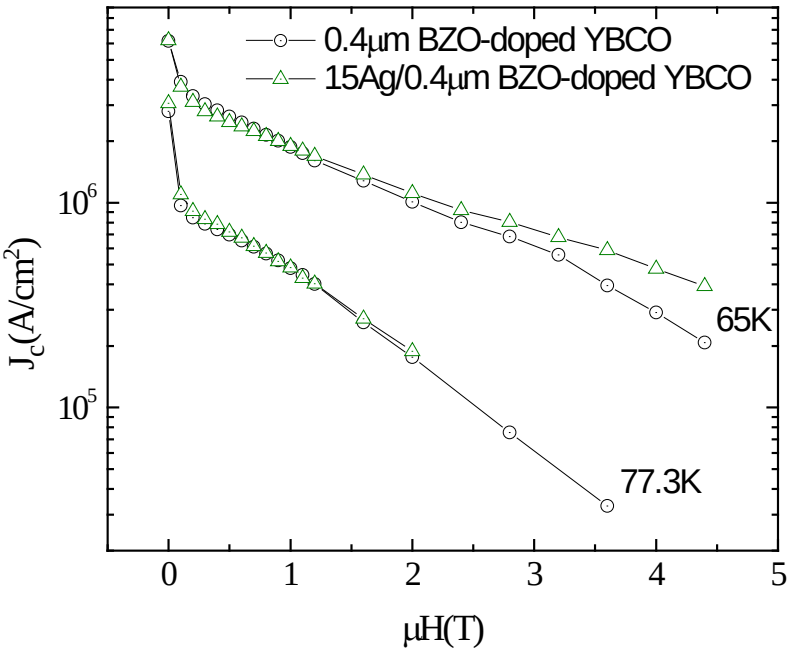

Figure 5-61 Dependence of J_c on applied magnetic fields at temperature of 65K and 77.3 K of Ag decorated film (triangles) and undecorated film (circle) with the same thickness of 0.4 μm

The dependence of J_c on applied magnetic fields of Ag decorated films and undecorated films at different thicknesses of 0.4, 1.2, 1.6 and 2.0 μm is displayed in Figure 5-61, Figure 5-62, Figure 5-63 and Figure 5-64, respectively. Figure 5-61 shows the dependence of J_c on applied magnetic fields of 0.4 μm thick of Ag decorated and undecorated film at 65 and 77.3 K. At a temperature of 65 K, the increase of J_c of the Ag decorated film is clearly seen at high applied field from 2 T and no enhancement of J_c of the decorated film at 65 K and applied field smaller than 2 T is observed. However, at 77.3K a small enhancement of J_c of the decorated film is observed at all applied fields ranging from 0 to 2.2 T. J_c data of the decorated film at applied fields higher than 2.2 T was not obtained due to too little signal of the thin sample. The J_c of the decorated film increases about 9% from 2.8 MA/cm^2 to 3.06 MA/cm^2 in comparison with undecorated film at 0 T and 77.3 K while J_c of the decorated film

increases about 34% from 0.29 MA/cm^2 to 0.39 MA/cm^2 in comparison with undecorated film at 4 T and 65 K.

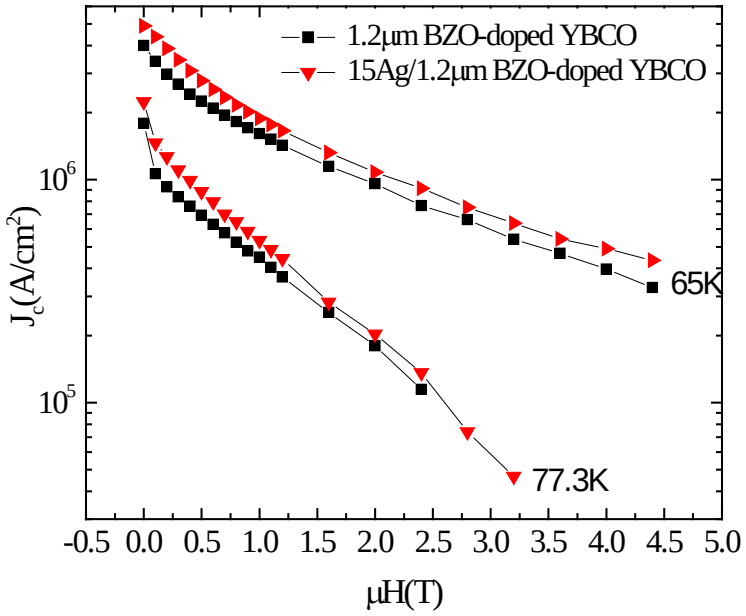

Figure 5-62 Dependence of J_c on applied magnetic fields at temperature of 65K and 77.3 K of Ag decorated film (triangles) and undecorated film (rectangular) at the same thickness of 1.2 μm

The enhancement of J_c of the Ag decorated film is more clearly seen with a thicker film in Figure 5-62 which shows the J_c dependence on applied magnetic field of a 1.2 μm thick BZO-doped YBCO film with and without Ag decoration on the STO substrate at 65 K and 77.3 K. The J_c of the decorated film at 0 T and 2 T increases by 25 % and 13 %, respectively, at 77.3 K while the enhancement of J_c of the decorated film at 65 K is about 23% at 0 T and 24 % at 4 T, respectively.

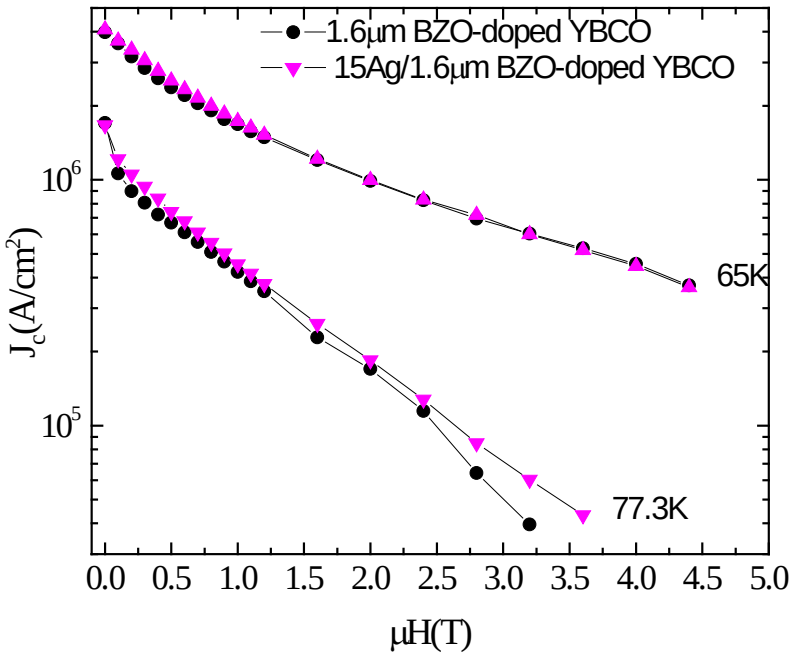

Figure 5-63 Dependence of J_c on applied magnetic fields at temperature of 65K and 77.3 K of Ag decorated film (triangles) and undecorated film (rectangular) with the same thickness of 1.6 μm

However, no increase of J_c of the Ag decorated films is observed when the film thickness increases up to 1.6 and 2 μm at a temperature of 65 K as shown in Figure 5-63 and Figure 5-64, respectively. An increase of J_c of the Ag decorated film of thickness 1.6 μm and 2 μm is only observed at high applied fields and at the temperature of 77.3 K. In more detail, the enhancement of J_c of the decorated films is about 50% and 56% for the film thickness of 1.6 μm and 2 μm, respectively, at temperature of 77.3 K and applied magnetic field of 3.2 T.

From these J_c measurements of decorated films and undecorated films, it is clear that Ag nano dots decoration increases flux pinning, which enhance J_c of the films especially at high applied field and temperatures of 77.3 K when the film is thicker than 0.4 μm.

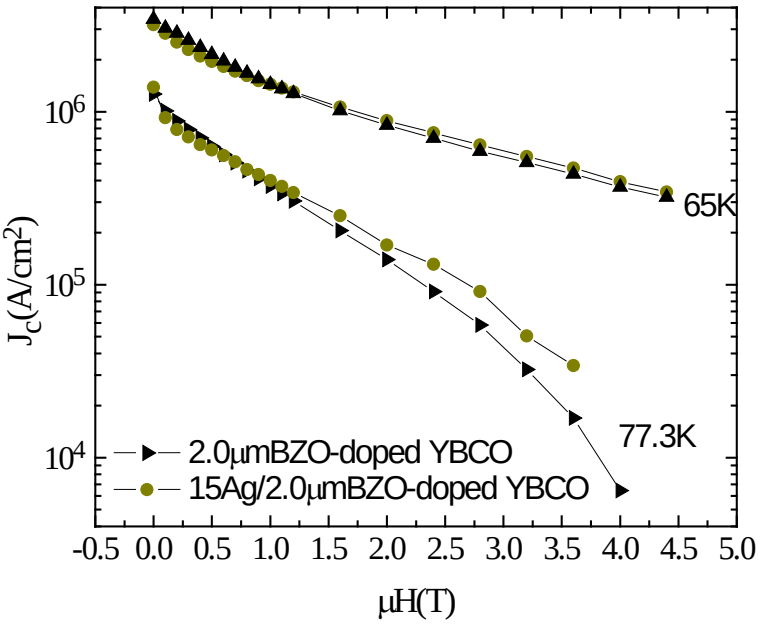

Figure 5-64 Dependence of J_c on applied magnetic fields at temperature of 65K and 77.3 K of Ag decorated film (circle) and undecorated film (triangles) with the same thickness of 2.0 μm.

5.3.2.2 Frequency dependence of J_c

The frequency dependence of J_c of a 2.0 μm thick Ag decorated BZO-doped YBCO film and a 1.2 μm undecorated BZO-doped YBCO film is shown in Figure 5-65. The frequency dependence of J_c, which was estimated from AC susceptibility measurements introduced in Chapter 4, showed that J_c of the Ag decorated film has higher values than that of the undecorated film at applied fields of 5 and 6 T, at 77.3 K and all frequencies even though the decorated film is thicker than the undecorated film. This is additional evidence that Ag is helping to increase J_c of the film especially at high applied field and 77.3 K for thick film of 2 μm. This result agrees with the field dependence of J_c of the Ag decorated film at 77.3 K and high applied field in Figure 5-64.

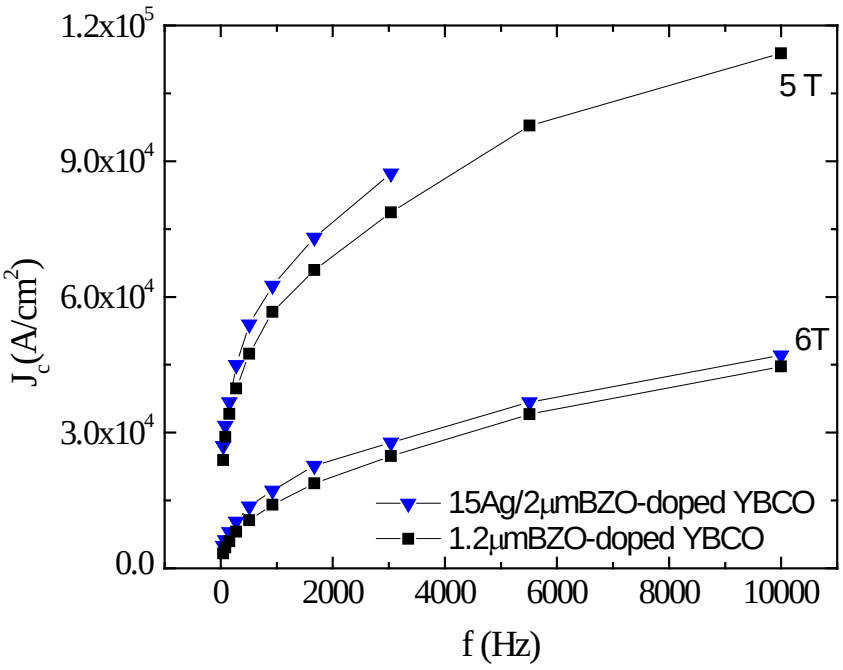

Figure 5-65 Frequency dependence of J_c of 2μm decorated film and 1.2μm undecorated film at temperature of 77.3 K and in DC applied fields of 5 and 6 T.

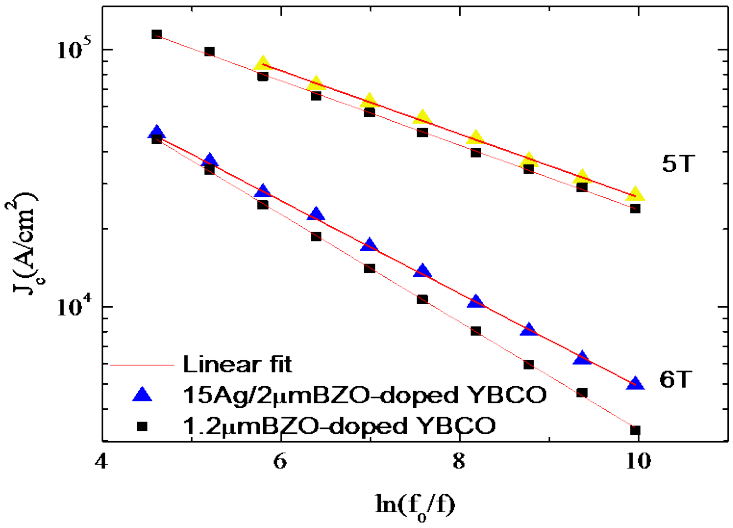

Figure 5-66 Double logarithmic plot of frequency dependence of J_c of Ag 2μm decorated film and 1. 2μm undecorated film at 77.3 K, solid line is linear fit.

The frequency dependencies of J_c for two types of films were fitted using Eq. 4.1 shown in Chapter 4 in a log-log plot as shown in Figure 5-66. The pinning potential, U_0, of the film was estimated by the slope b of the linear fitting in Eq. 4.1, the values of b and U_0 are shown in Table 5-1. The value of b and U_0 of the Ag decorated film at 4 T are not available due to an experimental limitation of the PPMS system. As can be seen, the pinning potential of the Ag decorated film is higher than the undecorated film at 5 and 6 T, and the values of U_0 of the Ag decorated BZO-doped YBCO film are also higher than Ag decorated pure YBCO films which were shown in Table 4.3 at 5 T. That we can see that the experimental observation of the combination of Ag and BZO-doped YBCO improves J_c of the films lead to calculation of increase of pinning potential.

Table 5-2 Experimental pinning potential of decorated and undecorated films calculated from slope of linear fitting.

Sample	slope (b)			U_0 (K)(k_B=1)		
	4T	5T	6T	4T	5T	6T
1.2μm BZO-doped YBCO	0.2	0.3	0.5	482	345	238
15Ag/2μm BZO-doped YBCO	na	0.3	0.4	na	350	263
1μm YBCO	0.5	1.2	na	247	142	na

5.3.2.3 Angular dependence of J_c

The angular dependence of J_c at 77.3 K, in various applied fields of a 0.4 μm Ag decorated BZO-doped YBCO film is shown in Figure 5-67, Figure 5-68 and Figure 5-69 with field criteria of 2, 1 and 0.01 μV/cm. A strong dominant c-axis pinning at low applied magnetic field and strong dominant ab-plane pinning at high applied magnetic fields is

observed in this sample which is similar to the BZO-doped YBCO undecorated film shown in Figure 5-20, Figure 5-21 and Figure 5-22.

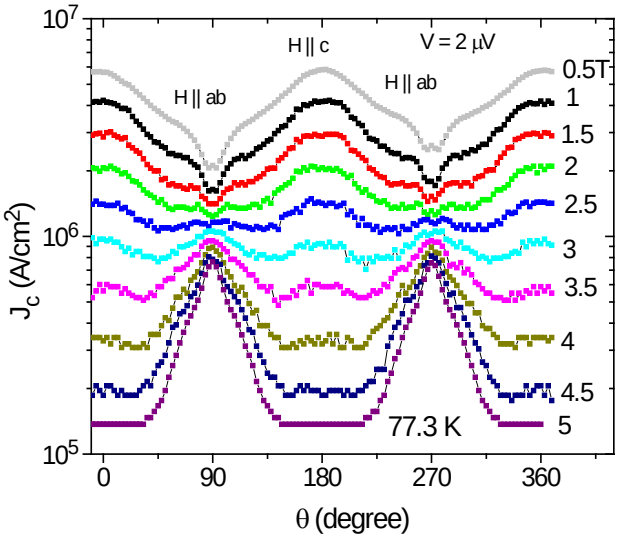

Figure 5-67 Angular dependence of J_c of 0.4μm thick Ag decorated BZO-doped YBCO film at 77.3 K and in applied fields from 0.5 T to 5 T as shown on the right hand side of each curve, using field criteria of 2 μV/cm.

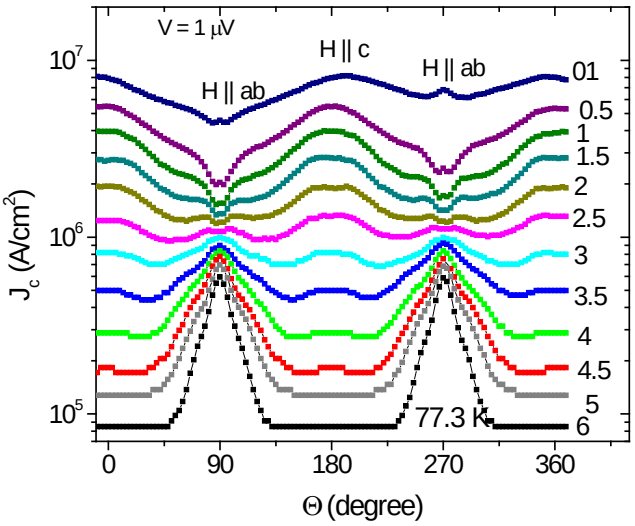

Figure 5-68 Angular dependence of J_c of 0.4μm thick Ag decorated BZO-doped YBCO film at 77.3 K and applied fields from 0.1 T to 5 T as shown on the right hand side of each curve, using field criteria of 1 μV/cm.

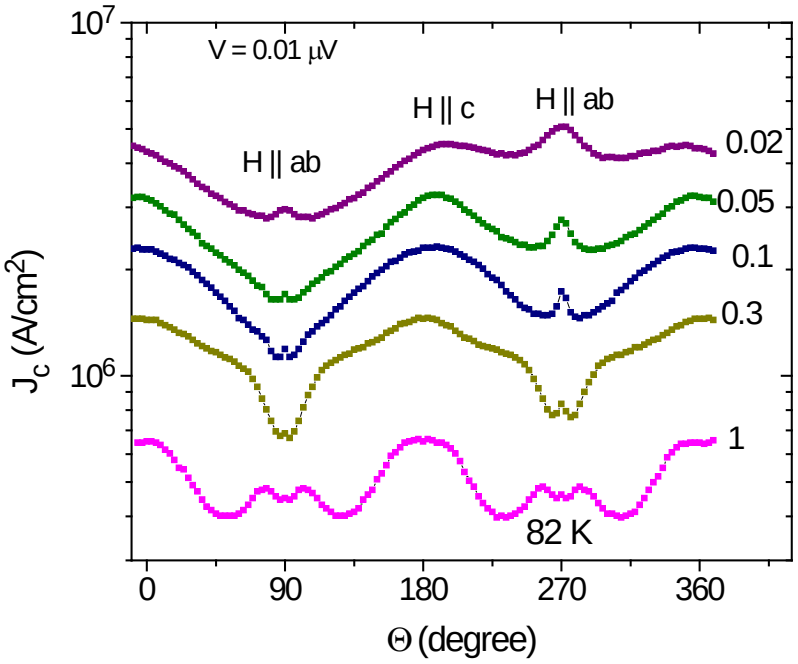

Figure 5-69 Angular dependence of J_c of 0.4μm thick Ag decorated BZO-doped YBCO film at 77.3 K and applied fields from 0.02 T to 1 T as shown on the right hand side of each curve, using field criteria of 0.01 μV/cm.

In low applied fields (smaller than 1 T), there is no peak of J_c along the ab-plane as can be seen in Figure 5-20. However, a small peak is observed along the ab-plane in the Ag decorated BZO-doped YBCO sample, especially at a low field criteria of 1 and 0.01 μV/cm, as shown in Figure 5-68 and Figure 5-69.

For comparison, in this chapter, the criterion of 1 μV was used for all the other measurements of angular dependence of J_c. The field dependence of J_c of the 0.4 μm Ag decorated BZO-doped YBCO film using transport measurement is shown in Figure 5-70 at 77.3 K. The figure shows a very high J_c for *H*//*c* and *H*//*ab* which is expected because of the very thin film.

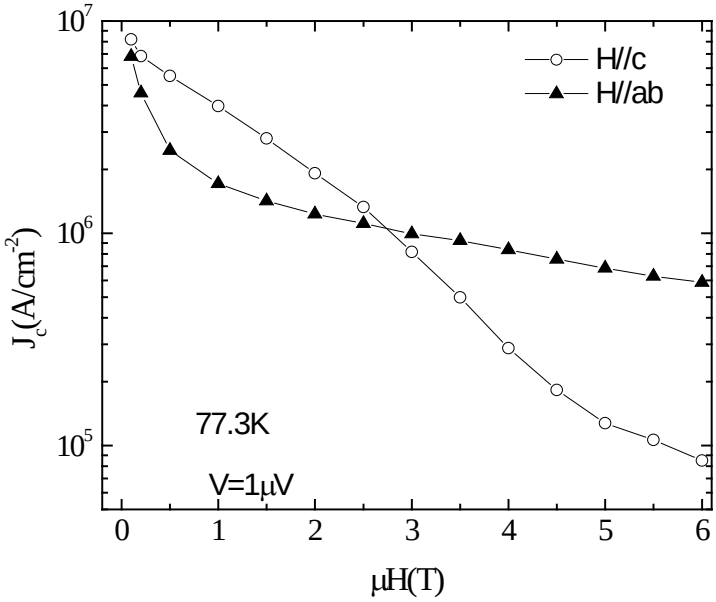

Figure 5-70 Field dependence of J_c of 0.4 μm Ag decorated BZO-doped YBCO film at *H*//*c* and *H*//*ab* at 77.3 K using 1μV/cm field criteria.

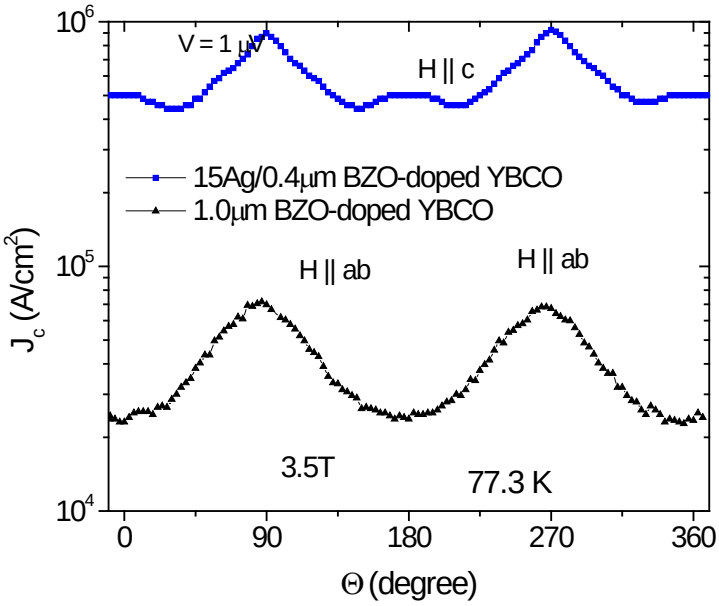

Figure 5-71 Angular dependence of J_c of the 0.4 μm-thick Ag decorated film and of 1 μm-thick undecorated film at 77.3 K and in applied field of 3.5 T, using 1μV/cm field criteria

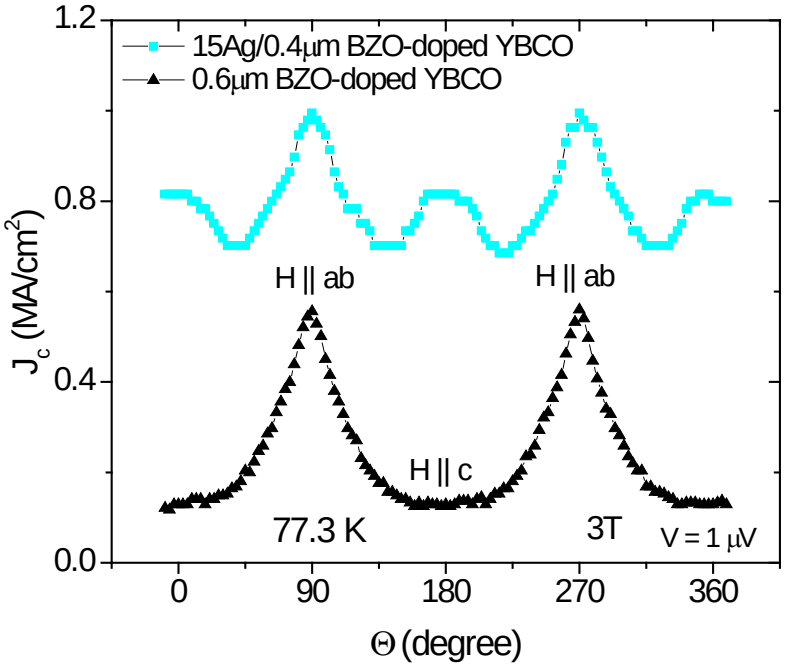

Figure 5-72 Angular dependence of J_c of the 0.4 μm-thick Ag decorated film and 0.6 μm-thick undecorated film at 77.3 K and applied field of 3.0 T, using field criteria of 1 μV/cm.

By using Ag decorated substrate, the angular dependence of J_c of the decorated film not only shows a small peak of J_c along the ab-plane at low applied field but also shows a small peak of J_c along the c-axis at high applied field from 3 to 5 T which are not presented in the undecorated film. The comparison of J_c of the Ag decorated film and undecorated film at 3.5 and 3 T is shown in Figure 5-71 and Figure 5-72, respectively, in range of angles from 0 to 360^o. We cannot compare the value of J_c at the ab-plane and the c-axis due to different thickness of the films; however, we can compare the sharp and the values of J_c^{ab}/J_c^{c}. In Figure 5-72, one clearly sees that the peaks of J_c at 0, 180 and 360^o are observed for the Ag decorated film (cyan squares). For the undecorated film, the peaks of J_c at 0, 180 and 360^o are absent. This is a feature similar to that observed for the Ag decorated pure YBCO film presented in Chapter 4.

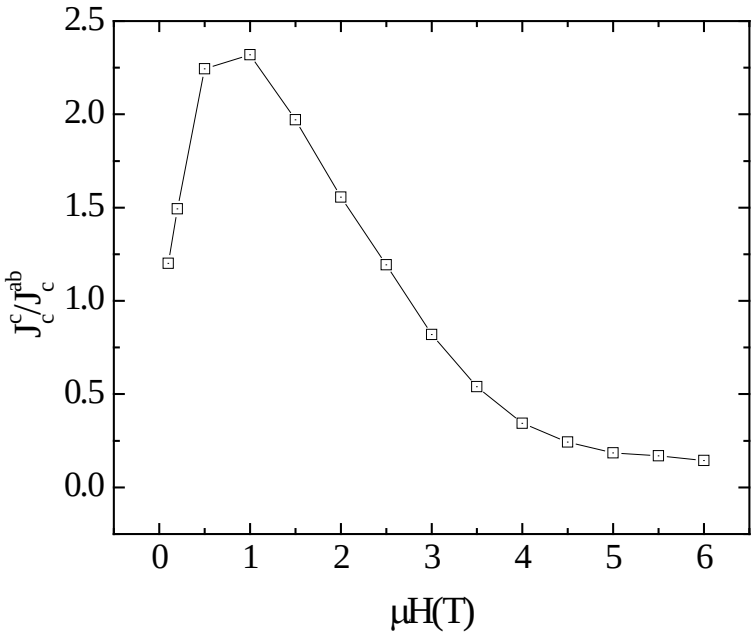

Figure 5-73 Field dependence of J_c^c/J_c^{ab} of the Ag decorated BZO-doped YBCO film at 77.3 K.

The appearance of peaks of J_c along the c-axis is other evidence that Ag nano dots are creating active pinning centres especially at 77.3 K and high applied field. These results agree with the in-field J_c measurement in which applied fields are parallel to the c-axis of the YBCO matrix. The $J_{c,}$ measured by magnetisation loops of the Ag decorated samples and presented in Figure 5-61 to Figure 5-64 in section 5.3.2.1 showed the enhancement of J_c up to 56% at applied field of 3.2 T.

The ratio of J_c^c/J_c^{ab} in various applied fields of the Ag decorated BZO-doped YBCO film is shown in Figure 5-73. From Figure 5-73, one can see that, the maximum peak of J_c^c/J_c^{ab} is about 2.32 which is a bit higher than 1.82 of the undecorated film shown in Figure 5-23. The position of the peak is the same for both decorated and undecorated films at 1 T. In applied fields of 3 T and 3.5 T the value of the J_c^{ab}/J_c^c is 0.82 and 0.54, respectively, while these values for undecorated film are 0.58 and 0.33 at 3 and 3.5 T, respectively. The increase of the

J_c^c/J_c^{ab} of the Ag decorated film in comparison with the undecorated film is due to the peak of J_c along the c-axis at high applied fields as shown in Figure 5-71 and Figure 5-72. However, the ratio of J_c^c/J_c^{ab} at 1T of the decorated film is also higher than that of the undecorated film. This indicates that Ag nano-dots may also help to increase J_c of the film along the c-axis at low applied fields. But this explanation is in conflict with J_c measured by the magnetic method shown in Figure 5-61 in which J_c (along the c-axis) of the decorated film and undecorated film is not much different in applied field of 1 T. It is possible that Ag nano-dots have reduced J_c along the ab-plane of the decorated film at low applied field resulting in the ratio of J_c^c/J_c^{ab} of the decorated film being higher than the undecorated film at low applied fields. However, for thicker decorated films the increase of J_c is observed in all applied fields parallel to the c-axis as shown in Figure 5-62.

5.3.2.4 Irreversibility and vortex melting lines

a. Vortex melting line by third harmonic AC susceptibility

The vortex melting line of undecorated and decorated film, estimated by third harmonic *AC* susceptibility introduced in the previous section, is shown in Figure 5-74. A small shift of melting line toward higher temperature and applied field is observed in the Ag decorated film. A small improvement is also observed at zero-field which is related to an improvement of T_c of the Ag decorated film as mentioned in the previous section. However, the improvement of T_m of the decorated film is not much. The improvement of T_m of the decorated film is also reflected in the increase of J_c in the Ag decorated film.

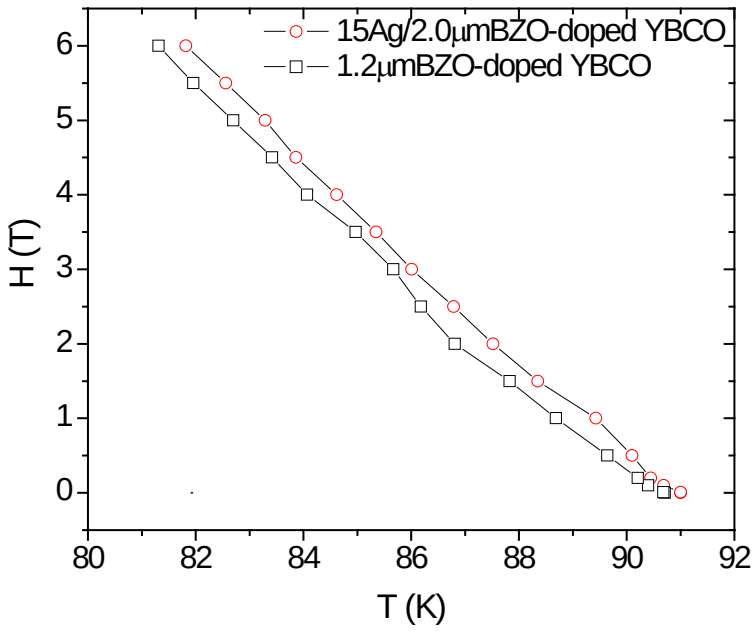

Figure 5-74 Vortex melting line of Ag decorated film and undecorated film estimated by third harmonic AC susceptibility measurement.

b. Irreversibility line by magneto-resistance

Figure 5-75 and Figure 5-76 show resistive transitions of the Ag decorated film in applied fields *H*//*c* and *H*//*ab*, respectively. The irreversibility line determined by this method is shown in Figure 5-77. A significant improvement of T_i of the Ag decorated sample in comparison with the undecorated film is observed in both directions. The improvement of T_i of the decorated film in comparison with T_i of the undecorated film is higher in the ab-plane than in the c-axis direction.

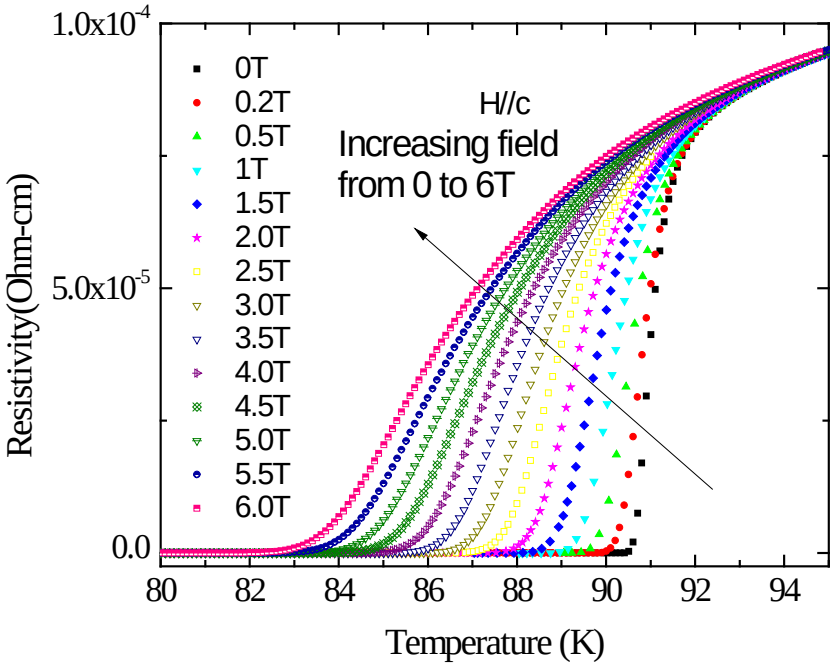

Figure 5-75 Resistive transition in applied fields of 0, 0.2, 0.5, 1, 1.5, 2, 2.5, 3, 3.5, 4, 4.5, 5, 5.5 and 6 T for *H*//c of 0.4 μm thick Ag decorated BZO-doped YBCO film.

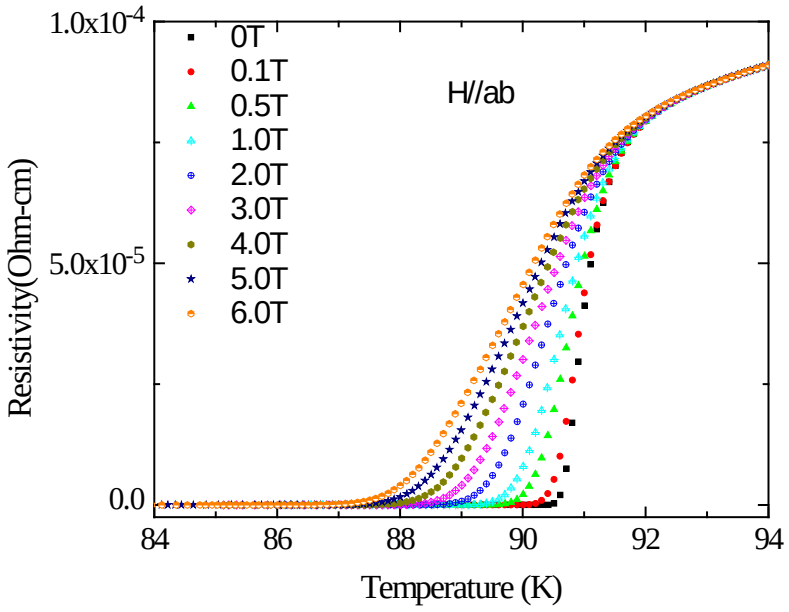

Figure 5-76 Resistive transition in applied fields of 0, 0.1, 0.5, 1, 2, 3, 4, 5, and 6 T for *H*//*ab* of 0.4 μm thick Ag decorated BZO-doped YBCO film.

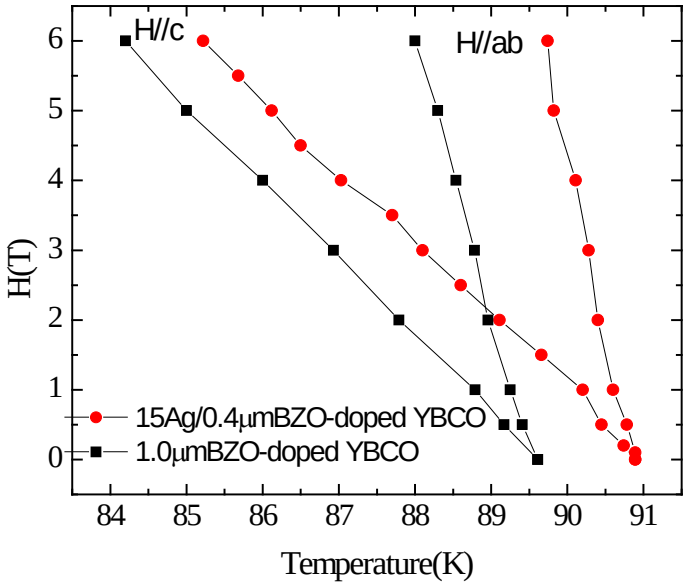

Figure 5-77 Irreversibility lines of Ag decorated film and undecorated film, legend is on the figure.

5.3.2.5 SEM images

SEM images of Ag decorated BZO-doped YBCO films with the thickness of 0.4, 1.2, 2 and 3 μm are shown in Figure 5-78 a, b, c, d, respectively. The SEM images of decorated films are the same as the undecorated film presented in section 5.2.5.2. The surface morphology of the Ag decorated films is characterized by pores and particulates. The size of the particulates increases when the film thickness increases, which may block super-current in the film leading to lower J_c for the thicker film.

With a very small amount of Ag added prior to the BZO-doped YBCO layer, one cannot expect any change on the surface of the film. However, change in the microstructure of the film near to the boundary between the film and the substrate may occur.

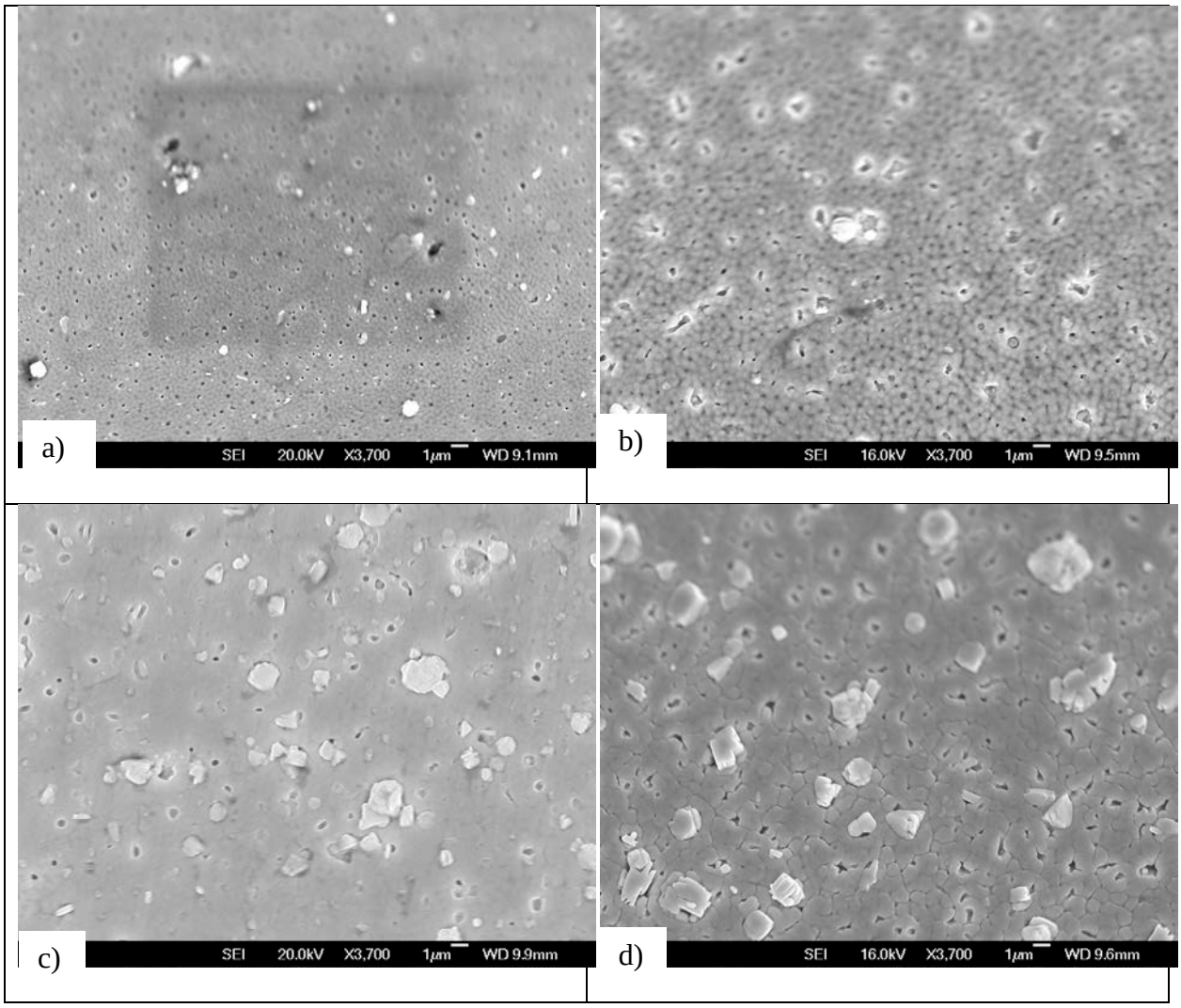

Figure 5-78 SEM image of a) 0.4 μm, b) 1.2 μm, c) 2 μm, d) 3 μm thick Ag decorated BZO-doped YBCO film

5.3.3 15Ag/BZO-doped YBCO multilayer architecture

5.3.3.1 Critical current density of multilayer films

In this section, the critical current of a double multilayer architecture of 15Ag/BZO-doped YBCO will be discussed.

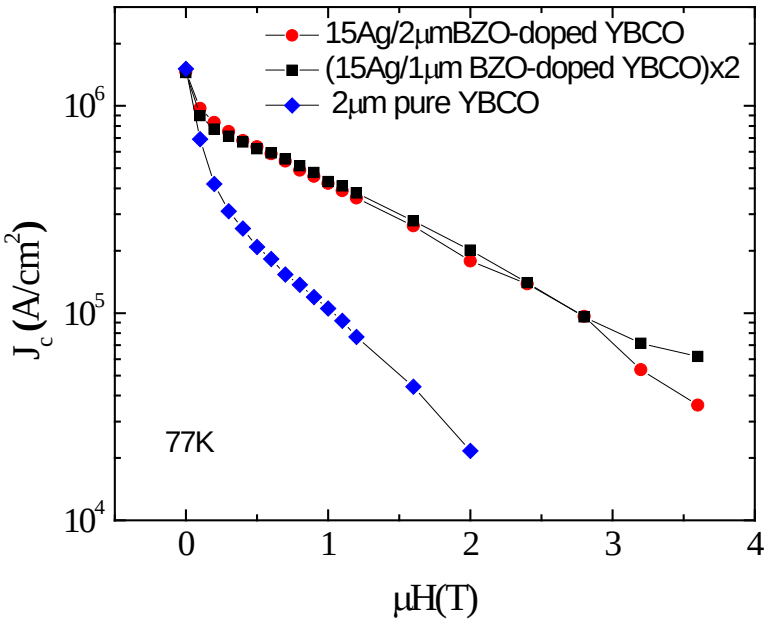

Figure 5-79 Field dependence of J_c at 77.3 K of the single layer and the double layer film with the same thickness.

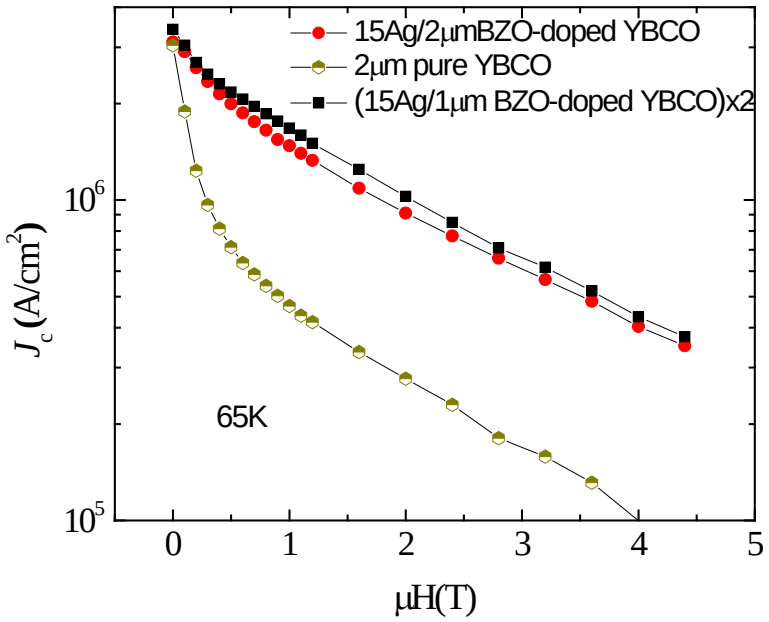

Figure 5-80 Field dependence of J_c at 65 K of single layer and double layer Ag/BZO-doped YBCO film with the same thickness in comparison with pure YBCO film.

The first multilayer architecture is 2 layers of (15Ag/1μm BZO-doped YBCO)x2, the total thickness of the film is 2 μm. J_c of the multilayer film is shown in Figure 5-79 and Figure 5-80 at 77.3 K and 65 K, respectively. In comparison with J_c of 15Ag/2 μm BZO-doped YBCO single layer, J_c of the two layer film does not exceed the J_c of the single layer at 77.3 K and applied fields lower than 2.8 T. An increase of J_c of the double multilayer layer film by 72% in comparison with J_c of single layer film with the same thickness is observed only at 77.3 K and in applied fields higher than 3.0 T.

At 65 K, J_c of the bi-layer film is higher than J_c of the single layer film with the same thickness in all applied fields as shown in Figure 5-80, but the enhancement of J_c of the bi-layer film is quite small, about 12%, in 1-3 T applied fields.

The second multilayer film is a 3 layer architecture of (15Ag/2μm BZO-doped YBCO)x3 film with total thickness of 6μm. J_c of this film at 65 K and 77.3 K is shown in Figure 5-81 and Figure 5-82, respectively, in comparison with a 2 μm-thick single layer film and with a 3.7 μm-thick single layer film.

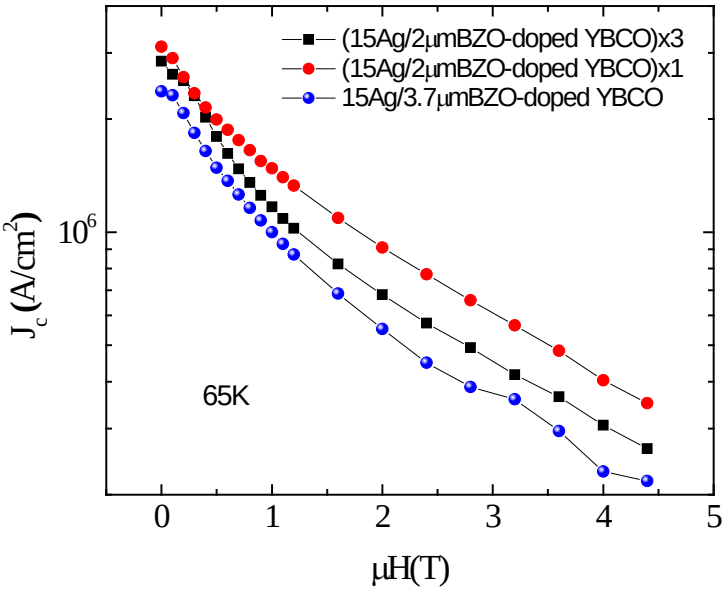

Figure 5-81 Field dependence of J_c at 65 K of 2μm-thick single layer, 6μm–thick trilayer and 3.7μm-thick single layer.

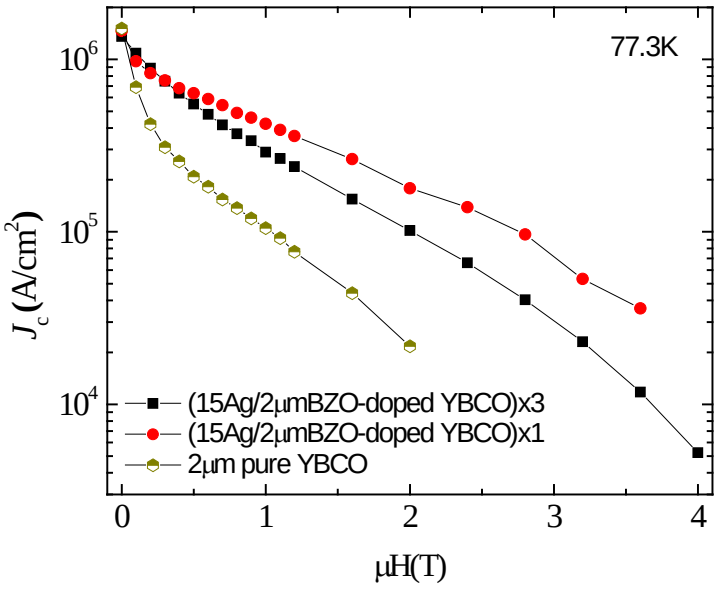

Figure 5-82 Field dependence of J_c at 77.3 K of 2μm-thick single layer, 6μm–thick trilayer and 3.7μm-thick single layer.

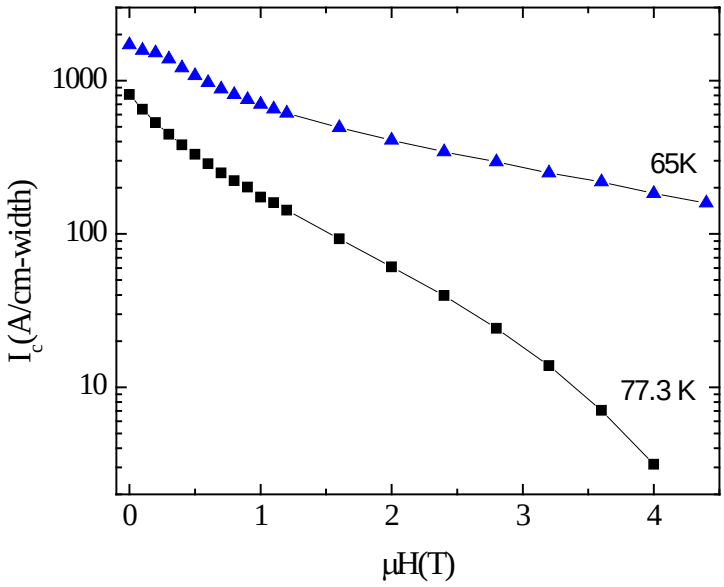

Figure 5-83 Critical current per cm width of the 6 μm-thick tri-layer film at 65 K and 77.3 K.

Despite of J_c decrease with increase of film thickness, it is clearly seen that J_c of the 6 μm multilayer is very close to that of the thinner 2 μm single layer at 65 K and 77.3 K. By using a multilayer architecture, J_c of a thick film still remains quite close to J_c of a 3-times-thinner single layer film. It means that the total current per cm width of a thick multilayer film is much higher than of a thin single layer. The total current per cm width of a 6 μm multilayer film is shown in Figure 5-83 in which I_c per cm width in self-field of the film is 1712 A/cm-width and 812 A/cm-width at 65 K and 77.3 K, respectively. Those values decrease to 1078 A/cm-width and 330 A/cm-width at 65 K and 77.3 K, respectively, in an applied field of 0.5 T, values that are comparable with best reported results.

5.3.3.2 Rotation transport measurement of multilayer film

The angular dependence of J_c in applied fields, at 77.3 and 82 K, of a two-layer architecture of (15Ag/1μm BZO-doped YBCO) is shown in Figure 5-84 and Figure 5-85,

respectively. Quite similar with the angular dependence of J_c of a single layer, the angular dependence of J_c at 77.3 K of the bi-layer film shows a maximum along c-axis in low applied fields (smaller than 2.5 T) and a maximum in the ab-plane in higher applied fields. At the higher temperature of 82 K this crossover field is about 1 T. At both temperatures there are range of applied fields in which the current anisotropy is quite small, important for practical applications.

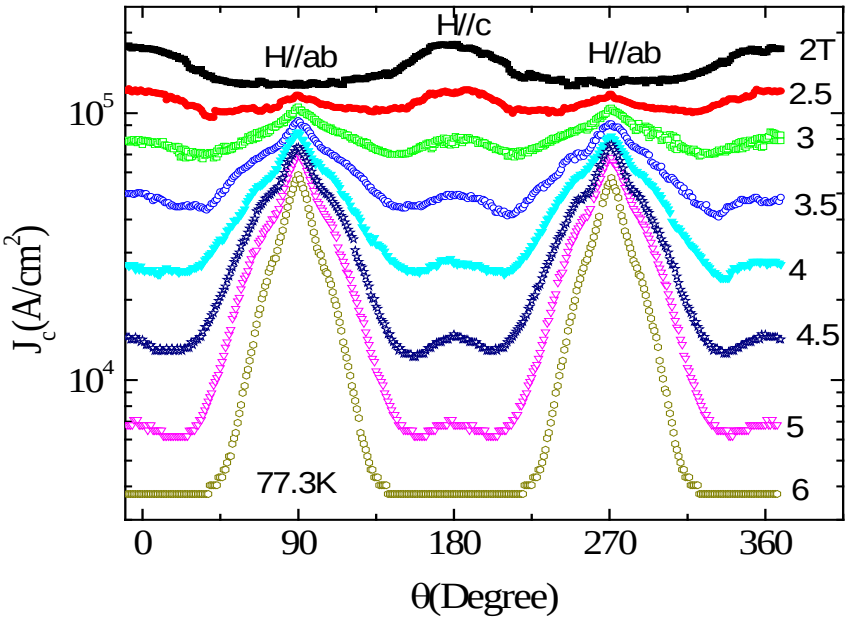

Figure 5-84 Angular dependence of J_c of (15Ag/1μm BZO-doped YBCO)x2 at 77.3 K and applied fields from 2 to 6 T

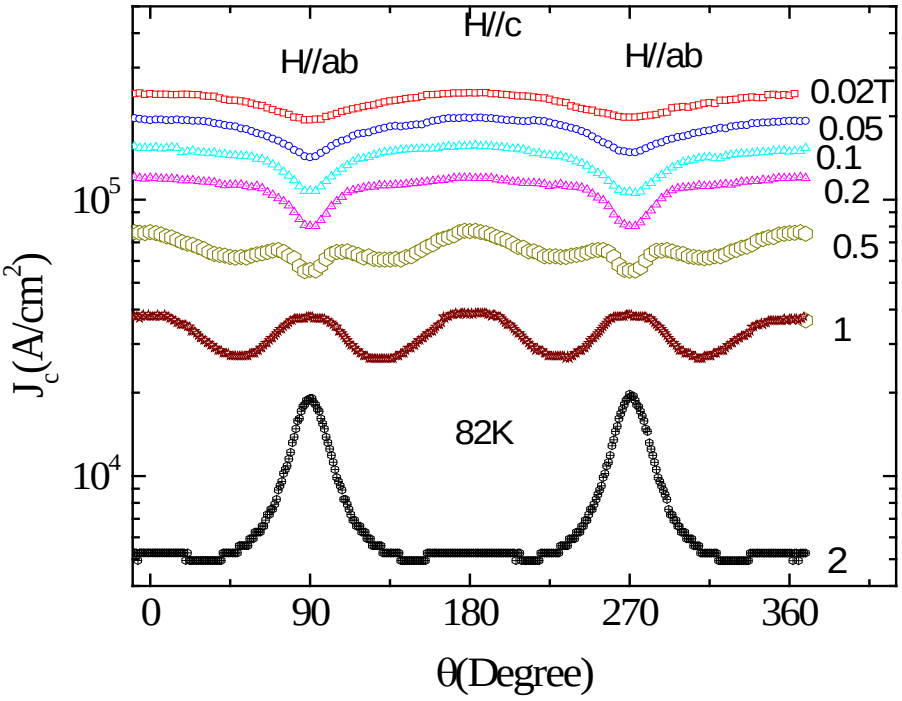

Figure 5-85 Angular dependence of J_c of (15Ag/1μm BZO-doped YBCO)x2 at 82 K and low applied fields

It is clear from the previous section that Ag nano-dots help to increase J_c along the c-axis. By adding one more quasi-layer of Ag nano-dots in between two BZO-doped YBCO layers in the architecture of (15Ag/1μm BZO-doped YBCO)x2 film, J_c of the bi-layer film shows a significant increase, up to 72 %, in comparison with the single layer decorated film with the same thickness, in applied fields parallel to the c-axis and higher than 3 T, as can be seen in Figure 5-79. A comparison of $J_c(\theta)$ at 77.3 K and in 4.5 T of (15Ag/1μm BZO-doped YBCO)x2 film and 1.8 μm-thick BZO-doped YBCO is shown in Figure 5-86. One can see the enhancement of J_c of the bi-layer film in all directions of applied field, but the increase in J_c is different in different directions. In detail, in applied field of 4.5 T parallel to the ab-plane of the YBCO matrix, J_c of the bi-layer film increases with about 16 %, while this increase is about 380% for the field parallel to the c-axis. One also clearly sees a small secondary peak of

J_c along the c-axis of the bi-layer film, which is absent in the J_c of the undecorated film but also appeared in the J_c of a single layer decorated film at applied fields lower than 4.5 T as shown in Figure 5-68. The increase of J_c of the bi-layer film is lower at low applied field, as shown in Figure 5-87. At applied field of 2 T and temperature of 77.3 K, J_c of the bi-layer film increases with 9% and 24% for applied field parallel to the ab-plane and the c-axis, respectively; and J_c of both films have the maximum value for the field along the c-axis.

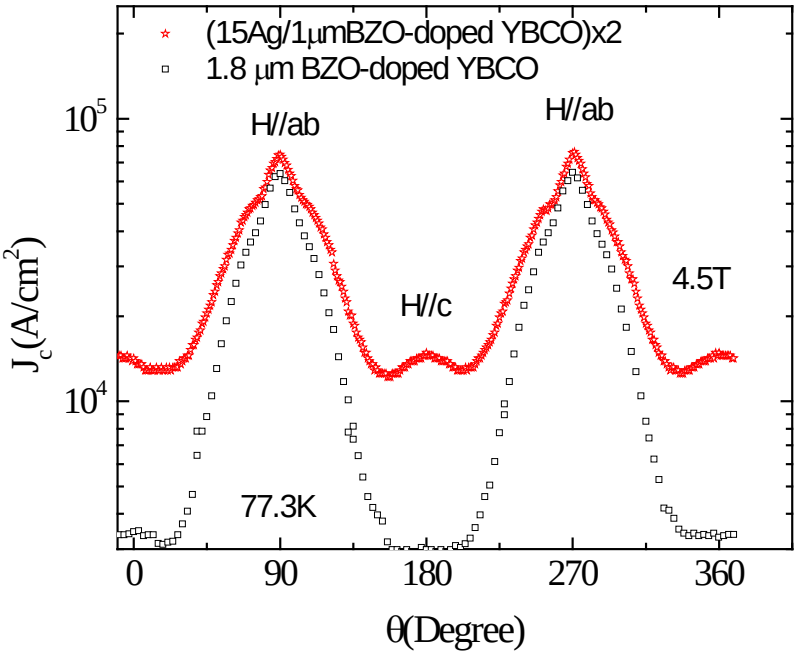

Figure 5-86 Angular dependence of J_c of (15Ag/1μm BZO-doped YBCO)x2 and, for comparison, of the 1.8μm-thick BZO-doped YBCO films at 77.3 K and applied field of 4.5 T.

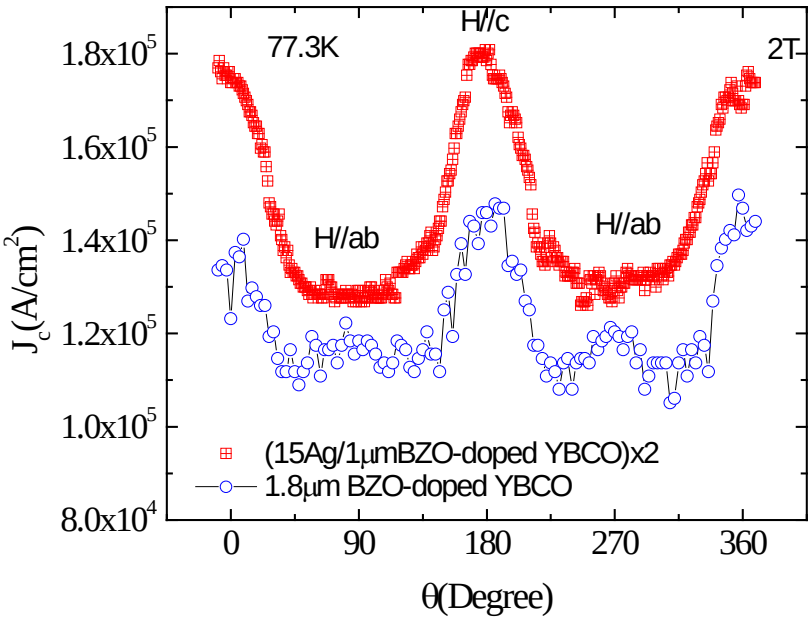

Figure 5-87 Angular dependence of J_c of (15Ag/1μm BZO-doped YBCO)x2 and 1.8μm BZO-doped YBCO films at 77.3 K and applied field of 2 T

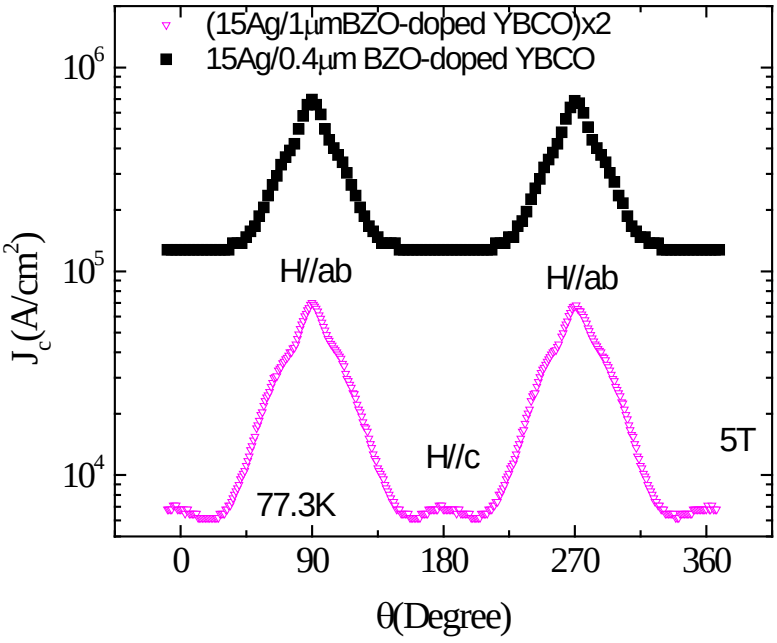

Figure 5-88 Angular dependence of J_c of (15Ag/1μm BZO-doped YBCO)x2 and (15Ag/0.4μm BZO-doped YBCO) films at 77.3 K and applied field of 5 T

It is also interesting to see the secondary peak of J_c at 0, 180 and 360^o, parallel to the c-axis, of the bi-layer film at high applied fields until 5 T. The peak of J_c in applied fields parallel to the c-axis was also observed in the angular dependence of J_c of the thin Ag decorated BZO-doped YBCO single layer film, but the peak disappeared at applied field of 5 T as shown in Figure 5-88. It is clear evidence that Ag nano-dots create strong, effective, c-axis correlated pinning centres effective even in high applied fields.

5.3.3.3 Vortex melting and irreversibility lines of multilayer films

a. Third-harmonic *AC* susceptibility

The vortex melting line of (15Ag/1.5μm BZO-doped YBCO)x2 determined by third harmonic *AC* susceptibility is shown in Figure 5-89 in comparison with T_m of 1.2 μm undecorated BZO-doped YBCO and of 2 μm Ag decorated BZO-doped YBCO films. As can be seen, there is no improvement of T_m of the multilayer film observed in comparison with the decorated film. The additional layers of Ag nano-dots do not help to improve T_m of the multilayer film in the direction of applied field parallel to the c-axis.

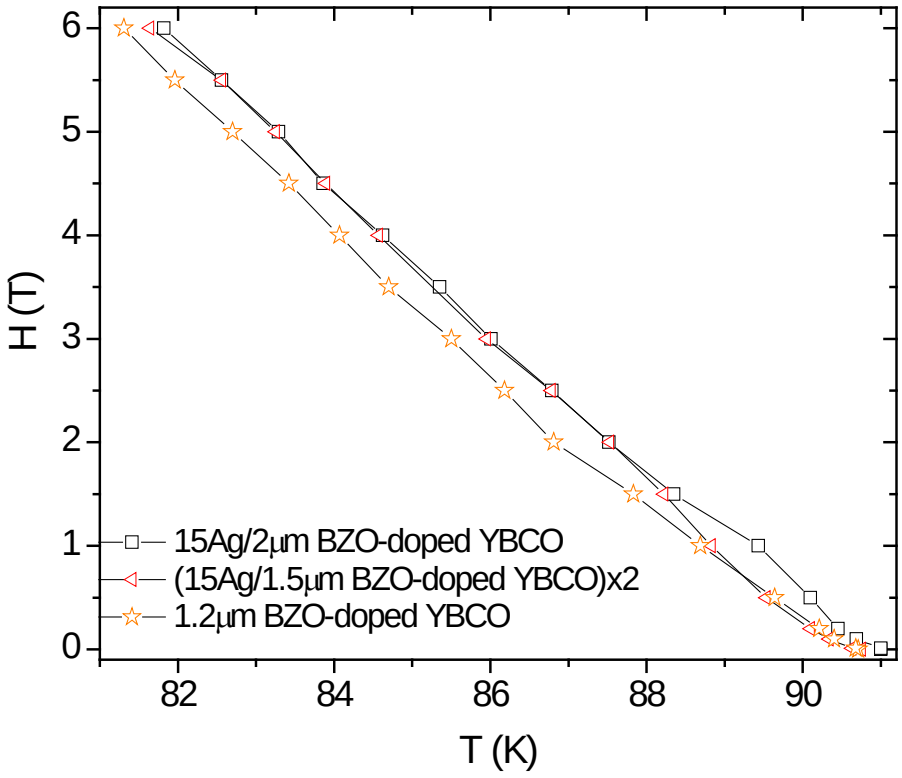

Figure 5-89 Vortex melting line of undecorated film (star), Ag decorated film (rectangular) and bi-layer film (triangles) in applied field H//c.

b. Irreversibility lines by magneto-resistance method

A bi-layer film of (15Ag/1 μm BZO-doped YBCO)x2 was chosen for magneto-resistance measurement. The resistive transition of the film is shown in Figure 5-90 and Figure 5-91 for *H*//*c* and *H*//*ab*, respectively.

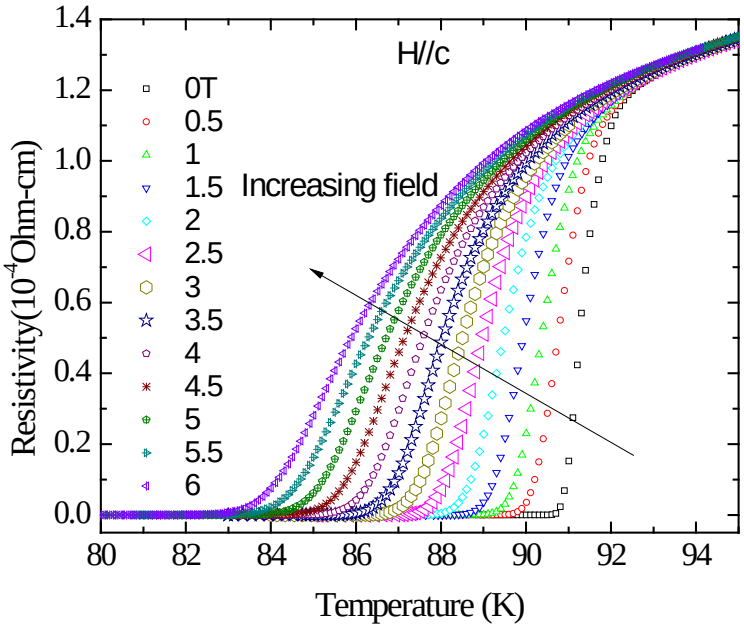

Figure 5-90 Resistive transition of (15Ag/1 μm BZO-doped YBCO)x2 film in applied fields as displayed in the figure and in *H//c*

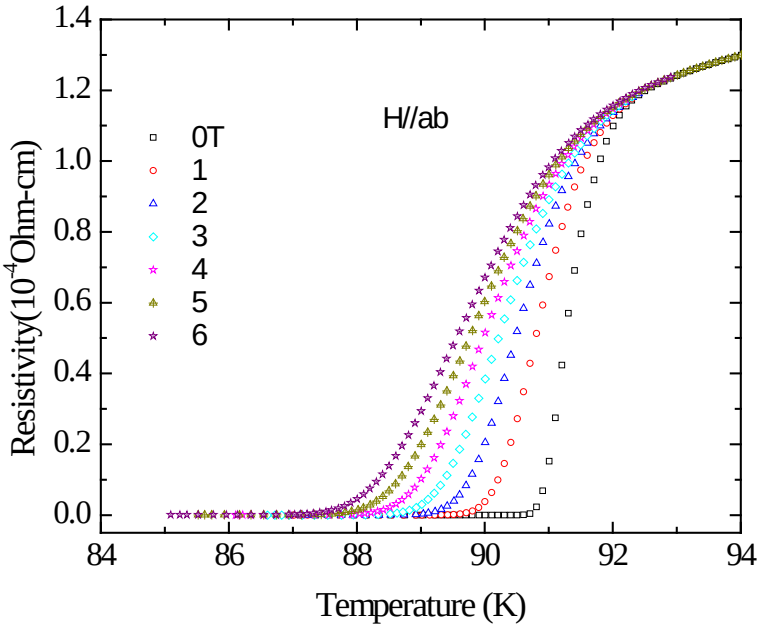

Figure 5-91 Resistive transition of (15Ag/1 μm BZO-doped YBCO)x2 film in applied fields as displayed in the figure and *H//ab*

The irreversibility lines estimated from these resistive transitions is shown in Figure 5-92 for *H*//*c* and *H*//*ab*, the legend is shown in the figure. The ratio of slopes of the linear fitting of T_i at *H*//*ab* over *H*//*c* is termed the "anisotropy factor" of the film which is 3.5 for (15Ag/1 μm BZO-doped YBCO)x2 film. This anisotropy factor is smaller, of about 1.8 in the case of 15Ag/0.4 μm BZO-doped YBCO single layer film. The comparison of T_i of those two films is shown in Figure 5-93.

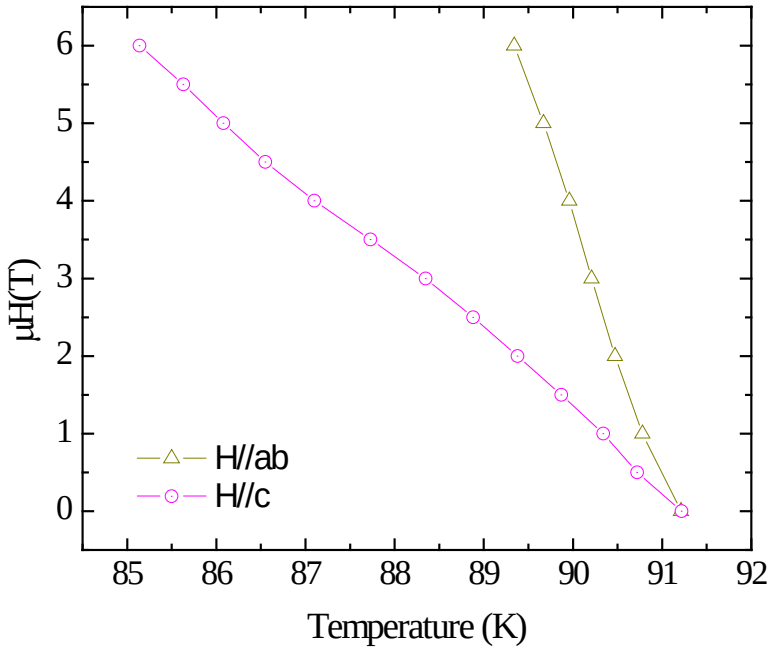

Figure 5-92 Irreversibility lines estimated by magneto-resistance for *H*//*c* and *H*//*ab* of (15Ag/1 μm BZO-doped YBCO)x2 film.

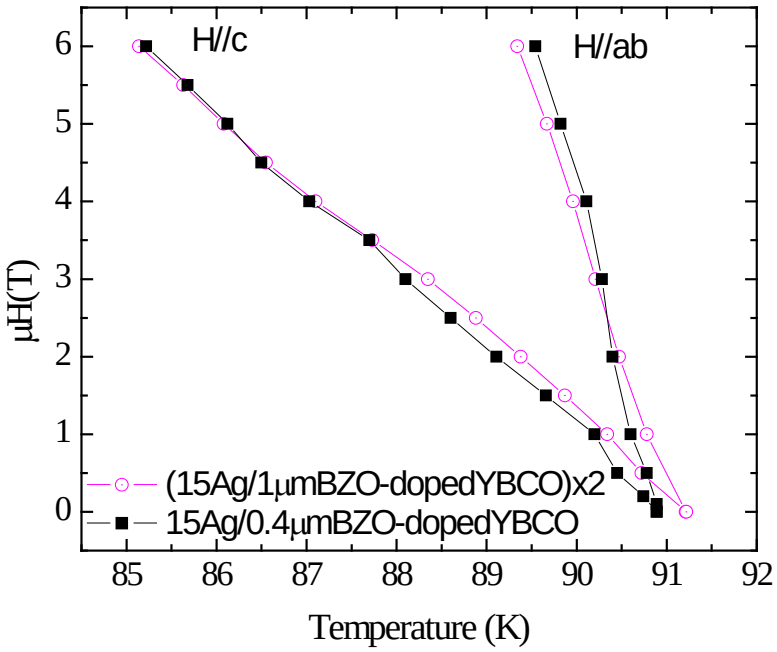

Figure 5-93 Irreversibility lines of decorated single layer film and of multilayer film for *H//c* and *H//ab*

5.3.3.4 TEM images of Ag/BZO-doped YBCO multilayer film

A TEM cross section of the bi-layer film with architecture of (15Ag/1μm BZO-doped YBCO)x2 is shown in Figure 5-94 and Figure 5-95. In Figure 5-94, nano-rods of BZO growth along the c-axis of the YBCO are seen, but some of them are not well aligned along the c-axis. In another area of the film, Figure 5-108, the growth of BZO nano-rods is clearly in the c-axis direction. One would expect to see the Ag layer in between the two BZO-doped YBCO layers, however, it is not clearly seen. There is no boundary between the two layers of BZO-doped YBCO because Ag was formed as nano-dots, with average height about few nanometres, and not a full layer of material. During deposition, Ag nano-dots may randomly move away from their initial position due to thermal energy of the deposition process.

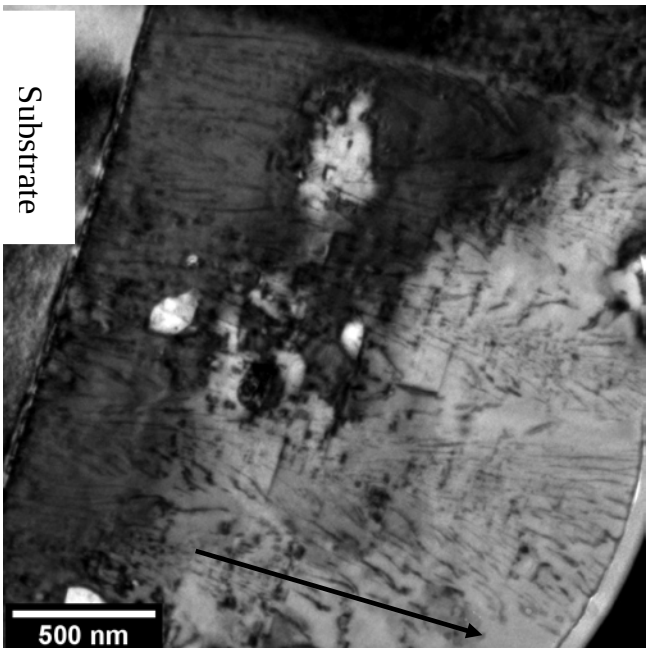

Figure 5-94 Bright field cross section TEM image of (15Ag/1 μm BZO-doped YBCO)x2, arrow shows c direction.

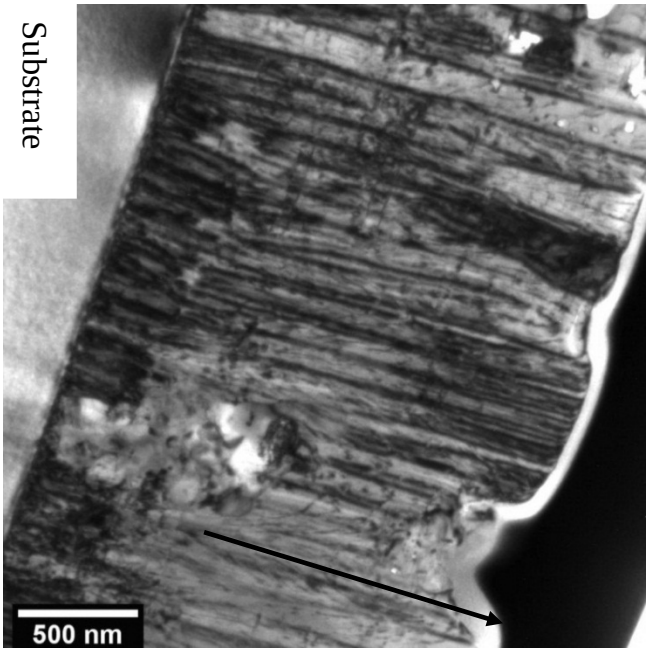

Figure 5-95 Cross section image of (15Ag/1 μm BZO-doped YBCO)x2, arrow shows c direction.

Element mapping of the bi-layer sample in the interface region between the STO substrate and the film is shown in Figure 5-96. Figure 5-96a shows STEM image of the sample with clear contrast between the STO substrate (black area) and the film (white area). The STEM image also shows a large dark contrast area and small white contrast areas (marked by circles) which are Cu-rich phase as shown in Figure 5-96d. Located close to the Cu-rich phase area is a Y-rich phase as seen in Figure 5-96e. There is no Ba present in the areas of Y- or Cu- rich phase as seen in Figure 5-96c, so the Y- and Cu- rich phases could be Y_2O_3 and CuO_2, confirmed by the O map shown in Figure 5-96b. Figure 5-96f show map of Sr which is in $SrTiO_3$ of the substrate, it is very reasonable that Sr is only present in the substrate area. However, the map of Zr shows its presence more in the substrate area than in the film area. This may be mistake of the system because Ti and Zr are in the same group.

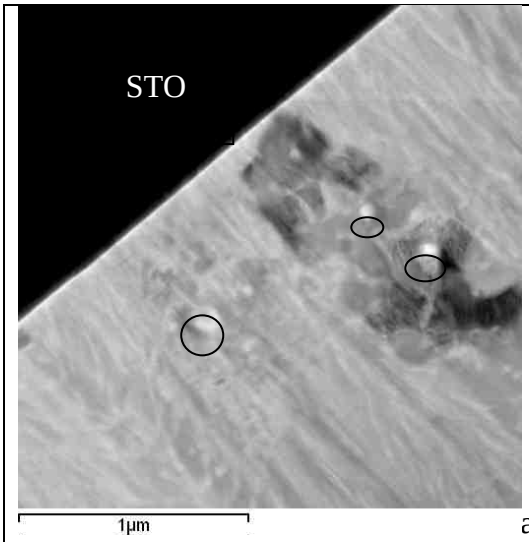

a)

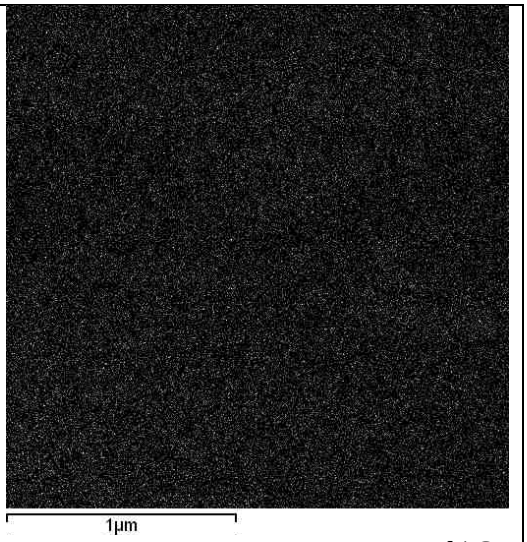

b)O_2

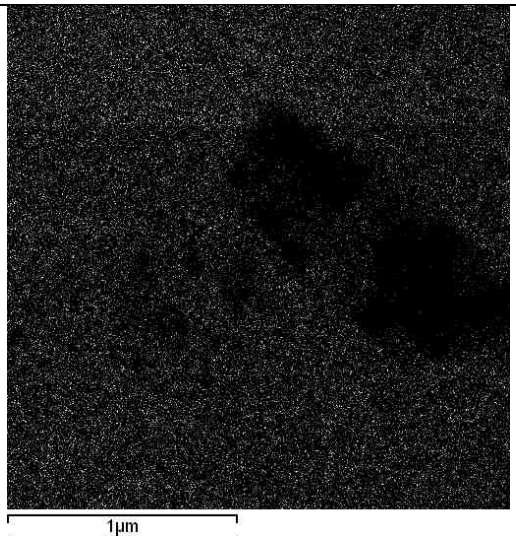

c)Ba

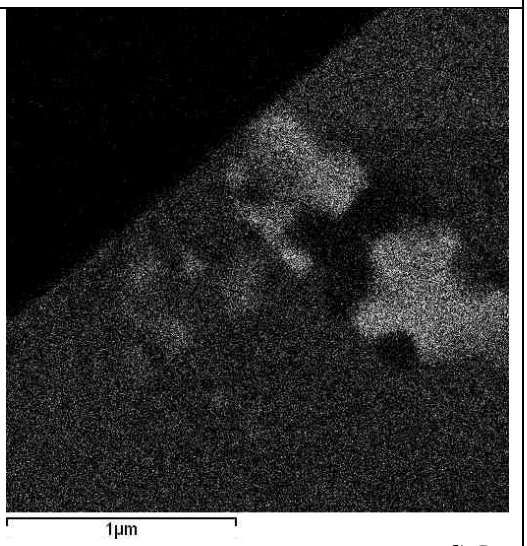

d)Cu

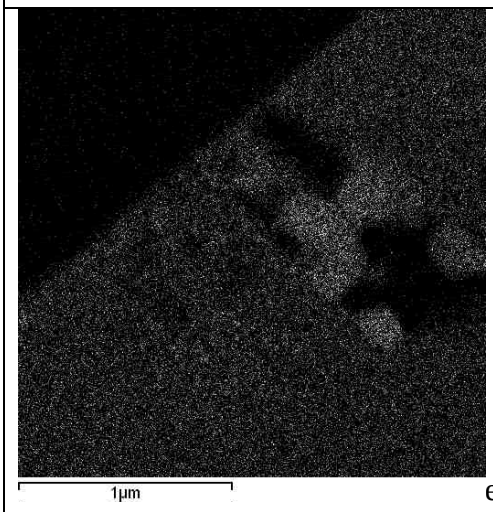

e)Y

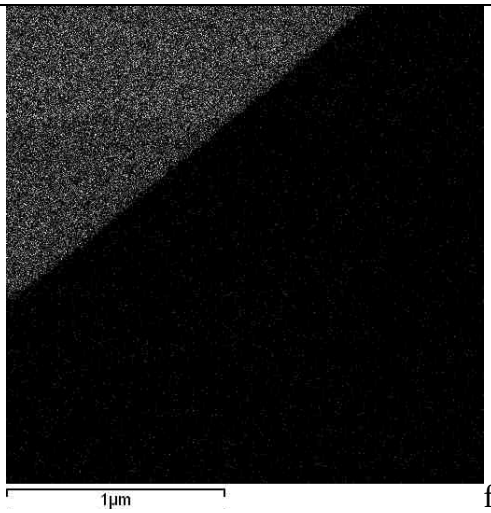

f)Sr

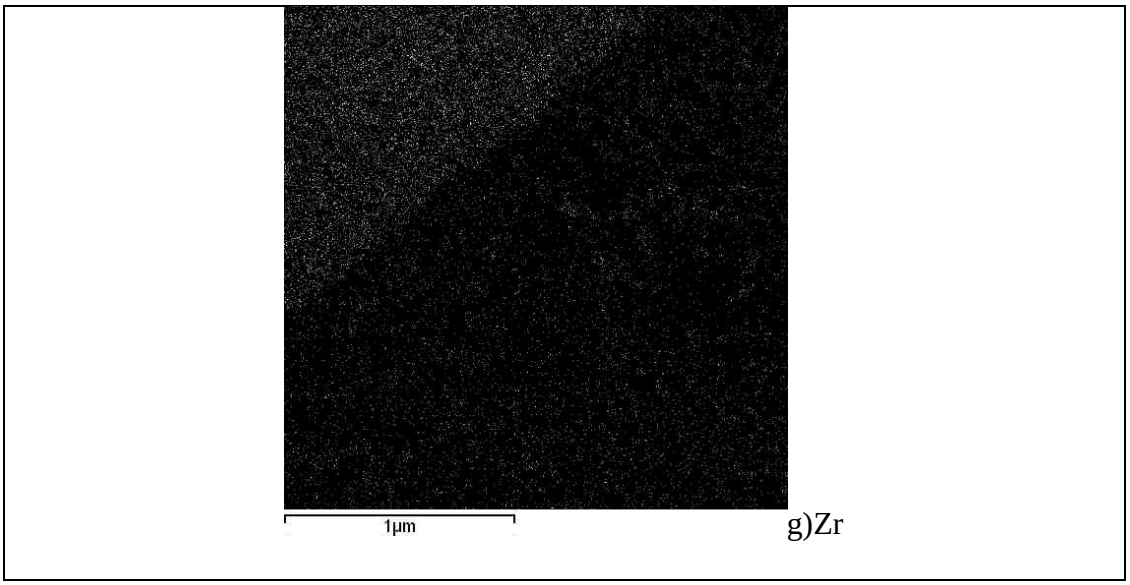

Figure 5-96 Element mapping in STEM mode of (15Ag/1 μm BZO-doped YBCO)x2 film in the boundary of film and substrate, a) STEM image, b) O_2 map, c) Ba map, d) Cu map, e) Y map, f) Sr map, g) Zr map.

The element maps of the sample in the middle area of the film are shown in Figure 5-97. There is a dark contrast area in the STEM image and bright lines as shown in Figure 5-97a. In the dark contrast area, marked by circles, one can recognise the absence of Ba in Figure 5-97b and Y in Figure 5-97e, but rich in Cu in Figure 5-97c. So the dark contrast area is either Cu rich phase, possibly, CuO_2 or Y rich phase, Y_2O_3, as O_2 map is shown in Figure 5-97d.

Figure 5-98 shows BZO nano-rods growing inside the YBCO matrix with quite high density. Most of BZO nano-rods align parallel to the c-axis of YBCO, but some of them are misaligned in different directions.

Figure 5-99 shows coexistence of Y_2O_3 whose lattice is perpendicular to the ab-plane of YBCO, marked by a circle, and a Cu rich phase and/or BZO phase. Figure 5-100 shows a complicated area with rich Cu-rich phase and/or BZO phase which created distortions of the ab-planes of YBCO.

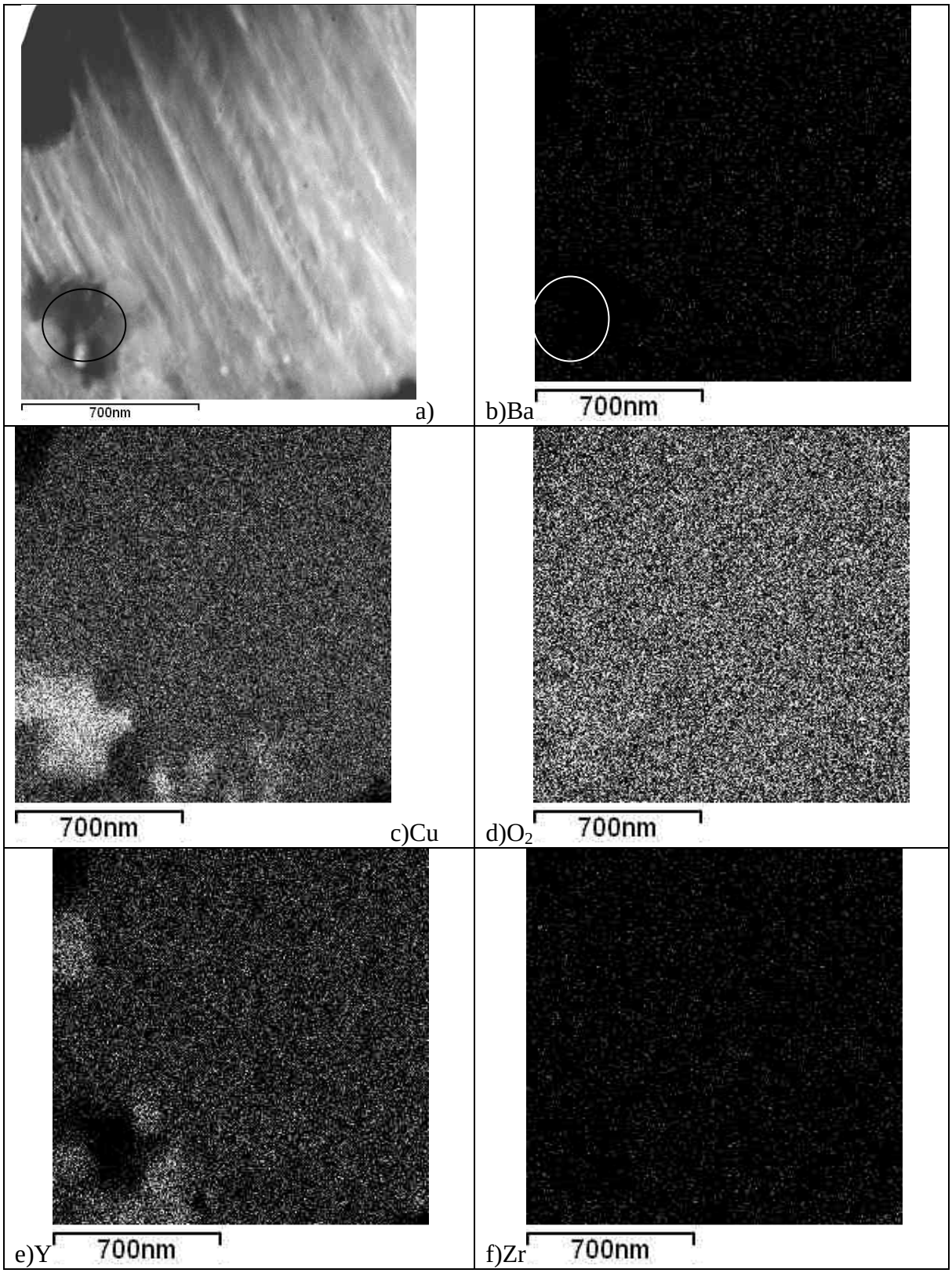

Figure 5-97 Element mapping of the 2 layer film in the middle area of the film, a) STEM image, b) Ba map, c) Cu, d) O_2, e) Y, f) Zr.

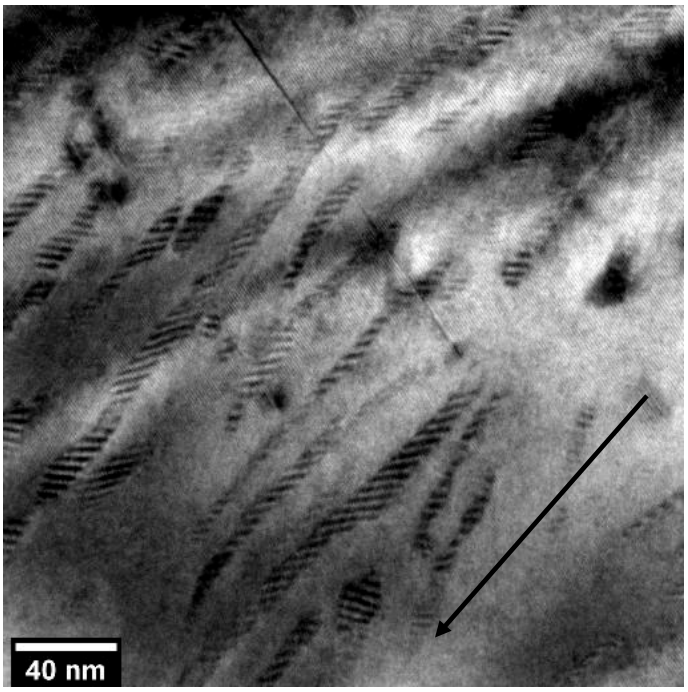

Figure 5-98 BZO nano-rods in the YBCO matrix

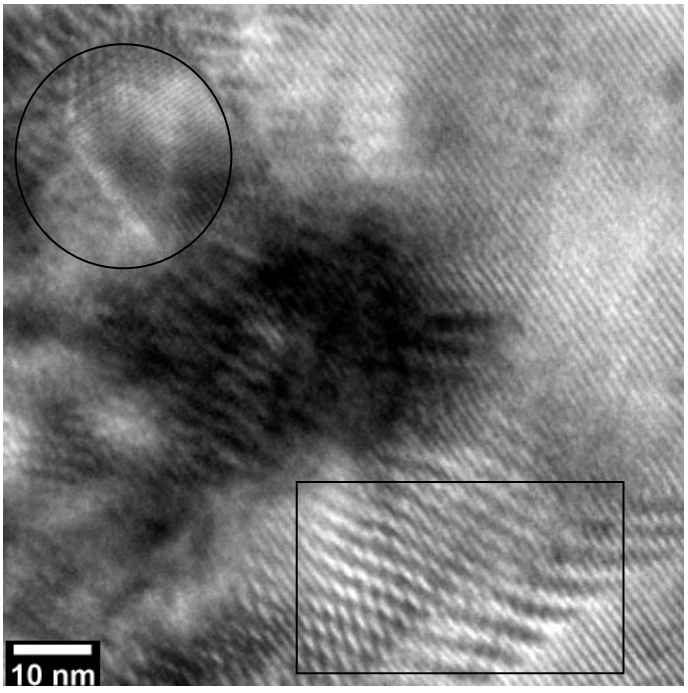

Figure 5-99 Co-existence of Y_2O_3 (circle) and Cu rich phase (rectangular) and/or BZO phase.

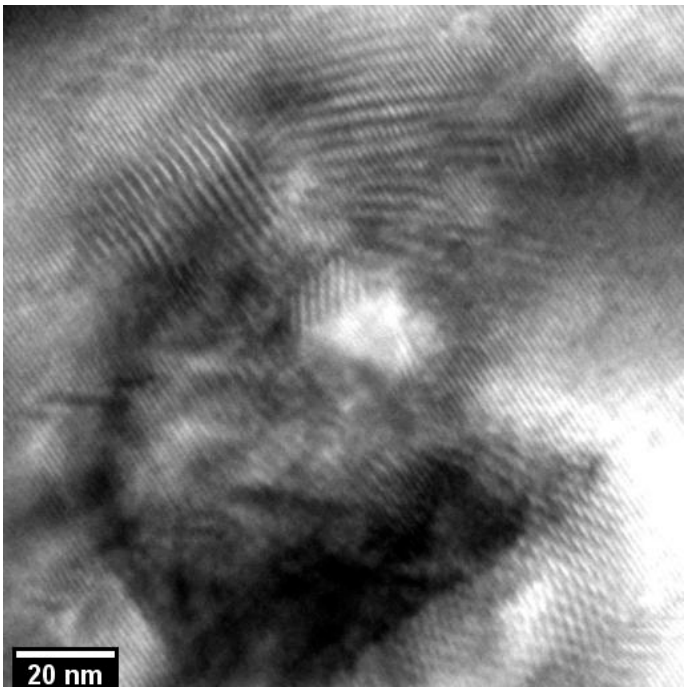

Figure 5-100 Defects caused by CuO_2 and/or BZO phase observed in the middle area of the film.

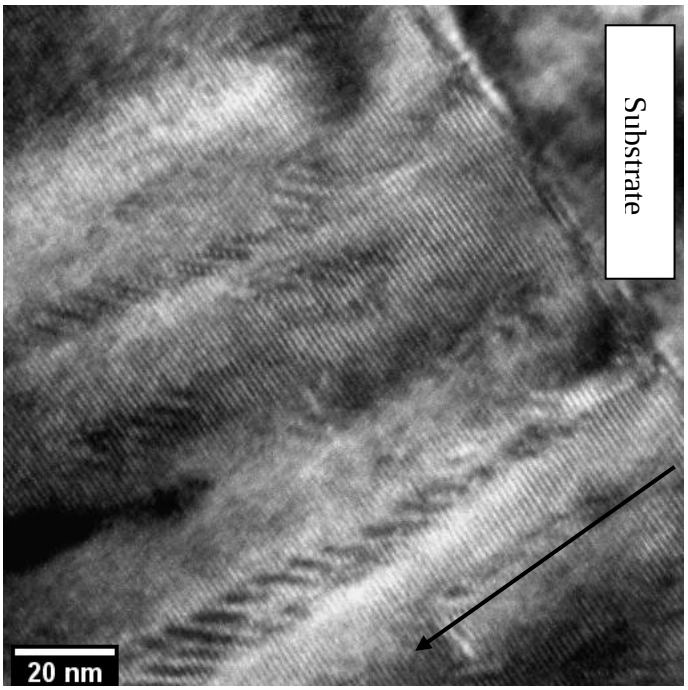

Figure 5-101 A cross section TEM image near the STO substrate, arrow show the c-axis of YBCO.

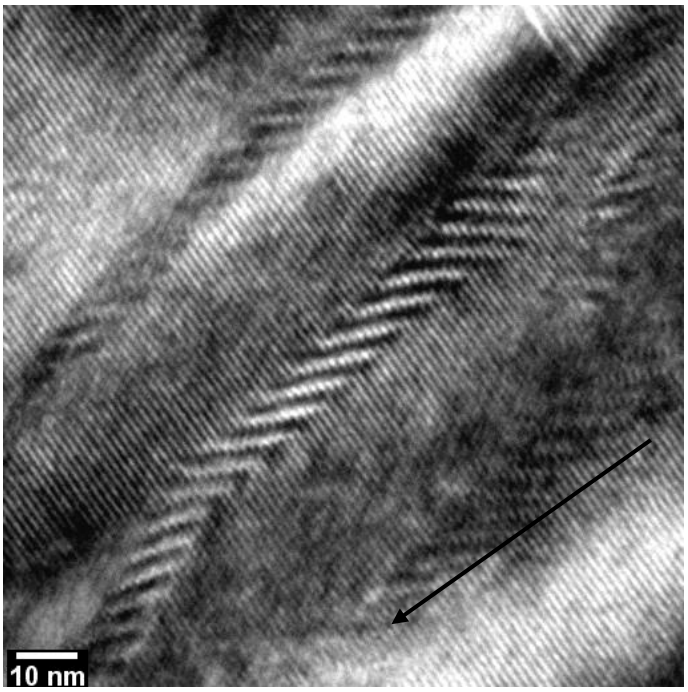

Figure 5-102 Long BZO nano-rods in the middle area of the film, arrow shows the c-axis of YBCO.

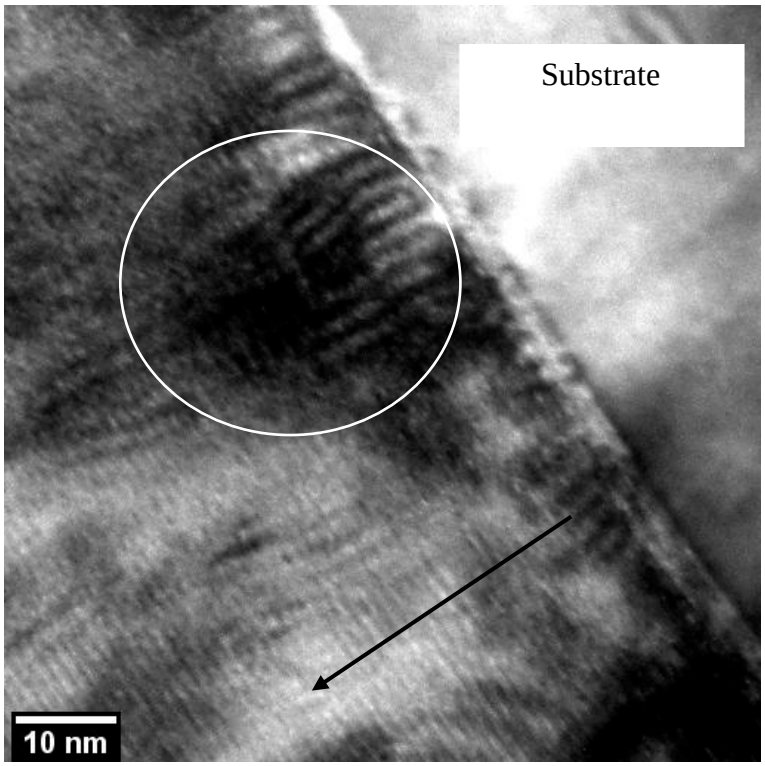

Figure 5-103 A distorted area near the STO substrate, the c-axis is indicated by arrow.

Figure 5-101 and Figure 5-102 show BZO nano-rods with diameter of about 10 nm grown from near the STO substrate and lengthened into the middle area of the film and aligned along the c-axis.

Unfortunately, Ag could not be detected in the substrate area as well as in the middle area of the film. As mentioned above, Ag nano-dots may move away from the substrate area into the YBCO film during deposition. However, one can see distortion of the YBCO lattice caused by the film/substrate interface and/or Ag nanoparticles. Many types of defects observed in the film are effective anisotropic and isotropic pinning centres able to enhance J_c, mainly along the c-axis of YBCO under applied fields.

5.4 YBCO and BZO-doped YBCO films on RABiTS Ni:5W substrate

5.4.1 Ni:5W RABiTS substrate

Biaxially textured Ni:5W, nickel with small doping of tungsten Ni-5at%W (Ni:5W), supplied by 3-Cs Ltd, Malvern, was used in this project. T he properties of the tapes were investigated by X-ray, EBSD, SEM. The Ni:5W tapes then were cut into small pieces of 5x5 mm for pulsed laser deposition.

Figure 5-104 shows the typical X-ray diffraction pattern of a Ni:5W substrate. Only a sharp peak at $2\theta = 52^{o}$ corresponding to the Ni (002) peak is observed.

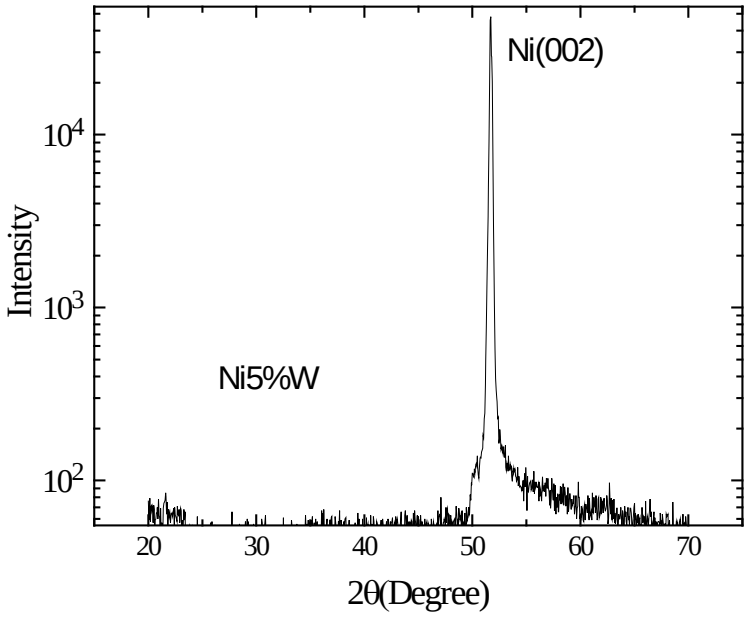

Figure 5-104 X-ray diffraction of Ni:5W substrate

A SEM image of a Ni:5W substrate is shown in Figure 5-105. The SEM image reveals a dense, uniform microstructure, but there is a small cracked area observed in the SEM image, which may subsequently affect the film deposition quality in this area.

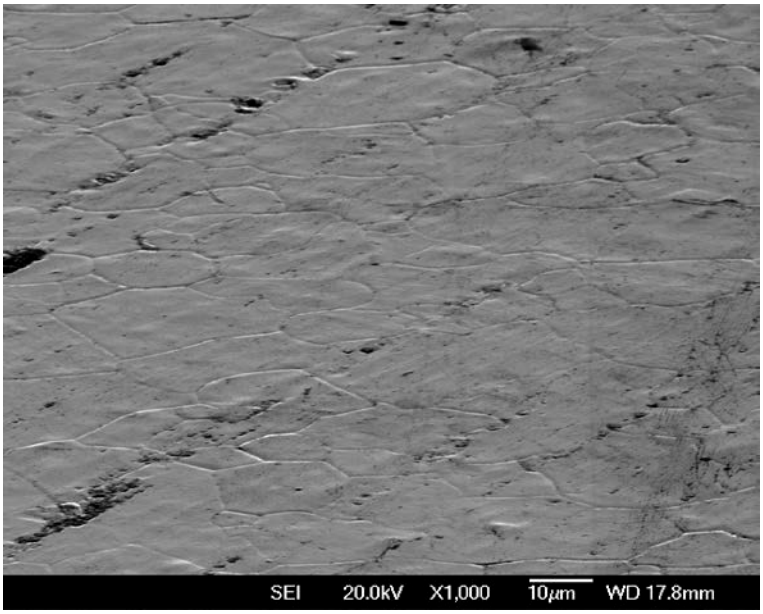

Figure 5-105 SEM image of Ni:5W substrate

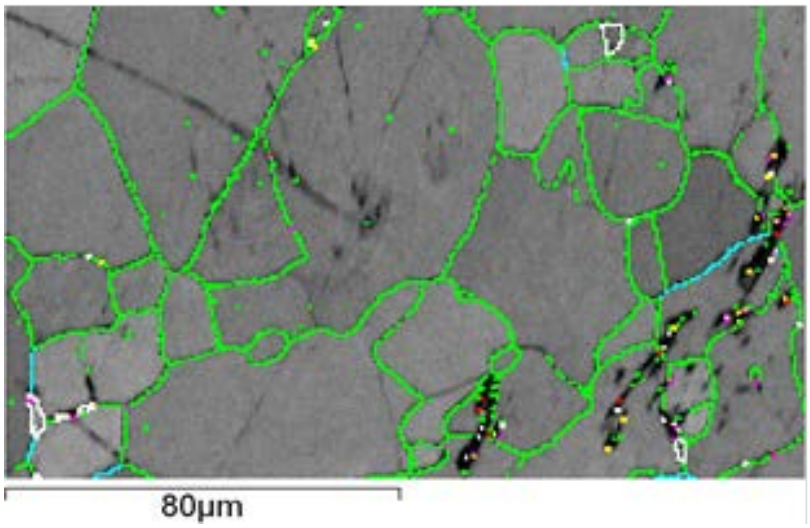

Figure 5-106 Grain boundary positions superimposed on the pattern quality map, the colour of boundaries corresponds to the histogram of misorientation angles shown in Figure 5-107

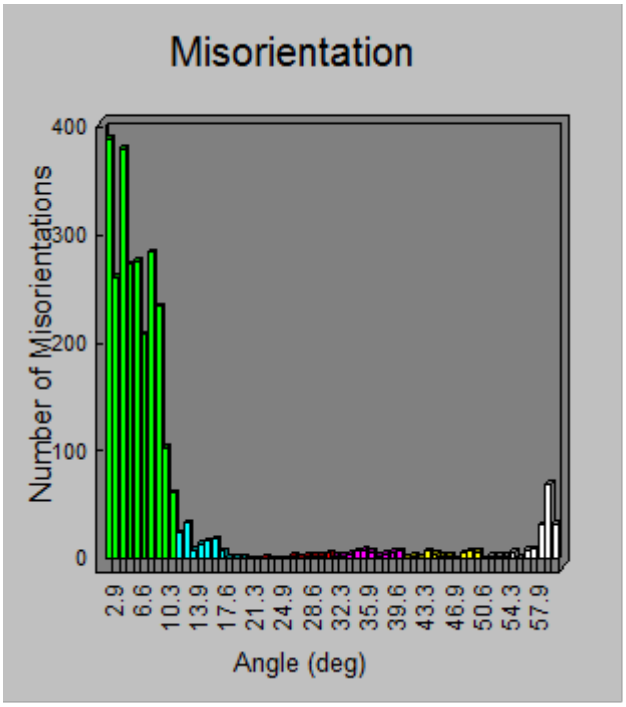

Figure 5-107 Misorientation histogram of the area shown in Figure 5-106

Grain boundary observations of the textured Ni:5W substrate were performed by EBSD. The grain boundary positions of the Ni:5W substrate are overlaid on the pattern quality image, as shown in Figure 5-106. The colour of the boundaries corresponds to the colour of the histogram of misorientation angles shown in Figure 5-107. The histogram of misorientation angle shows that most of the boundaries have a low angle misorientation smaller than 10^{o}, however, some high angle misorientation is also observed from 25 to 60^{o}. High angle misorientations are undesirable for the deposition of YBCO film but we could not obtain better quality substrates. The black lines in Figure 5-106 are unsolved areas which the software could not index. Those may be due to micro- cracks in the substrate.

The grain boundaries and histogram of misorientation angles of a smaller area of the Ni:5W substrate is shown in Figure 5-108 and Figure 5-109. In this selected small area, only low misorientations smaller than 12^{o} are observed. Better quality substrates would be more

homogeneous, but all RABiTS materials have statistical fluctuations of grain size and misorientation angle distribution.

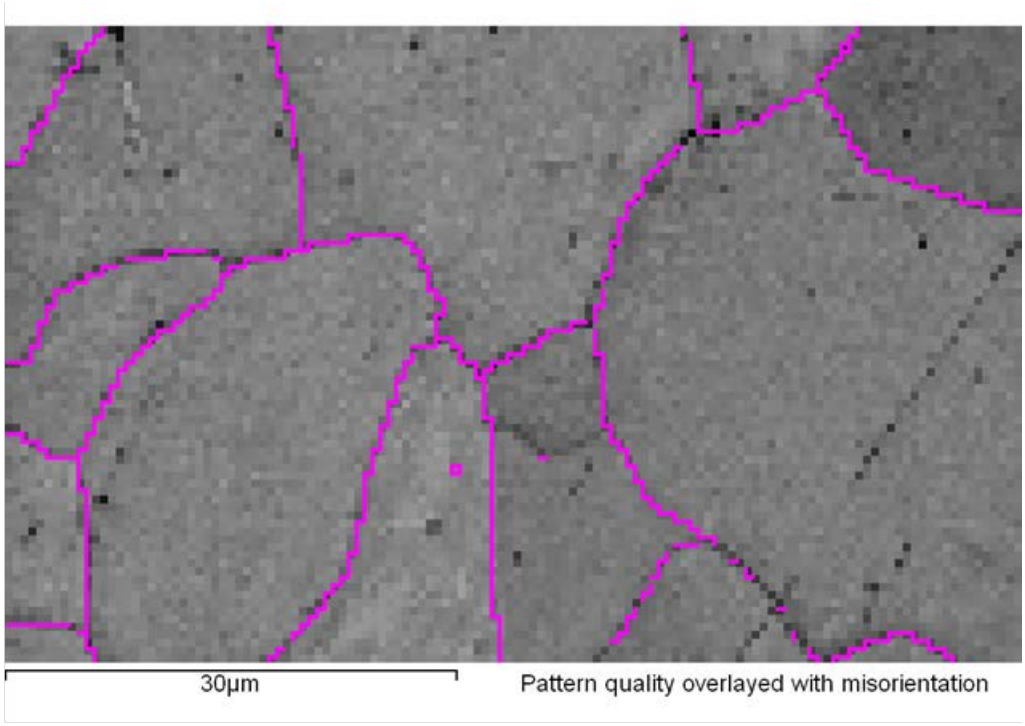

Figure 5-108 Higher resolution of grain boundary (colour line) and pattern quality map

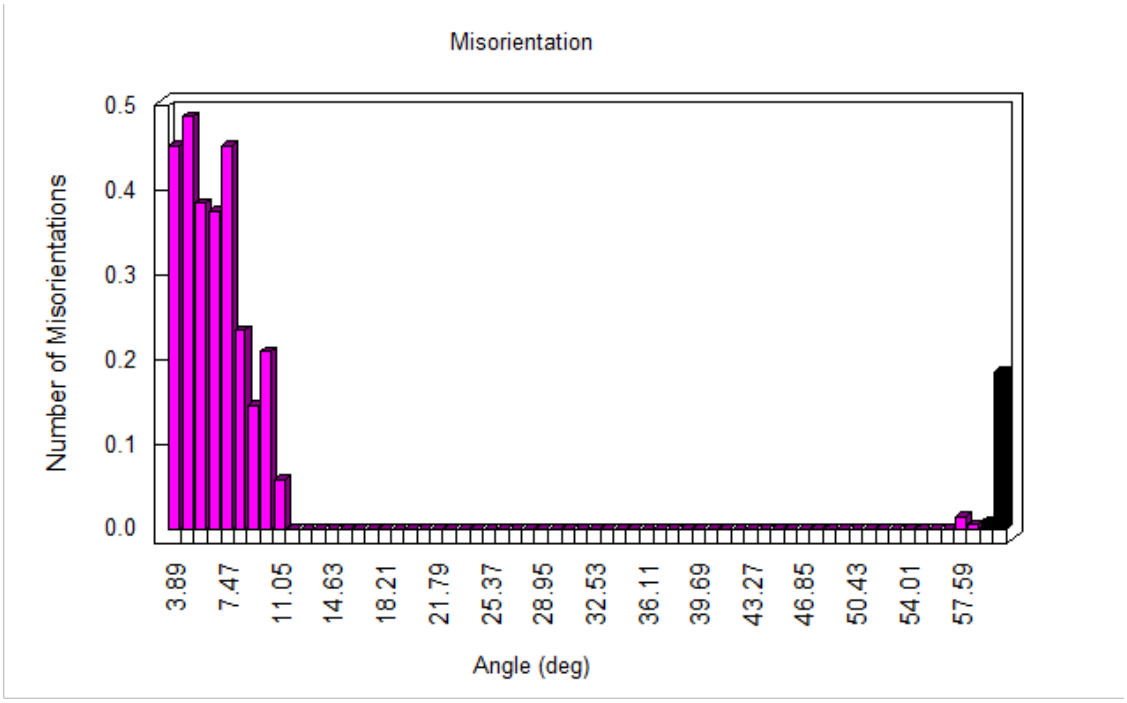

Figure 5-109 Misorientation histogram for the area shown in Figure 5-108

5.4.2 Buffer layers

As mentioned in Chapter 2, buffer layers are required to grow YBCO on RABiTS substrates. Each buffer layer plays a different role. In this section, three "typical" buffer layers of CeO_2/YSZ/CeO_2 were used to grow YBCO and BZO-doped YBCO films. The thickness of the first CeO_2 layer was 95 nm and YSZ was 600 nm. The buffer layers were grown at a temperature of 700^o C and in low oxygen pressure of $8x10^{-4}$ Torr. The first 40 nm CeO_2 of the first CeO_2 layer was deposited in vacuum to avoid oxidation of the Ni:5W substrate. The thickness of the cap CeO_2 layer was 95 nm.

An X-ray 2θ scan of a buffered Ni:5W substrate is shown in Figure 5-110. The X-ray diffraction shows the excellent copying of the texture of the buffered Ni:5W since only CeO_2 (002), YSZ (002) and Ni (002) peaks were observed.

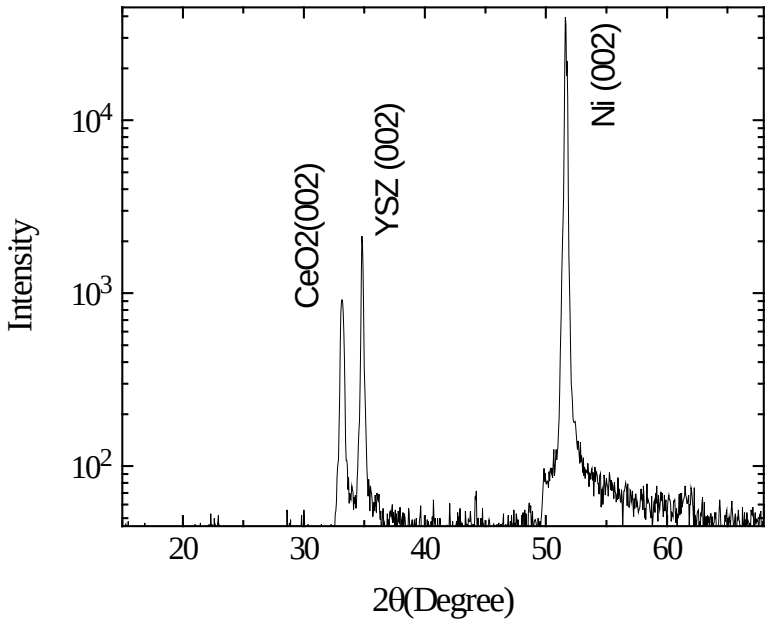

Figure 5-110 X-ray diffraction pattern for Ni:5W/CeO_2/YSZ/CeO_2

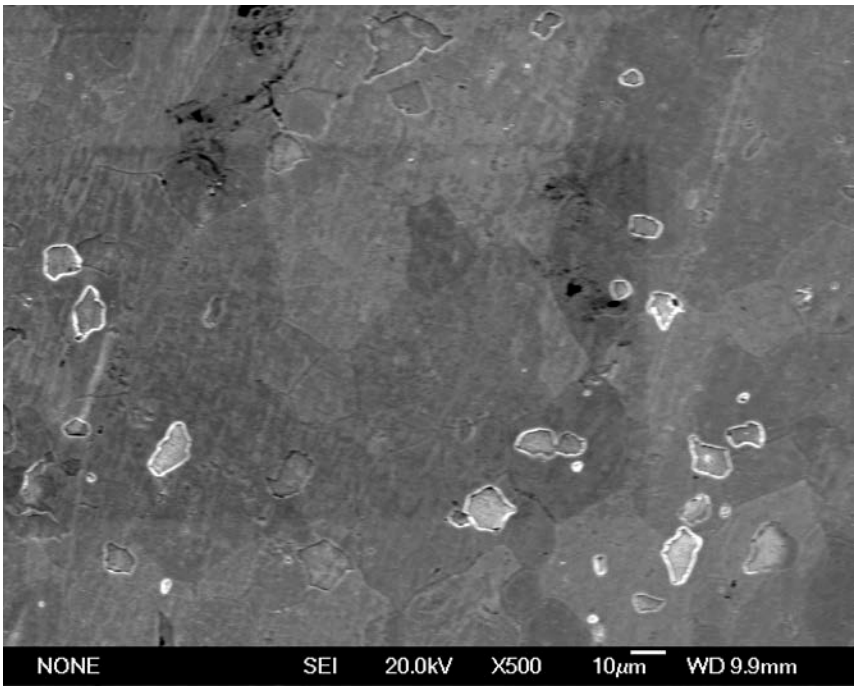

Figure 5-111 SEM image of the "cap" CeO_2 buffer layer

Grain boundaries are clearly seen in the SEM image (Figure 5-142) of the "cap" CeO_2 layer of the buffered substrate; however, the surface of the cap CeO_2 layer may be different when YBCO subsequently grows on the as-deposited buffer layer (*i.e.*, without taking the sample out of the chamber for SEM examination).

5.4.3 YBCO films on Ni:5W substrates

5.4.3.1 Critical temperature of YBCO films deposited on buffered Ni:5W substrate

The critical temperature of a YBCO film deposited on buffered Ni:5W substrate was measured by *AC* susceptibility and is shown in Figure 5-112 a, with T_c of 90 K and a sharp transition. But a small shoulder from 84 to 89 K from the real part of *AC* susceptibility measurement was observed, which sometimes appears also in YBCO films on STO substrates. It is known that Ag could help to improve not only J_c but also T_c of the film, and so Ag nano-dots were added to the last layer of CeO_2 buffer layer with the same number of 15

laser pulses as normal. The superconducting transition of the YBCO film deposited on Ag decorated buffered Ni:5W is shown in Figure 5-112 b, which shows a T_c of 91 K. This value of T_c is almost equal to T_c of a pure YBCO film on STO single crystal deposited at the same conditions as shown in Figure 5-112 c.

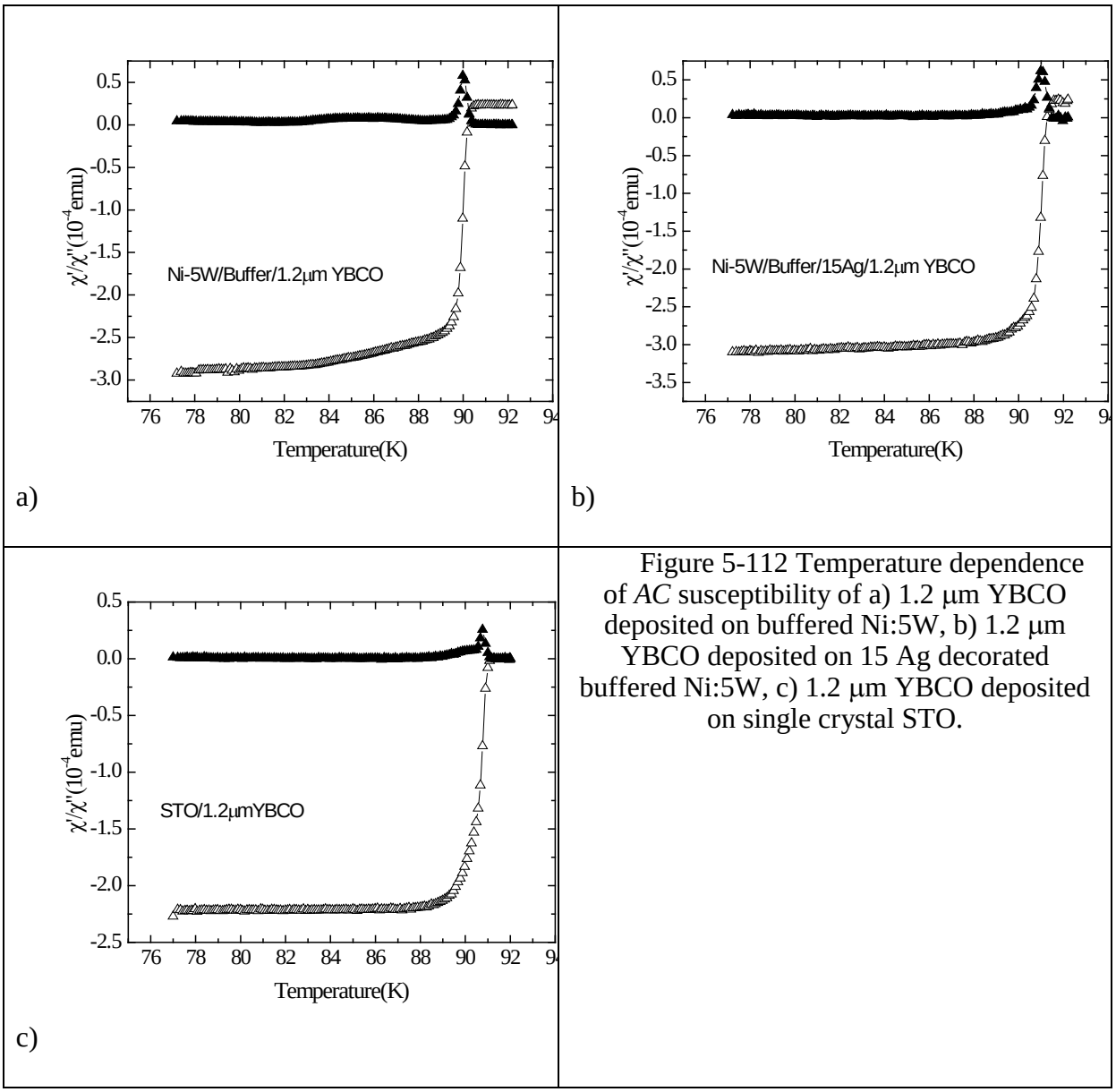

Figure 5-112 Temperature dependence of *AC* susceptibility of a) 1.2 μm YBCO deposited on buffered Ni:5W, b) 1.2 μm YBCO deposited on 15 Ag decorated buffered Ni:5W, c) 1.2 μm YBCO deposited on single crystal STO.

5.4.3.2 SEM images of the surface of YBCO film on buffered Ni:5W substrates

Figure 5-113 and Figure 5-114 show morphological SEM images of YBCO grown on buffered Ni:5W substrate at different magnifications. SEM images reveal no visible cracks on

the YBCO surface and the YBCO has a dense and homogeneous microstructure similar to that on a STO single crystal substrate as shown in Chapter 4. Sub-micron defects such as precipitates, pores, are observed similar to that on a STO substrate.

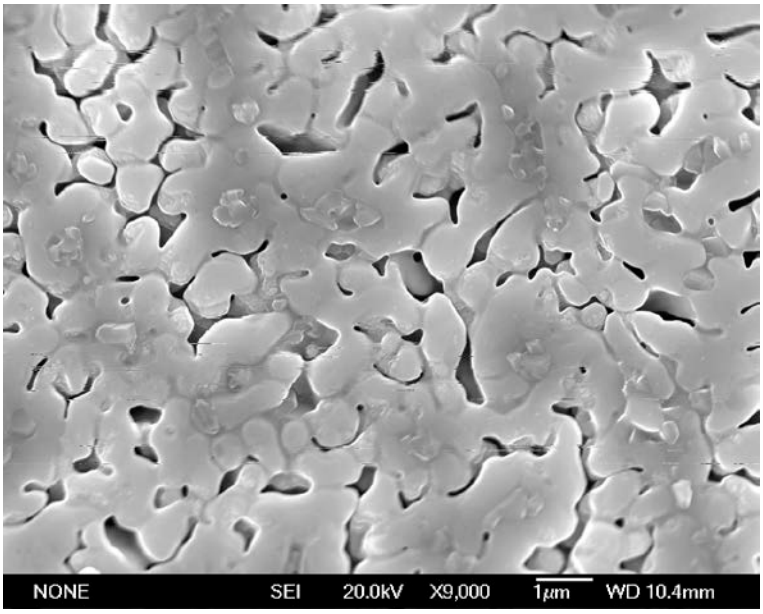

Figure 5-113 SEM image of 1.2 μm YBCO film on buffered Ni:5W substrate.

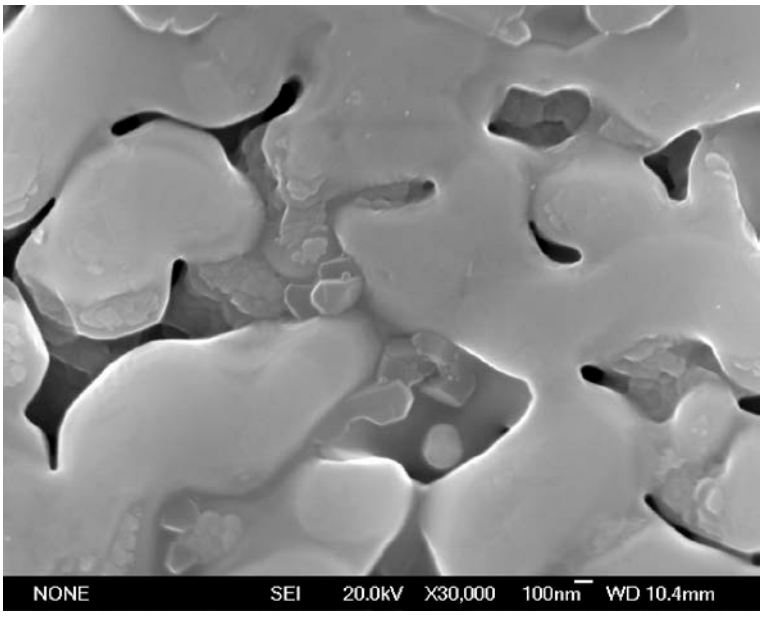

Figure 5-114 High magnification SEM image of 1.2 μm YBCO film on buffered Ni:5W substrate.

5.4.3.3 X-ray diffraction

An XRD 2θ scan obtained for 1.2 μm YBCO film on buffered Ni:5W substrate is shown in Figure 5-115. No a-axis growth or polycrystalline peaks are found, only sharp (00*l*) peaks of the orthorhombic YBCO reflections are observed indicating the epitaxy of the YBCO films. A NiO (111) peak was found in the sample as the Ni:5W substrate was naturally oxidised before and during the growth of buffer layers and the YBCO layer.

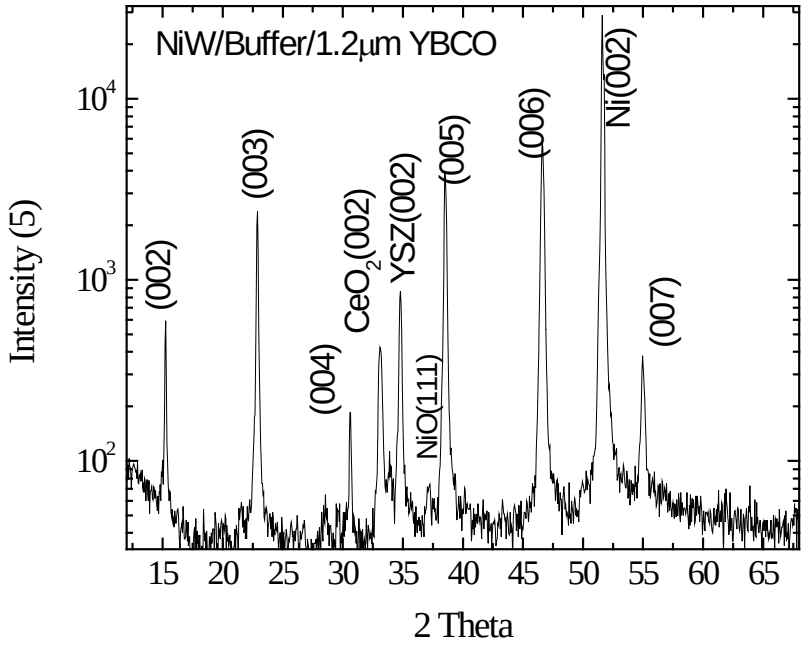

Figure 5-115 X-ray diffraction pattern of 1.2 μm YBCO on buffered Ni:5W

5.4.3.4 Transport measurement of critical current density

The angular dependence of J_c of 1.2 μm YBCO film deposited on Ag decorated buffered Ni:5W at a temperature of 77.3 K is shown in Figure 5-116. Similar to YBCO on STO, the angular dependence of J_c of the film on Ni:5W reveals ab-plane dominant J_c in applied fields. A small secondary peak at *H*//*c* is observed in applied field smaller than 5.5 T. This peak is also observed in Ag decorated YBCO film deposited on STO substrate. However, the value of

J_c at self-field of the film on Ni:5W is one order of magnitude lower than that on the STO single crystal, more works need to be carried out to optimise deposition conditions. Figure 5-117 shows the field dependence of J_c of the film on buffered Ni:5W. The J_c of the film on Ag decorated buffered Ni:5W is quite good in high applied fields. In general, J_c of the film on Ni:5W is comparable with that of on STO substrate at high applied fields. However, J_c of the film on Ni:5W at self-field and low applied fields (< 2T) need to be improved. The low J_c at low applied field of the film may be due to high angle misorientations of the Ni:5W substrate. A better Ni:5W substrate and optimisation of buffer layers could solve this problem.

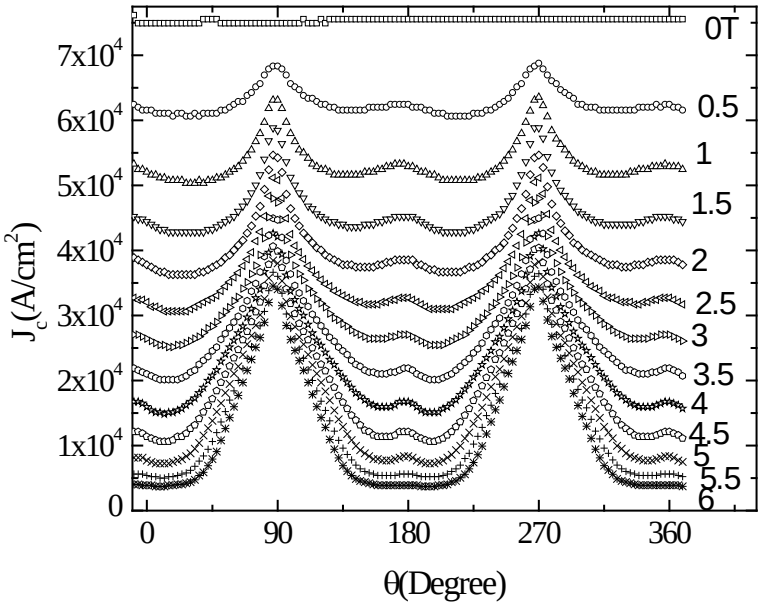

Figure 5-116 Angular dependence of J_c of 1.2 μm YBCO deposited on Ag decorated buffered Ni:5W.

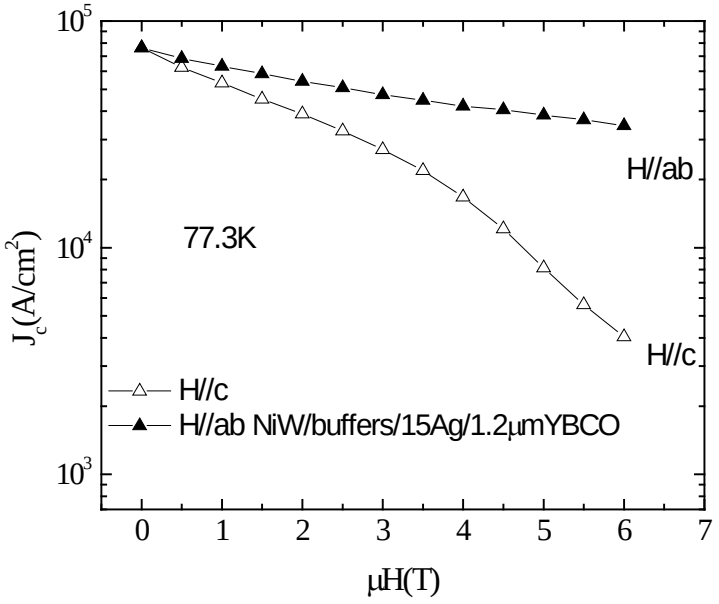

Figure 5-117 Field dependence of J_c of the film on Ag decorated buffered Ni:5W

5.4.4 BZO-doped YBCO film on Ni:5W substrate

5.4.4.1 Critical temperature

The *AC* susceptibility measurements for BZO-doped YBCO films of different thicknesses on Ag decorated buffered NiW substrate with are shown in Figure 5-118 a, b, c. T_c is found at about 89.5 K, 89.8 K and 90 K for the film thickness of 0.4, 1.2 and 2 μm, respectively. Similar to the films on STO, the thicker film shows the sharper transition. At the film thickness of 2 μm, T_c of the film is 90 K which is slightly lower than 90.7 K for the film on Ag decorated STO substrate. All thick films (thicker than 1.2 μm) on Ag decorated buffered Ni:5W substrate show high and sharp T_c and can be competitive with that of the films on Ag decorated STO substrate.

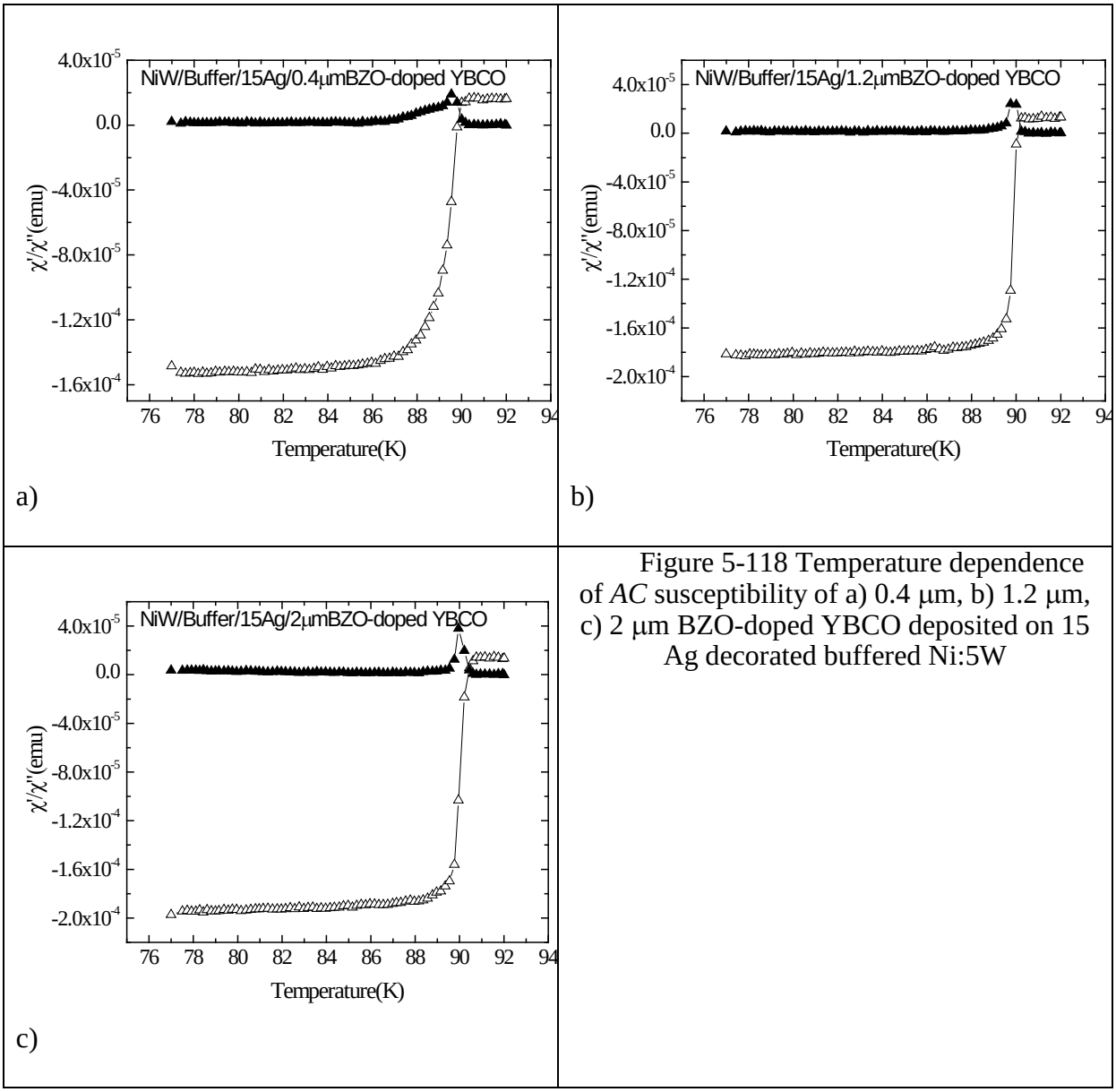

Figure 5-118 Temperature dependence of *AC* susceptibility of a) 0.4 μm, b) 1.2 μm, c) 2 μm BZO-doped YBCO deposited on 15 Ag decorated buffered Ni:5W

5.4.4.2 SEM images of the surface of BZO-doped YBCO on Ag decorated buffered Ni:5W substrates

SEM images of 0.4 μm BZO-doped YBCO on Ag decorated buffered Ni:5W is shown in Figure 5-119 and Figure 5-120. The Figure 5-119 shows clearly grain boundaries as seen in

the cap buffer layer of CeO_2. A higher magnification image shows the specific microstructure of the BZO-doped YBCO film with nano-precipitates and pores.

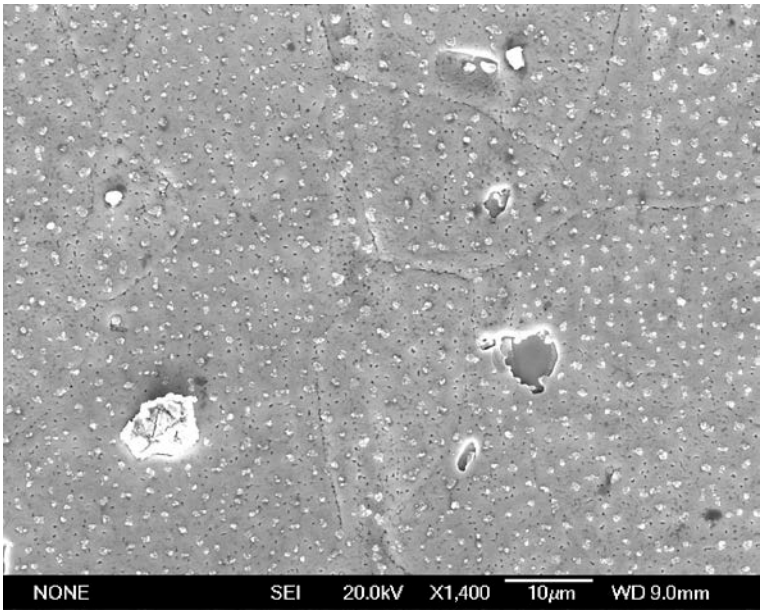

Figure 5-119 SEM image of 0.4 μm BZO-doped YBCO deposited on 15 Ag decorated buffered Ni:5W

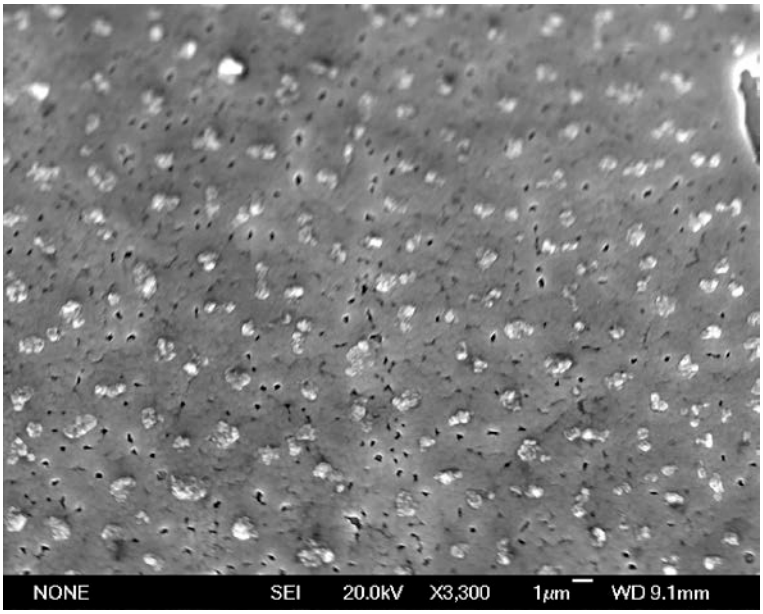

Figure 5-120 Higher resolution of SEM image of 0.4 μm BZO-doped YBCO deposited on 15 Ag decorated buffered Ni:5W

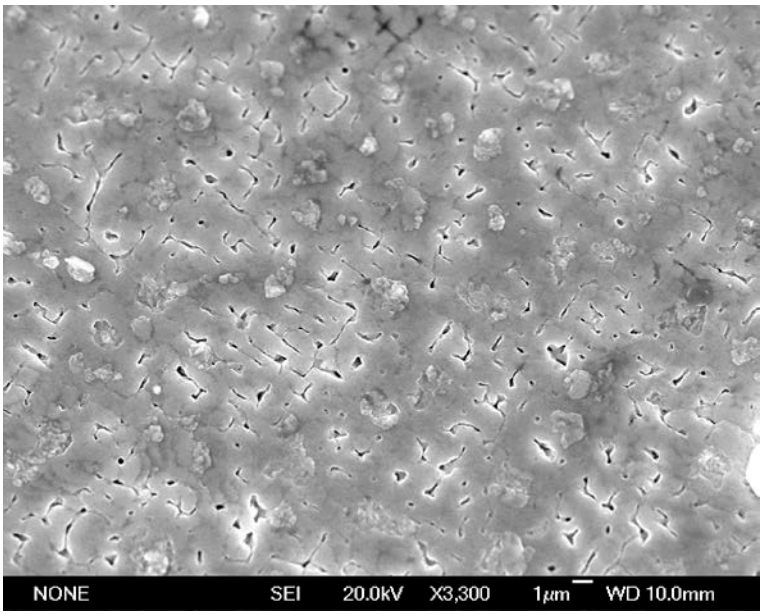

Figure 5-121 SEM image of 1.2 μm BZO-doped YBCO deposited on 15 Ag decorated buffered Ni:5W.

The SEM image of 1.2 μm BZO-doped YBCO on Ag decorated buffered Ni:5W as shown in Figure 5-121 is similar to that of the film on STO with the same thickness. In the thicker film, larger precipitates and a smoother surface were observed.

The SEM image of a 2 μm thick BZO-doped YBCO on Ag decorated buffered Ni:5W at different magnifications is shown in Figure 5-122, Figure 5-123 and Figure 5-124. Up to micron-sized precipitates were observed on the surface of the 2 μm thick film, similar to those seen on the film deposited on STO in section 5.3. However, clusters of precipitates up to 10 μm were also observed in the film on Ni:5W substrate as shown in Figure 5-122 and Figure 5-123, which were absent on the film on STO substrate.. Figure 5-161 shows a region between clusters at high magnification.

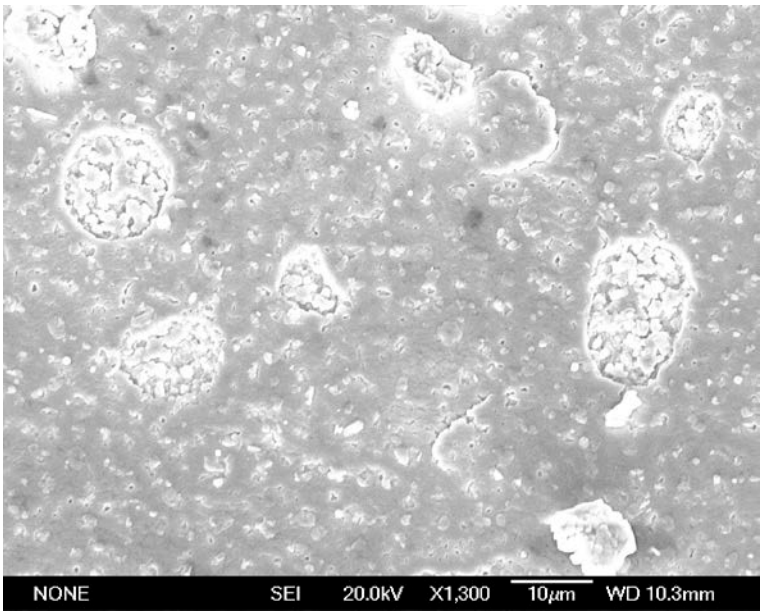

Figure 5-122 SEM image of 2 μm BZO-doped YBCO deposited on 15 Ag decorated buffered Ni:5W.

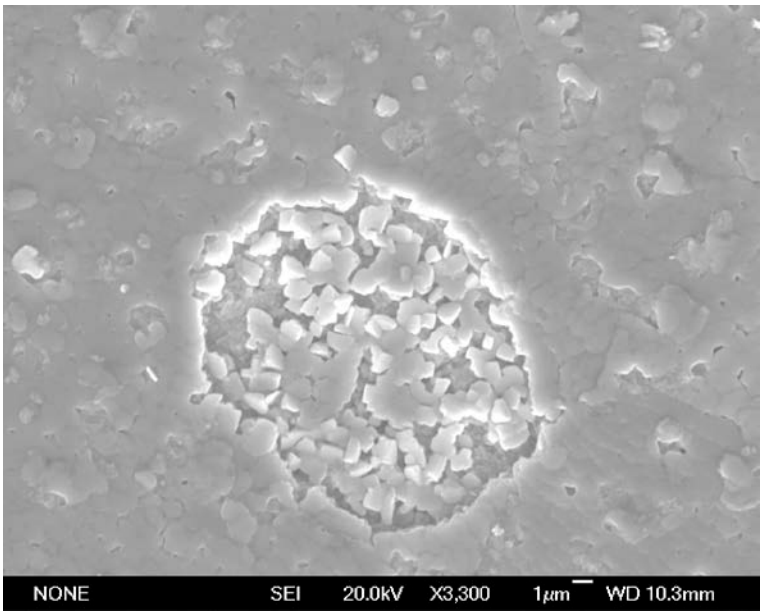

Figure 5-123 Higher resolution of SEM image of 2 μm BZO-doped YBCO deposited on 15 Ag decorated buffered Ni:5W.

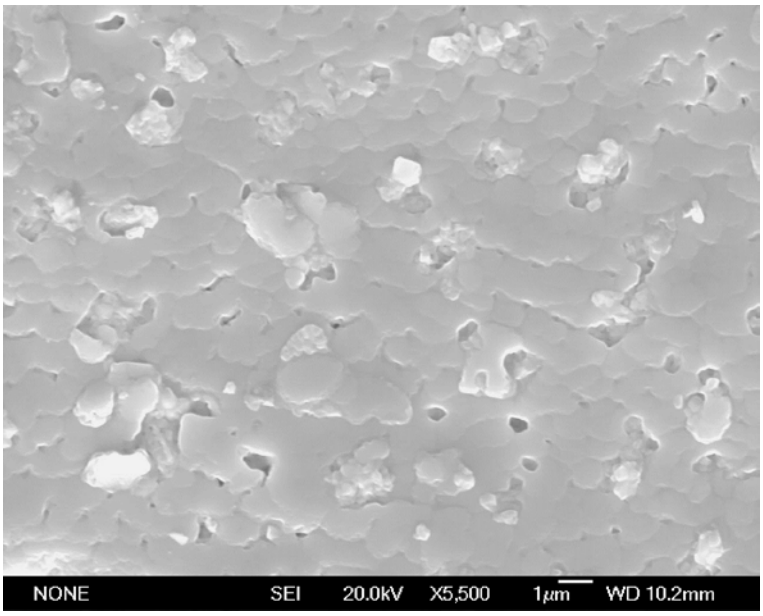

Figure 5-124 Another SEM image of 2 μm BZO-doped YBCO deposited on 15 Ag decorated buffered Ni:5W

5.4.4.3 X-ray diffraction

An XRD 2θ scan of a 1.2 μm BZO-doped YBCO film on Ag decorated buffered Ni:5W substrate is shown in Figure 5-125. The XRD data reveals the highly textural structure of the film as only (00*l*) peaks are observed. Again, a NiO (111) peak is observed in XRD of the film due to naturally oxidised of the Ni:5W substrate. The BZO (002) peak is also observed in the XRD.

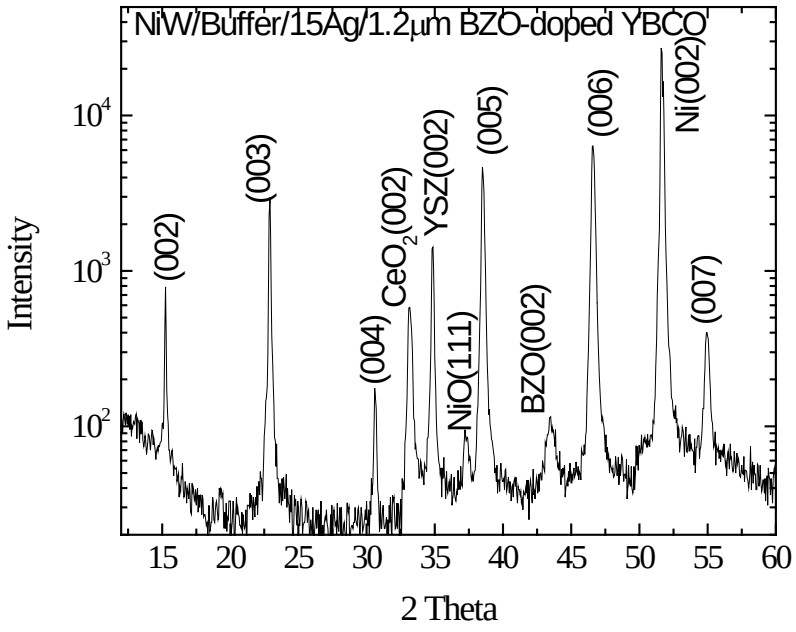

Figure 5-125 X-ray diffraction of 1.2 μm BZO-doped YBCO deposited on 15 Ag decorated buffered Ni:5W

5.4.4.4 Transport measurement of critical current density

The angular dependence of J_c of 2 μm thick BZO-doped YBCO film on buffered Ni:5W substrate at 77.3 K is shown in Figure 5-126. J_c of the film in self-field is 0.2 MA/cm^2 which is one order of magnitude lower than J_c of the film on STO substrate with the same thickness. Instead of dominant J_c along the c-axis at low applied fields as seen in film on STO substrate, the angular dependence of J_c of the film on buffered Ni:5W shows dominant J_c along the ab-plane in applied fields.

A comparison of J_c at different angles, applied field of 0.5 T and temperature of 77.3 K between 2 μm films on buffered Ni:5W and 1.6 μm films on STO substrate is shown Figure 5-127.

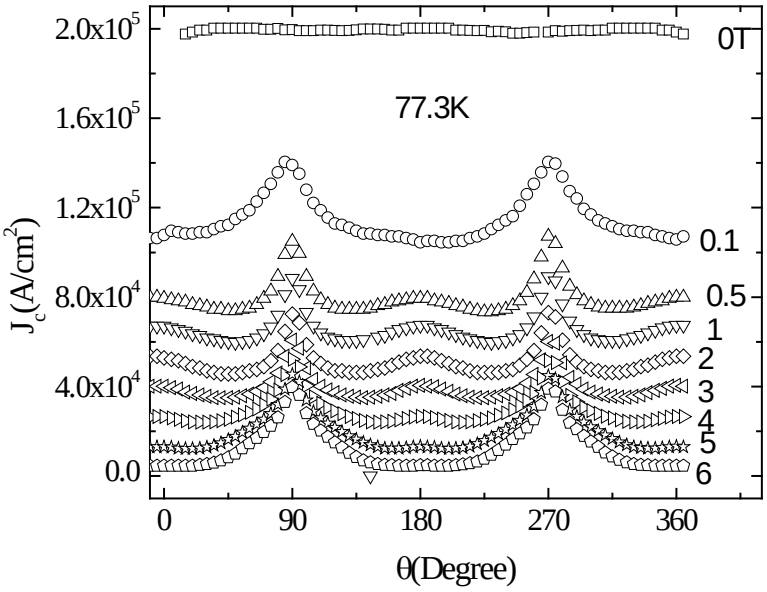

Figure 5-126 Angular dependence of 2 μm BZO-doped YBCO deposited on buffered Ni:5W

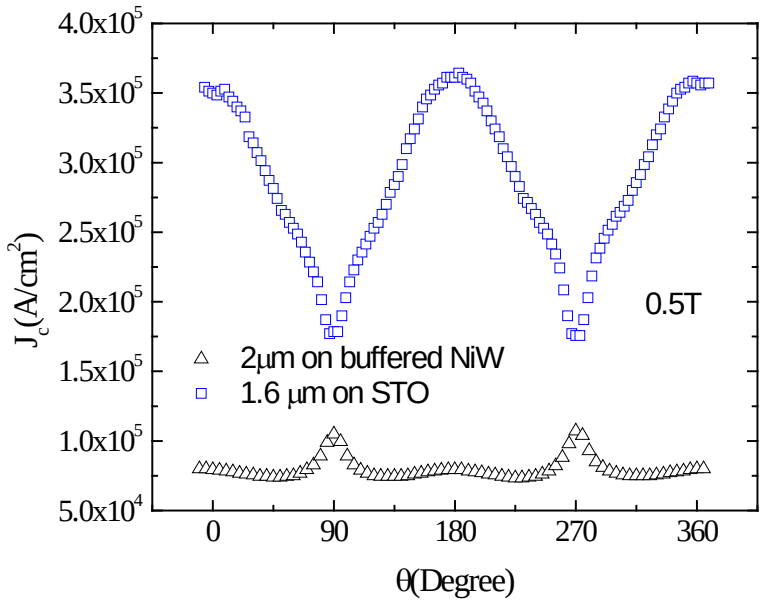

Figure 5-127 Angular dependence of J_c of 2 μm BZO-doped YBCO film on buffered Ni:5W and 1.6 μm film on STO single crystal at 0.5 T and 77.3 K

J_c of the film on Ni:5W substrate is lower than that of film on STO, moreover, J_c of the film on STO shows maximum along the *c-axis* while J_c of the film on buffered Ni:5W shows maximum along the ab-plane as peaks at 90 and 270^o are much higher than peaks at 0, 180 and 360^o. The same situation is observed at angular dependence of J_c of the films at 2 T and 77.3 K as shown in Figure 5-128. However, in applied field of 4 T, J_c at 0, 180 and 360^o of the film on buffered Ni:5W is higher than that of film on STO despite the film on Ni:5W being thicker than the film on STO.

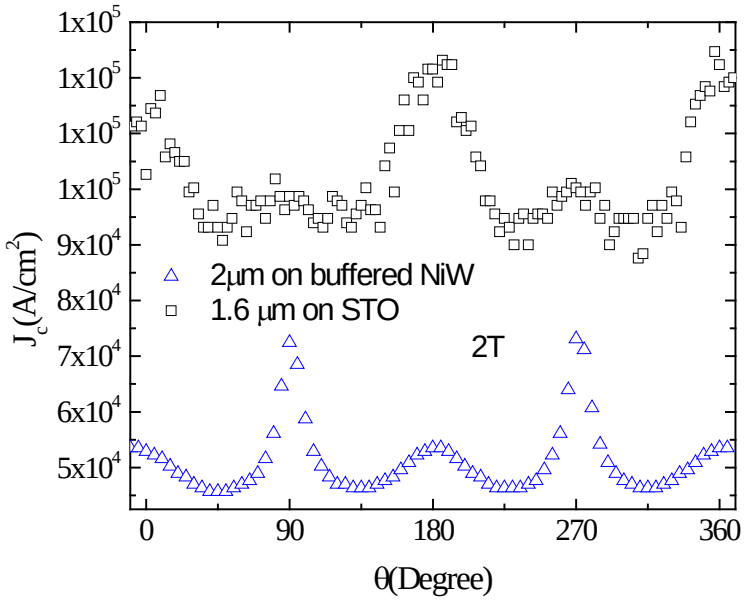

Figure 5-128 Angular dependence of J_c of 2 μm BZO-doped YBCO film on buffered Ni:5W and 1.6 μm film on STO single crystal at 2 T and 77.3 K

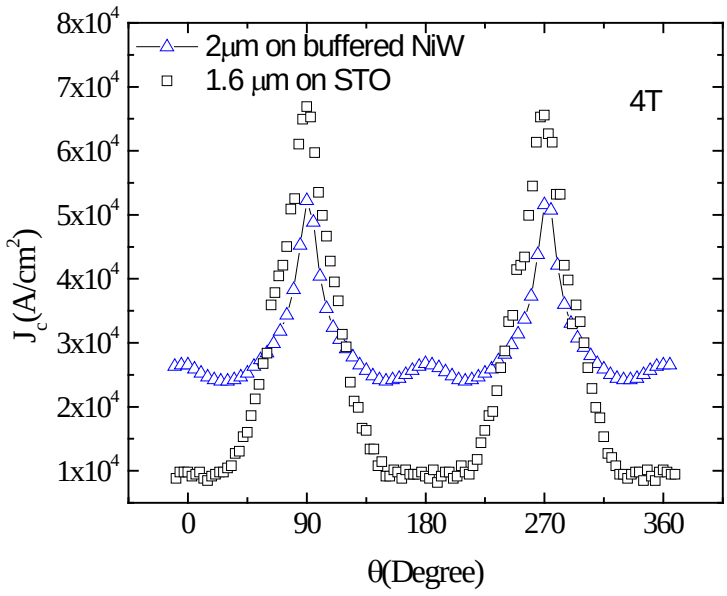

Figure 5-129 Angular dependence of J_c of 2 μm BZO-doped YBCO film on buffered Ni:5W and 1.6 μm film on STO single crystal at 4 T and 77.3 K

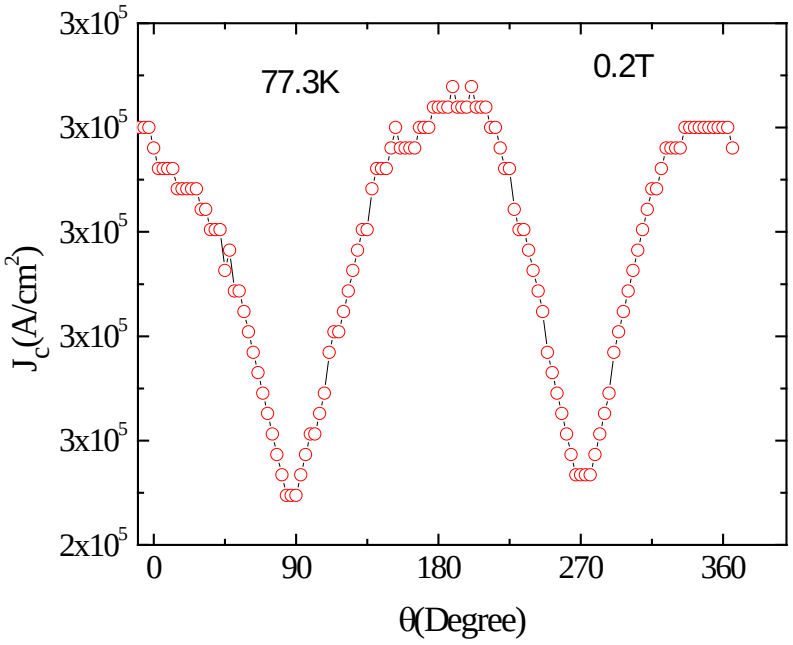

Figure 5-130 Angular dependence of J_c of 0.4 μm BZO-doped YBCO on Ag decorated buffered Ni:5W substrate at 0.2 T and 77.3 K

J_c of a thinner film on buffered Ni:5W was carried out as shown in Figure 5-130, the angular dependence of J_c of 0.4 μm thick BZO-doped YBCO film on Ag decorated buffered Ni:5W substrate. Surprisingly, dominant J_c along the *c-axis* is observed on the thin film at 0.2 T and temperature of 77.3 K. However, things changed at a temperature of 80 K as shown in Figure 5-131. J_c of the film on buffered Ni:5W is 6 times lower than that of the same thickness film on STO substrate at 6 T and 77.3 K in all directions of applied field as shown in Figure 5-132.

A comparison of J_c of a 0.4 μm film on Ag decorated buffered Ni:5W and a1 μm film on STO substrate at an applied field of 3 T and temperature of 77.3 K is shown in Figure 5-133. The J_c of the film on buffered Ni:5W is higher than that of film on STO substrate in all field directions, probably due to its smaller thickness. Moreover, one can see the peak of J_c at 180^o of the film on buffered Ni:5W which is absent on J_c of the film on STO substrate. The peak of J_c at 0, 180 and 360^o may be caused by Ag decoration as normally seen in the Ag decorated STO film. But Figure 5-134 shows J_c of the film on buffered Ni:5W with and without Ag decoration at 3 T and 77.3 K. In both curves, one can see a small peak at 0, 180 and 360^o. This confirms that, in this system, the peak along the c-axis is caused not only by Ag decoration, but also by the lattice defects of CeO_2 layer and the film.

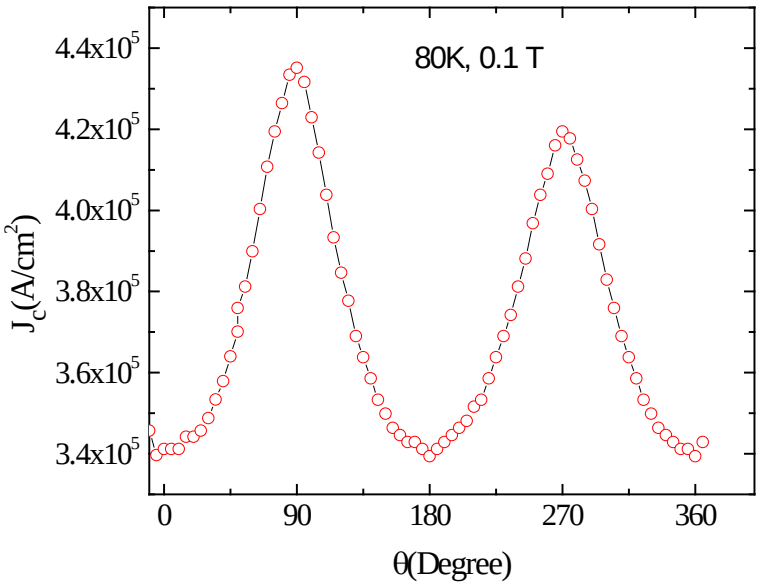

Figure 5-131 Angular dependence of J_c 0.4 μm BZO-doped YBCO on Ag decorated buffered Ni:5W substrate at 0.1 T and 80 K

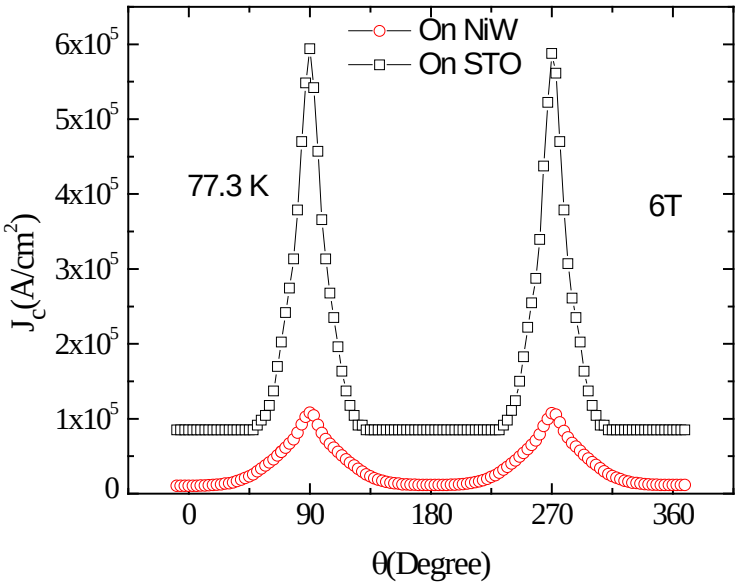

Figure 5-132 Angular dependence of J_c of the film on Ag decorated buffered Ni:5W and Ag decorated STO of the same thickness of 0.4 μm at 6 T and 77.3 K

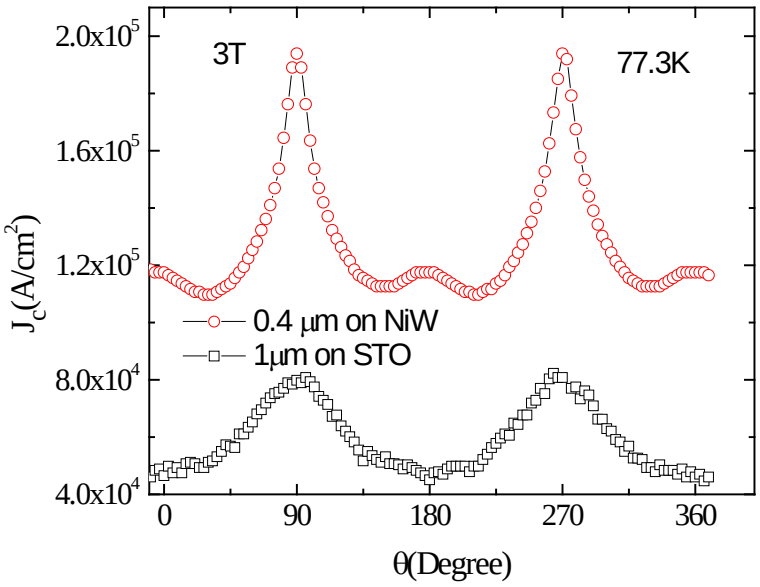

Figure 5-133 Angular dependence of J_c of 0.4 μm thick film on Ag decorated buffered Ni:5W and 1 μm film on undecorated STO at 3 T and 77.3 K

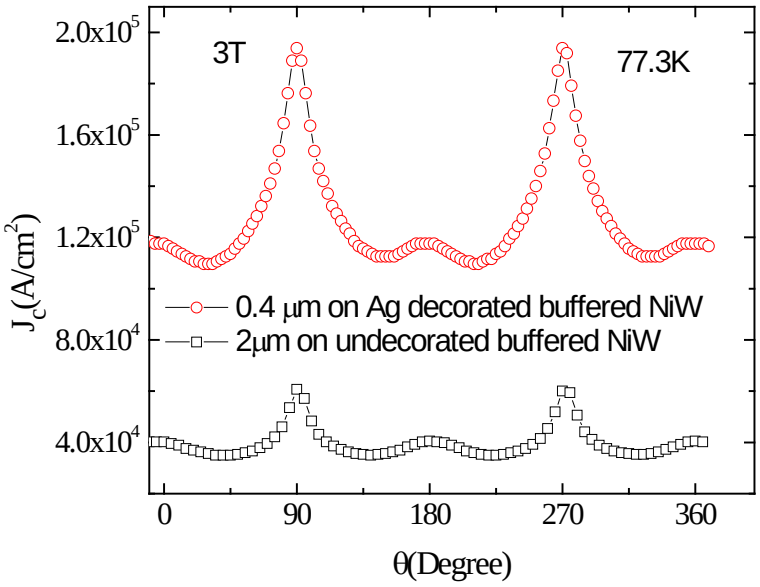

Figure 5-134 Angular dependence of J_c of 0.4 μm thick film on Ag decorated buffered Ni:5W and 2 μm film on undecorated buffered Ni:5W at 3 T and 77.3 K

5.4.4.5 Irreversibility lines of BZO-doped film Ag decorated buffered Ni:5W substrate

Irreversibility lines for 2 μm BZO-doped film on buffered Ni:5W in comparison with that of film on STO is shown in Figure 5-137. The irreversibility lines are determined from magneto-resistance measurements in applied fields *H*//*ab* and *H*//*c* as shown in Figure 5-135 and Figure 5-136, respectively. The irreversibility line of the film on buffered Ni:5W substrate is lower than that of the film on a STO substrate. However, the lines are closer at high applied field. This may correspond to a high J_c of the film on buffered Ni:5W substrate in high applied fields. The anisotropy J_c of the film determined by the ratio of the slopes of the irreversibility is about 3.8 which is somewhat higher than 3.5 of the film on STO substrate.

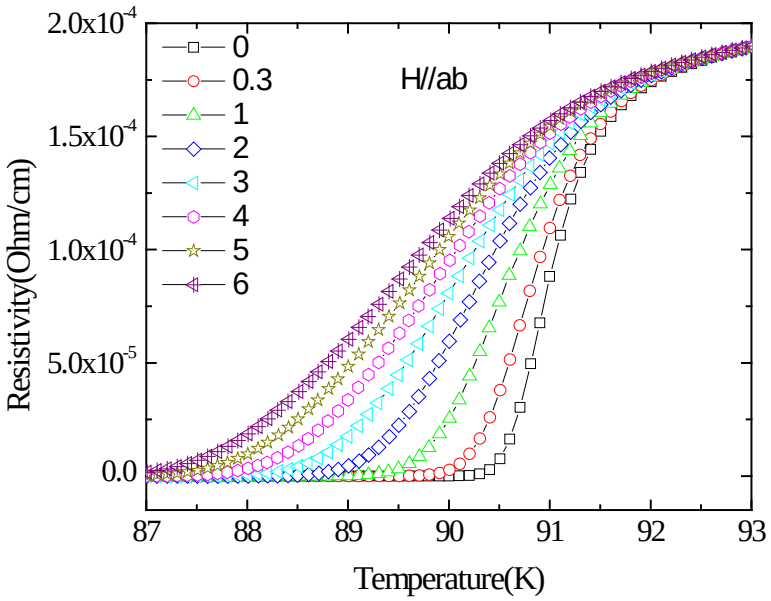

Figure 5-135 Temperature dependence of resistivity of 2 μm film on buffered Ni:5W at *H*//*ab* and applied fields

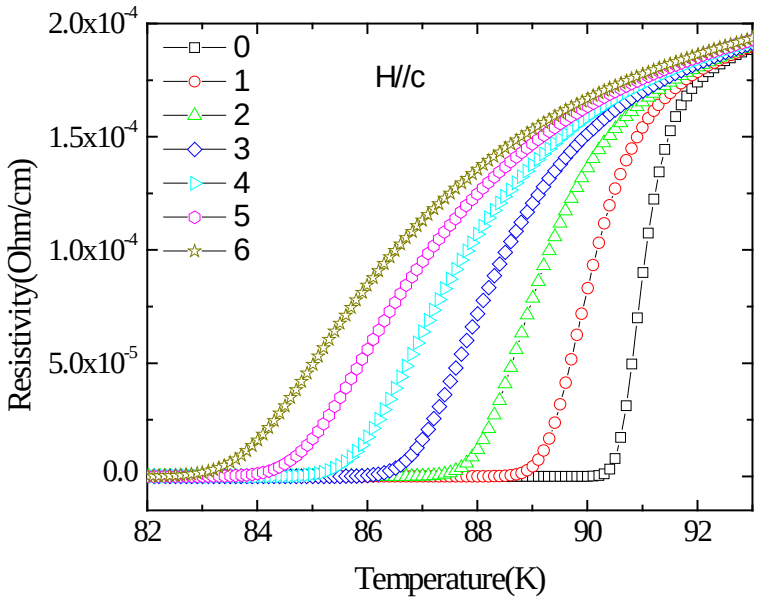

Figure 5-136 Temperature dependence of resistivity of 2 μm film on buffered Ni:5W at *H*//*c* and applied fields

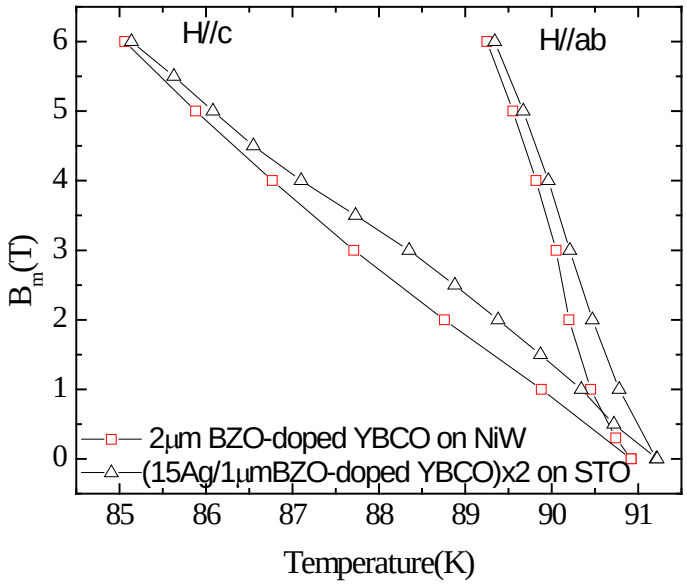

Figure 5-137 Irreversibility lines of BZO-doped YBCO film on buffered Ni:5W and STO single crystal

5.4.4.6 TEM images of BZO doped film on Ag decorated buffered Ni:5W substrate

Interfaces of Ni:5W substrate with buffer layers and the YBCO film are clearly seen in Figure 5-138, the thickness of CeO_2 layers is 95 nm and YSZ layer is 600 nm. The image shows very sharp boundaries between the different layers. An element line scan across the interfaces in STEM mode is shown in Figure 5-139. This is expanded in Figure 5-140 and more detail for each individual element is shown in Figure 5-141. It is clearly seen that no significant diffusion of Ni into the buffer layer or YBCO layer is observed. The oxidation of the Ni:5W substrate is observed as oxygen is present in Ni:5W substrate area. A NiO layer was formed invariably before or during buffer layer deposition [20].

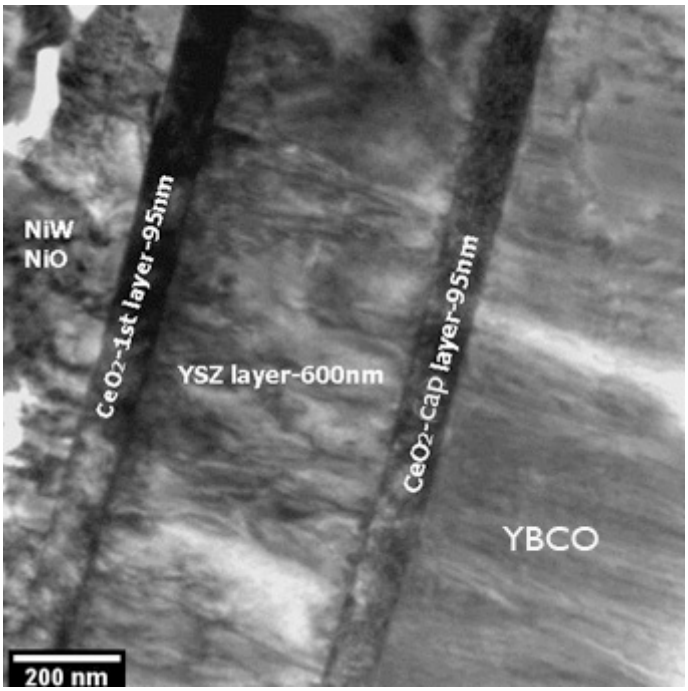

Figure 5-138 Bright field cross section TEM image of the interfaces Ni:5W/CeO_2/YSZ/CeO_2/BZO-doped YBCO

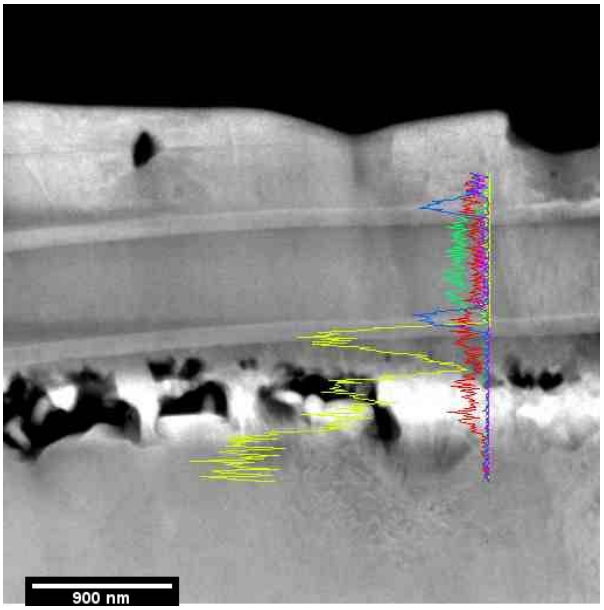

Figure 5-139 STEM image of the interfaces of Ni:5W/CeO_2/YSZ/CeO_2/BZO-doped YBCO, colour line is line scan map

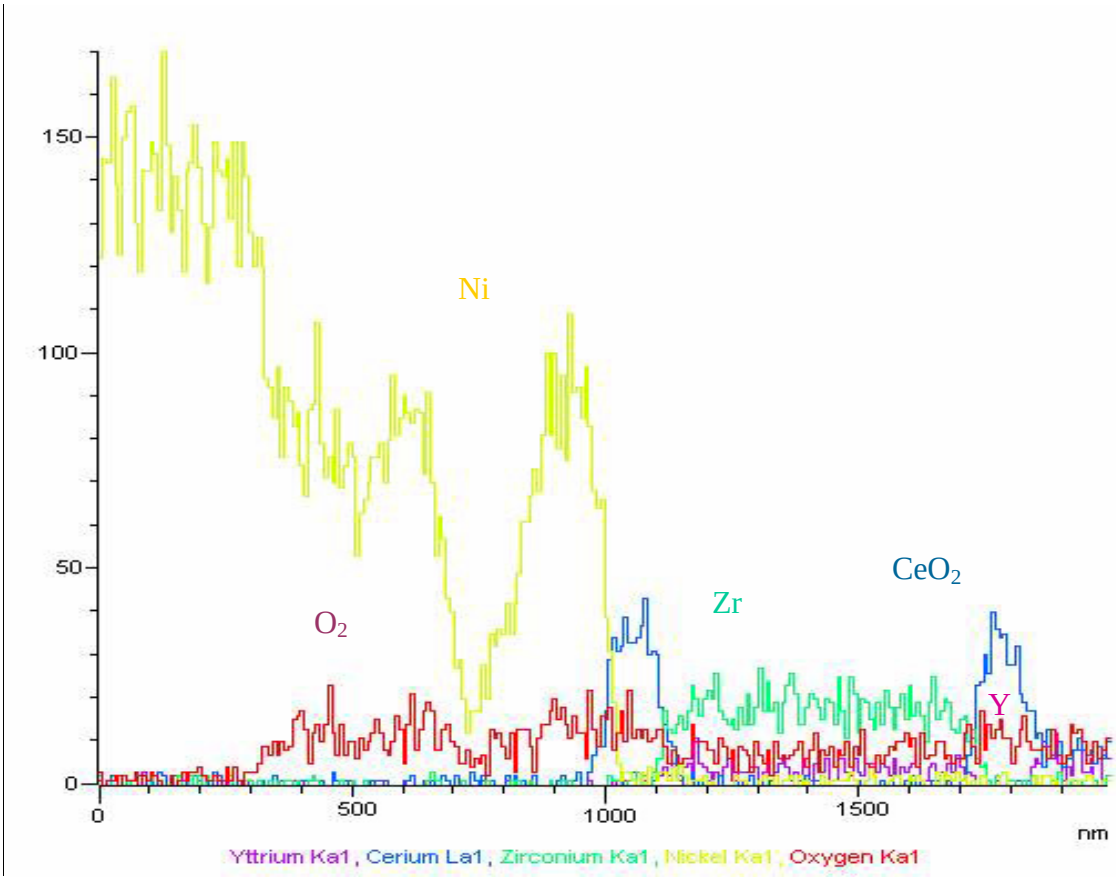

Figure 5-140 Line scan map at the interfaces of substrate/buffers/film for Ni, O_2, Zr, CeO_2, Y

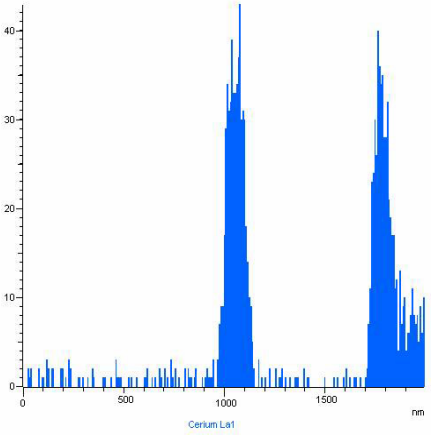

CeO_2

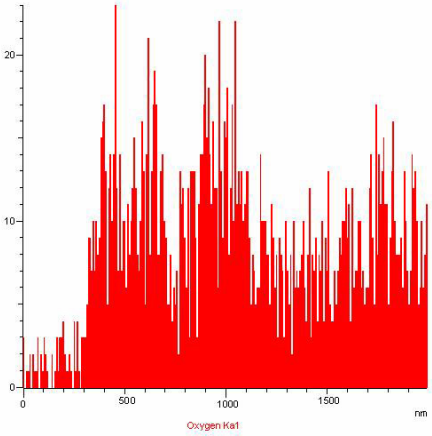

O_2

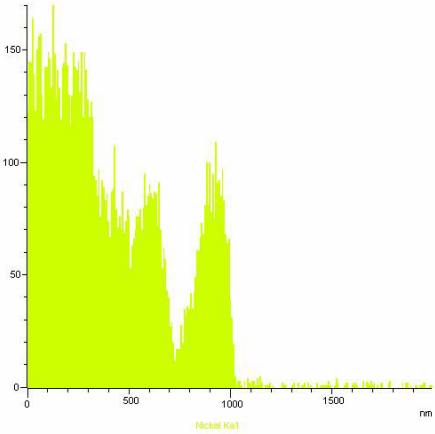

Ni

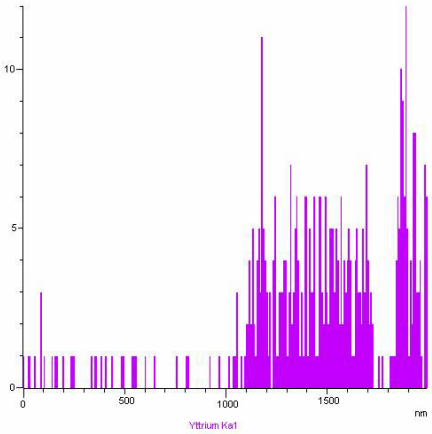

Y

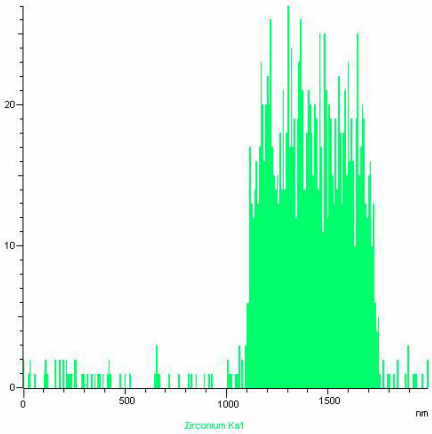

Zr

Figure 5-141 EDX line scan detail for CeO_2, O_2, Ni, Y and Zr from up to down, left to right

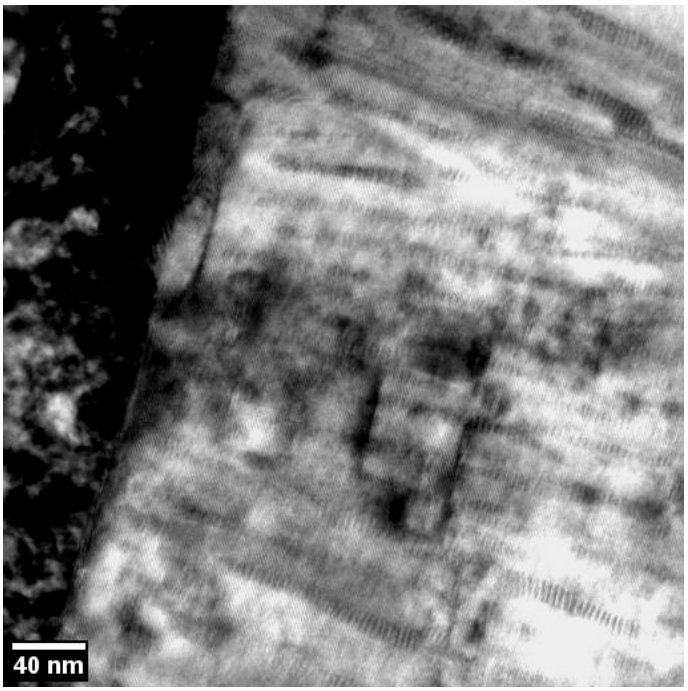

Figure 5-142 Cross section TEM image at film interface between the cap layer and YBCO layer

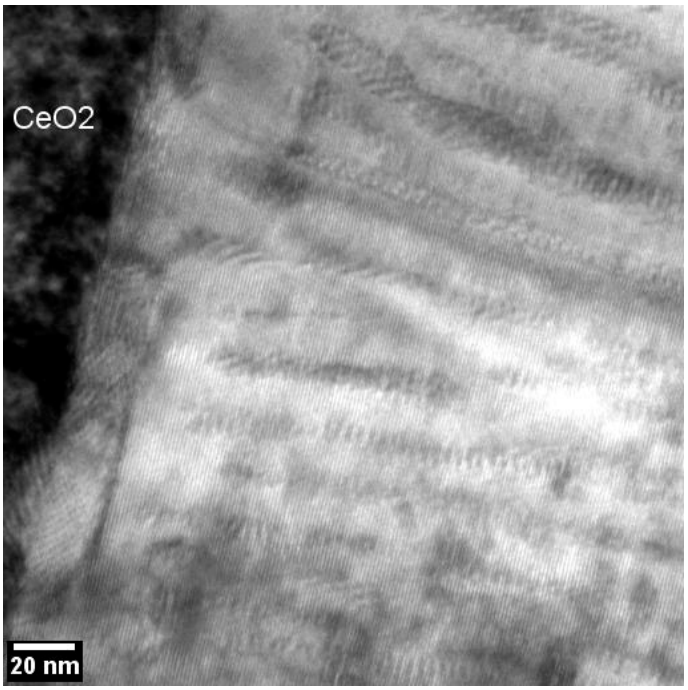

Figure 5-143 Mismatch at CeO_2/YBCO interface

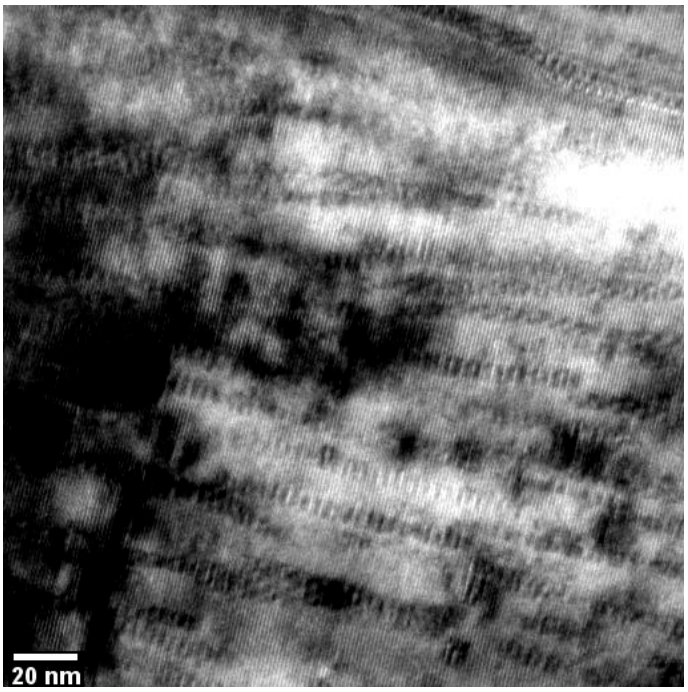

Figure 5-144 Growth of BZO nano-rods in the central area of the BZO-doped YBCO film

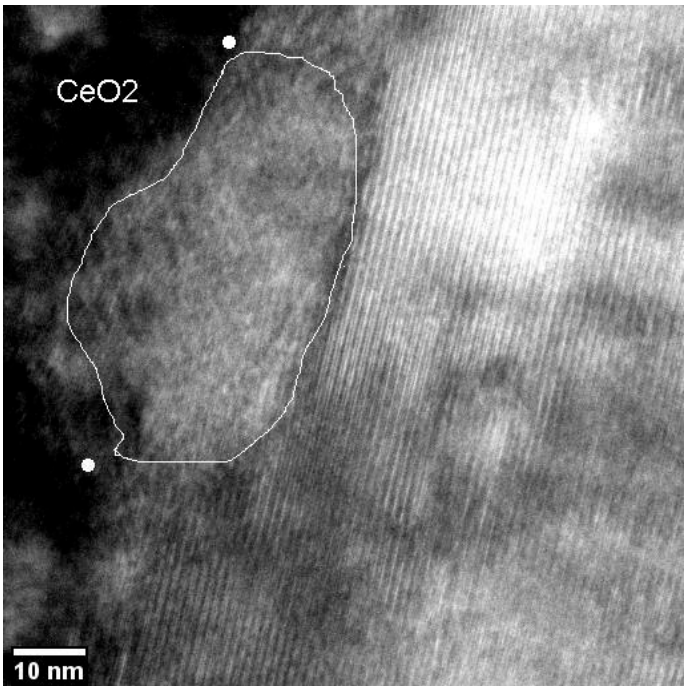

Figure 5-145 A particle of about 20 nm diameter in the boundary of the film and CeO_2 cap layer

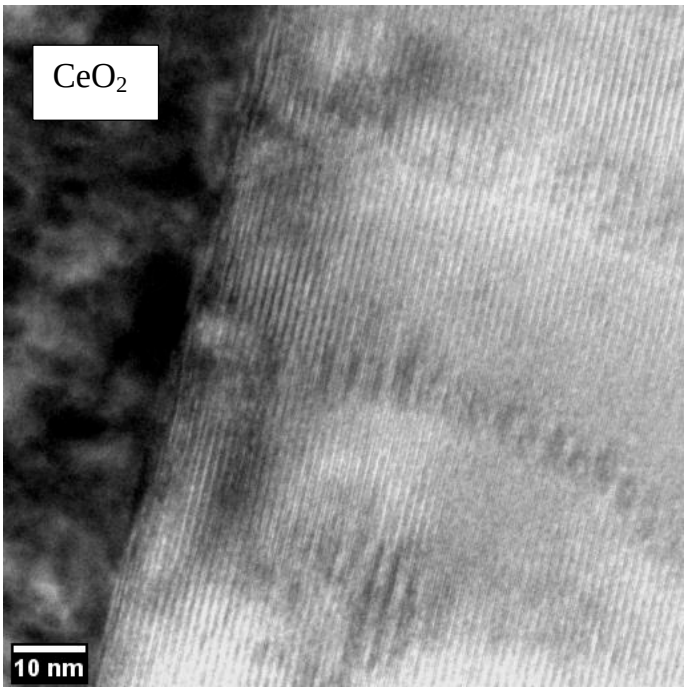

Figure 5-146 Small defects observed in boundary area

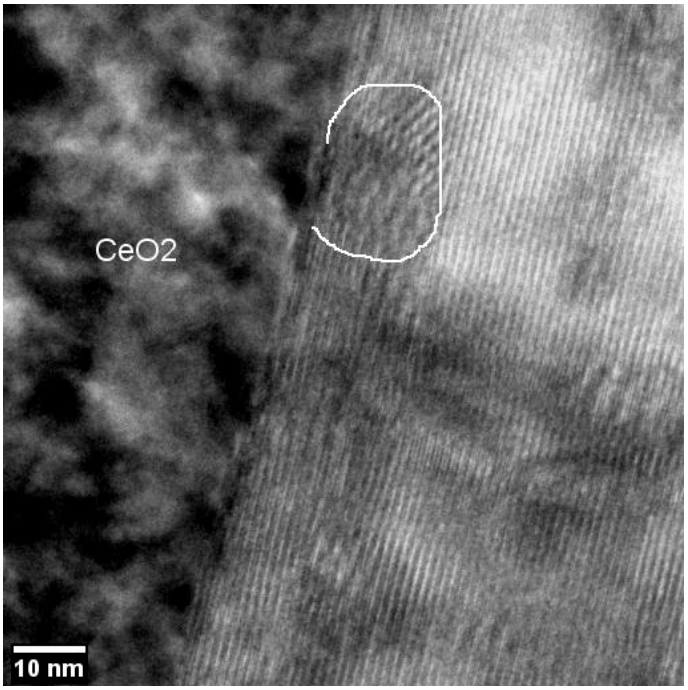

Figure 5-147 Misorientation observed in the boundary area

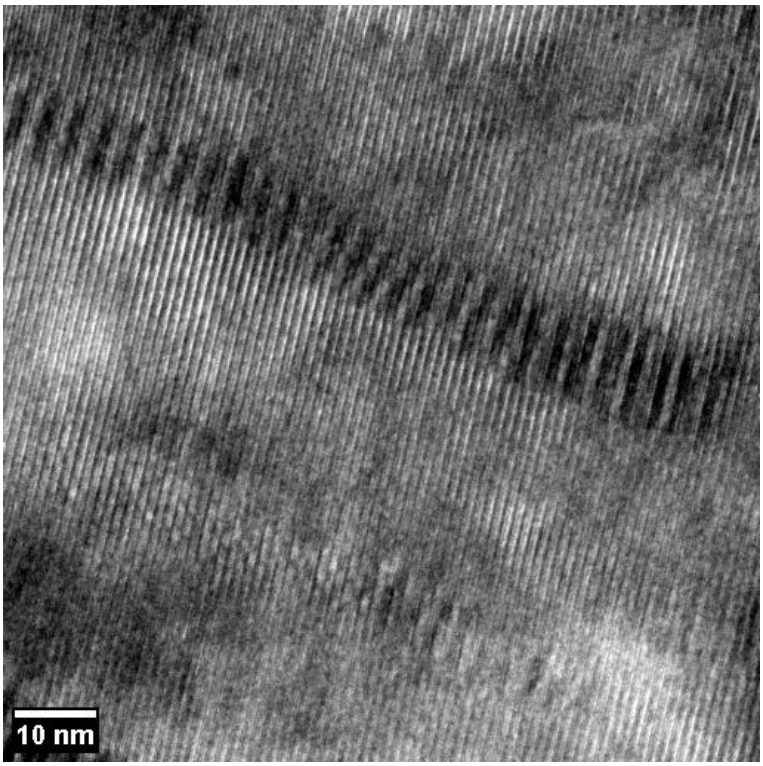

Figure 5-148 BZO nano-rod highly aligned to the c-axis

Similar to BZO-doped YBCO films grown on STO single crystal substrates, the growth of BZO nano-rods is observed in the film deposited on buffered Ni:5W substrate as shown in Figure 5-142, Figure 5-143 and Figure 5-144. In the interface between the film and the cap CeO_2 layer, one can see a defect in the YBCO caused by CeO_2 underlying layer as shown in Figure 5-145, Figure 5-146 and Figure 5-147. Figure 5-148 shows a high magnification image of a single BZO nano-rod inside the YBCO matrix, with the nano-rod aligned highly aligned to the c-axis.

References

[1] J.L. Macmanus-Driscoll, S.R. Foltyn, Q.X. Jia, H. Wang, A. Serquis, L. Civale, B. Maiorov, M.E. Hawley, M.P. Maley, D.E. Peterson, Nature Materials 3/7 (2004) 439.

[2] M. Peurla, P. Paturi, Y.P. Stepanov, H. Huhtinen, Y.Y. Tse, A.C. Boodi, J. Raittila, R. Laiho, Superconductor Science & Technology 19/8 (2006) 767.

[3] H. Huhtinen, M. Peurla, M.A. Shakhov, Y.P. Stepanov, P. Paturi, J. Raittila, R. Palai, R. Laiho, Ieee Transactions on Applied Superconductivity 17/2 (2007) 3620.

[4] G. Blatter, V.B. Geshkenbein, A.I. Larkin, Physical Review Letters 68/6 (1992) 875.

[5] L. Civale, B. Maiorov, A. Serquis, J.O. Willis, J.Y. Coulter, H. Wang, Q.X. Jia, P.N. Arendt, M. Jaime, J.L. MacManus-Driscoll, M.P. Maley, S.R. Foltyn, Journal of Low Temperature Physics 135/1-2 (2004) 87.

[6] N.J. Long, N.M. Strickland, E.F. Talantsev, Ieee Transactions on Applied Superconductivity 17/2 (2007) 3684.

[7] N.J. Long, Superconductor Science & Technology 21/2 (2008).

[8] D.S. Fisher, M.P.A. Fisher, D.A. Huse, Physical Review B 43/1 (1991) 130.

[9] W.K. Kwok, S. Fleshler, U. Welp, V.M. Vinokur, J. Downey, G.W. Crabtree, M.M. Miller, Physical Review Letters 69/23 (1992) 3370.

[10] M. Tihkham, Introduction to Superconductivity, Second edition (1996).

[11] A. Crisan, A. Iyo, Y. Tanaka, Applied Physics Letters 83/3 (2003) 506.

[12] P. Fabbricatore, S. Farinon, G. Gemme, R. Musenich, R. Parodi, B. Zhang, Physical Review B 50/5 (1994) 3189.

[13] Q.X. Jia, S.R. Foltyn, P.N. Arendt, J.F. Smith, Applied Physics Letters 80/9 (2002) 1601.

[14] H. Zhou, B. Maiorov, S.A. Baily, P.C. Dowden, J.A. Kennison, L. Stan, T.G. Holesinger, Q.X. Jia, S.R. Foltyn, L. Civale, Superconductor Science & Technology 22/8 (2009).

[15] P. Mele, K. Matsumoto, T. Horide, O. Miura, A. Ichinose, M. Mukaida, Y. Yoshida, S. Horii, Physica C-Superconductivity and Its Applications 445 (2006) 648.

[16] S.R. Foltyn, H. Wang, L. Civale, Q.X. Jia, P.N. Arendt, B. Maiorov, Y. Li, M.P. Maley, J.L. MacManus-Driscoll, Applied Physics Letters 87/16 (2005).

[17] X. Wang, J.Z. Wu, Applied Physics Letters 88/6 (2006).

[18] Y.L. Cheung, I P Jones, J S Abell, T W Button, E F Maher. Superconductor Science and Technology 20/3 (2007) 216.

[19] S.R. Foltyn, L. Civale, J.L. Macmanus-Driscoll, Q.X. Jia, B. Maiorov, H. Wang, M. Maley, Nat Mater 6/9 (2007) 631.

[20] E. Maher, J. S.Abell, R. I. Chakalova, Y. L. Cheung, TWButton, P. Tixador, Superconductor Science and Technology 17 (2004) 1440.

Chapter 6. **Conclusions and future work**

After optimisation of the growth conditions of YBCO films by PLD using a scanning laser beam, nanostructured YBCO films with artificial pinning centres were fabricated and studied. Both structural and superconducting properties were thoroughly investigated. Film nanostructuring was performed using several techniques: substrate decoration, quasi-multilayer approach, multilayer approach, targets with secondary phase nanoinclusions, and combinations of the above.

6.1 Nano-dots materials

For substrate decoration and quasi-layers noble-metals (Ag) and $PrBa_2Cu_3O_x$ (PBCO) nano-dots were used, and for each nano-dot material the best deposition conditions (substrate temperature, atmosphere in the chamber, number of laser pulses and pulse repetition rate) were determined in an attempt to improve the current transport capability

The optimum conditions in which Ag nano-particles uniformly distributed on the STO substrate and produced the largest improvement of critical current were successfully found to be a deposition temperature of 400^o C and 15 laser pulses on the Ag target and target-substrate distance of about 5.8 cm. Ag nano-particles are uniformly distributed on the STO substrate, with an average diameter of 13 nm and average height of 3.4 nm. The same temperature and number of laser pulses on PBCO target led to the growth of a high number density of PBCO nano-dots, the substrate being almost entirely covered.

6.2 Growth of YBCO films, deposition conditions

Good quality YBCO films were reproducibly grown in our PLD chamber. The optimum growth temperature for YBCO films was found to be 780^o C. All the films deposited at 780^o C have higher J_c than the ones deposited at 800^o C in all applied fields except for zero field.

T_c of the films deposited in optimum conditions is about 90K and ΔT_c< 0.5 K as shown in Table 6-1 .

Table 6-1 Deposition temperature of 780 ^oC was chosen because of sharp T_c and high J_c of the film.

Deposition temperature (^oC) (At the same laser pulse energy, substrate-target distance)	T_c(K)	ΔT_c(K)	J_c(A/cm^2) At 1 T, 77.3 K
750	85.3±0.09	7	Low
780	90±0.09	0.5	1.5x10^5
800	90.7±0.09	1.5	9.8x10^4

Table 6-2 T_c and J_c of the films grown on the STO and MgO substrates at the same conditions

Substrates	T_c (K)	J_c(MA/cm^2) at 0 T and 70 K, film thickness of 800 nm
MgO single crystal	89±0.09	1.8±0.2
STO single crystal	90±0.09	3.7±0.4

STO substrates were chosen for most of the films grown in this project due to higher J_c in comparison with the films deposited on MgO substrate for the same thickness and same deposition conditions as shown in Table 6-2.

The characteristic of pores and particulates on the YBCO surface was observed by SEM and AFM for our YBCO films grown in optimum conditions.

X-ray patterns show only (00l) peaks, while the ratio between intensities of (005) and (004) peaks reveal an oxygen deficiency below 0.1.

6.3 YBCO films on Ag decorated STO substrate

Optimum conditions in terms of achieving high critical current in YBCO grown on Ag-decorated substrates by PLD were found: 15 laser pulses on the Ag target with STO temperature of 400^{o} C, in vacuum, the optimum conditions for YBCO growth being the same as for YBCO on single crystal un-decorated STO substrate (780^{o} C).

Whilst J_c of the films grown on Ag-decorated substrates does not improve for very thin films, significant improvement is observed, in all applied fields, for film thicknesses of 1 μm or higher. This is important for power applications, including cables, in which the relevant parameter is the critical current. An increase of 30% in J_c at 0 T is achieved for the 1 μm-thick film grown on Ag-decorated STO (15 pulses 400^{o} C), in comparison with a YBCO film of the same thickness grown on bare STO as, the increase in J_c is much higher in higher applied magnetic fields.

The X-ray diffraction shows strong (00*l*) peaks. A (103) peak also appears in the thick YBCO film grown on Ag-decorated STO. Despite this misalignment peak, the superconducting properties of the thick film are still very good, with sharp transition and high J_c. The T_c of the 1μm-thick film grown on Ag-decorated substrate is 89.7 K which is somewhat lower than that of an YBCO film on a bare STO substrate.

6.4 Quasi-multilayer of Ag/YBCO films

By using quasi-multilayer architecture of Ag/YBCO, J_c of thick films remains quite high in comparison with single layer YBCO thin film as shown in Table 6-4. Quasi-multilayers of (15Ag/1.5μm YBCO)xN with N = 2 and 3, having thickness of 3 and 4.5 μm, respectively, have been successfully fabricated with high J_c in self-field and in applied fields, so that an

extrapolated maximum I_c of 1141 A/cm-width has been achieved at 70 K from results on small samples with in the 3-layer film. With quasi-multilayer architecture of (15Ag/450nm YBCO)xN, a maximum I_c of 767 A/cm-width has been achieved with N = 5 at 70 K. In both quasi multilayer architectures, the T_c of the optimum films is still as high as 89.9 K with a very sharp transition width $\Delta T < 0.5$ K.

J_c measured using the *AC* susceptibility method shows that, in high applied fields of 3, 4 and 5 T, multilayers (15Ag/1.5μmYBCO)xN (N = 2 and 3) and (15Ag/450nm YBCO)x5 have J_c higher than pure thin YBCO in the same applied field and at the same frequency. The frequency dependence of J_c of our films is very well described by Zeldov's model (a linear dependence in a double logarithmic scale). From this fit, the average pinning potential of the pinning centres in the films was found. The higher pinning potential in high fields of 4 and 5 T occurs in the (15Ag/1.5μmYBCO)x2 film, while at 3 T the higher pinning potential is found for the (15Ag/450nm YBCO)x5 quasi-multilayer.

Pinning mechanisms in the multilayer films were analysed using the Dew-Hughes model. The main types of pinning in our multilayer films were classified as normal-core surface pinning, Δκ-core volume pinning and normal-core point pinning, with the dominant pinning mechanism being the normal-core surface pinning, with more than 80% contribution to the total pinning force.

Field-orientation (angular) dependence of J_c of the films was determined from transport measurement. The results show no secondary peak of J_c along the c-axis in the (15Ag/450nm YBCO)x1 film, while small secondary peaks of J_c along the c-axis were observed in thicker films (15Ag/450nm YBCO)x10 and (15Ag/1.5μm YBCO)x1 in high fields. The films have a reduced effective anisotropy of critical currents, with small anisotropy factors of 3 or 3.5 which are smaller than the 5 – 7 range typical of pure YBCO. This reduced anisotropy of

critical current makes the multilayer architectures more appealing for practical applications, especially coils in high fields and at temperature not far below T_c. The secondary peak in J_c along the c-axis is clear evidence of the existence of extended defects along the c-axis.

Thick multilayer films show imperfect epitaxial growth, as indicated by the additional (103) peak in the XRD. The film surface is structured by islands with hundreds of nanometre, diameter and with a smaller number of pores than in thin films. Clear evidence of Y-rich (Y_2O_3) nano particles is observed in the multilayer films, by TEM, STEM and EDX mapping. Such nanoparticles are effective isotropic pinning centres which enhance J_c of the film in all directions. The columnar structure of the film observed by TEM is responsible for the secondary J_c peak along the c-axis observed in several quasi-multilayers in various conditions.

6.5 BZO-doped YBCO films

The optimum conditions of 800^o C and laser frequency of 3 Hz for BZO-doped YBCO film were found for the growth of BZO nano-rods. The improvement of J_c of the BZO-doped YBCO film deposited at optimum conditions was observed in applied fields. However, in self-field, J_c of the BZO-doped YBCO film did not exceed J_c of the pure YBCO film. The dominant J_c along the c-axis in low applied fields was observed in the film deposited at high temperature and low frequency.

4wt % BZO-doped YBCO films were successfully fabricated in optimum conditions which promote the c-axis columnar growth of BZO. The critical temperature of 89.7 K of the films produced in optimum conditions is very close to the value of T_c of pure YBCO film of 91 K with very sharp transition of 0.5 K. J_c of BZO-doped YBCO films show large improvement in applied fields (but not in self-field) in comparison with J_c of pure YBCO

films under the same deposition conditions. The growth of BZO nano-rods leads to the improvement of J_c of the film along the c-axis in low applied fields, but the usual larger J_c along the ab-plane was observed in high applied fields. Low anisotropy of critical current density in magnetic fields between 2 to 3 T, an important range of fields for some practical applications, especially MRI, was also observed. The angular dependence of J_c of the film is very well fitted with the Long model in all applied fields at 77.3 K. The fitting of frequency-dependent J_c shows a high pinning potential of BZO-doped YBCO film in comparison with that of YBCO films or Ag/YBCO multilayer films. The formation of BZO nano-rods provides not only high J_c but also high vortex melting temperature in a wide range of magnetic fields in relatively thick YBCO films. The TEM images reveal the formation of BZO nano-rods and self-growth of Y_2O_3 and CuO_2 in the YBCO matrix. The film defects which are candidates for flux pinning centres observed by TEM and SEM are summarised in Table 6-3.

Table 6-3 Film defects observed by TEM and SEM

Defects	Planar	Points	Surface roughness	Columns	Precipitates
Observed	Yes	Yes (nano-particles)	Yes	Yes (dominant)	Yes

6.6 Combination of Ag substrate decoration and deposition of BZO-doped YBCO films

Ag-decorated BZO-doped YBCO single layer and multilayer films show a significant improvement of J_c in applied fields and self-field in comparison with that of BZO-doped

YBCO film on non-decorated STO substrate. However, the improvement of J_c at self-field of the BZO-doped YBCO film on Ag-decorated substrate is still lower than that of the pure YBCO film with the same thickness. Ag nano-dots also help to improve T_c of the film up to 1 K more than the best BZO-doped YBCO film without Ag decoration. The angular dependence of J_c of decorated films shows a small secondary peak of J_c in applied field parallel to the c-axis even in high fields of 4 to 5.5 T at 77.3 K, which is absent in undecorated film. The evidence of active pinning centres caused by Ag nano-dots was also observed in the vortex melting temperature which shows an improvement in comparison with undecorated films. High critical current per cm width of thick Ag/BZO-doped YBCO film was achieved in a 6 μm-thick -trilayer film which has I_c of 1712 A/cm-width and 812 A/cm-width at self-field and temperature of 65 K and 77.3 K, respectively; in an applied field of 0.5 T those values become 1078 A/cm-width and 330 A/cm-width in applied field of 0.5 T and temperature of 65 K and 77.3 K, respectively. Quasi multilayer architecture may not be suitable for long length coated conductors due to long deposition times and many traverses of the tape through the different deposition processes. However, this is quite suitable for applying in the cylindrical coated conductor geometry.

The existence of Ag nano-dots in the film and at the STO substrate interface still remains a question. No evidence of Ag nano-dots is observed by TEM images. More detail of this work needs to be done in this regard.

6.7 YBCO and BZO-doped YBCO films on RABiTS Ni:5W substrate

YBCO and BZO-doped YBCO films have been successfully deposited on buffered Ni:5W with or without Ag decoration. The T_c of the film on buffered Ni:5W is close to the T_c of the film on STO single crystal substrates. J_c of the film on buffered Ni:5W is about one

order of magnitude lower than that of films on the STO substrates in applied fields smaller than 3 T. Dominant J_c along the c-axis in low applied fields and 77.3 K was not observed as was the case of the BZO-doped YBCO film on the STO substrate. That is why J_c of the film in low applied field perpendicular to the film surface is lower than that of the film on the STO substrate. The growth of dense BZO nano-rods was also observed in the film on buffered Ni:5W substrates. A summary of all J_c of all the best samples is shown in Table 6-4.

Table 6-5 Comparison of T_c and J_c at 0 T, 1 T, and 3 T at 77.3 K of BZO-doped YBCO film on Ag decorated STO and non-decorated STO and pure YBCO on non-decorated STO, and BZO-doped YBCO on buffered Ni5W

Samples	T_c(K)	J_c(0T) (MA/cm^2)	J_c(1T) (MA/cm^2)	J_c(3T) (10^4 A/cm^2)
BZO-doped YBCO (2μm) on non-decorated STO	89.2±0.09	1.2±0.08	0.3±0.02	3±0.1
BZO-doped YBCO (2μm) on 15 Ag decorated STO	90.8±0.09	1.4±0.09	0.4±0.02	5±0.3
YBCO (2μm) on non-decorated STO	90±0.09	1.8±0.1	0.1±0.02	1±0.08
2 μm BZO-doped YBCO on buffered Ni:5W	90±0.09	0.2±0.05	0.07±0.004	4±0.2
(15Ag/1.5 μm YBCO)x2 on STO	89.5±0.09	2.2±0.1	0.2±0.01	0.9±0.04
(15Ag/ 450nm YBCO)x5 on STO	89.5±0.09	2.0±0.1	0.2±0.01	0.5±0.02

6.8 Future work

For future work on nanostructured YBCO films on single crystal substrates the use of targets with other types of nano-inclusions (zirconates, tantalates, $RE_2Ba_4CuMO_y$ (RE-rare-earth, M= W, Nb), double-perovskites, combinations), in conjunction with Ag quasi-layers should be investigated. More studies on Au and PBCO nano-dot materials are necessary.

The improvement of J_c of the Ag decorated YBCO or BZO-doped YBCO is clearly observed in this project. However, the mechanism of pinning caused by Ag nano-dots is still not very clearly understood. More work on TEM and STEM needs to be done to clarify the position of Ag nano-dots in the YBCO matrix.

The Ag decorated YBCO film and BZO-doped YBCO film were successfully deposited on buffered Ni:5W substrates. However, three buffer layers as used in this project may be too costly for implementing into a scaled-up fabrication process. Simplification of the buffer layer architecture is suggested for future work. Improvement of critical current density of the film on buffered Ni:5W substrate in both self-field and applied fields is needed for future work. Such improvement will be most likely related to the fabrication of much better buffered metallic substrates, with a much smaller content of grains with high angles of misalignment. Any new results should be applied to the Ag decorated YBCO film and BZO-doped YBCO film.

The role of the Ag decoration on the buffer layer of the Ni:5W substrate is still not clear, because the surface of the buffer layer is not as smooth as the surface of STO single crystal.

The IBAD substrate is better for most real applications than Ni:5W due to its non-ferromagnetic property, and consequent lower ac losses, and so moving to IBAD substrates is also suggested for future work to obtain films with higher critical current density for

applications in magnetic fields. For reasons of cost, and especially in cable applications, Ni:W RABiTS-based coated conductor will co-exist with IBAD-based equivalents for some time to come.

.